Doctoral Dissertation

Development of Coupled CFD-FEA Method for Ship Structural Load and Its Application to Extreme Value Prediction by FORM

(船体構造荷重のためのCFD-FEA連成解析法の開発とFORMによる極値推定への応用)

TOMOKI TAKAMI

December 2018

Graduate School of Engineering,
Osaka University

Contents

1. INTRODUCTION……1
1.1 Background……1
1.2 Literature Reviews……3
1.2.1 Structural response assessment under combined loads……3
1.2.2 Extreme load and structural response predictions……7
1.3 Objectives……10
1.4 Outline of Thesis……12
References in Chapter 1……13
2. MATHEMATICAL FORMULATION……20
2.1 CFD Formulation……20
2.2 FEA Modeling……24
2.2.1 1D beam model……24
2.2.2 Scale FE model……25
2.2.3 Prototype full scale ship……27
2.3 CFD+FEA by One-way Coupling……28
2.4 CFD+FEA by Two-way Coupling……31
2.4.1 Weakly coupled method……31
2.4.2 Strongly coupled method……34
References in Chapter 2……37
3. SUBJECT SHIP AND EXPERIMENTAL MODEL……38
3.1 Description of Models……38
3.1.1 Segmented model with backbone (Backbone model)……38
3.1.2 Segmented model with beam specimen (OU model)……40
3.2 Measurement……47
3.2.1 Natural frequency and damping……47
3.2.2 MPWE generation by wave maker……49
3.2.3 PoE evaluation by OU model……51
References in Chapter 3……53
4. VERIFICATION AND VALIDATION OF CFD-FEA COUPLED METHOD……54
4.1 Mesh Size and Time Increment Verification of CFD……54
4.2 Numerical Methods for Validation……56
4.2.1 Linear strip method……57
4.2.2 Nonlinear strip method……57

4.2.3 Combination of 3D panel method and FEA……58
4.3 Rigid Body Motion Benchmarks……58
4.3.1 Benchmarks with other methods……58
4.3.2 Validation of two-way coupled methods……59
4.4 Local Pressure…… 63
4.4.1 Rigid body CFD……63
4.4.2 Validation of two-way coupled methods……63
4.5 Wave-induced and Whipping VBM……67
4.5.1 Benchmarks of one-way coupled method with other methods……67
4.5.2 Validation of two-way coupled methods……68
4.6 Application to DBM evaluation……73
4.6.1 General……73
4.6.2 Results and discussion……73
4.7 Summary of Chapter 4……78
References in Chapter 4……80
5. FORM BASED EXTREME VALUE PREDICTION……82
5.1 Theoretical Background……82
5.1.1 General……82
5.1.2 Design point detection……84
5.2 Predictor-Corrector Approach……86
5.3 Reduced Order Method……87
5.3.1 ROM for wave-induced VBM……88
5.3.2 ROM for DBM……91
5.3.3 ROM for whipping VBM……92
5.4 Limit State Functions for VBM and DBM……96
5.4.1 LSF for VBM……96
5.4.2 LSF for combined VBM and DBM……97
References in Chapter 5……99
6. EXTREME VALUE PREDICTION BY PREDICTOR-CORRECTOR AND FORM...101
6.1 Premises……101
6.2 MPWE Generation by CFD……101
6.3 Wave-induced VBM……102
6.4 Combined Wave-induced VBM and DBM……105
6.5 Combined Wave-induced and Whipping VBM……111
6.6 Summary of Chapter 6……114
References in Chapter 6……116

7. EXTREME VALUE PREDICTION BY ROM AND FORM……117
7.1 Introduction……117
7.2 Verification of ROM……118
7.2.1 Wave-induced VBM……118
7.2.2 DBM……125
7.2.3 Whipping VBM……129
7.3 Validation of ROM+FORM approach……135
7.3.1 Validation under deterministic MPWEs……136
7.3.2 Validation of PoE……142
7.4 Investigation into Effect of DBM……147
7.5 Summary of Chapter 7……149
7.6 Suggestions for Future Study……150
References in Chapter 7……153
8. CONCLUSIONS……155
ACKNOWLEDGEMENTS……159

Nomenclature

VBM	Vertical Bending Moment
IACS	International Association of Classification Societies
DBM	Double-bottom Bending Moment
GWM	Generalized Wagner Method
FEA	Finite Element Analysis
ALE	Arbitrary-Lagrangian-Eulerian
CFD	Computational Fluid Dynamics
RANS	Reynolds Averaged Navier Stokes
OpenFOAM	Open Source Field Operation and Manipulation
FSI	Fluid-Structure Interaction
CSS	Conventional Serial Staggered
NK	Nippon Kaiji Kyokai
RAO	Response Amplitude Operator
DLP	Design Load Parameter
DRW	Design Regular Wave
ABS	American Bureau of Shipping
MLER	Most Likely Extreme Response
CRRW	Conditional Random Response Waves
DIW	Design Irregular Wave
MPWE	Most Probable Wave Episode
MCS	Monte Carlo Simulations
CPU	Central Processing Unit
FORM	First Order Reliability Method
MCF	Model Correction Factor
ROM	Reduced Order Method
PoE	Probability of Exceedance
FVM	Finite Volume Method
SIMPLE	Semi-Implicit Pressure Linked Equations
VOF	Volume-of-Fluid
DOF	Degree-of-Freedom
EOM	Euler Overlay Method
SST K-ω	Shear stress transport K-omega
IDW	Inverse Distance Weighting

RBM	Rigid body motion
TEU	Twenty-foot Equivalent Unit
NMRI	National Maritime Research Institute
OU	Osaka University
LPF	Low-pass filter
ISSC	International Ship and Offshore Structures Congress
FFT	Fast Fourier Transform
BPF	Band-pass filter
WF	Wave Frequency
HF	High Frequency
NSM	New Strip Method
NMRIW-II	Nonlinear Motion in Regular & Irregular Wave-Integrated Intelligence
STFM	Salvesen-Tuck-Faltinsen Method
IFFT	Inverse Fast Fourier Transform
RSM	Response Surface Method
TF	Transfer Function
CoG	Center of Gravity
LSF	Limit State Function
BHD	Bulkhead
RO	Reduced Order
EDW	Equivalent Design Wave
POT	Peak-over-threshold

Chapter 1
INTRODUCTION

1.1 Background

From a view point of structural safety of ships, ensuring the hull girder strength is one of the main concerns among ship designers. In fact, several maritime incidents are considered to have been caused by the collapse of ships' hull girder, e.g. the Nakhodka accident in 1997 [1.1], the Erika accident in 2004 [1.2], and the Prestige accident in 2002 [1.3]. These accidents resulted in immense damages on the maritime environment due to the oil spills from the broken ships. Among those causes were the vertical bending moment (VBM) acted on the hull girders and a decrease of capacity of hull girders due to aged deterioration. From these accidents onwards, requirements on the ultimate strength of the hull girder capacity have been stipulated by International Association of Classification Societies (IACS).

When the recent maritime accidents on container ships are highlighted, the MSC Napoli accident in 2007 should be listed first [1.4]. The main factor of this serious accident was considered to be an effect of the increase of structural load due to the hydroelastic vibration induced by the bow-flare slamming impact, namely whipping vibration. This incident posed a great concern regarding recent trend of container ships, i.e. ships are becoming larger in size and faster in speed in pursuit of scale economy. Recent large container ships also tend to have a big bow flare which increases a risk of high slamming impact pressure and following damages. Consequently, rule strengthening on the vertical bending strength of ships has been implemented by IACS [1.5]. Whether the strengthened rule provides a sufficient safety level or not, will turn out in the future. But, checking the structural design based on numerical simulations in which the direct analysis of the wave induced load considering the hydroelastic vibration is used, so-called a 'design by analysis' method, has been considered to be highly important to enhance the safety of ship structures.

As for more recent shipwrecking events, the container ship MOL-COMFORT accident should be also highlighted [1.6]. Decisive factors of this accident have not been specified yet, but there were two conceivable causes. One was the above-mentioned slamming and hydroelastic vibration effects. The other was the combination of vertical (global) bending moment and local bending moment, in particular the double-bottom bending moment (DBM). Several studies demonstrated that the local bending moment reduces the

structural capacity of the double bottom structure under hogging conditions to some extent [1.7], [1.8]. These studies implied that the compressive force is induced in the double bottom structure due to the local water pressure, or DBM (see Figure 1.1). It is apparent that a reasonable consideration should be made on the whipping and DBM in the design of large container ships. Then, a consistent method for predicting the structural response taking account of the combined VBM (with whipping) and DBM needs to be developed.

Next, let us assume that such a method is established. The final concern of the ship designers would be whether or not the designed ship is capable of surviving in the most severe sea states. Therefore, it is expected that the method for evaluating those combined loads can also be applied to the prediction of the extreme response of the ship under the given sea conditions. Furthermore, it is ideal that the predicted extreme response is associated with its occurrence probability during ships' operational period.

In the subsequent sections, a thorough review study is made to point out the research front and set the appropriate goal clearly.

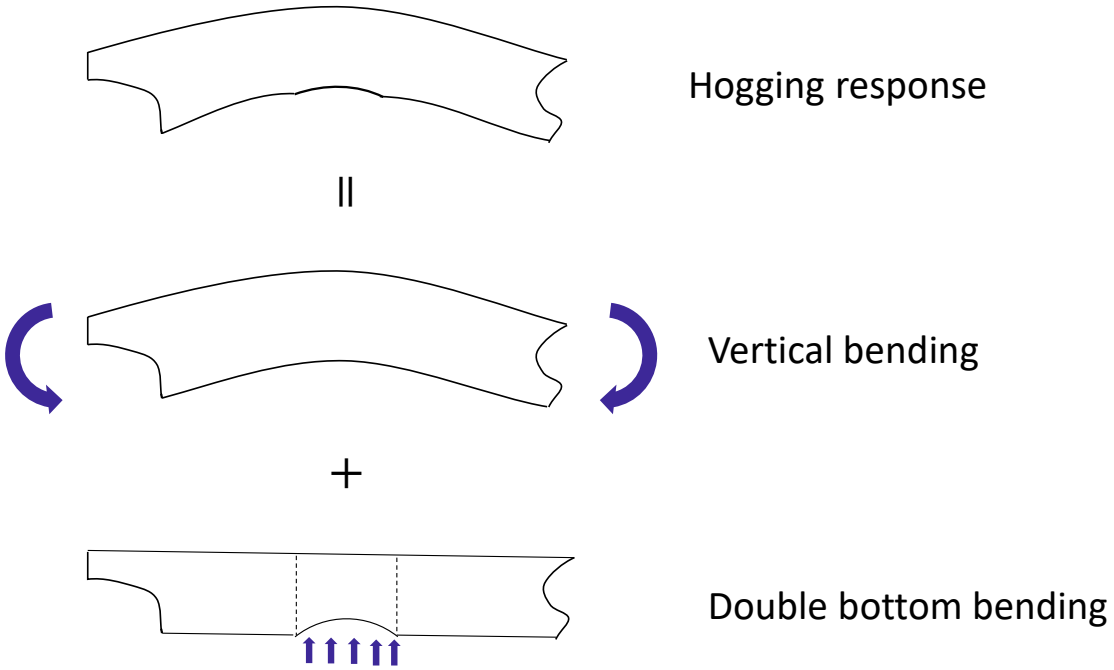

Figure 1.1 Combined bending moment applied on the double bottom structure

1.2 Literature Reviews

1.2.1 Structural response assessment under combined loads

The slamming impact problem on a body has been addressed by many researchers for a long time. Von Karman [1.9] developed a theory for estimating water impact pressure force on 2D rigid body by presuming that the impact pressure is obtained from the temporal variation of added masses. Based on von Karman's theory, Wagner [1.10] developed a water impact theory considering the water surface pile-up around the body. Wagner theory is generally used for estimating the pressure distribution on 2D sharp body like a wedge. Wagner theory was later extended to 2D arbitrary bodies based on a generalization of Wagner theory (Generalized Wagner Method, GWM) [1.11]. The common recognition for Wagner theory among recent researchers is that Wagner theory tends to overestimate the pressure in the case of low dead-rise angles in which the compressibility of air is relevant. Efforts were made to address this problem by assessing air trapping effects. Chuang [1.12] carried out a series of drop tests of wedge-shaped bodies into water then proposed experimental formulae to predict the peak value of impact pressure. Analytical approaches were also made by Abrahamsen et al. [1.13]. They derived an analytical formula to track the 2D air trapping pressure, in addition to evaluation of the oscillation frequency of entrapped air, by comparing with their experimental results [1.14].

Above researches were conducted on the basis of 2D rigid body assumptions. There are

also several researches addressing 3D water impact problems which may be applicable to slamming impact load of ships. Moore et al. [1.15] extended the conventional Wagner theory to the normal impact of 3D axisymmetric rigid bodies. Numerical simulation techniques were also utilized to calculate the 3D slamming load distribution on the ship hull. Wang et al. [1.16] adopted explicit Finite Element Analysis (FEA) for 3D profiles. They indicated that the Arbitrary-Lagrangian-Eulerian (ALE) approach is capable of solving the water impact pressure both in the dropping cases and in the constant impact velocity cases on 3D bodies with good accuracy. However, a high mesh density is required to calculate the impact pressure with sufficient accuracy, which results in an increase of computational efforts.

In applying numerical simulations to actual ship design stages, sufficiently accurate methods with less computational expense based on a simplification of the problem are of practical use. In practical ship design stages, the strip methods have been widely applied [1.17]. Nonlinear strip method has been subsequently developed to account for the nonlinearity of wave-induced load in conjunction with a slamming impact load model due to the entry of bow into water [1.18]. However, since the strip theory is based on the approximation of the 3D ship hull form to a collection of 2D cross sectional strips, no hydrodynamic interferences among the strips are considered. To tackle with the issue of three-dimensionalities, potential theory based hydrodynamic codes using a 3D panel method have been developed by many researchers [1.19], [1.20].

The seakeeping theories were combined with the structural mechanics, then the evaluation of hydroelastic responses might be made. However, it was still common to adopt von Karman's approach in evaluating slamming forces in these methods. Kim et al. [1.21], [1.22] coupled the 3D panel method with GWM to overcome this issue and made it possible to derive the impact pressure distribution. Their results implied that the code can estimate the whipping moment time histories with good accuracy when compared with experimental results in moderate forward speed cases. But it was reported that for a speed above 20 knots, their methods tend to overestimate the whipping moments. Kobayakawa et al. [1.23] developed a time domain solver by coupling the Rankine source method and 3D FEA, including 3D effects of impact loads. However, it may be open to some doubt for very severe wave cases.

Meanwhile, Computational Fluid Dynamics (CFD) making use of the Reynolds Averaged Navier Stokes (RANS) equations has been also adopted for the evaluation of both slamming impact pressure and subsequent whipping response. Concerning the impact pressure assessment, Nguyen et al. [1.24] performed the numerical studies by unsteady RANS solver using various 3D geometries then compared them with

experimental results [1.25]. They indicated that the CFD could predict the temporal sequence of impact pressure with good accuracy and with reasonable computational expense. For the sake of the whipping response evaluation, Moctar et al. [1.26] and Ley et al. [1.27] developed a straightforward one-way coupling system of CFD and dynamic FEA. They demonstrated that the CFD and dynamic FEA coupling techniques can well predict the wave-induced loads and whipping moments in both regular and irregular heading wave conditions. Seng [1.28] also developed a coupling method using open source code OpenFOAM [1.29] and Timoshenko beam model for the whipping evaluation. These works suggest that the numerical simulation method by combining CFD and a structural analysis method can potentially be a consistent method for the slamming impact and hydroelastic response estimations.

To take account of added mass effect from elastic deformation of ship hull due to the whipping vibration appropriately, mutual (two-way) coupling of fluid and structural simulations in time domain is ideal. There are generally two approaches to be adopted to the numerical simulations. The first one is the monolithic approach [1.30], [1.31], where the fluid equations and the structural equations are solved simultaneously. The monolithic approach has its advantage in terms of the stability and the accuracy of the Fluid-Structure Interaction (FSI) evaluation. However, the monolithic approach demands such a huge computational effort to solve the equations per time step that adopting the monolithic approach to such hydroelastic problem on 3D ship might not be practical yet.

The second one is the partitioned approach [1.32], where the distinct fluid solver and the structure solver are alternatingly integrated. In applying the partitioned approach, information about force and displacement are transferred via the interface between the fluid and structure domain. The most basic method in the partitioned approach is so-called weakly coupled method. An elementary but popular procedure for the weakly coupled method is the conventional serial staggered (CSS) procedure [1.33], where the FSI solution by coupling the fluid and the structure solver is advanced once per coupling time step. Indeed, the weakly coupled method guarantees less computational efforts than the monolithic approach, but it is also well-known that the weakly coupled method occasionally causes instabilities due to so-called artificial added mass effect [1.34], in particular when the FSI problems concerning the incompressible fluid with flexible structures suffered from large deformations are solved. The artificial added-mass effect is considered to be originated from a fact that no rigorous equilibrium between the fluid and the structure domain is established in each coupling time step, which may be inevitable when the partitioned approach is adopted. To overcome this defect, the

strongly coupled method has been devised and validated by several researchers [1.35], [1.36]. Within the strongly coupled method, sub-iterations between the fluid and the structure solver are implemented in each coupling time step in order to find out the convergence between fluid and structure implicitly. It was also pointed out that the strongly coupled method ensures a better stability and accuracy at the expense of computational efforts than the weakly coupled method in solving FSI problems.

As regards the structural response estimation accounting for a combination of different loads, several efforts have been spent by researchers so far. A number of researches has been conducted concerning an elementary rectangular panel unit, e.g. a simply supported panel subjected to combined thrust and lateral pressure [1.37]–[1.40]. Thereafter, Fujikubo et al. established simplified methods to evaluate the ultimate strength of continuous plates or stiffened panels under combined thrust and lateral pressure [1.41], [1.42]. Nowadays there are several research activities directed towards assessing the double bottom structure strength under combined loads. Amlashi et al. addressed a series of evaluations of double bottom strength of a bulk carrier in which the double bottom structure is subjected to the lateral water pressure and VBM [1.43], [1.44]. As to the double bottom structure strength of container ships, a simplified formula, from which the stress distribution of double bottom under DBM due to water pressure and cargo loads can be estimated, was suggested by Matsui et al. [1.45]. Tatsumi et al. established a simple estimation method of the double bottom structure strength under combined VBM and DBM [1.7], [1.8], [1.46]. They modified conventional Smith's method [1.47], [1.48] so that the DBM effect can be taken into account for ultimate strength analyses.

Above-mentioned evaluations of the double bottom structure strength were performed on the basis of static loading conditions. For a consistent evaluation considering the slamming and hydroelastic vibration effects, structural response assessments under a dynamic loading condition is obviously vital. Research efforts in the context of dynamic loading effect of combined VBM and DBM are quite limited so far. Up until now, Kawasaki et al. [1.49], [1.50] tackled with this problem by leveraging a time domain solver by coupling the Rankine source method and 3D FEA, preliminarily developed by Kobayakawa et al. [1.23]. They accomplished a series of evaluations of the double structure strength under both of the regular and irregular waves, but as mentioned earlier, further verifications regarding an applicability to severe wave cases might be necessary.

1.2.2 Extreme load and structural response predictions

A significant amount of researches has been made concerning the prediction of extreme loads and structural responses of ships in the past [1.51]–[1.53], and these achievements were reflected on rule requirements stipulated by classification societies [1.54]. In recent guidelines provided by Class NK, a utilization of direct load analysis to structural strength assessment is recommended. According to the 'Guidelines for Direct Load Analysis and Strength Assessment' [1.55], a guideline for conducting extreme structural strength assessment is introduced, which is based on the long-term statistical prediction [1.56] and RAOs (Response Amplitude Operators), of which detailed procedure can be written down below:

1. Select evaluation areas and target members.
2. Direct load analysis is carried out in regular waves and then loads corresponding to each regular wave are applied to structural FE models. The RAOs on DLPs (Design Load Parameter) or stress for target members can be calculated through FEA.
3. Short-term and long-term statistical predictions are carried out by using wave scatter diagram specified in IACS Recommendation NO. 34 [1.57] for each stress component, and then the maximum and minimum stresses for anticipated service period are calculated.
4. Design Regular Waves (DRWs) which reproduce responses equivalent to those specified in 3. and design loads based on such waves are created, then perform structural analysis.

In order to estimate the long-term distributions of wave-induced VBM of ships during ships' expected operational years, above approaches have been becoming common in initial design stages recently.

On the other hand, an alternative procedure for conducting extreme structural strength assessment is also introduced into 'Guidelines for Direct Load Analysis and Strength Assessment' [1.55]. The second one is based on worst short-term sea states [1.58], [1.59] of which detailed procedure can be written down below:

1. Select evaluation areas, target members, and respective DLPs.
2. Direct load analysis is carried out in regular waves and then RAOs on DLPs are derived.
3. Short-term predictions are carried out for each DLP and the maximum expected value for 1000 waves of the DLP in the worst short-term sea state is calculated. Average wave period in which the result of the short-term prediction (i.e., the standard deviation of response) becomes the maximum is taken as the average

wave period of the worst short-term sea state.

4. DRWs reproducing responses equivalent to those in 3. are created for each DLP.

This procedure is based on an assumption that the extreme structural response corresponding to occurrence probability 10^{-8} is approximately equivalent to the maximum expected value for 1000 waves in the worst short-term sea state [1.58], [1.60].

Notwithstanding the usefulness of above approaches, a difficulty may arise when the VBM includes the hydroelastic component, in particular the whipping vibration. Although the time domain numerical simulation techniques have been intensively evolved, as mentioned in the previous sub-section, application of such techniques to the long-term prediction is not realistic yet. Hence, simplified prediction formulae of the whipping moment were given by Kirtley et al. and Jensen et al. [1.61], [1.62]. Their approaches were adopted in the guidance notes for whipping assessment of the classification society ABS (American Bureau of Shipping) [1.63]. Ćorak et al. [1.64] proposed an efficient procedure to calculate long-term distribution of VBM with whipping moment to investigate the influence of environmental and operational uncertainties on combined wave-induced and whipping VBM of a container ship. Their methods was based on a combination of a seakeeping analysis for the wave-induced VBM and Timoshenko beam model for whipping vibration, where the slamming impact load was estimated as per the von Karman added mass variation method with pile-up correction presented by Pedersen et al. [1.65]. Their methods may be used for in the preliminary stage of ships' structural design to determine the long-term distribution of wave-induced VBM, whipping vibration and combination of them.

It should be borne in mind that the whipping vibration depends on operational conditions of ships, in particular ship speed, to a large degree. But, the uncertainty with respect to the operational conditions has not been taken into account explicitly in the current structural design rules [1.66], [1.67]. Some attempts to set a limitation of operational condition within the long-term prediction or the worst short-term sea state based methods were made by Toki [1.68], [1.69], but a rational method to determine it has not been established yet. Investigations into the effect of uncertainties of operational conditions on the wave-induced load have been carried out by several researchers. Papanikolaou et al. [1.70] emphasized the importance of integrating uncertainties in the context of prediction tools for the assessment of wave-induced design loads, by elaborating on some indicative examples. Iijima et al. [1.71] delved into the operational effects on hydroelastic response of three types of ships by using a series of numerical simulations based on a 3D panel method. Although the modeling uncertainty in terms of wave-induced motions and loads represented by Hirdaris et al. [1.72] and Rajendran et

al. [1.73] resides, the importance of taking account of operational conditions was advocated. Meanwhile, the monitoring technique in recent days is getting to be evolved so that enormous numbers of data can be aggregated. So-called hull monitoring system [1.74] through which real stress values of ship structure members can be obtained has been progressively installed on recent commercial ships. Attempts to utilize the measured data towards extreme stress value assessments were made by Gaidai et al. [1.75] and Kim et al. [1.76]. With regard to encountered short-term sea states estimation, some efforts were made by using ships' location histories [1.77], [1.78] or by using measured ship responses [1.79], [1.80]. Even though the feedback of onboard measured data towards the ship design stages is still uncommon, it can be expected that the uncertainties of operational conditions would be clarified through analyzing measured data on each individual ship in the near future.

Provided that the critical short-term sea state is specified, predicting extreme structural response under the prescribed sea state is further needed. It is ideal to perform nonlinear time domain simulations under irregular waves to predict the extreme response, but obviously it is impractical as a matter of practice unless the simulations are sped up by High-performance computing etc. Moreover, the accuracy of the DRWs is in doubt due to the lack of transparency in the DRWs. To provide more accurate prediction of extreme structural response, estimation methods of conditional irregular wave associated with given response levels were proposed by several researchers. These are known as the Most Likely Extreme Response (MLER) method (Adegeest et al. [1.81]), the Conditional Random Response Waves (CRRW) method (Dietz [1.82]), and the Design Irregular Wave (DIW) method (Fukasawa et al. [1.83], [1.84]), in which conditional irregular wave trains are derived based on the linear superposition of response functions of target response under component regular waves. Their methods have been considered to be applicable to capture the slight non-linearity seen in the wave-induced VBM of ships sailing in moderate seaways, cf. Jensen et al. [1.85].

However, if the whipping component plays an important role in VBM, their approaches do not give good representations of the most probable wave episodes (MPWEs), as is mentioned by Drummen et al. [1.86]. One possible solution is to apply direct Monte Carlo Simulations (MCS) in conjunction with time domain numerical simulations. Oberhagemann et al. [1.87] proposed a method making use of MCS and CFD for small response levels while applying CRRW method for large response levels. They estimated that 50 CFD simulations with CRRW during 50 physical seconds may be required to cover one response level, which would require approximately 50 days with 1000 CPU cores in case of conducting long-term extreme value predictions. From a viewpoint of

practical use, more efficient method to keep the computational efforts at the bare minimum is required.

As an alternative to MCS, Der Kiureghian [1.88] indicated that the First Order Reliability Method (FORM) is an efficient method not only for structural reliability analysis but for the extreme value prediction. The FORM approach also enables us to identify the MPWEs leading to the given extreme responses linked with a failure exceeding probability. An effectiveness of applying the FORM approach to extreme wave-induced VBM prediction was demonstrated by Jensen [1.89], then further extension of this work was conducted for evaluating VBM with whipping component based on the combination of FORM and the nonlinear strip theory [1.90]. When we consider the combination of FORM and CFD, there is still a problem regarding computational efforts as FORM requires a series of response surface determination processes, even though it may be fairly smaller than MCS. To deal with this issue, Jensen et al. [1.91] and Seng et al. [1.92] adopted so-called *predictor-corrector* approach in lieu of the absolute combination of FORM and CFD. They used a simplified method (i.e. strip theory) at predictor steps for predicting design points while CFD with Timoshenko beam model (Seng et al. [1.93]) at a corrector step with Model Correction Factor (MCF) approach [1.94]. A noteworthy point of this work was that they successfully overcame an issue concerning the computational efforts in predicting extremes by this means. But, their approach failed to predict extreme VBM with whipping, as the strip theory was not a good *predictor* for what happens with respect to whipping using the 3D hydrodynamic model based on CFD. Since the large contribution of whipping vibration was indeed reported by recent full scale measurements of a container ship, cf. Andersen et al. [1.95], further work is needed to resolve this issue.

1.3 Objectives

Based on the reviews in the previous sections, it is emphasized that a rational and consistent method to estimate structural response under combined load is still needed. Further, in view of structural safety of ships, it is highly necessary that the method can be applied to extreme value and MPWE predictions under the combined load in ships. The primary goal of this thesis is to develop a promising method for predicting extreme values of structural responses under the combined load of a container ship, i.e. the combination of wave-induced VBM, DBM, and whipping VBM. To this end, the following works are contained in this thesis:

- Firstly, a numerical simulation method making use of 3D CFD and FEA is developed.

A straightforward one-way coupling method between CFD and FEA is applied then a series of validations in terms of ship's rigid body motion, local pressure values and VBM is conducted by comparing the towing tank experiment, the nonlinear/linear strip theories and the 3D panel theory.

- The developed one-way coupling method is then applied to a realistic full scale container vessel in order to clarify the contribution of the DBM to the double bottom structural response.
- To represent the fluid-structure interaction effect properly, the one-way coupling method is extended towards the two-way coupled method. The weakly two-way coupling method of the CFD and FEA in which only one solution of CFD/FEA is implemented per coupling time step is firstly developed. Then, the strongly two-way coupled method of the CFD and 3D FEA where the sub-iteration processes between CFD and FEA is implemented per coupling time step is also developed. A validation study is also conducted by comparing with the one-way coupling method, the two-way coupling method, and the experiment.
- For the sake of extreme value predictions, a method to estimate the MPWEs is prepared based on the FORM theory. The *predictor-corrector* approach along with MCF in which the nonlinear strip theory is used as the *predictor* is adopted first, in order to determine the design point based on the one-way coupled CFD and FEA. Two types of limit state functions are used in estimating longitudinal stress level at the outer bottom surface in order to investigate the DBM effect.
- An efficient alternative to the *predictor-corrector* approach for extreme VBM prediction considering whipping effect of a container ship is proposed. The newly developed method in this thesis is named the Reduced Order Method (ROM). ROMs for predicting both of the wave-induced VBM, whipping VBM, and DBM are developed. A series of numerical demonstrations during which the developed ROMs are combined with FORM for predicting the extremes estimated from the one-way coupling of CFD and FEA is carried out.
- To validate the proposed ROM and FORM based approach, a series of towing tank tests using a scaled model of a recent container ship is carried out. VBMs with whipping component under MPWEs identified by the above new ROM approach are measured, then the validity of the developed ROM is discussed. Finally, the estimation accuracy of the probability of exceedance (PoE) by the proposed ROM and FORM approach is validated by comparing with the experiment.

1.4 Outline of Thesis

In Chapter 2, basic formulation and numerical modeling of CFD and FEA used in this study are firstly introduced. Then, the one-way and two-way coupling methods between CFD and FEA for evaluating loads in a ship and structural responses are explained.

In Chapter 3, a subject container ship used in this study is introduced. Then, the scale models to be used for the towing tank tests for verification studies, the outline of the towing tank tests, the measurement methods, and the measurement items are described.

Chapter 4 provides validations about the accuracy of the coupled CFD-FEA methods. To this effect, benchmarks are carried out by comparing with numerical results from the strip theory and the 3D panel method in terms of rigid body motion, local pressure values and whipping vibrations. The present coupled CFD-FEA methods give reasonable results. Then the CFD-FEA coupled method is applied to a full scale container ship to evaluate the effect of DBM on the double bottom structure, then the validity of the method is indicated.

In Chapter 5, the theoretical background of FORM based method to predict the extremes under severe short-term sea states is described. Then, the *predictor-corrector* approach and the ROMs to predict the extreme structural responses are explained. Limit state functions for predicting extreme values of VBM and DBM are finally introduced.

Chapter 6 provides discussions about the extreme value prediction results on the combined VBM and DBM thorough the *predictor-corrector* approach. The problem in applying the *predictor-corrector* approach to extreme VBM predictions including whipping vibration is finally described.

Chapter 7 provides the verification and validation of the ROM and FORM approach. Verification of the ROM is first conducted against the one-way coupled CFD-FEA simulation results in terms of the wave-induced VBM, DBM, and whipping VBM. Validation studies of the estimation accuracy by the proposed ROM and FORM approach are then carried out by comparing with a series of towing tank experiments.

Chapter 8 concludes this thesis, and some tasks to be addressed further on are suggested.

References in Chapter 1

[1.1] T. H. Moller, “The NAKHODKA Oil Spill Response - The Technical Adviser’s Perspective,” 1997.

[1.2] M. Le Moigne and L. Laubier, “The Erika oil spill: Environmental contamination and effects in the Bay of Biscay,” 2004.

[1.3] WWF, “The Prestige oil tanker disaster – the facts,” 2002.

[1.4] Marine Accident Investigation Branch, “Report on the investigation of the structural failure of MSC Napoli,” 2008.

[1.5] IACS, *Unified Rule Requirement UR-11A Longitudinal Strength Standard for Container Ships.* 2015.

[1.6] Class NK, “Investigation Report on Structural Safety of Large Container Ships,” 2014.

[1.7] A. Tatsumi and M. Fujikubo, “Ultimate Longitudinal Strength Analysis of Container Ships Considering Bottom Local Loads - Part 1: Nonlinear Finite Element Analysis -,” *J. Japan Soc. Nav. Archit. Ocean Eng.*, vol. 24, pp. 189–198, 2017.

[1.8] A. Tatsumi and M. Fujikubo, “Ultimate Longitudinal Strength Analysis of Container Ships Considering Bottom Local Loads - Part 2: Development of Practical Method of Progressive Collapse Analysis -,” *J. Japan Soc. Nav. Archit. Ocean Eng.*, vol. 24, pp. 199–210, 2017.

[1.9] Th. Von Karman, “THE IMPACT ON SEAPLANE FLOATS DURING LANDING,” *Tech. Notes Natl. Advis. Comm. Aeronaut.*, vol. 321, 1929.

[1.10] H. Wagner, “Über Stoß und Gleitvorgänge an der Oberfläche von Flüssigkeiten, Zeitschrift für Angewandte Mathematik und Mechanik,” *Zeitschrift für Angew. Math. und Mech.*, vol. 12, no. 4, pp. 193–215, 1932.

[1.11] R. Zhao, O. Faltinsen, and J. Aarsnes, “Water Entry of Arbitrary Two-Dimensional Sections with and Without Flow Separation,” *Proc. 21th Symp. Nav. Hydrodyn.*, pp. 408–423, 1997.

[1.12] S.-L. Chuang, “SLAMMING OF RIGID WEDGE-SHAPED BODIES WITH VARIOUS DEADRISE ANGLES,” *NSRDC Rep. 2268*, 1966.

[1.13] B. C. Abrahamsen and O. M. Faltinsen, “A numerical model of an air pocket impact during sloshing,” *Appl. Ocean Res.*, vol. 37, pp. 54–71, 2012.

[1.14] B. C. Abrahamsen and O. M. Faltinsen, “The effect of air leakage and heat exchange on the decay of entrapped air pocket slamming oscillations,” *Phys. Fluids*, vol. 23, no. 102107, 2011.

[1.15] M. R. Moore, S. D. Howison, J. R. Ockendon, and J. M. Oliver, “Three-dimensional oblique water-entry problems at small deadrise angles,” *J. Fluid Mech.*, vol. 711, no. 25, pp. 259–280, 2012.

[1.16] S. Wang and C. Guedes Soares, “Numerical study on the water impact of 3D bodies by an explicit finite element method,” *Ocean Eng.*, vol. 74, pp. 73–88, 2014.

[1.17] M. Takagi and M. Ganno, “On the accuracy of the strip theory, used for a calculation of ship

motions in waves," *J. Zosen Kiokai*, vol. 121, pp. 48–61, 1967.

[1.18] Y. Yamamoto, M. Fujino, and T. Fukasawa, "Motion and Longitudinal Strength of a Ship in Head Sea and the Effects of Non-Linearities," *J. Soc. Nav. Archit. Japan*, vol. 144, pp. 214–218, 1978.

[1.19] C.-H. Lee and J. N. Newman, "Computation of wave effects using the panel method," *WIT Transactions on State-of-the-art in Science and Engineering*, p. 41, 2005.

[1.20] K. Iijima, T. Yao, and T. Moan, "Structural response of a ship in severe seas considering global hydroelastic vibrations," *Mar. Struct.*, 2008.

[1.21] J.-H. Kim, K.-H. Kim, D.-Y. Lee, B.-H. Jung, and Y. Kim, "A Fully Coupled BEM–FEM Analysis on Ship Structural Hydroelasticity and Experimental Validation," in *Proceedings of the PRADS2013*, 2013, pp. 603–611.

[1.22] J.-H. Kim, Y. Kim, Y. Kim, and K.-H. Kim, "STUDY ON SHIP STRUCTURAL HYDROELASTICITY AND FATIGUE ASSESSMENT IN IRREGULAR SEAWAYS," in *Proceedings of the ASME 2013 32nd International Conference on Ocean, Offshore and Arctic Engineering, OMAE2013*, 2013.

[1.23] H. Kobayakawa, H. Kusumoto, and I. Neki, "Strength Evaluation of Containerships Based on Dynamic Elastic Response Calculation of Hull Girder 1st Rerpot – Unsteady Time Domain Analysis of Ship Motions in Head Seas," *J. Japan Soc. Nav. Archit. Ocean Eng.*, vol. 22, pp. 161–173, 2015.

[1.24] V. T. Nguyen, D. T. Vu, W. G. Park, and Y. R. Jung, "Numerical analysis of water impact forces using a dual-time pseudo-compressibility method and volume-of-fluid interface tracking algorithm," *Comput. Fluids*, vol. 103, no. 1, pp. 18–33, 2014.

[1.25] G. De Backer *et al.*, "Experimental investigation of water impact on axisymmetric bodies," *Appl. Ocean Res.*, vol. 31, no. 3, pp. 143–156, 2009.

[1.26] O. El Moctar, J. Ley, J. Oberhagemann, and T. Schellin, "Nonlinear computational methods for hydroelastic effects of ships in extreme seas," *Ocean Eng.*, vol. 130, no. 15, pp. 659–673, 2017.

[1.27] J. Ley and O. Moctar, "AN ENHANCED 1-WAY COUPLING METHOD TO PREDICT ELASTIC GLOBAL HULL GIRDER LOADS," in *Proceedings of the ASME 2014 33rd International Conference on Ocean, Offshore and Arctic Engineering, OMAE2014*, 2014.

[1.28] S. Seng, "Slamming And Whipping Analysis Of Ships," Technical University of Denmark, 2012.

[1.29] OpenFOAMFoundation, "OpenFOAM User Guide," no. July. 2018.

[1.30] C. Michler, S. J. Hulshoff, E. H. van Brummelen, and R. de Borst, "A Monolithic Approach to Fluid Structure Interaction," *Comput. Fluids*, vol. 33, no. 5–6, pp. 839–848, 2004.

[1.31] H. Y. U. Langer, "Recent development of robust monolithic fluid-structure interaction solvers," 2016.

[1.32] J. Degroote, "Partitioned Simulation of Fluid-Structure Interaction," *Arch. Comput. Methods*

Eng., vol. 20, no. 3, pp. 185–238, 2013.

[1.33] C. Farhat, K. G. van der Zee, and P. Geuzaine, "Provably second-order time-accurate loosely-coupled solution algorithms for transient nonlinear computational aeroelasticity," *Comput. Methods Appl. Mech. Eng.*, vol. 195, no. 17–18, pp. 1973–2001, 2006.

[1.34] P. Causin, J. F. Gerbeau, and F. Nobile, "Added-mass effect in the design of partitioned algorithms for fluid-structure problems," *Comput. Methods Appl. Mech. Eng.*, vol. 194, no. 42–44, pp. 4506–4527, 2005.

[1.35] H. G. Matthies and J. Steindorf, "Partitioned but strongly coupled iteration schemes for nonlinear fluid–structure interaction," *Comput. Struct.*, vol. 80, pp. 1991–1999, 2002.

[1.36] J.-M. Vaasen, P. DeVincenzo, H. Charles, and L. Benoit, "Strong coupling algorithm to solve fluid-structure-interaction problems with a staggered approach," in *Proceedings of the 11th InternationalWS on Simulation & EGSE Facilities for Space Programmes (SESP '10)*, 2010, no. 1.

[1.37] A. E. Mansour, "Gross Panel Strength under Combined Loading," 1977.

[1.38] Y. Fujita, T. Nomoto, O. Niho, and A. Yoshie, "Ultimate Strength of Rectangular Plates Subjected to Combined Loading (2nd Report) Rectangular Plates under Compression and Lateral Pressure," *J. Soc. Nav. Archit. Japan*, vol. 1979, no. 146, pp. 289–297, 1979.

[1.39] T. Yao, M. Fujilkubo, and K. Mizutani, "Collapse Behaviour of Rectangular Plates Subjected to Combined Thrust and Lateral Pressure," *Trans. West-Japan Soc. Nav. Archit.*, vol. 92, pp. 249–262, 1996.

[1.40] W. Cui, Y. Wang, and P. T. Pedersen, "Strength of ship plates under combined loading," *Mar. Struct.*, vol. 15, no. 1, pp. 75–97, 2002.

[1.41] M. Fujikubo, T. Yao, M. R. Khedmati, M. Harada, and D. Yanagihara, "Estimation of ultimate strength of continuous stiffened panel under combined transverse thrust and lateral pressure Part 1: Continuous plate," *Mar. Struct.*, vol. 18, no. 5–6, pp. 383–410, 2005.

[1.42] M. Fujikubo, T. Yao, M. R. Khedmati, M. Harada, and D. Yanagihara, "Estimation of ultimate strength of continuous stiffened panel under combined transverse thrust and lateral pressure Part 2: Continuous stiffened panel," *Mar. Struct.*, vol. 18, no. 5–6, pp. 383–410, 2005.

[1.43] H. K. K. Amlashi and T. Moan, "Ultimate strength analysis of a bulk carrier hull girder under alternate hold loading condition - A case study. Part 1: Nonlinear finite element modelling and ultimate hull girder capacity," *Mar. Struct.*, vol. 21, no. 4, pp. 327–352, 2008.

[1.44] H. K. K. Amlashi and T. Moan, "Ultimate strength analysis of a bulk carrier hull girder under alternate hold loading condition, Part 2: Stress distribution in the double bottom and simplified approaches," *Mar. Struct.*, vol. 22, no. 3, pp. 522–544, 2009.

[1.45] S. Matsui, C. Murakami, T. Arima, and M. Fujikubo, "Simplified Estimation of Stress Distribution of Double Bottom Structure of Container Ship under Local Loads," in *Proceedings*

of the Twenty-sixth (2016) International Ocean and Polar Engineering Conference, 2016, pp. 526–532.

[1.46] A. Tatsumi and M. Fujikubo, "Ultimate Longitudinal Strength Analysis of Container Ships Considering Bottom Local Loads- Part 3: Development of Simplified Estimation Method of Ultimate Longitudinal Bending Strength -," *J. Japan Soc. Nav. Archit. Ocean Eng.*, vol. 25, pp. 133–142, 2017.

[1.47] C. S. Smith, "Influence of Local Compressive Failure on Ultimate Longitudinal Strength of a Ship's Hull," 1977, pp. 73–79.

[1.48] R. S. Dow, R. C. Hugill, J. D. Clarke, and C. S. Smith, "Evaluation of Ultimate Ship Hull Strength," *Extrem. Loads Response Symp.*, pp. 133–148, 1981.

[1.49] Y. Kawasaki *et al.*, "A Study on Forced Vibration of Double Bottom Structure Due to Whipping on an Ultra Large Container Ship," in *Proceedings of the ASME 2017 36th International Conference on Ocean, Offshore and Arctic Engineering*, 2017.

[1.50] Y. Kawasaki *et al.*, "Strength Evaluation of Containerships Based on Dynamic Elastic Response Calculation of Hull Girder. 2nd Report - Influence of Hull Girder Rigidity and Correlation between Double Bottom Bending and Hull Girder Bending," *J. Japan Soc. Nav. Archit. Ocean Eng.*, vol. 25, pp. 191–203, 2017.

[1.51] C. Guedes Soares, N. Fonseca, and R. Pascoal, "Long term prediction of non-linear vertical bending moments on a fast monohull," *Appl. Ocean Res.*, vol. 26, no. 6, pp. 288–297, 2004.

[1.52] E. V. Lewis and R. B. Zubaly, "Predicting Hull Bending Moments for Design," *Extrem. Loads Response Symp.*, pp. 31–62, 1981.

[1.53] H. Kawabe, "Estimation method of long-term distribution of wave-induced load based on the worst short-term sea state," in *Symposium on Seakeeping performance*, 1969.

[1.54] N. K. Kyokai, "Guidelines for Container Carrier Structures." 2012.

[1.55] Class NK, "Guidelines for Direct Load Analysis and Strength Assessment." 2018.

[1.56] J. Fukuda, "Predicting Long Term Trends of Deck Wetness for Ships in Ocean Waves," *J. Soc. Nav. Archit. Japan*, vol. 1968, no. 124, pp. 141–158, 1968.

[1.57] IACS, "Standard Wave Data." pp. 1–4, 2001.

[1.58] H. Kawabe, H. Shigeyuki, T. Hiroshi, S. Kouta, and S. Hiroshi, "Contribution of Supposed Wave Condition on Long-term Distribution of Wave Induced Load (1st Report Relation between The Maximum Wave Induced load and Supposed Wave Condition)," *J. Soc. Nav. Archit. Japan*, vol. 1999, no. 186, pp. 319–339, 1999.

[1.59] H. Kawabe, H. Tanaka, and K. Shibazaki, "Contribution of Supposed Wave Condition on Long-term Distribution of Wave Induced Load 2nd Report Relation between Fatigue Damage Ratio and Supposed Wave Condition," *J. Soc. Nav. Archit. Japan*, vol. 2000, no. 187, pp. 253–263, 2000.

[1.60] H. Mano and H. Ueno, "A Simplified Estimation of Long-Term Distributions of Various Random

Variables Induced by Ocean Waves, and a Study on the Influences of Operating Conditions on the Extremes," *J. Soc. Nav. Archit. Japan*, vol. 1972, no. 132, pp. 235–247, 1972.

[1.61] E. K. N. Kirtley, K. V Sultani-wright, J. M. Morgan, and B. L. Hutchison, "Prediction of Whipping Response during Preliminary Design," in *11th International Symposium on Practical Design of Ships and Other Floating Structures (PRADS2010)*, 2010, pp. 1315–1324.

[1.62] J. J. Jensen, P. T. Pedersen, B. Shi, S. Wang, M. Petricic, and A. E. Mansour, "Wave induced extreme hull girder loads on containerships," *Trans. SNAME*, no. 116, pp. 128–152, 2008.

[1.63] ABS, "Whipping Assessment for Container Carriers," no. December. 2010.

[1.64] M. Ćorak, J. Parunov, and C. Guedes Soares, "Long-term prediction of combined wave and whipping bending moments of container ships," *Ships Offshore Struct.*, vol. 10, no. 1, pp. 4–19, 2015.

[1.65] P. T. Pedersen and J. J. Jensen, "Estimation of hull girder vertical bending moments including non-linear and flexibility effects using closed form expressions," *Proc. Inst. Mech. Eng. Part M J. Eng. Marit. Environ.*, vol. 223, no. 3, pp. 377–390, 2009.

[1.66] A. Nitta, H. Arai, and M. Atsushi, "Basis of IACS unified longitudinal strength standard," *Mar. Struct.*, vol. 5, no. 1, pp. 1–21, 1992.

[1.67] IACS, "TB Reports - Detailed technical documents for various CSR subjects," 2018.

[1.68] N. Toki, "A Study on the Determination of Design Wave Condition," *Trans. West-Japan Soc. Nav. Archit.*, vol. 89, pp. 191–208, 1994.

[1.69] N. Toki, "A Study on the Determination of Design Wave Condition (2nd Report)," *Trans. West-Japan Soc. Nav. Archit.*, vol. 93, pp. 121–133, 1996.

[1.70] A. Papanikolaou, E. Alfred Mohammed, and S. E. Hirdaris, "Stochastic uncertainty modelling for ship design loads and operational guidance," *Ocean Eng.*, vol. 86, pp. 47–57, 2014.

[1.71] K. Iijima, R. Ueda, and M. Fujikubo, "Numerical Investigation into Uncertainty of Wave-Induced Vibration of Large Container Ships Due to Ship Operation," in *Proceedings of the ASME 2017 36th International Conference on Ocean, Offshore and Arctic Engineering*, 2017.

[1.72] S. E. Hirdaris *et al.*, "The influence of nonlinearities on the symmetric hydrodynamic response of a 10,000 TEU Container ship," *Ocean Eng.*, vol. 111, pp. 166–178, 2016.

[1.73] S. Rajendran, N. Fonseca, and C. Guedes Soares, "A numerical investigation of the flexible vertical response of an ultra large containership in high seas compared with experiments," *Ocean Eng.*, vol. 122, pp. 293–310, 2016.

[1.74] DNVGL, "HULL MONITORING SYSTEM." 1997.

[1.75] O. Gaidai, G. Storhaug, and A. Naess, "Statistics of extreme hydroelastic response for large ships," *Mar. Struct.*, vol. 61, no. April, pp. 142–154, 2018.

[1.76] Y. Kim, B. H. Kim, B. K. Choi, S. G. Park, and S. Malenica, "Analysis on the full scale measurement data of 9400TEU container Carrier with hydroelastic response," *Mar. Struct.*, vol.

61, no. April, pp. 25–45, 2018.

[1.77] M. Oka, T. Takami, and C. Ma, “A research for the actual encounter wave of ships utilizing the AIS data,” in *Conference Proceedings of The Japan Society of Naval Architects and Ocean Engineering*、*Vol.26*, 2018.

[1.78] Y. Tahara, Y. Ichinose, T. Takami, and A. Kaneko, “Simulation Based Global Concept and Local Geometry Optimization for Ship Design Considering Propulsive Performance in Actual Seas and Fatigue Damage Evaluation by Using Global Oceanographic Model and Onboard Monitored Data,” in *32nd Symposium on Naval Hydrodynamics*, 2018.

[1.79] N. Montazeri, U. D. Nielsen, and N. Jensen, “Trend modelling of wave parameters and application in onboard prediction of ship responses,” in *Proc. of MTS/IEEE OCEANS’15*, 2015.

[1.80] N. Montazeri, U. D. Nielsen, and J. Juncher Jensen, “Estimation of wind sea and swell using shipboard measurements - A refined parametric modelling approach,” *Appl. Ocean Res.*, vol. 54, pp. 73–86, 2016.

[1.81] L. J. M. Adegeest, A. Braathen, and R. M. Lseth, “Use of Non-Linear Sea-Loads Simutations in Design of Ships,” in *Proceedings of 7th Practical Design of Ships and Other Floating Structures*, 1998, pp. 53–58.

[1.82] J. S. Dietz, “Application of ConditionalWaves as CriticalWave Episodes for Extreme Loads on Marine Structures,” 2004.

[1.83] T. Fukasawa, “Maximum Response Estimation by means of Design Irregular Wave,” *J. Japan Soc. Nav. Archit. Ocean Eng.*, vol. 2, pp. 123–129, 2005.

[1.84] T. Fukasawa, Y. Kanehira, and S. Miyazaki, “Maximum Response Estimation by means of Design Irregular Wave : 2nd Report : Estimation of Local Stress of a Container Ship,” *J. Japan Soc. Nav. Archit. Ocean Eng.*, vol. 4, pp. 221–227, 2006.

[1.85] J. J. Jensen and P. T. Pedersen, “Wave-induced bending moments in ships – a quadratic theory,” *Trans. RINA*, vol. 121, pp. 151–165, 1979.

[1.86] I. Drummen, M. K. Wu, and T. Moan, “Numerical and experimental investigations into the application of response conditioned waves for long-term nonlinear analyses,” *Mar. Struct.*, vol. 22, no. 3, pp. 576–593, 2009.

[1.87] J. Oberhagemann, V. Shigunov, and O. El Moctar, “Application of CFD in long-term extreme value analyses of wave loads,” *Sh. Technol. Res.*, vol. 59, no. 3, pp. 4–22, 2012.

[1.88] A. Der kiureghian, “The geometry of random vibrations and solutions by FORM and SORM,” *Probabilistic Eng. Mech.*, vol. 15, pp. 81–90, 2000.

[1.89] J. J. Jensen, “Extreme value predictions and critical wave episodes for marine structures by FORM,” *Ships Offshore Struct.*, vol. 3, no. 4, pp. 325–333, 2008.

[1.90] J. J. Jensen, “Stochastic procedures for extreme wave load predictions - Wave bending moment in ships,” *Mar. Struct.*, vol. 22, no. 2, pp. 194–208, 2009.

[1.91] J. J. Jensen, I. M. V. Andersen, and S. Seng, “Stochastic procedures for extreme wave induced responses in flexible ships,” *Int. J. Nav. Archit. Ocean Eng.*, vol. 6, no. 4, pp. 1148–1159, 2014.

[1.92] S. Seng and J. J. Jensen, “An Application of a Free Surface CFD Method in the Short-Term Extreme Response Analysis of Ships,” in *Proceedings of PRADS2013*, 2013, pp. 747–754.

[1.93] S. Seng, J. J. Jensen, and Š. Malenica, “Global hydroelastic model for springing and whipping based on a free-surface CFD code (OpenFOAM),” *Int. J. Nav. Archit. Ocean Eng.*, vol. 6, no. 4, pp. 1024–1040, 2014.

[1.94] D. Ove and A.-N. Torben, “Model-correction-factor method in structural reliability,” *J. Eng. Mech.*, vol. 120, no. 1, pp. 1–10, 1994.

[1.95] I. M. V. Andersen and J. J. Jensen, “Measurements in a container ship of wave-induced hull girder stresses in excess of design values,” *Mar. Struct.*, vol. 37, pp. 54–85, 2014.

Chapter 2

MATHEMATICAL FORMULATION

2.1 CFD Formulation

The finite volume method (FVM) is applied in the CFD computation phases throughout this thesis. A transport equation in terms of scalar function ϕ (e.g. velocity, volume fraction and so on) over a control volume V can be written as Eq. (2.1), with Gauss's divergence theorem applying.

$$\frac{d}{dt}\int_V \rho\phi dV + \int_A \rho\phi \mathbf{v}\cdot d\mathbf{a} = \int_A \Gamma\nabla\phi\cdot d\mathbf{a} + \int_V S_\phi dV \tag{2.1}$$

where ρ represents the density, $\mathbf{v}$ is the fluid velocity vector, $d\mathbf{a}$ is the surface vector, Γ is the diffusion parameter, and S_ϕ is the source term for the scalar. When ϕ is defined, e.g. the velocity, and appropriate values for Γ and S_ϕ are selected, then Eq. (2.1) gives the conservation equation of momentum or mass and so on. By applying integration approximations in terms of the surface and volume integrals, the following semi-discretized equation is obtained.

$$\frac{d}{dt}\left(\rho\phi_0 V_0\right) + \sum_f \left\{\rho\phi_f\left(\mathbf{v}_f\cdot\mathbf{a}_f\right)\right\} = \sum_f\left(\Gamma\nabla\phi_f\cdot\mathbf{a}_f\right) + S_{\phi_0}V_0 \tag{2.2}$$

In Eq. (2.2), values with subscript 0 denote those of cell center and values with subscript f denote those of cell face center. The velocity field and the pressure field should be obtained from the momentum equation and the continuity equation. FVM implemented in a commercial CFD solver STAR-CCM+ 10.06.009-R8 [2.1] is applied in the CFD calculation phases. To achieve an implicit coupling between pressure and velocity, Semi-Implicit Pressure Linked Equations (SIMPLE) is employed. In the SIMPLE algorithm, the pressure field is calculated as follows:

$$p^{n+1} = p^n + \alpha p' \tag{2.3}$$

where p^{n+1} is the updated pressure, p^n is the current pressure, p' is the predicted pressure,

and α is the under-relaxation factor. Value of α is set to constant value, and within the range of 0.2 to 0.5 is preferred empirically [2.1]. In computing the CFD, α=0.3 with the number of iteration in SIMPLE scheme be 5 is adopted throughout this thesis unless otherwise stated.

An example of overall CFD mesh for computing a container ship operating over the head seas is shown in Figure 2.1. Two phase flow solver with Volume-of-Fluid (VOF) formulation [2.2] is adopted to capture the free surface of water (or air). Numerical regular or irregular waves are generated by prescribing the velocity and the free surface elevation at the inlet boundary. The wave model at the inlet is based on the fifth-order Stokes wave [2.3].

6-DOFs of rigid body motion of the ship are allowed during the computations. The whole size of the solution domain is taken large enough to envelop the ship's hull. As seen in cross section at Z=0 in Figure 2.1, the mesh size around the hull boundary is finer than that in other fields. Mesh size at the free-surface zone is also refined to reproduce VOF wave correctly, see cross section at mid-ship or Y=0, in Figure 2.1. To reproduce VOF wave correctly, the grids have the same spacing in X-direction and Z-direction over the free-surface zone. While in Y-direction, on the other hand, the grid spacing is little wider. It is intended to reduce the computational effort without losing the accuracy of the results. In consideration of the symmetricity of the problem, half size models cut off at Y=0 surface are also adoptable by setting a symmetry boundary condition at Y=0 section.

The mesh size on the hull surface is the finest over the whole model in order to calculate the impact pressure on the hull with high accuracy [2.4]. The wider refinement zone can be found near the inlet boundary as given with red dotted lines, see cross section at Y=0, in Figure 2.1. This wider region is to prevent the free-surface from getting out of the refined region due to the large pitch motion of the ship. A result example of regular VOF wave reproduction under low and high pitch angles are shown in Figure 2.2. In Figure 2.2, the wave height and the ratio between wave length and ship length are Hw=6m and λ/L_{pp}=1.0, respectively. As seen from Figure 2.2, the free-surface zone under a high pitch angle is still inside the refinement zone, while the free-surface is smoothly generated as well as the low pitch angle case.

In solving VOF wave problems, the reflection of surface waves from the boundaries or the free-surface disturbance due to the ship motion might occur because of the limited solution domain. To reduce these effects, the Euler Overlay Method (EOM) [2.5], [2.6] is applied to the solution by replacing the source term in each conservation equation with below.

$$S_\phi^* = S_\phi - \gamma\rho\left(\phi - \phi^*\right)$$
$$\gamma = -\gamma_0 \cos^2\left(\pi x / 2\right) \tag{2.4}$$

where γ is a function that changes from zero at the inner area of the solution region to constant value γ_0 at the boundaries, ρ is the fluid density, ϕ is the scalar function derived from the current transport equations, and ϕ^* is the scalar function to be enforced. Value ϕ^* is determined by the specified wave shapes. The damping zone of the wave by using EOM is shown in Figure 2.3. The optimal value of γ_0 was not clarified in the past studies, but a larger absolute value is considered to be ideal. In this study, γ_0=-10 is chosen. The radiation condition at infinity is replaced by numerical matching conditions at the domain boundary, S_R, i.e.,

$$v\left(x,y,z,t\right) = v_w\left(x,y,z,t\right), \quad \zeta\left(x,y,t\right) = \zeta_w\left(x,y,t\right) \ on S_R \tag{2.5}$$

where $v(x,y,z,t)$ is the velocity and $z=\zeta(x,y,t)$ is the free surface elevation. v_w and ζ_w are the known incoming wave solution pair which satisfy the initial-boundary-value problem.

The calculation setup of CFD is described in Table 2.1. Compressibility of air is accounted for in the simulation in order to avoid the non-physical high pressure when an air trap phenomenon occurs on the hull [2.4]. For the sake of simulating the flow around the ship with high Reynolds number, the RANS based CFD is one of the authentic methods to compute it. In this study, SST K-ω turbulence model is adopted for an unsteady RANS simulation. Pressure on the grids at the hull is extracted at each solution time step, and applied to FE model as described later. Since only the head sea condition is assumed in this study, motions other than pitch and heave are constrained. In order to increase the stability of the CFD simulation, the ship body motion is clamped during the first few seconds after start of the calculation.

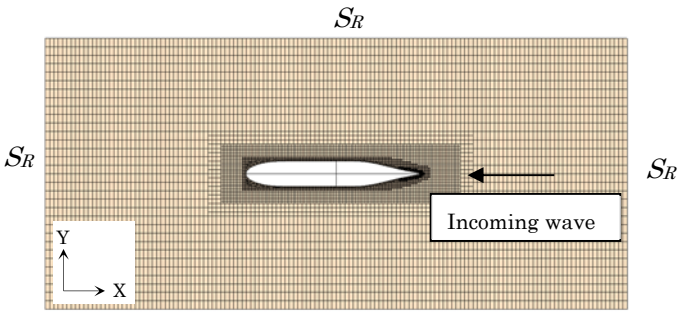

(Cross section at Z=0)

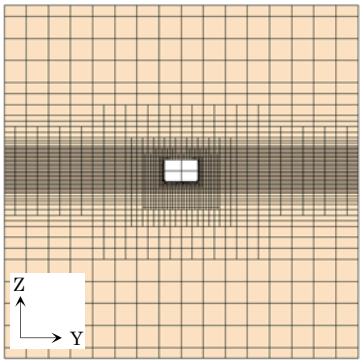

(Cross section at mid-ship)

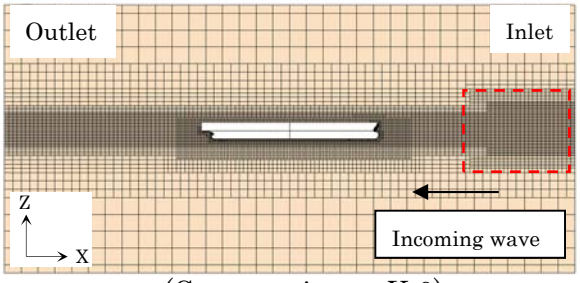

(Cross section at Y=0)

Figure 2.1 Overview of CFD meshing of the ship

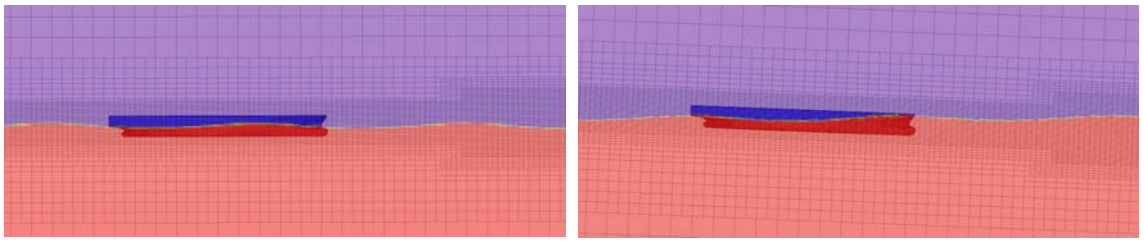

Figure 2.2 Results of VOF wave reproduction under low pitch angle (left) and high pitch angle (right)

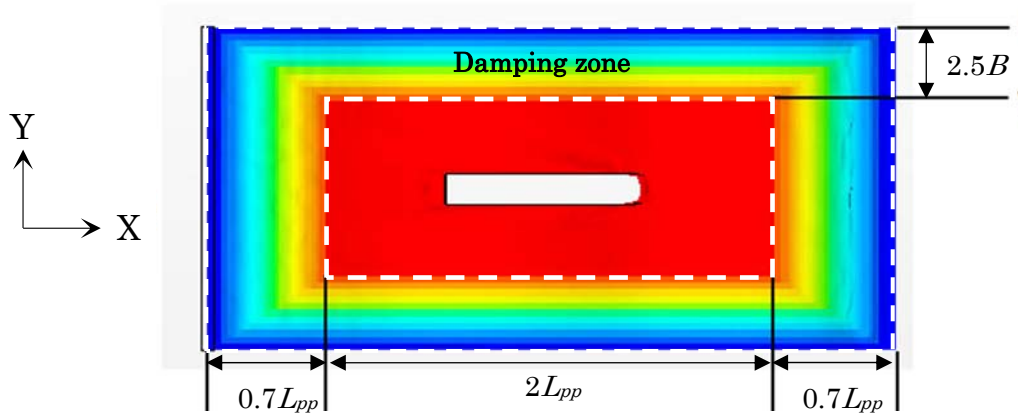

Figure 2.3 Damping zone of the wave by using EOM

Table 2.1 Calculation setup of CFD

Free-surface	Volume of Fluid (VOF)
Physical model of water	Constant density (incompressible)
Physical model of air	Ideal gas (compressible)
Turbulence model	SST K-ω model
Field mesh	Trim mesh
Solution	Unsteady implicit analysis

2.2 FEA Modeling

The coupling model between CFD and FEA is newly developed in this study. Three types of FE models are applied for the sake of VBM and DBM calculations; 1D beam model, scale FE model, and prototype full scale ship. The former two models are used for a series of the VBM estimations, and the latter one is used for both the VBM and DBM estimations. The latter two models take into account the three dimensionality of the ship hull. This section elaborates on the fundamental methodologies adopted in modeling them. Commercial FEA solver in LS-DYNA [2.7] is adopted.

2.2.1 1D beam model

The first FE model is the 1D beam model for evaluating VBM. In this study, 20 Euler beam elements of which overall length is equal to the length between perpendiculars of the subject ship are used. The mass distribution is taken from the prototype full scale ship (described later). Young's modulus of the beam elements are determined so that the natural frequency of the 2-node vertical bending mode of the model (see Figure 2.4)

becomes equal to that of subject ship. In performing FEA, gravity acceleration is applied to the FE model in the whole solution period since the hydrodynamic forces from the CFD are given considering the gravity acceleration. Rayleigh type damping defined below is introduced in the FE model:

$$[C] = \alpha [M] + \beta [K] \tag{2.6}$$

where $[C]$, $[M]$, and $[K]$ are the damping, mass, and stiffness matrices, respectively. The constants α and β are the mass and stiffness proportional damping constants [2.7]. In case of taking the stiffness damping into account, the time step size should be forced to a significantly small value for a stable calculation since the stiffness proportional damping constant largely affects the high frequency mode. Thus in this study, β is set zero then only mass dependent constant α is considered in the FEA to reflect the target logarithmic damping ratio δ. Consequently, α is derived in terms of δ and natural frequency of 2-node vibration f_{2n}.

$$\alpha = 2\delta f_{2n} \tag{2.7}$$

The 1D beam model is applied to a series of extreme value predictions for combined wave-induced VBM and whipping VBM, as described in Chapter 7.

Figure 2.4 2-node vibration mode shape of the 1D beam model

2.2.2 Scale FE model

The second FE model is the scale FE model implemented a backbone which represents the vertical stiffness of a ship. The whole ship hull is discretized into shell elements. A procedure or modeling are summarized as follows:

- The U-shaped backbone (Figure 2.5) is discretized with shell elements. The material characteristics and moment of inertia of area are determined so as to reproduce the vertical stiffness of the subject ship.
- The hull surface is modeled with shell elements and is divided into 6 segments.
- In order to reproduce the measured weight distribution, the mass of ballast weights is added to the backbone mass itself. All mass densities on the hull elements are adjusted considering the target center of gravity, gyration radius and the mass distribution of the subject ship at each section.
- The hull and the backbone are connected firmly via rigid beam elements at boundaries of neighboring sections (see Figure 2.5).
- To suppress surge motion of the FE model, displacements of nodes in longitudinal direction (in Figure 2.5, X-direction) at the vicinity of gravity center are constrained. Rotations around X and Z direction are constrained over the hull so that local torsional mode can be suppressed.
- Rayleigh type damping (Eq. (2.6)) is introduced in the FE model as well as the 1D beam model in computing FEA.
- Each calculation time step in the FEA is found at 1.0×10^{-7} to 5.0×10^{-7} seconds determined by the Courant-Friedrichs-Levy-criterion [2.8], which is far smaller than the CFD calculation.

Figure 2.6 represents the 2-node vibration mode shape in dry condition. The scale FE model is applied to a series of validations of developed CFD-FEA coupling method in regular wave conditions by comparing the towing tank test results of the backbone model, as described in Chapter 4.

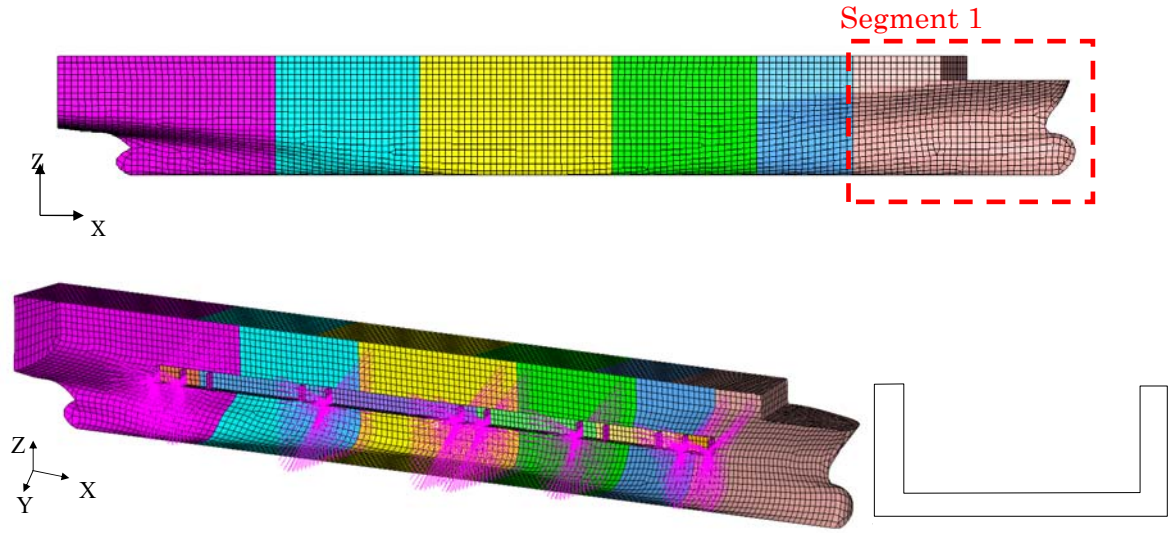

Figure 2.5 Overview of the FEA meshing of the scale FE model and cross section shape of the backbone

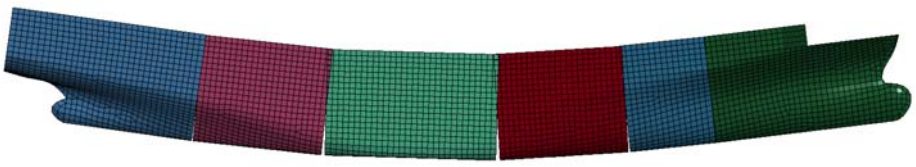

Figure 2.6 2-node vibration mode shape of the scale FE model

2.2.3 Prototype full scale ship

The last FE model is a prototype full scale ship model for evaluating both of the VBM and DBM. An overview of the FE meshing of the full scale ship is depicted in Figure 2.7. Container cargoes are modeled by using solid elements with container masses. Geometrical nonlinearity and material nonlinearity are not accounted for; simulations are performed within linear elastic range. The material properties of the structure are defined based on those of the normal steel material used in the real ship while the rigidity of cargo elements is set low so that the cargo elements does not affect the overall bending rigidity. The FEA model includes a fine mesh domain at its mid-span region (from SS4.0 to SS6.0), as found from Figure 2.7. The mesh size of the model region other than the mid-span region is defined girder-floor space length while that of the mid-span region is defined so that the girder-floor space is divided into 5 or 6 panels. Stiffened panels in the model region are modeled by using orthotropic shell elements taking the

bending stiffness of stiffeners into account.

The first 2-node vibration mode of the prototype full scale ship model is depicted in Figure 2.8. Rayleigh damping method is also adopted into the full scale FEA model as described in Eq. (2.6) in computing FEA.

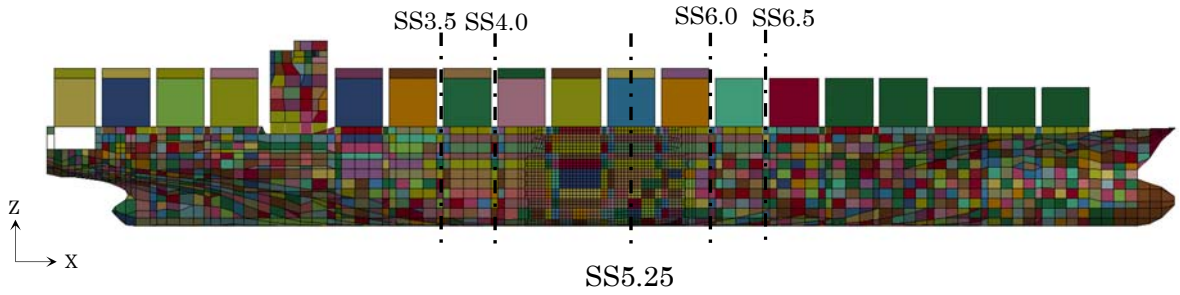

Figure 2.7 Overview of the FEA meshing of prototype full scale ship

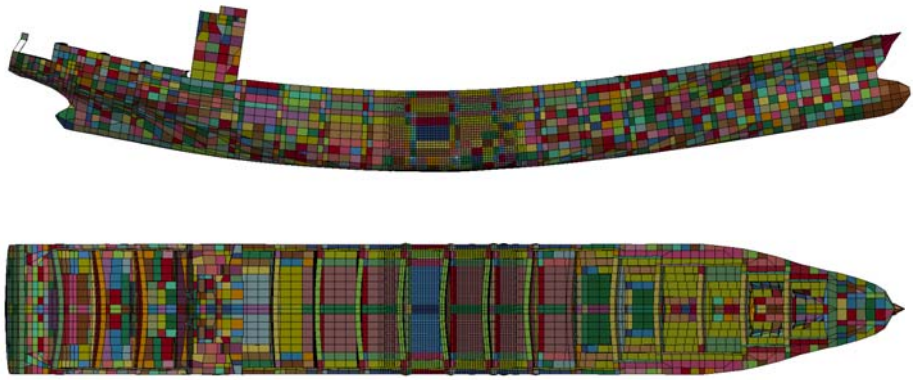

Figure 2.8 2-node vibration mode shape of prototype full scale ship model

2.3 CFD+FEA by One-way Coupling

The first coupling method employed in this study is the one-way coupling method between CFD and FEA of which procedure is schematically explained in Figure 2.9. Δt in Figure 2.9 means the time increment of each coupling stage. Instantaneous values of the rigid body motions of the ship along with the hydrodynamic forces at each time step are derived from each CFD solution, and they will be taken over to the next step CFD. Instantaneous values of the hydroelastic response of the ship body can be calculated with the FE phase at each time step by applying the pressure and inertia forces from the rigid body motions in CFD phase, over the surface of the model. The hydroelastic response, velocities on FE nodes and accelerations on FE nodes are also conserved and taken over to the next step FEA. As the rigid body motion of the ship is solved in the CFD phase, pressure values from the CFD include the hydrostatic components and the

hydrodynamic components with inertia forces from the rigid body motion containing. Here, it is noted that the added mass effects from elastic deformation of the ship are not included.

In coupling the CFD and the 1D beam model, see sub-section 2.2.1, CFD mesh on the hull surface is discretized into 21 groups then the loads integrated over the respective groups are added to the respective structural nodes. There may be small errors in terms of the interpolation converting from the loads on the three dimensional hull surface to the one dimensional forces. In this study, correction factor c_l is introduced to balance the total force applied on the hull between CFD and FEA. It means,

$$f_{zFEA,i}(t) = c_l \int_{L_i} f_{zCFD}(x,t)dx \tag{2.8}$$

where $f_{zFEA,i}$ denotes the vertical force exerted on the ith FE node, $f_{z,CFD}$ denotes the vertical force exerted on the hull at location x, and L_i denotes the length of integral range. The vertical load distribution on a calm water surface is calculated by CFD beforehand, then the value of c_l is determined so that the sum of the vertical loads agrees between CFD and FEA.

In coupling the CFD and 3D FE models, i.e. the scale FE model or the prototype full scale model, pressure values on the hull surface derived from CFD are directly applied to the FE model hull surfaces through the load transfer processing. Pressure values from the CFD are obtained over the hull surface grids every Δt, then the time series data is directly applied to the FE nodes at the same sequence. To translate the pressure from CFD into FEA, a mapping analysis is vital as the mesh discretization differs among CFD and FEA. In this study, so-called Inverse Distance Weighting (IDW) method [2.9] is used as a mapping algorithm. IDW algorithm is described as follows:

$$P(x,t) = \frac{\sum_{j=0}^{N} w_j(x,t)P(x_j,t)}{\sum_{j=0}^{N} w_j(x,t)}, \quad w_j(x,t) = \frac{1}{d(x,x_j)^2} \tag{2.9}$$

In Eq. (2.9), $P(x,t)$ is a pressure value at the target FE node of interest in each time step, $P(x_i,t)$ are pressure values at CFD grids in each time step, w_j are the weighting functions of each CFD grid, and d are each distance between CFD grids and target FE nodes. In this study N=4 is adopted, it means that four CFD grids closest to target FE nodes are

selected to calculate d.

Force equilibriums between CFD results and mapped results are checked at each time step. As a reference, a comparison of the vertical force time histories acted on the bow part segment, Segment 1 (see in Figure 2.5), under regular head seas (wave height: 10m, λ/L_{pp}=1.0, Fn=0.179) is shown in Figure 2.10. Slight differences are found which are caused by the difference in mesh discretization between CFD and FEA. To keep the force equilibrium between CFD and FEA, vertical forces on 6 hull segments (see in Figure 2.5) are once calculated by integrating pressure values estimated from the mapping processes, then correct the applied pressure values so that the total forces at each time step are balanced.

In this study, the dynamic explicit solver is employed on FEA. Each calculation time step in the FEA are found at far smaller than the CFD calculation. Although the explicit FEA solver requires considerably smaller time step than the implicit FEA solver, it guarantees computational stability in particular when solving any rapid phenomena such as slamming. The pressure values at each time step are given by linearly interpolating the temporal variations at every Δt.

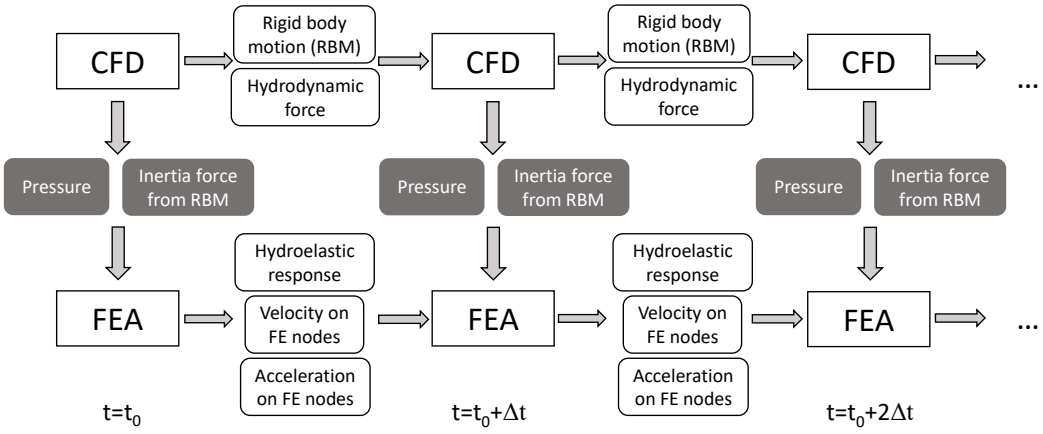

Figure 2.9 Flowchart of one-way coupling of CFD-FEA

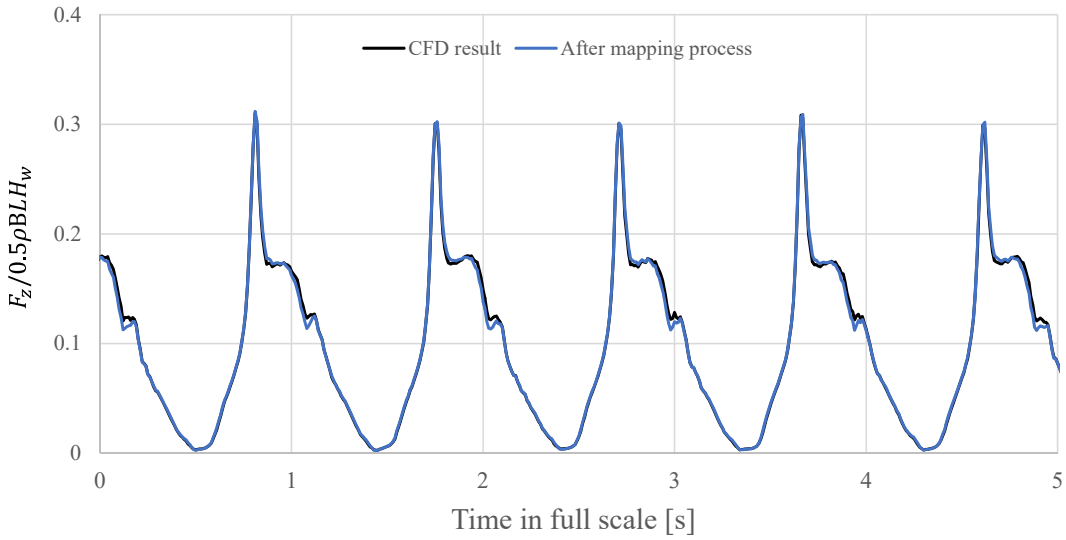

Figure 2.10 Comparison of the vertical force time history acted on the Segment 1

2.4 CFD+FEA by Two-way Coupling

In this study, the weakly coupled and strongly two-way coupled methods are applied in order to solve the hydroelastic (whipping) behavior of the subject ship accounting for the Fluid-Structure Interaction (FSI) effect. In this section, methodologies for these two-way coupling between CFD and FEA (using 3D model) are introduced.

2.4.1 Weakly coupled method

The weak coupling of the CFD and the FEA is assembled by combining those solutions in a staggered manner. The generic cycle of the weakly coupled scheme according to the conventional serial staggered (CSS) procedure can be described as follows [2.10]:

1. Advance the CFD solution to the next time step using the updated fluid meshes.
2. Convert the forces from the new CFD solution to the external pressures on FEA via mapping process.
3. Advance the FEA solution to the next time step by applying the updated external pressures to the FE model of the previous time step.
4. Transfer the calculated hull deformation from FEA to the CFD mesh then update the fluid mesh via mapping process.
5. Repeat from step 1 to 4.

A flowchart of weakly coupled scheme is shown in Figure 2.11. The mesh morphing solver implemented in STAR-CCM+ 10.06.009-R8 is adopted to reflect the elastic deformation of the ship hull derived from the previous FEA solution. CFD solution in each coupling time steps are conducted considering both the local and global velocity, which are taken

over from the previous step. Through the data exchanging processes as implied by red arrows in Figure 2.11, the added mass effect from the elastic deformation estimated from the FEA in previous time step is included into the pressures from CFD at each solution time step.

The FE model used in this study does not constraint anywhere to suppress the rigid body motion (RBM), hence deformation results from FEA include both the RBM and the elastic deformation. In case of feedback the displacement including both the RBM and the elastic deformation from FEA to next CFD stage via the morphing process, extremely small time step may be required to obtain stable morphing calculations, and it results in significant increase of simulation time. To prevent this, the deformation obtained from FEA is once decomposed into heave, pitch motion and the elastic component at each time step then only the elastic deformation is used for morphing analyses. By this means, magnitudes of mesh movements between the coupling time steps are reduced therefore the stability of morphing analyses can be enriched. Figure 2.12 indicates the decomposition method schematically. Increments of the heave motion at each coupling time step are concisely calculated by translational displacement of the gravity center. It means,

$$\begin{aligned}\Delta h(t_n+\Delta t) &= G_z(t_n+\Delta t)-G_z(t_n)\\ &= \frac{\sum_i^{Nnode} m_i\{z_i(t_n+\Delta t)-z_i(t_n)\}}{\sum_i^{Nnode} m_i}\end{aligned} \tag{2.10}$$

where Δh means the heave motion increment at $t_n+\Delta t$, m_i means the mass of each FE nodes, and z_i means the vertical position of each FE nodes. Pitch motion increment $\Delta\theta$ is calculated by applying the linear approximation method, i.e. the least squares method, to the vertical displacement of FE nodes along the backbone. Consequently, the elastic deformation at $t_n+\Delta t$ is derived from the following.

$$\begin{aligned}&\mathbf{\Delta x}_g^{Elastic}(t_n+\Delta t) = \mathbf{x}_g(t_n+\Delta t)-\mathbf{x}_g^{RBM}(t_n+\Delta t)\\ &\mathbf{x}_g^{RBM}(t_n+\Delta t) = \mathbf{Q}(t_n+\Delta t)\mathbf{x}(t_n)\\ &\qquad = \begin{bmatrix}\cos(-\Delta\theta) & 0 & -\sin(-\Delta\theta)\\ 0 & 1 & 0\\ \sin(-\Delta\theta) & 0 & \cos(-\Delta\theta)\end{bmatrix}\begin{Bmatrix}x(t_n)\\ y(t_n)\\ z(t_n)\end{Bmatrix}\end{aligned} \tag{2.11}$$

where values with suffix g are the coordinate values under local coordinate system of

which their origin is the gravity center. Mapping analyses are carried out after each solution in order to convey the force or the elastic deformation to FEA or CFD input. IDW algorithm, Eq. (2.9), is also used in these mapping analyses in the same manner as the one-way coupling. In the case of application on the elastic deformation feedbacks, $P(x,t)$ and $P(x_i,t)$ in Eq. (2.9) shall be reread as a displacement value at target CFD node in each coupling time step and displacement values at FEA nodes in each coupling time step, respectively.

A sigmoid function is adopted for interpolating the pressure values between consecutive coupling time steps in order to avoid applying abrupt pressure change at each coupling time step. The kth interpolated pressure field between the time t_n and $t_n+\Delta t$ can be described as:

$$\mathbf{P}(t_n + \frac{k}{N_{in}}\Delta t) = \frac{\mathbf{P}(t_n + \Delta t) - \mathbf{P}(t_n)}{\exp\{-(k - N_{in}/2)\} + 1} + \mathbf{P}(t_n) \tag{2.12}$$

where N_{in} denotes the number of interpolating points, and $\mathbf{P}(\cdot)$ denotes the pressure field. In order to maintain the stability of the coupling solution, the deformation of the FE model is suppressed by increasing the damping ratio at the early stage of the coupling. Coupling time step size Δt is set being equal to that of the CFD computation.

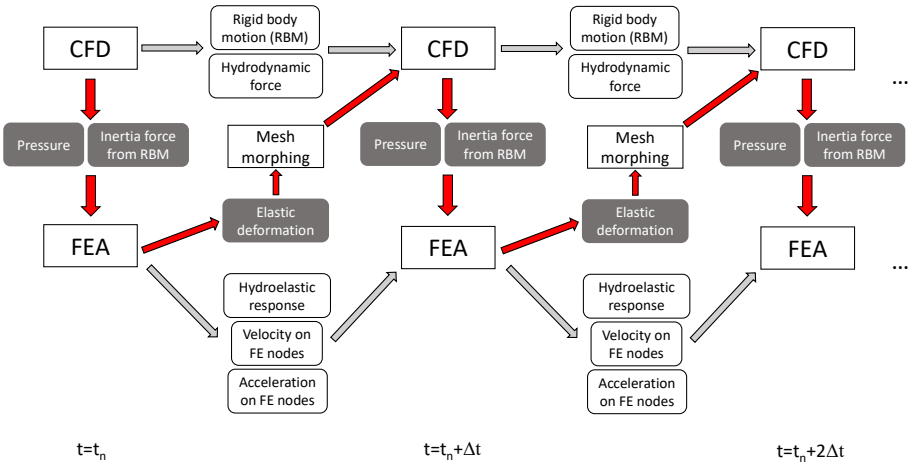

Figure 2.11 Flowchart of weak two-way coupling of CFD-FEA

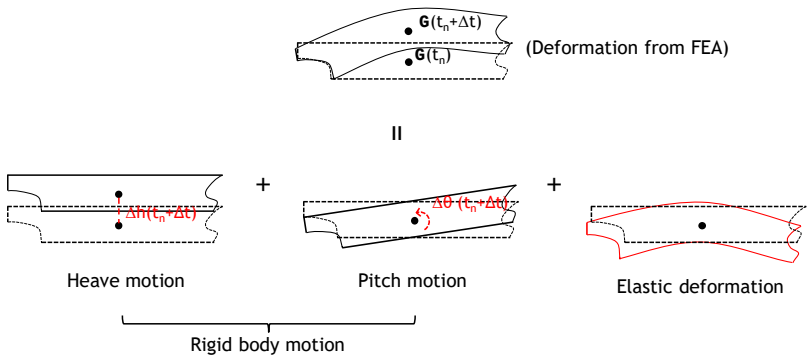

Figure 2.12 Schematic of decomposition of deformed body

2.4.2 Strongly coupled method

The strong coupling of the CFD and the FEA is also established in this study. The fundamental approach to assemble the strong coupling is conformed to the algorithm presented by Storti et al. [2.11]. The generic cycle of the strongly coupled scheme at time $t=t_n$ can be described as follows:

1. Advance the CFD solution to the next time step by using the prescribed fluid mesh then obtain the load field at kth sub-iteration ($\mathbf{F}_{tn}^{k}$).
2. Convert the load field $\mathbf{F}_{tn}^{k}$ to the external pressure field ($\mathbf{P}_{ex,tn}^{k}$) for the FEA input via mapping process.
3. Advance the FEA solution to the next time step by using the external pressure field $\mathbf{P}_{ex,tn}^{k}$ then obtain the displacement field at kth sub-iteration ($\mathbf{u}_{tn}^{k}$).
4. Transfer the displacement field $\mathbf{u}_{tn}^{k}$ to the CFD mesh then update the prescribed fluid mesh ($\mathbf{X}_{tn}^{k}$) via mapping process.
5. Check the convergence of $\mathbf{F}_{tn}^{k}$ and/or $\mathbf{u}_{tn}^{k}$. If the solution is converged, determine the current fields as $\mathbf{F}_{tn}= \mathbf{F}_{tn}^{k}$, $\mathbf{X}_{tn}= \mathbf{X}_{tn}^{k}$. If not, update $k=k+1$ and repeat from step 1 to 5.
6. Advance the CFD solution to the next time step by using the determined fluid mesh $\mathbf{X}_{tn}$.

Note that if only one sub-iteration is implemented, the above-mentioned procedure becomes the weakly coupled method. As regards the convergence of the force and displacement fields as described at step 5, there are several ways to find those convergences. As the partitioned approach leverages distinct fluid and structure solvers, in this study CFD and FEA, finding the absolute converged fields in terms of the fluid and the structure is extremely difficult. Hence among the strong coupling partitioned approaches, it is general that convergence criteria for the force or displacement field is defined then the sub-iteration stage is repeated until the convergence condition will be

satisfied [2.12]. However, it can also be anticipated that significant increase of the computational efforts might be required in case that the solution does not converge quickly. In this study, the so-called *predictor-corrector* method [2.13] is adopted in the strongly coupled scheme to find approximate convergence throughout the sub-iteration stages and to decrease the number of sub-iteration processing. To facilitate the convergence, we adopt the Aitken's accelerator [2.14] in the sub-iteration scheme. It is well-known that the Aitken's accelerator works properly if the target sequence has a convergence. The target field to be found the convergence is set to the force field. In this study, the corrected force field is obtained by using 3 estimations during the sub-iteration scheme and Eq. (2.13).

$$\mathbf{F}_{t_n}^{\text{correct}} = \mathbf{F}_{t_n}^{1} - \frac{(\mathbf{F}_{t_n}^{2} - \mathbf{F}_{t_n}^{1})^2}{\mathbf{F}_{t_n}^{3} - 2\mathbf{F}_{t_n}^{2} + \mathbf{F}_{t_n}^{1}} \tag{2.13}$$

The overall strongly coupled FSI procedure at time $t=t_n$ in this study can be summarized as follows (see also Figure 2.13):

<u>k=1 (the predictor):</u>

1. Compute the CFD where changing the fluid mesh from $\mathbf{X}_{tn\text{-}\Delta t}^{\text{correct}}$ to $\mathbf{X}_{tn}^{\text{predict}}$, then obtain $\mathbf{F}_{tn}^{1}$.
2. Convert the force field $\mathbf{F}_{tn}^{1}$ to the external pressure field ($\mathbf{P}_{ex,tn}^{1}$) for the FEA input via mapping process.
3. Compute the FEA where changing the external pressure field from $\mathbf{P}_{ex,tn\text{-}\Delta t}^{\text{correct}}$ to $\mathbf{P}_{ex,tn}^{1}$ then obtain the displacement field $\mathbf{u}_{tn}^{1}$.
4. Transfer calculated displacement field $\mathbf{u}_{tn}^{1}$ to the CFD mesh then update the fluid mesh ($\mathbf{X}_{tn}^{1}$) via mapping process.

<u>k=2 or 3 (the corrector):</u>

5. Compute the CFD where changing the fluid mesh from $\mathbf{X}_{tn\text{-}\Delta t}^{\text{correct}}$ to $\mathbf{X}_{tn}^{1}$ or $\mathbf{X}_{tn}^{1}$, then obtain $\mathbf{F}_{tn}^{2}$ or $\mathbf{F}_{tn}^{3}$.
6. Obtain the external pressure field $\mathbf{P}_{ex,tn}^{2}$ or $\mathbf{P}_{ex,tn}^{\text{correct}}$ via mapping process.
7. Compute the FEA where changing the external load field from $\mathbf{P}_{ex,tn\text{-}\Delta t}^{\text{correct}}$ to $\mathbf{P}_{ex,tn}^{2}$ or $\mathbf{P}_{ex,tn}^{\text{correct}}$ then obtain the displacement field $\mathbf{u}_{tn}^{1}$ or $\mathbf{u}_{tn}^{\text{correct}}$.
8. Transfer calculated displacement field $\mathbf{u}_{tn}^{1}$ or $\mathbf{u}_{tn}^{\text{correct}}$ to the CFD mesh then update the fluid mesh ($\mathbf{X}_{tn}^{2}$ or $\mathbf{X}_{tn}^{\text{correct}}$) via mapping process.
9. (k=2): Go back to step 5.
   (k=3): Compute the CFD where changing the fluid mesh from $\mathbf{X}_{tn\text{-}\Delta t}^{\text{correct}}$ to $\mathbf{X}_{tn}^{\text{correct}}$,

then return to step 1 and advance the time ($t=t_n+\Delta t$).

As for step 1, $\mathbf{X}_{tn}^{predict}$ should be set in any ways. In this study, $\mathbf{X}_{tn}^{predict}$ is decided based on the linear extrapolation of the deformation from the previous time step, i.e. $\mathbf{X}_{tn}^{predict}$ is simply determined by extrapolating $\mathbf{u}_{tn-\Delta t}^{correct}$. The decomposition of the deformation from FEA is also applied as with the case of the weakly coupled method. The interpolation of the pressure fields between consecutive coupling time steps is conducted by using Eq. (2.12) as well as the weakly coupled method. The damping ratio applied in the FEA model is increased at the early stage of the coupling in the same manner. Coupling time step size Δt is set being equal to that of the CFD computation.

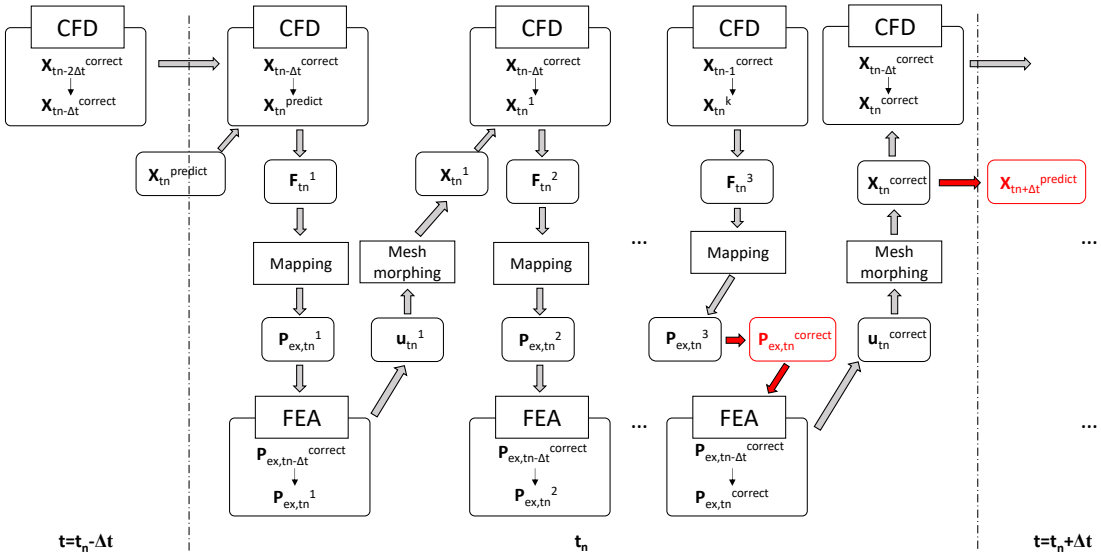

Figure 2.12 Workflow of strong two-way coupling of CFD-FEA

References in Chapter 2

[2.1] CD-ADAPCO, “User Guide STARCCM+ 10.06.009.” 2015.

[2.2] C. W. Hirt and B. D. Nichols, “Volume of fluid (VOF) method for the dynamics of free boundaries,” *J. Comput. Phys.*, vol. 39, no. 1, pp. 201–225, 1981.

[2.3] J. D. Fenton, “A Fifth Order Stokes Theory for Steady Waves,” *J. Waterw. Port, Coastal, Ocean Eng.*, vol. 111, no. 2, pp. 216–234, 1985.

[2.4] T. Takami, M. Oka, and C. Ma, “Study on Evaluation of Structural Response Caused by Slamming Impact using CFD,” in *Proceedings of 3rd International Conference on Violent Flows, VF-2016*, 2016.

[2.5] J. Kim, J. O’Sullivan, and A. Read, “Ringing Analysis of a Vertical Cylinder by Euler Overlay Method,” in *Proceedings of the ASME 2012 31st International Conference on Ocean, Offshore and Arctic Engineering, OMAE2012*, 2012.

[2.6] J. W. Kim, J. H. Kyoung, K. J. Bai, and R. C. Ertekin, “A Numerical Study of Nonlinear Diffraction Loads on Floating Bodies due to Extreme Transient Waves,” in *25th Symposium on Naval Hydrodynamics*, 2004, pp. 8–13.

[2.7] Livermore Software Technology Corporation, *LS-DYNA THEORY MANUAL*. 2006.

[2.8] D. J. Benson, “Computational methods in Lagrangian and Eulerian hydrocodes,” *Comput. Methods Appl. Mech. Eng.*, vol. 99, no. 2–3, pp. 235–394, 1992.

[2.9] N. Nishikawa, “An Immersed Boundary Method with Adaptive Selection of Interpolating Polynomials,” *Trans. Japan Soc. Comput. Eng. Sci.*, no. 20120018, 2012.

[2.10] C. Farhat, K. G. van der Zee, and P. Geuzaine, “Provably second-order time-accurate loosely-coupled solution algorithms for transient nonlinear computational aeroelasticity,” *Comput. Methods Appl. Mech. Eng.*, vol. 195, no. 17–18, pp. 1973–2001, 2006.

[2.11] M. A. Storti, N. N. Nigro, R. R. Paz, L. D. Dalc´ın, G. A. Rios Rodriguez, and E. Lopez, “Fluid-structure interaction with a staged algorithm,” vol. XXV, pp. 1–78, 2006.

[2.12] S. Ghelardi, C. Rizzo, and D. Villa, “Three-dimensional fluid-structure interaction case study on cubical fluid cavity with flexible bottom,” *J. Mar. Sci. Appl.*, vol. 16, no. 4, pp. 382–394, 2017.

[2.13] S. Seng, J. J. Jensen, and Š. Malenica, “Global hydroelastic model for springing and whipping based on a free-surface CFD code (OpenFOAM),” *Int. J. Nav. Archit. Ocean Eng.*, vol. 6, no. 4, pp. 1024–1040, 2014.

[2.14] B. M. Irons and R. T. Morgan, “A version of the Aitken accelerator for computer iteration,” *Int. J. Numer. Methods Eng.*, vol. I, no. 3, pp. 275–277, 1969.

Chapter 3
SUBJECT SHIP AND EXPERIMENTAL MODEL

3.1 Description of Models

The subject ship used in this study is a POST PANAMAX type container ship (6,600TEU in size). Results from a series of tank tests on the two different scaled ship models of this container ship are used for the validations. One is the segmented model with a backbone installed, the other is the segmented model with a beam specimen installed. In this section, details and experimental setup of each model are explained.

3.1.1 Segmented model with backbone (Backbone model)

The principal particulars of the backbone model (see Figure 3.1) are described in Table 3.1. The tank test was performed in the towing tank of National Maritime Research Institute (NMRI) [3.1], in 2010. The model is 3.0m in length and 0.45m in width. The total mass is about 126kg. The model is composed of six segments rigidly fixed to an aluminum backbone which is used for the reproduction of vertical bending flexibility of the ship. A schematic of the model is given in Figure 3.2.

Figure 3.3 shows a comparison of weight distribution among the backbone model, the scale FE model (see 2.2.2), and the prototype full scale ship (see 2.2.3). The weight distribution of the scale FE model is taken from the backbone model. Though there is some discrepancy of the weight distribution between the backbone model and the prototype full scale ship, the gyration radius with regards to pitch motion (k_{yy}) is adjusted by ballasting to take a value close to the prototype full scale ship (k_{yy}/L_{pp}=0.244). Figure 3.4 shows a comparison of vertical bending stiffness distribution between the backbone model and prototype full scale ship. The vertical bending stiffness of the scale FE model, see 2.2.2, is taken from the experimental model in the figure.

In the towing tank tests, the vertical bending moments were measured along the backbone. In addition, instantaneous pressure values were measured in the experiment by using micro pressure gauges (P306V-02S). Wave elevation was also measured. The sampling frequency was taken 500Hz and sampled data were stored via the low-pass filter (LPF) with cutoff frequency 300Hz.

Table 3.1 Principle particulars of the backbone model

	Full scale	Backbone model
Ship length (L_{pp})	283.8 m	3.0 m
Breadth (B)	42.8 m	0.452 m
Depth (D)	24.0 m	0.254 m
Draft in full loading condition (d_f)	14.0 m	0.148 m
Displacement	109480 ton	126.2 kg
Scale ratio	-	94.6
k_{yy}/L_{pp}	0.244	0.244

Figure 3.1 Segmented model with backbone (backbone model) [3.1]

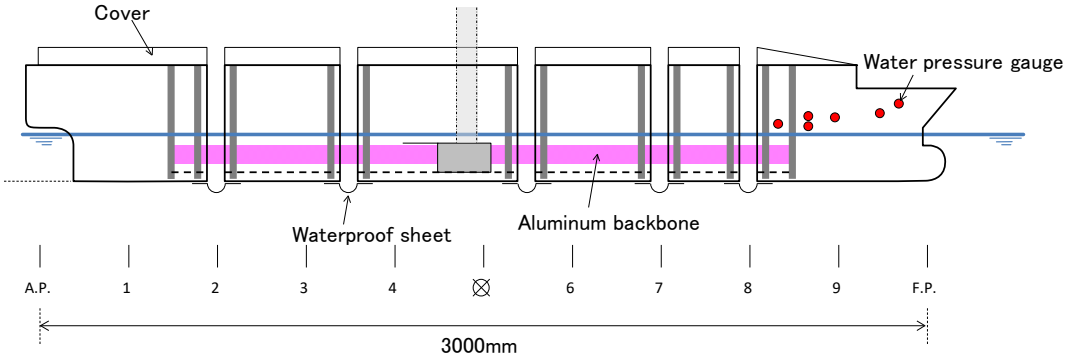

Figure 3.2 Schematic of backbone model

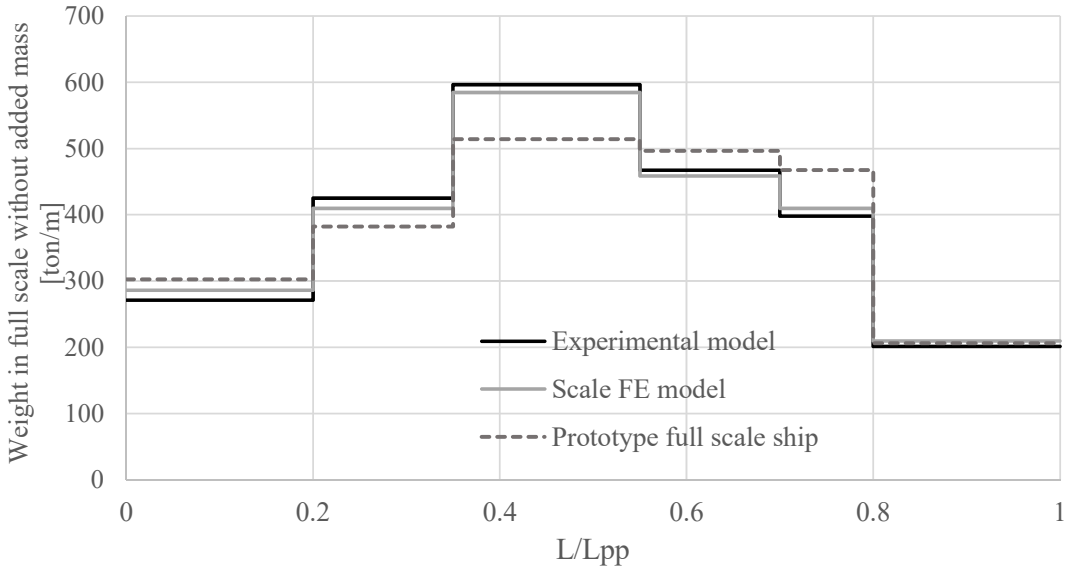

Figure 3.3 Comparison of weight distribution

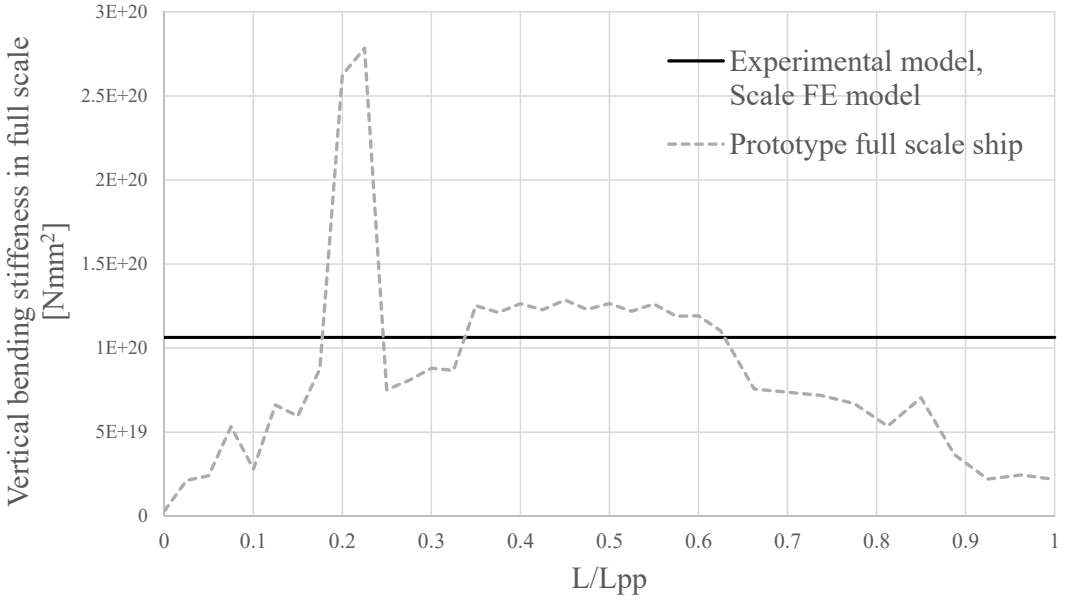

Figure 3.4 Comparison of vertical bending stiffness distribution

3.1.2 Segmented model with beam specimen (OU model)

The other segmented model in which a beam shape specimen has been installed on its amidships, named OU (Osaka University, Figure 3.5) model, is opted for a series of validations under irregular waves. A series of towing tank tests using the OU model was carried out in the 150m towing tank of NMRI. Strategies for designing the OU model conform to the previous works [3.2]–[3.4]. The whole ship hull is 2.838m in length,

0.428m in breadth and 0.240m in depth, and is divided into two rigid bodies at its amidships. Its scale ratio is assumed to be 1/100, see Table 3.2. A sacrificial beam shape specimen is installed amidships and it bends and bears shear force when hull girder deforms around the hinge when it is subjected to the VBM. The measurement of VBM is conducted by using the axial loads (L_1, L_2 and L_3) measured via load cells (LUX-B-ID, Kyowa Electronic Instruments Co., Ltd.) at the cross section (Figure 3.6). Given the measured axial loads and the vertical height of load cells H_l, VBM at the Section 1 is calculated by [3.4]:

$$M_v = -\frac{H_l}{3}\left\{2L_1 - \left(L_2 + L_3\right)\right\} \tag{3.1}$$

here, measured H_l is 0.130m. The cross section of the specimen is called "trough type" [3.4] ,see Figure 3.7, which aims to reproduce the realistic relationship between the bending moment and rotational angle of a ship hull girder. The scantling of the specimen is listed in Table 3.3.

The three-point bending test of the OU model (Figure 3.8) is conducted to calibrate measured VBM by load cells. Calibration result is shown in Figure 4.9. Here, the distance between two supported points L=1.7028 [m] and loading position is a=1.1352 [m]. As found from Figure 4.9, the present OU model could capture the target VBM within the range of at most 6% errors.

As mentioned earlier, towing tank tests using the OU model are conducted under irregular head seas and under pre-determined MPWEs. Two short-term sea states described in Table 3.4 are selected to be measured. The irregular heading waves are generated by using a plunger type wave maker equipped at the end of the towing tank. Time histories of the irregular waves are prepared according to Eq. (3.2) by generating random numbers u_i and $\bar{u}_i$.

$$\eta(t) = \sum_{i=1}^{N} u_i \sqrt{S(\omega_i)d\omega_i}\cos(\omega_i t) + \sum_{i=1}^{N} \bar{u}_i \sqrt{S(\omega_i)d\omega_i}\sin(\omega_i t) \tag{3.2}$$

The ISSC wave spectra within ω_i range of 0.3-1.5 [*rad/s*] (in model scale, 3.0-15.0 [*rad/s*]) is adopted in formulating the irregular wave, Eq. (3.2), and the number of discrete harmonic wave components N is equal to 100. The increment of wave frequencies, $d\omega_i$, is set to be non-equidistant in order to avoid repetition of similar wave sequences. 80 sets of random numbers u_i and $\bar{u}_i$ are generated to measure the extreme VBM statistics.

Measurement period of the test under one set of u_i and $\bar{u}_i$ is 5 minutes for State 1 and 3.5 minutes for State 2, respectively. These correspond to the total measurement periods of 66.7 hours and 46.7 hours in full scale, see Table 3.4.

Figure 3.10 is a snapshot of the installed model into the towing tank. The model is connected with the towing carriage via two towing rods. Ship motions other than heave, pitch, and roll motions are constrained. The setup of the model under irregular waves on State 1 is schematically shown in Figure 3.11. The model is initially set up at the position where the distance from the wave maker, *X,* is 20m. Measurements are initiated after sufficient time has elapsed in order for the shortest wavelength component to arrive at *X*=20 [m]. The setup of the model under irregular waves on State 2 is schematically shown in Figure 3.12. The model is initially set up at the position where the distance from the wave maker, *X*, is 125m. The towing carriage with the model will start to move forward after sufficient time has elapsed for the shortest wavelength component to arrive at *X*=125 [m], then measurements will be initiated after the towing carriage becomes constant speed. As for the MPWE tests on State 2 with forward speed, the encountering wave on the model should be in accord with that expected beforehand. To this effect, in the case of the MPWE tests on State 2, the towing carriage is started to move forward in advance then the measurements and wave maker activation are simultaneously initiated at *X*=70 [m], schematically depicted in Figure 3.13. Two servo type wave height meters (SH-301N, KENEK Coop. (amidships), NWS630, DENSHI KOGYO Co., Ltd. (6.766m ahead from midship)) are installed as shown in Figure 3.14. These wave height meters move forward (or backward) along with the towing carriage to measure the incoming wave elevation histories during the experiment. The sampling frequency of the measurement is taken 100Hz and sampled data are stored via the LPF with cutoff frequency 30Hz.

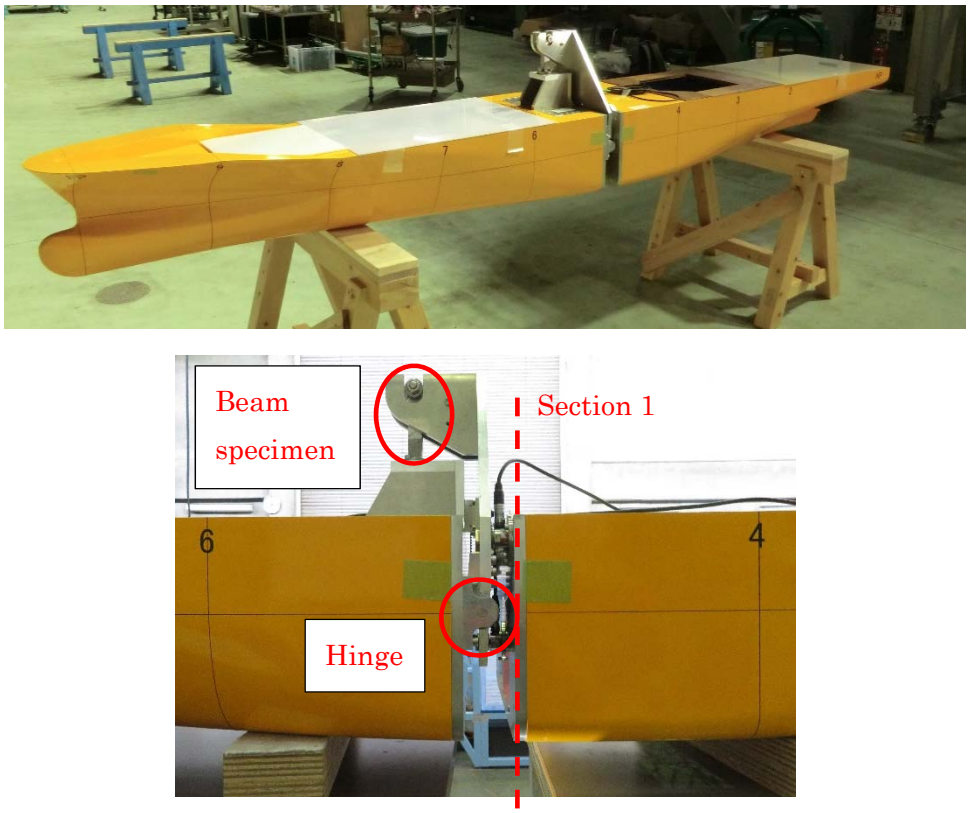

Figure 3.5 Segmented model with beam specimen (OU model)

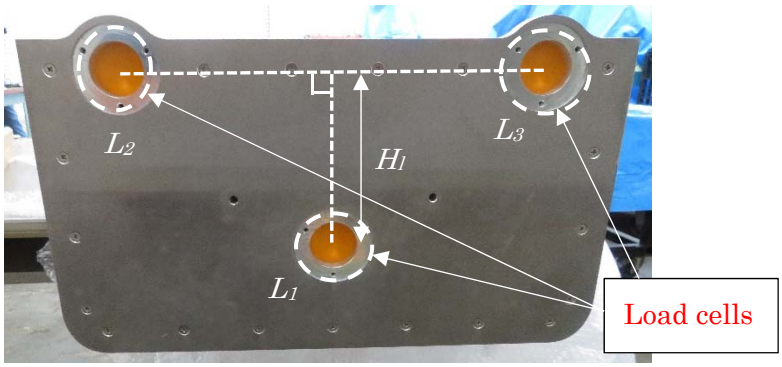

Figure 3.6 Cross section at Section 1 of OU model

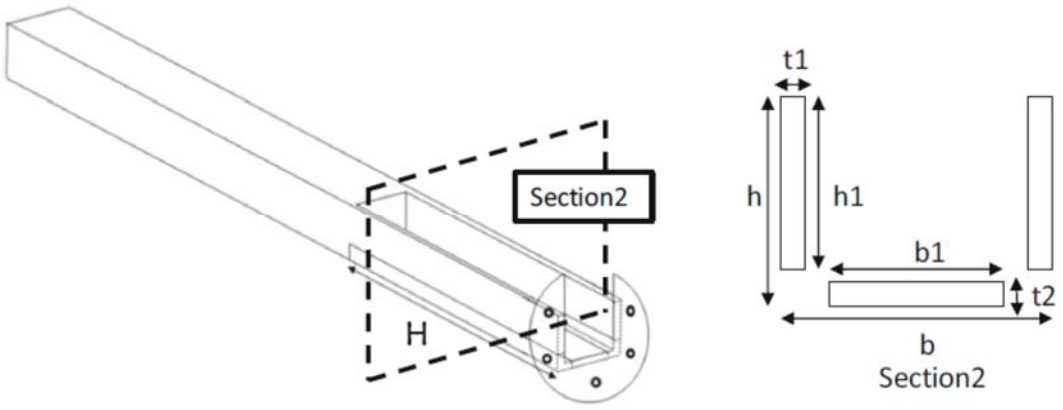

Figure 3.7 Sketch and dimensions of trough-type specimen

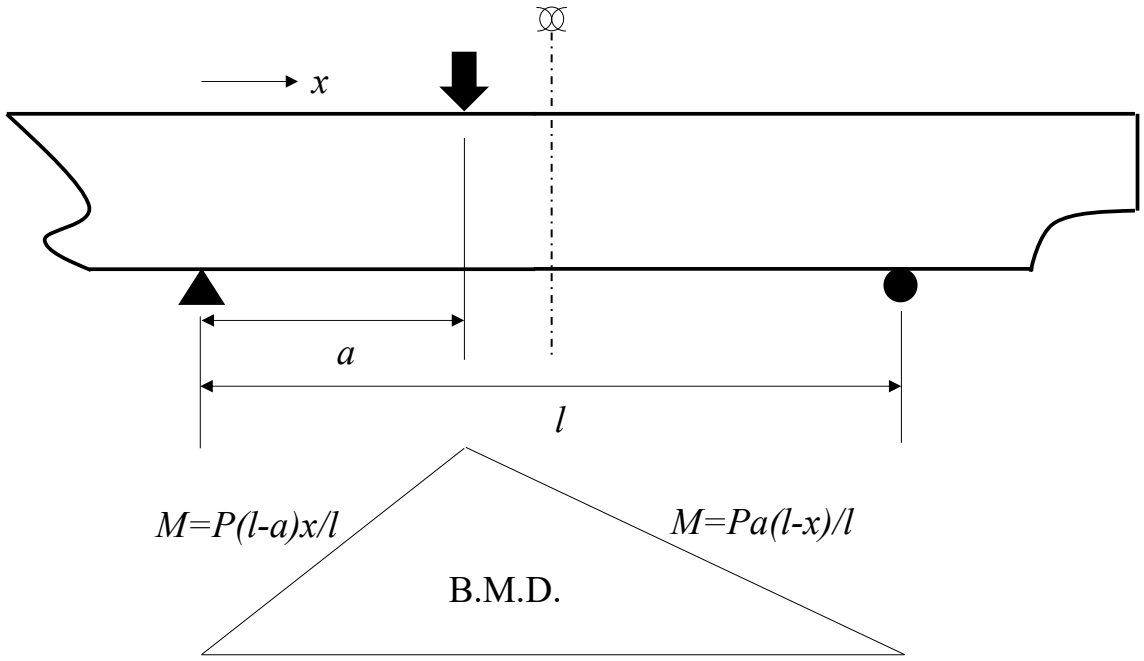

Figure 3.8 Three-point bending test of the OU model

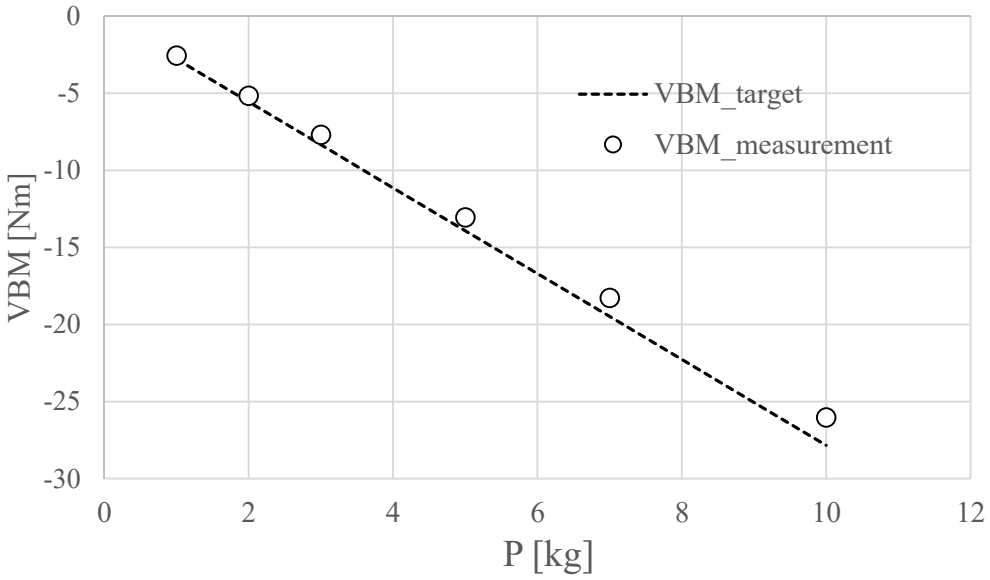

Figure 3.9 Result of VBM calibration

Table 3.2 Principle particulars of the OU model

	Full scale	OU model
Ship length (L_{pp})	283.8 m	2.838 m
Breadth (B)	42.8 m	0.452 m
Depth (D)	24.0 m	0.254 m
Draft in full loading condition (d_f)	14.0 m	0.160 m
Displacement	109480 ton	122.16 kg
Scale ratio	-	100.0

Table 3.3 Scantlings of the sacrificial beam specimen

H (mm)	h (mm)	b (mm)	t_1 (mm)	t_2 (mm)	h_1 (mm)	b_1 (mm)	I (m^4)
40	10	12	2	2	7	6	3.72×10^{-10}

Table 3.4 Short-term sea states for towing tank test of OU model under irregular waves

	Significant wave height (H_s)	Mean wave period (T_z)	Froude number (Fn)	Total measurement period (full scale)
State 1	6.5 m	15.0 seconds	0.000	66.7 hours
State 2	11.5 m	15.0 seconds	0.078	46.7 hours

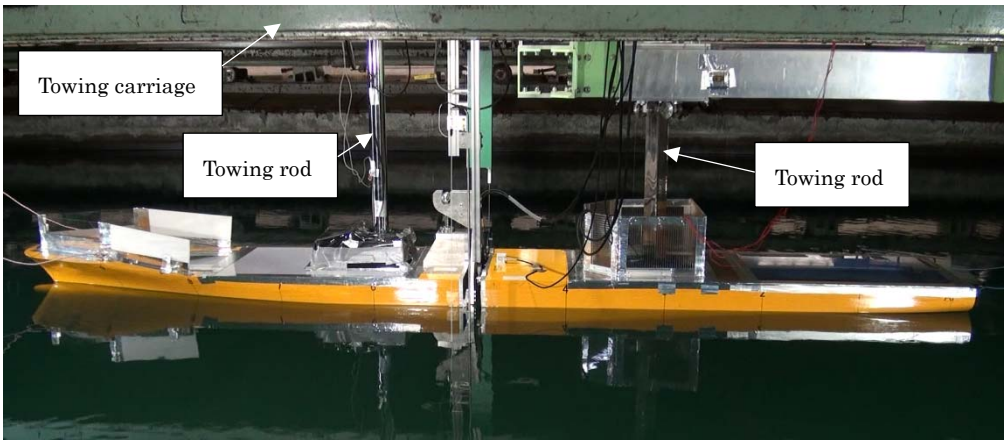

Figure 3.10 Installation of OU model into towing tank

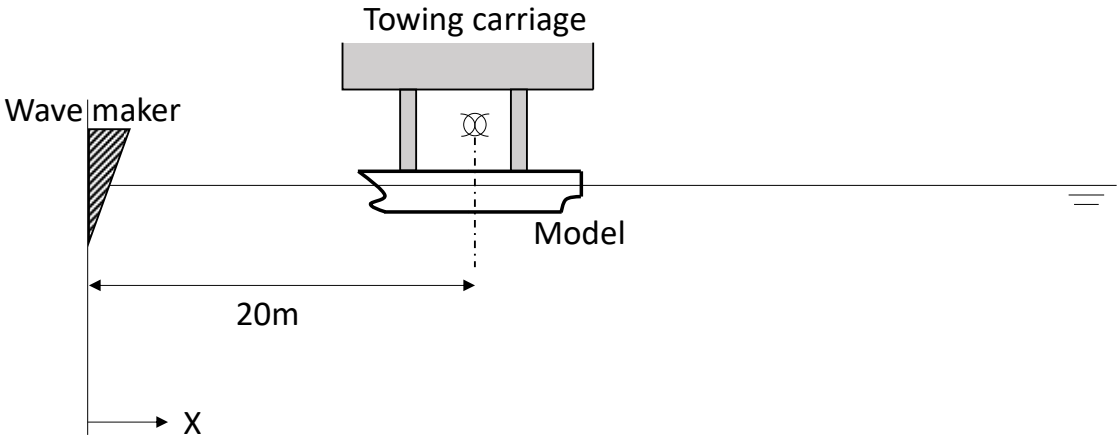

Figure 3.11 Tank test configuration under irregular waves on State 1

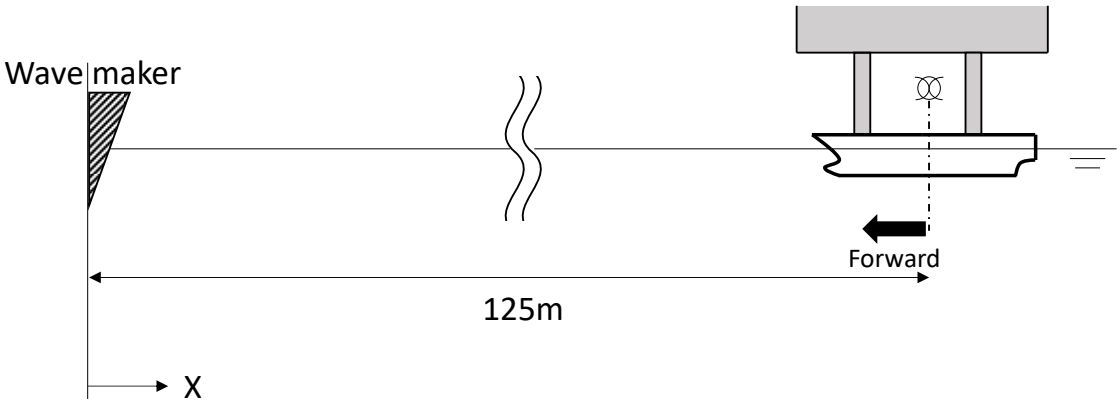

Figure 3.12 Tank test configuration under irregular waves on State 2

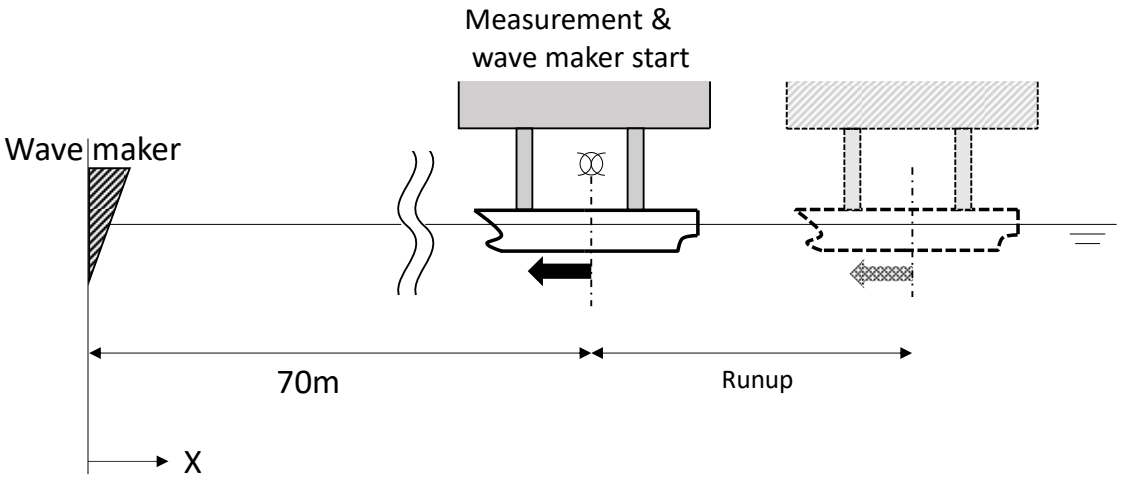

Figure 3.13 Tank test configuration under MPWEs on State 2

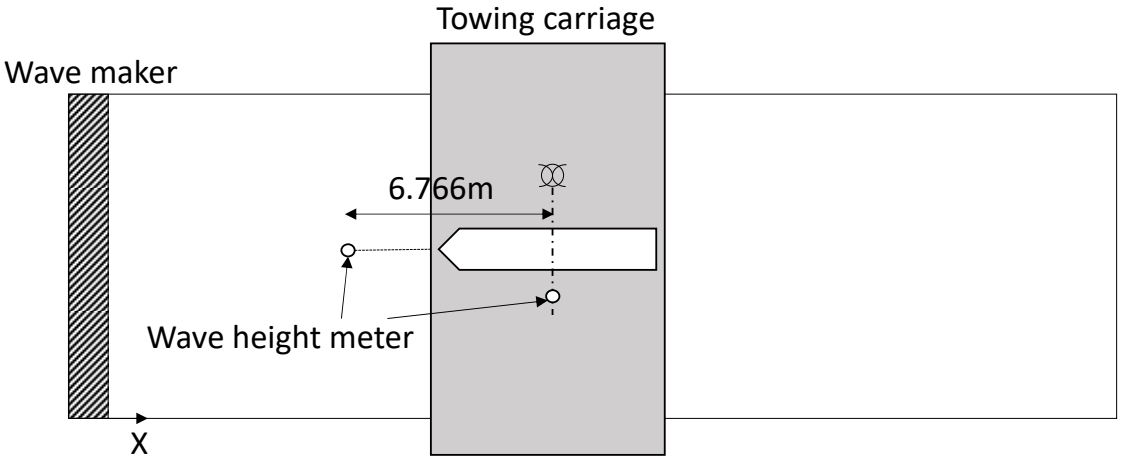

Figure 3.14 Installation position of wave height meters

3.2 Measurement

3.2.1 Natural frequency and damping

The natural frequency of 2-node vertical vibration mode of the backbone model was measured both in dry and wet conditions. To measure the 2-node vibrational characteristics in dry condition, the ship model was hoisted up by ropes at the node points of 2-node vibration then hammering tests were performed [3.5]. Hammering tests to the model afloat on the water were also performed in order to determine the natural frequency and the logarithmic damping ratio in wet condition. Natural frequencies were detected by using measured vertical bending moment of the backbone and FFT analysis. Logarithmic damping ratios were estimated by collecting the natural logarithms of

absolute amplitude values from measured temporal variations. The logarithmic damping ratio was calculated as a slope of the regression line defined as Eq. (3.3):

$$\delta = \frac{\sum_{i=1}^{N}\left(i-\frac{N+1}{2}\right)\left\{\ln(a_i)-\overline{\ln(a_i)}\right\}}{\sum_{i=1}^{N}\left(i-\frac{N+1}{2}\right)^2} \tag{3.3}$$

where N is the number of amplitude, $\overline{\ln(a_i)}$ denotes an average of $\ln(a_i)$. a_i is the ith total amplitude derived from measured temporal variations. 14 hammering tests in each condition (dry or wet) were conducted to obtain natural frequencies, and logarithmic damping ratios at various forward speeds of the model are described in Table 4.5. It is observed that natural frequencies in wet condition at each forward speed take approximately a constant value while the damping ratios increase slightly with an increase of the forward speed.

The natural frequency of 2-node vertical vibration mode of the OU model is measured only in wet condition. Hammering tests to the model afloat on the water is performed as well as the backbone model. Detected 2-node natural frequency and the logarithmic damping ratio are 5.47Hz and 0.057, respectively, see Table 3.6.

Table 3.5 Vibrational characteristics of the backbone model

Condition	*Fn* (Froude number)	Natural frequency of 2-node vibration (Hz)	Logarithmic damping ratio δ
WET	0.000	6.8	0.054
	0.060	6.8	0.058
	0.179	6.8	0.076
	0.236	6.8	0.087
DRY	-	9.2	0.052

Table 3.6 Vibrational characteristics of the OU model

	Full scale	OU model
2-node natural frequency	0.67 Hz (from prototype full scale model)	5.47 Hz
Logarithmic damping ratio δ	-	0.057

3.2.2 MPWE generation by wave maker

As to the experiment of the OU model, MPWEs are generated by using a plunger type wave maker. In order to generate arbitrary irregular waves, one should determine the wave maker displacement histories so that the target wave fields can be successfully reproduced. According to Ref. [3.6], the wave elevation history η generated by a plunger type wave maker can be given by:

$$\eta(X,t) = \sin\theta \int_0^t v(\tau)\eta_I(X, t-\tau)\, d\tau \tag{3.4}$$

where v denotes the velocity of wave maker, η_I denotes the impulse response function of the wave maker, and θ denotes the angle of the wave maker. Consider the two dimensional water channel, η_I is approximately given by:

$$\eta_I(X,t) = \frac{4\sqrt{X}}{\sqrt{\pi g}} \left\{ \frac{1 - \exp\left(-dgt^2 \Big/ 4X^2 \right)}{t} \right\} \cos\left(\frac{gt^2}{4X} - \frac{\pi}{4} \right) \tag{3.5}$$

where d is the height of the wave maker, see Figure 3.15. In this study, X=20 [m], d=1 [m], and θ=40 [deg] is adopted based on equipped wave maker in the 150m towing tank. Once the wave elevation history η is given, the vertical displacement of the wave maker $s(t)$ can be calculated as follows.

$$s(t) = \frac{1}{2\pi} \int_{-\infty}^{\infty} S^*(\omega) \exp(i\omega t)\, d\omega = \frac{1}{2\pi} \int_{-\infty}^{\infty} \frac{V^*(\omega)}{i\omega} \exp(i\omega t)\, d\omega \tag{3.6a}$$

$$V^*(\omega) = \frac{H^*(\omega)}{H_I^*(\omega)\sin\theta} \tag{3.6b}$$

where H^*, H_I^*, V^* and S^* are the Fourier transform of η, η_I, v and s, respectively.

A result of tentative MPWE generation by above-mentioned means, Eq. (3.4)-(3.6), is shown in Figure 3.16. There may be deviations from the target MPWE in terms of the amplitude and phase. Since the η_I given by Eq. (3.5) is the approximated expression based on the two dimensional water channel assumption, it would be necessary to

improve the wave-making signals according to the measured wave elevations. Given the measured wave elevation η_m and its Fourier transform H_m^*, let modified vertical displacement of the wave maker $s'(t)$ be:

$$\begin{aligned} s'(t) &= \frac{1}{2\pi}\int_{-\infty}^{\infty} S'^{*}(\omega)\exp(i\omega t)\,d\omega \\ &= \frac{1}{2\pi}\int_{-\infty}^{\infty}\left\{M(\omega)S^{*}(\omega)\right\}\exp(i\omega t)\,d\omega \end{aligned} \tag{3.7a}$$

$$M(\omega) = \frac{H_m^{*}(\omega)}{H^{*}(\omega)}k(\omega) \tag{3.7b}$$

where $k(\omega)$ is the weighting function in terms of ω, which is to be determined so that $s'(t)$ results in a successful reproduction of target wave elevation. After several trials of determining $k(\omega)$, a comparison between measured wave elevation and the target MPWE is shown in Figure 3.17. As found from the figure, the amplitude and phase are successfully corrected via the correction Eq. (3.7), and it can be concluded that the target MPWE can be reproduced in the towing tank in a sufficient manner.

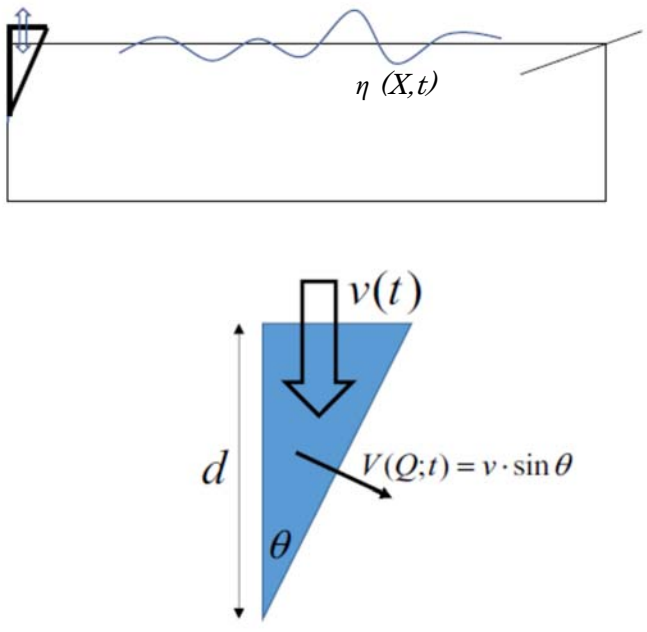

Figure 3.15 Schematic of wave maker in two dimensional water channel

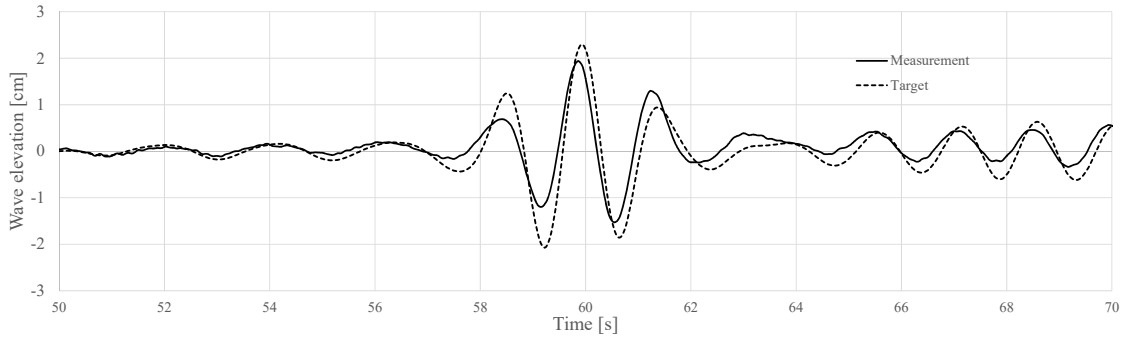

Figure 3.16 Comparison between measured wave elevation and target MPWE (w/o correction)

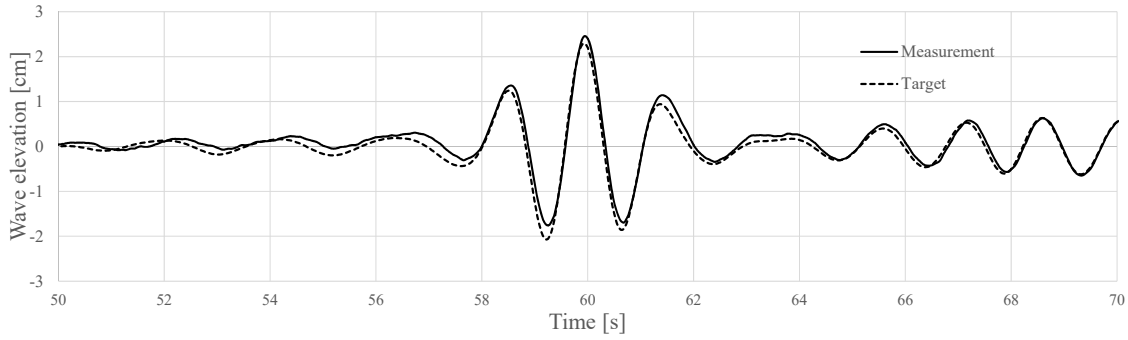

Figure 3.17 Comparison between measured wave elevation and target MPWE (w/ correction)

3.2.3 PoE evaluation by OU model

PoEs of the VBM on State 1 and State 2 are evaluated from the experiment of OU model under irregular waves. In order to count the individual peak VBMs over the measurement, the zero-upcrossing periods are to be detected first from the wave-induced VBM. The wave-induced components from the measurement (WF) are derived by applying the band-pass filter (BPF) to the measured (with whipping, WF+HF) VBM. The cut-off frequency of BPF is set 3.0Hz to exclude 2-node vibration component of the OU model. Figure 3.18 provides an example. Once the zero-upcrossing periods are detected, the individual peaks are determined as the maximum (or minimum) value during each period. The number of counted peaks are 16538 and 13721 for State 1 and State 2, respectively.

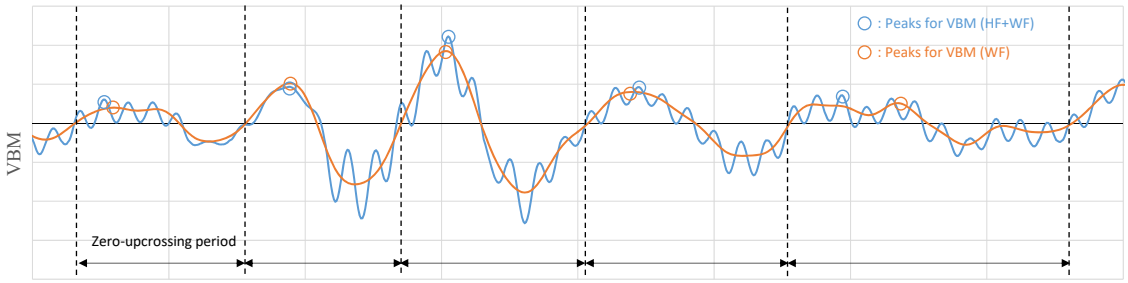

Figure 3.18 Counting individual peaks based on zero-upcrossing period from experiment with OU model

References in Chapter 3

[3.1] M. Oka, K. Hattori, and O. Yoshitaka, “Reproduction of wave induced vibrations of a ship by using a new type backbone model,” in *Proceedings of The 10th Research Presentation Meeting in National Maritime Research Institute*, 2010, pp. 297–298.

[3.2] K. Iijima, Y. Suzaki, and M. Fujikubo, “Scaled model tests for the post-ultimate strength collapse behaviour of a ship’s hull girder under whipping loads,” *Ships Offshore Struct.*, vol. 10, no. 1, pp. 31–38, 2015.

[3.3] K. Iijima, K. Kimura, W. Xu, and M. Fujikubo, “Hydroelasto-plasticity approach to predicting the post-ultimate strength behavior of a ship’s hull girder in waves,” *J. Mar. Sci. Technol.*, vol. 16, no. 4, pp. 379–389, 2011.

[3.4] K. Iijima and M. Fujikubo, “Cumulative collapse of a ship hull girder under a series of extreme wave loads,” *J. Mar. Sci. Technol.*, vol. 20, pp. 530–541, 2015.

[3.5] I. Drummen, G. Storhaug, and T. Moan, “Experimental and full scale investigation of the importance of fatigue damage due to wave-induced vibration stress in a container vessel,” *Trans. R. Inst. Nav. Archit. Conf. Des. Oper. Contain. Ships*, vol. 13, no. 4, pp. 61–74, 2006.

[3.6] S. Ohmatsu, “On the Transitional Wave Making Phenomena by Wave Maker,” *Trans. West-Japan Soc. Nav. Archit.*, vol. 55, pp. 105–116, 1978.

Chapter 4
VERIFICATION AND VALIDATION OF CFD-FEA COUPLED METHOD

In this chapter, a series of verification and validation of the developed CFD-FEA coupled method is presented. Regular head sea condition with forward speed is assumed. First, the verification of the CFD is presented through the case studies changing the mesh size and time increment. To validate the coupled CFD-FEA, numerical results from the linear/nonlinear strip method and 3D panel method (+FEA) are referred. Thus, a brief introduction of those methods is subsequently made. As for the experimental results, those from the towing tank tests with the backbone model are referred. The validation of the coupled CFD-FEA, where the scale FE model of which 2-node natural frequency in dry condition f_{2n}=8.7 [Hz] (in model scale) is used in FEA, is conducted in terms of the rigid body motion, local pressure, the wave-induced VBM, and the whipping VBM. Finally, an application of the coupled CFD-FEA to the DBM evaluation is made by using the prototype full scale ship model of which 2-node natural frequency in dry condition f_{2n}=0.67 [Hz] (in full scale), then the DBM effect on the double bottom structure is investigated.

4.1 Mesh Size and Time Increment Verification of CFD

Table 4.1 shows the calculation cases. The computations of CFD are conducted in the model scale with the stale ratio 94.6, to compare with the towing tank test using the backbone model. Five regular wave cases are investigated. Cases 1-3 compare the time increment step while Cases 4 and 5 compare the mesh size. The wave length λ/L_{pp}=1.0 and the forward speed Fn=0.179 are common in all the cases. Wave heights are varied from 10m (Cases 1-3) to 6m (Cases 4 and 5) in full scale. CFD simulations are carried out by using 8 cores parallel computation of a workstation with Intel Xeon E5-1680 processor. Elapsed wall clock time for computing each case to simulate 30 wave cycles is summarized in Table 4.2. Aspect ratio of the mesh between X(horizontal) and Z(vertical) direction on the free surface domain is kept 6.0 among those cases. For other modeling strategies of CFD, see Chapter 2.

Results of time series of free surface elevation, $\zeta(t)$, for Case 1, Case 2, Case 3 and the experimental measurement are shown in Figure 4.1. The results after 25 wave cycles are

presented in the figure to exclude the transient part. Case 1 has a significant difference from Case 2 and Case 3. Case 2 and Case 3, however, seems to give almost identical results which are close to the experimental measurement. One may conclude that the time increment 0.002 seconds is sufficient to have accurate results by the CFD simulation.

Results for Cases 4 and 5 where the wave height is taken 6m, are presented in a comparative manner in Figure 4.2. CFD computed results are compared after 25 wave cycles. The relative ratios in all mesh sizes throughout the solution domain are the same in Case 4 and Case 5 in order to keep the consistency of calculation qualities. As seen from Figure 4.2, despite a quite small difference between Case 4 and Case 5, these cases have slightly overestimated the free surface elevation. This may be attributed to less number of meshes in the wave height wise in Case 4 and 5 than Case 1, Case 2 and Case 3 thus the refinement of CFD mesh would be necessary. Nonetheless, further refinement of the CFD mesh will lead to a huge increase of calculation time. The benchmark studies described in this chapter are done by setting time step size to 0.001s or 0.002s and the number of meshes to 0.52 million to reduce the calculation time while keeping the accuracy of the solution.

Table 4.1 Calculation cases for CFD validation

Calculation case	Time step	Number of meshes in whole model	Wave height	Number of meshes per wave length	Number of meshes per wave height
Case 1	0.005 s	0.52 million	10 m	40	8.5
Case 2	0.002 s	0.52 million	10 m	40	8.5
Case 3	0.001 s	0.52 million	10 m	40	8.5
Case 4	0.002 s	0.52 million	6 m	40	5.0
Case 5	0.002 s	1.11 million	6 m	50	6.3

Table 4.2 Calculation time for computing CFD

Calculation case	Calculation time
Case 1	9.9 hours
Case 2	21.4 hours
Case 3	41.4 hours
Case 4	21.2 hours
Case 5	39.8 hours

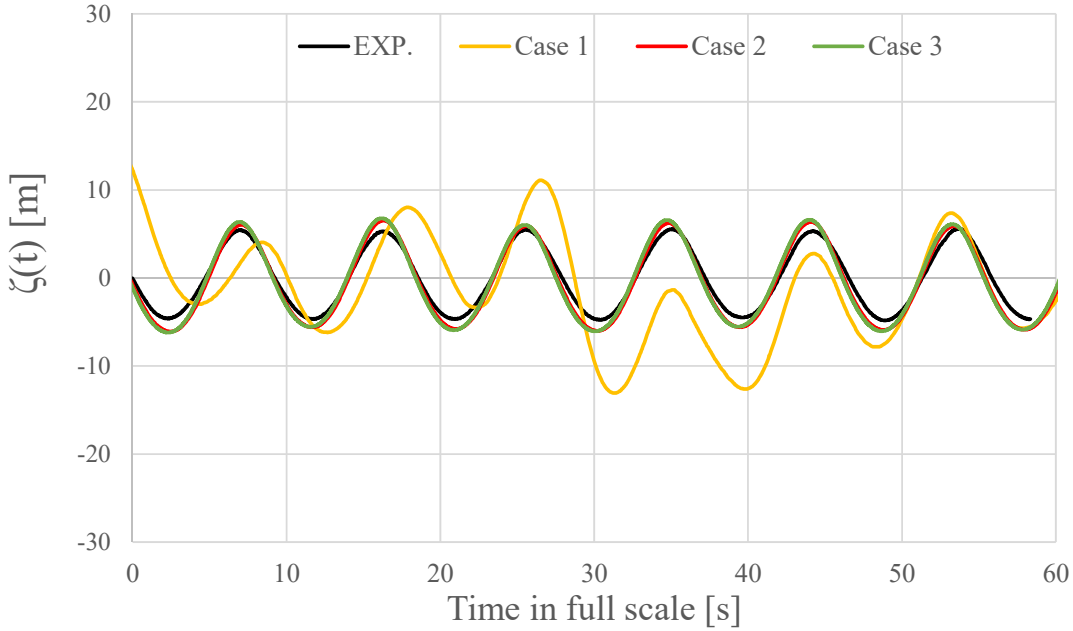

Figure 4.1 Comparisons of free surface elevation by changing time step size

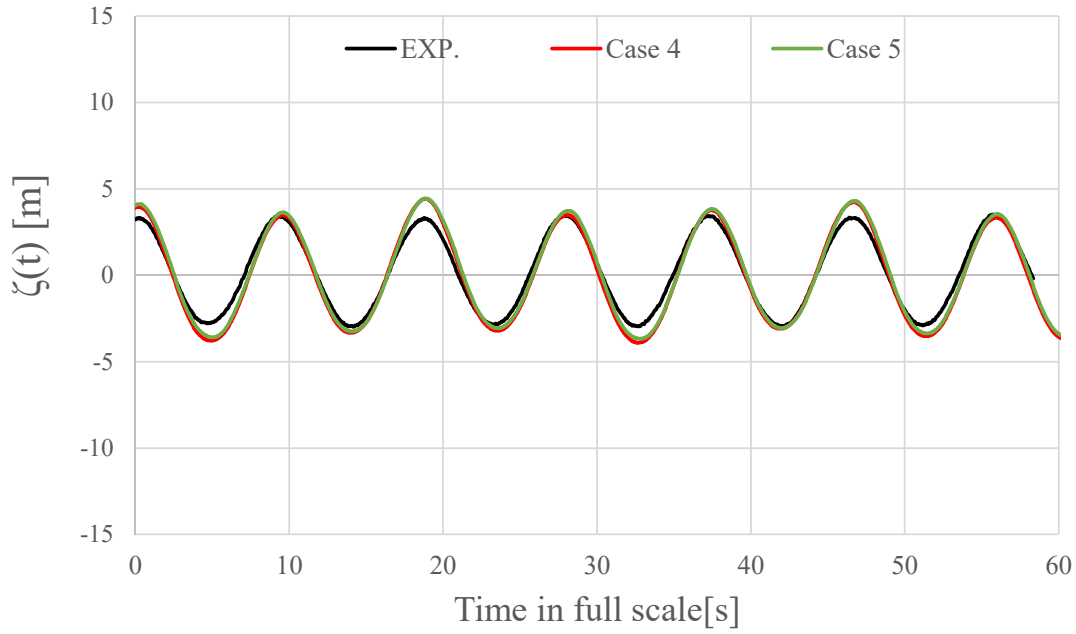

Figure 4.2 Comparisons of free surface elevation by changing mesh size

4.2 Numerical Methods for Validation

A linear strip method, nonlinear strip method and 3D panel based method are adopted for validation of the new numerical model. These conventional models are briefly introduced here. Details of these methods may be found in the respective references.

4.2.1 Linear strip method

Conventional linear strip method is the first method for comparison. Theoretical background of the linear strip method is known as New Strip Method (NSM), which is found in Takagi, et al. [4.1]. NSM calculation is carried out by assuming the conditions below.

- Slender body approximation for ship hull form.
- Diffraction force is calculated using the radiation flow.
- Cross section of ship is approximated by using Lewis form.
- Inviscid, incompressible and irrotational fluid.

The mass distribution in each strip section is taken from the prototype full scale model (see Figure 3.3) ship to estimate the total mass, radius of gyration and center of gravity. It gives a robust solution in frequency domain. In this study, rigid body motions are given for comparison by the linear strip method.

4.2.2 Nonlinear strip method

The nonlinear strip method is also adopted in this study to benchmark the rigid body motions and vertical bending moments. In this study, the in-house code NMRIW-II [4.2] is used. Features of NMRIW-II are described below.

- Nonlinear time domain solver is implemented.
- Salvesen-Tuck-Faltinsen Method (STFM) [4.3] is used for the hydrodynamic modeling while slamming forces are determined by a von Karman momentum theory [4.4].
- Close-Fit method is used for the calculation of 2D hydrodynamic forces.
- Explicit solution with Runge-Kutta-Gill method is applied.
- Hydrodynamic forces on the deck is calculated to account for green water effects. In order to consider green water effects simply, undisturbed incident wave pressure acting on the deck is calculated.
- Whipping response of a ship is derived based on a modal decomposition method considering first 3 free vertical vibration modes of a Bernoulli-Euler beam. The method of structural modeling is followed the conventional nonlinear strip method [4.5]. The horizontal and torsional modes are not taken into account.
- The mass distribution in each strip section is taken from the prototype full scale model.

It gives a robust solution in terms of rigid body motions and vertical bending moments in time series. Whipping vibrations are also accounted for.

4.2.3 Combination of 3D panel method and FEA

The third method is based on a combination of the 3D panel method and linear FEA [4.6]. Hydrodynamic behavior is evaluated under the conventional linear potential theory, i.e., fluid be inviscid, incompressible and irrotational. A Green function with encounter frequency correction is used [4.7]. The hydrodynamic pressure is given in time domain by inverse Fourier Transform. Nonlinearity of the loads is considered partly by integrating the hydrodynamic and hydrostatic pressure over the wetted hull surface which is defined by the instantaneous position of the hull under the incident wave surface. Slamming impact load is evaluated separately by a von Karman momentum theory using temporal variation of added mass [4.4]. The slamming impact load is added to the equation of motion.

For the calculation of structural deformation, a modal superposition method is adopted. The modes in dry condition are extracted based on FE model. In the present analysis, the whole structure is discretized into FE beam elements for the structural modeling. A more concrete analysis procedure is summarized as follows. For more detail along with theories employed, see [4.6].

- Structural model is firstly established by using FEA to evaluate the natural frequencies and the associated modes. 14 Euler beam elements are used for the representation of the present model.
- The mass distribution is taken from the prototype full scale model.
- The hydrodynamic load properties in frequency domain are evaluated. Radiation from the flexible vibration modes is also considered. The hydrodynamic mesh surface is discretized into 15 groups then the loads integrated over the respective groups are added to the respective structural nodes.
- A system of equations of motion is established and solved in modal space. Inverse FFT (IFFT) is used to evaluate the time domain loads. Weakly nonlinear term is also considered while so-called memory effects are not considered.
- Modal superposition technique is used to evaluate the motions and structural deformation at the respective cross sections.

The code has been used for various applications. In this study, it is applied to benchmark the rigid body motions and vertical bending moments including whipping vibrations.

4.3 Rigid Body Motion Benchmarks

4.3.1 Benchmarks with other methods

Rigid body motions under regular heading waves predicted by the different methods and the experimental results using the backbone model are compared. Figures 4.3 and

4.4 show the RAO (Response Amplitude Operator) for the different conditions, respectively. Figure 4.3 shows the results for the waves with the wave height Hw=6m (in full scale) and with the forward speed Fn=0.179, while Figure 4.4 shows the results for the waves with the wave height Hw=10m (in full scale) and with the forward speed Fn=0.179. When processing the RAOs over the experiment and (rigid body) CFD time series results, the peak-to-peak analysis is applied. Peak-to-peak analyses are performed using times series data of 6 seconds in the experiment and 10 physical seconds in the CFD. In CFD results, each motion amplitude are analyzed after 15 wave cycles have passed in order to obtain the stationary results. Values in the vertical axis are plotted in a non-dimensional manner. Symbols z and θ denote the amplitudes of heave and pitch motions, k and h denote wavenumber and wave amplitude, and λ the wave length, respectively. An overall agreement amongst the results is confirmed.

When CFD results are closely looked at, a noticeable difference from the experimental results is found in Figures 4.3 and 4.4 as the wave length ratio λ/L_{pp} increases. The difference may be partly due to the accuracy loss of the VOF free surface. As a reference, a temporal variation of free surface elevation from CFD is compared with that from the experiment in the case of Hw=10m, Fn=0.179, λ/L_{pp}=1.25 in Figure 4.5. In this case, the CFD result overestimates the free surface elevation as seen from the figure. To give more accurate results in the long wavelength cases, further extension of the solution domain, in particular the depth direction, might be ideal [4.8]. Nevertheless, as one can be seen from Figures 4.3 and 4.4, the present CFD gives the rigid body motion predictions with comparatively good accuracy where λ/L_{pp} is up to 1.0, as compared with other numerical simulation methods.

4.3.2 Validation of two-way coupled methods

Next the rigid body motions of the ship evaluated from the two-way coupled methods (weak and strong coupling) are compared with the experimental results and the rigid body CFD results, in the case of Hw=10m, Fn=0.179, λ/L_{pp}=1.0. Time series of the pitch and heave motion of the ship are compared among the experiment, the rigid body CFD results and the two-way coupling results in Figure 4.6 and Figure 4.7, respectively. Results are compared in the model scale (scale ratio 94.6). As for the two-way coupling methods and the rigid body CFD, time step size during the CFD computations is kept 0.002 seconds, i.e. Case 2 model. The time step of the coupling methods Δt is set 0.002 seconds as well. The rigid body motions are derived from CFD computation results at each coupling time step. Results from the rigid body CFD are presented after 25 wave cycles to exclude the transient part. Symbol a, being described in the legends of the

figures, denotes the under-relaxation factor used in the SIMPLE scheme (see Eq. (2.3)).

$$p^{n+1} = p^n + \alpha p' \tag{2.3}$$

As regards the pitch motion from the weakly coupling method (α=0.05), unstable fluctuations are found in its peak values and periods, as seen from Figure 4.6. On the other hand, the stable pitch motion time series is evaluated from the strongly coupled method, and this is comparable to that from the rigid body CFD or the experiment in terms of estimated peak values and periods. This lack of stability in weakly coupled method may be due to that the under-relaxation factor is too small. In terms of the heave motions evaluated from the weakly coupled method, see Figure 4.7, deviation from the experiment or the rigid body CFD is small. This may indicates that effect of the under-relaxation factor on the heave motion would be small. In the case of strongly coupled method, it represents close amplitudes and periods on heave motion compared with the experiment or the rigid body CFD. Further extension of the solution time in the two-way coupling methods would be necessary to obtain more stable results for the rigid body motion, as the transient parts may be remained in the presented results.

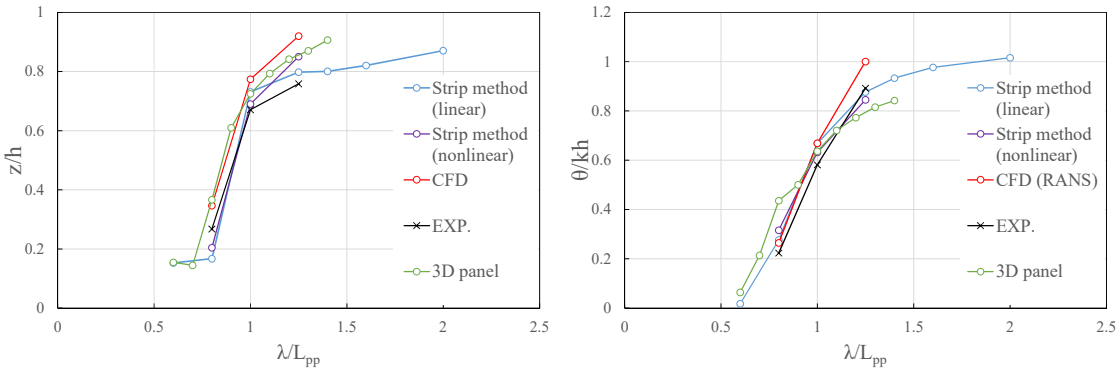

Figure 4.3 Comparisons of heave and pitch motion (Hw=6m, Fn=0.179 in full scale)

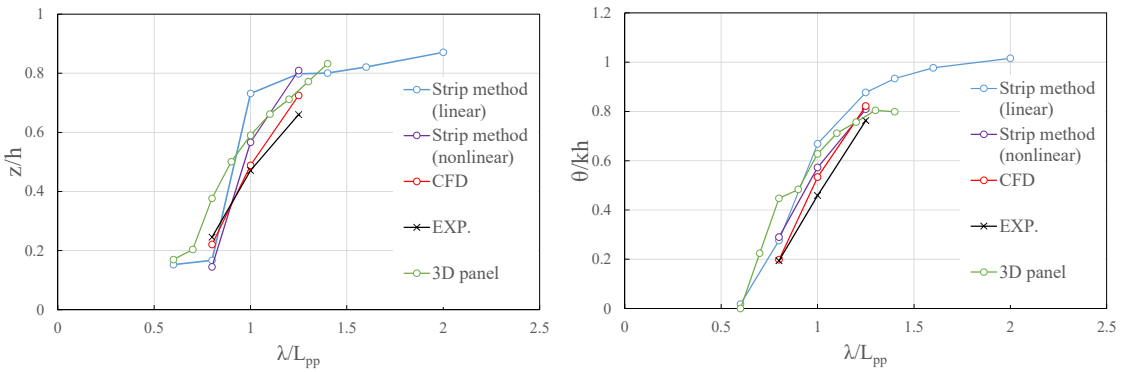

Figure 4.4 Comparisons of heave and pitch motion (*Hw*=10m, *Fn*=0.179 in full scale)

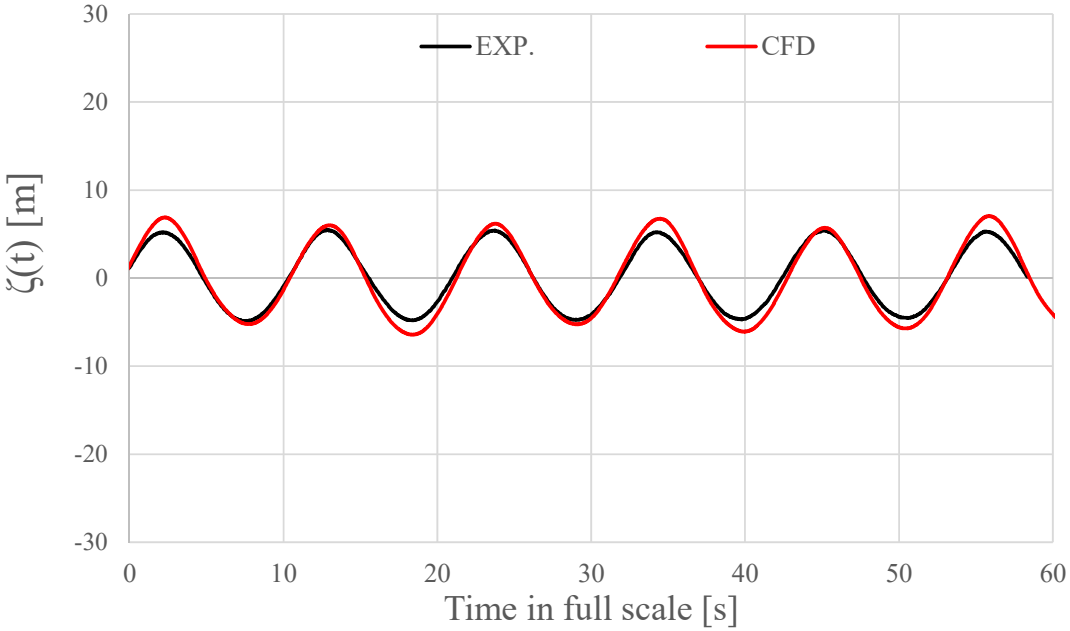

Figure 4.5 Comparison of wave elevation between CFD and the experiment (*Hw*=10m, *Fn*=0.179, *λ/Lpp*=1.25 in full scale)

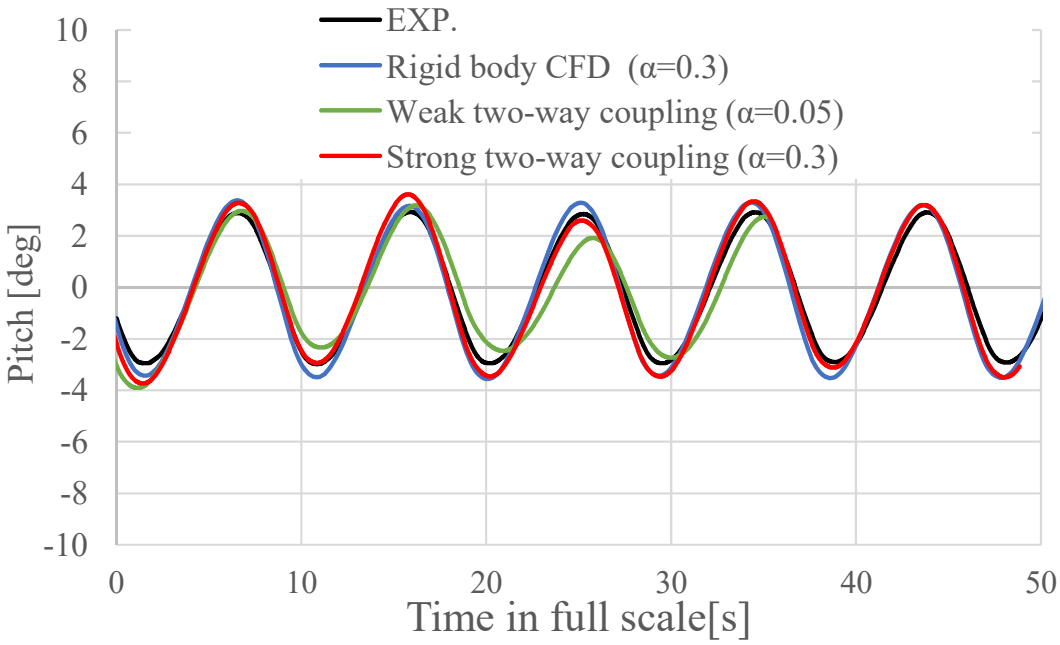

Figure 4.6 Comparison of pitch motion time series between the experiment and numerical methods (Hw=10m, Fn=0.179, λ/L_{pp}=1.0 in full scale)

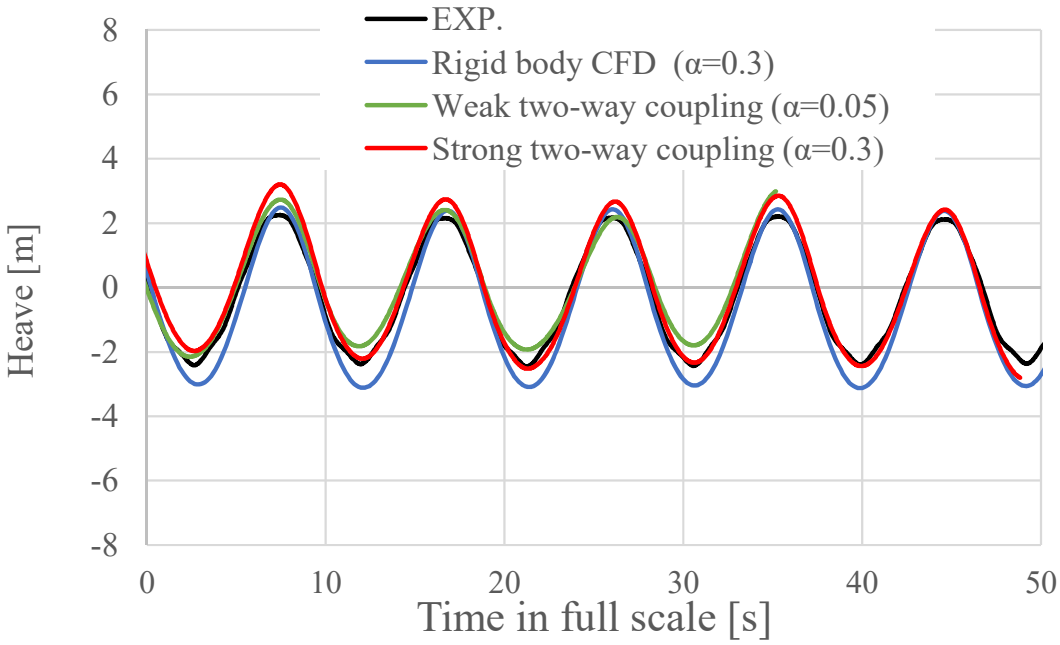

Figure 4.7 Comparison of heave motion time series between the experiment and numerical methods (Hw=10m, Fn=0.179, λ/L_{pp}=1.0 in full scale)

4.4 Local Pressure

4.4.1 Rigid body CFD

The slamming impact pressure is compared between the experiment using the backbone model and the rigid body CFD, in the case of Hw=10m, Fn=0.179, λ/L_{pp}=1.0. Time step size during the CFD computations is kept 0.002 seconds (Case 2 model). Figures 4.8 and 4.9 show comparisons of pressure time series at PS1 and PS2 (see Figure 4.7) obtained by the experiment and the rigid body CFD results. In the CFD results, the area averaged values within 1 mesh area at the target points are calculated. The red lines denote the CFD results and the black dashed lines denote the experimental results. Figure 4.8 shows the results at the bow flare point at SS9.75 (height 21m from keel, in full scale) at which the hull surface has a steeply inclined shape. From the experimental results in Figure 4.8, instantaneous high pressure value is measured corresponding to bow flare slamming. As seen from CFD results, CFD can also capture the period and peak values of water pressure. Figure 4.9 shows the results at the bow part point at SS9.0 (height 18m from keel, in full scale), at which the hull surface has a higher flare angle than SS9.75. From Figure 4.9, time series from CFD represents the period and peak values close to the experiment as well as Figure 4.8.

As a reference, the pressure peak values calculated by using the conventional Wagner theory based on the two dimensional wedge impact problem [4.9] are also given as in Figures 4.8 and 4.9. As observed from these figures, Wagner theory overestimates the pressure peak values. This overestimation may be due to ignoring 3D effects on water impact, thus it can be concluded that a water impact pressure prediction based on the two dimensional approximation approach is not capable of capturing the slamming impact pressure acting on the three dimensional ship.

When Figures 4.8 and 4.9 are revisited, it is found that the experimental results include vibratory components which oscillates approximately at 5 to 8Hz in model scale (at 0.51Hz to 0.82Hz in full scale). By looking the natural frequency of 2-node vibration of the backbone model in wet condition (see Table 3.4), it is interpreted that the 2-node elastic deformation caused these vibrations. In the rigid body CFD phase, the ship has been assumed as a non-deformed rigid body. Thus, such vibrations have not been reproduced.

4.4.2 Validation of two-way coupled methods

The validation of the two-way coupling methods in terms of the representation of local pressure values on the hull is conducted. Time series of the pressure at PS1 in Figure 4.7 are compared in Figure 4.10, among the experimental result, the rigid body CFD,

and the two-way coupled method results, in the case of Hw=10m, Fn=0.179, λ/L_{pp}=1.0. Results are compared in the model scale (scale ratio 94.6). Time step size during the CFD computations is kept 0.002 seconds (Case 2 model), for both the rigid body CFD and the two-way coupled methods plotted in the figure. As to the weakly coupled method, two results are presented of which the under-relaxation factor α is set 0.3 or 0.05. The number of iteration in SIMPLE scheme is 5 in all numerical results. The time step of the coupling methods Δt is set 0.002 seconds. As seen from Figure 4.10, when the weak coupling with α=0.3 is adopted, the solution has diverged. The possible cause of this divergence may be due to the artificial added mass effect, as implied by Causin et al [4.10]. On the other hand, when α=0.05 is adopted, good estimations of pressure peak values can be obtained. When the strongly coupled result is focused on, its solution is successfully proceeded even when α=0.3 is applied. This may be due to a fact that the artificial added mass effect is mitigated by means of the sub-iteration processes implemented in the strongly coupled method.

Time series of the pressure at the bottom point, PS3 in Figure 4.7, are compared each other in Figure 4.11. The static component of the pressure is eliminated from all results. One can find from the experimental result that the pressure history includes oscillations about 6 to 8Hz in frequency domain. These oscillations are attributed to the 2-node vibration of the ship model since the natural frequency of 2-node vibration in wet condition was measured at 6.8Hz. This 2-node vibratory component is apparently responsible for the discrepancy between the rigid body CFD and the experiment. When the weakly coupled result is looked, the vibratory component can be recognized in the pressure time series as the effect of elastic displacements is reflected in CFD simulation at every moment, however its amplitude is rather small compared with the experimental result. In the case of the strongly coupled result on the other hand, the 2-node vibratory component is sufficiently represented in terms of both its amplitude and period. The frequency of the 2-node vibratory component has appeared about 5 to 6Hz in the strongly coupled result. This frequency is a little smaller than the experimental result, as it may be attributed to the accuracy of FE modeling. Note that the 2-node natural frequency in dry condition of the scale FE model is 8.7Hz, which is smaller than the experimental model (9.2Hz). Meanwhile, one may conclude that the decrease of the frequency of 2-node vibration due to the FSI effect can be reproduced with sufficient accuracy by means of the strongly coupled method.

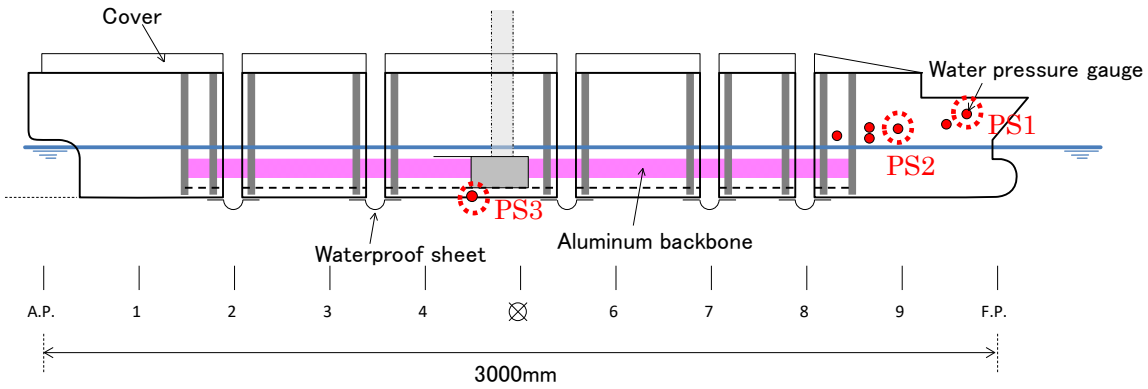

Figure 4.7 Water pressure gauges employed for validations

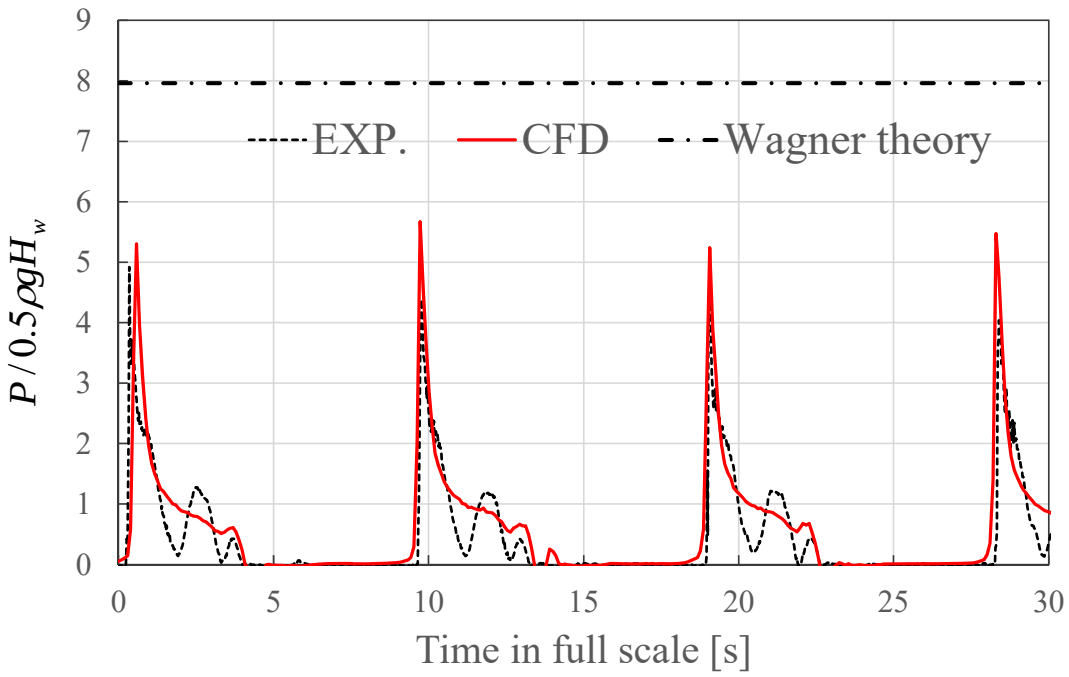

Figure 4.8 Comparison of pressure time series among experiment, Wagner theory and CFD at SS9.75, 21m from keel (PS1, Hw=10m, Fn=0.179, λ/L_{pp}=1.0 in full scale)

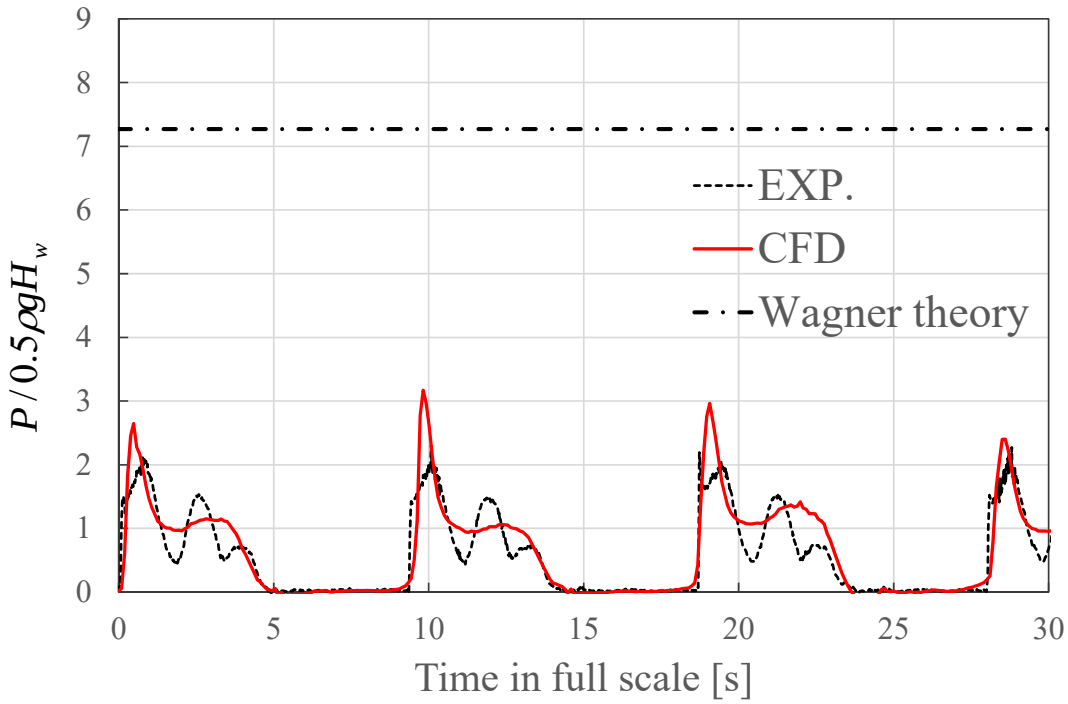

Figure 4.9 Comparison of pressure time series among experiment, Wagner theory and CFD at SS9.0, 18m from keel (PS2, Hw=10m, Fn=0.179, λ/L_{pp}=1.0 in full scale)

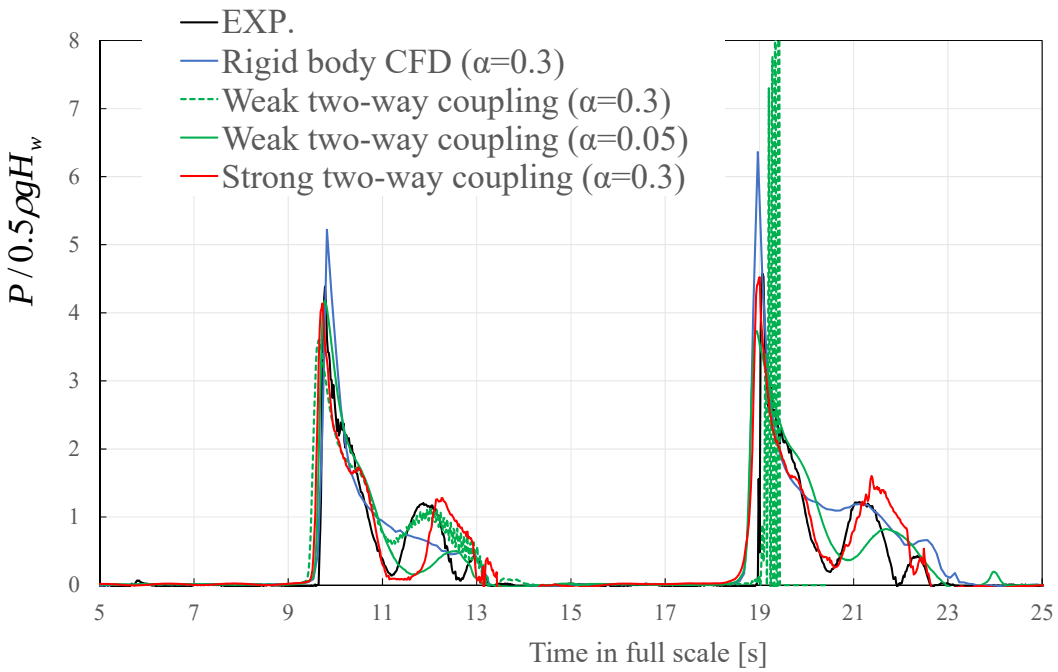

Figure 4.10 Comparison of pressure time series at PS1 between the experiment and numerical methods (PS1, Hw=10m, Fn=0.179, λ/L_{pp}=1.0 in full scale)

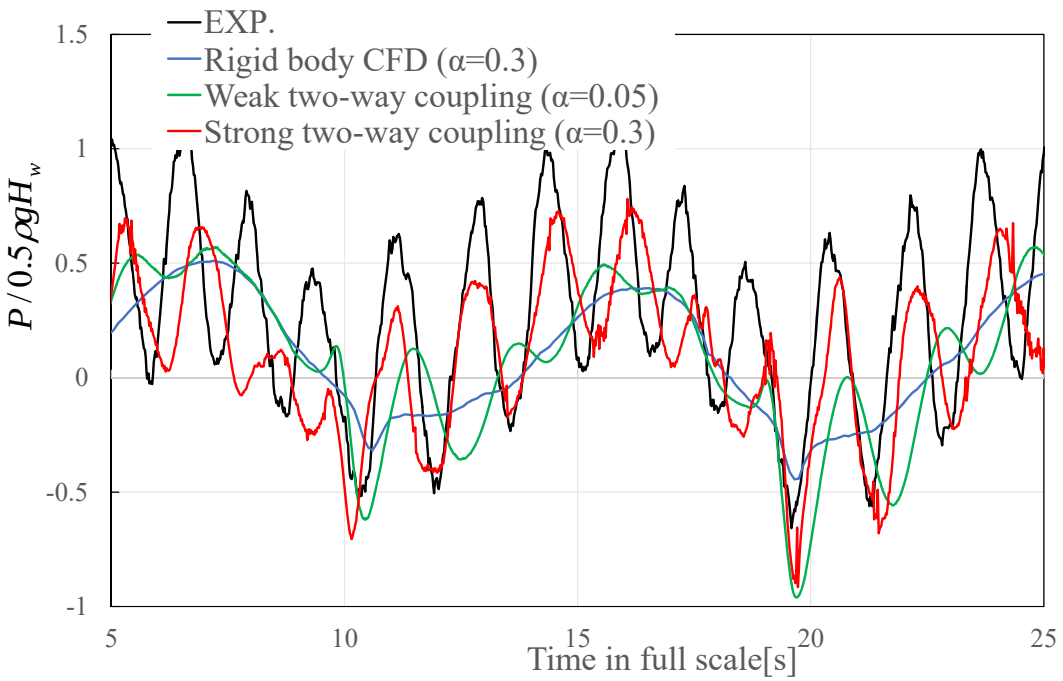

Figure 4.11 Comparison of pressure time series at PS3 between the experiment and numerical methods (PS3, Hw=10m, Fn=0.179, λ/L_{pp}=1.0 in full scale)

4.5 Wave-induced and Whipping VBM

4.5.1 Benchmarks of one-way coupled method with other methods

VBMs obtained by the nonlinear strip method, the 3D panel method combined with FEA, the one-way coupled CFD-FEA, and the experiment are compared with each other. Time step size during the CFD computations is kept 0.002 seconds (Case 2 model). The pressure values to be applied on the scale FE model are given from the CFD at every 0.01 seconds by linearly interpolating the temporal variations. The initiation time of coupling the CFD and FEA is set as the time when 15 wave periods of the CFD solution is ended, to exclude the transient part. The VBMs obtained from each result are decomposed into the normal wave-induced component (M_{v_wave}) and the high frequency (whipping) components (M_{v_whip}) by applying the band-pass filter (BPF) to the time series results. Frequency range of BPF is determined considering the wave period and eigen frequency of 2-node vibration on each model.

Figure 4.12 shows a comparison of wave-induced components of VBM at the midship section (SS5.5, see Figure 4.7) where Hw is 10m, Fn is 0.179 and λ/L_{pp} is 1.0. In these results, positive value of M_{v_wave} indicates the hogging moment. To eliminate the static bending moment, a CFD-FEA coupled analysis using the ship model on a calm water

surface is preliminarily performed. The black lines denote results from the experiment, the blue lines denote results from nonlinear strip method, the green lines denote results from coupling of 3D panel method and FEA, and the red lines denote results from the CFD- FEA coupling. The results from nonlinear strip method, 3D panel-FEA method and the CFD- FEA coupling, seem to show a qualitative agreement in terms of the amplitudes of the wave-induced VBMs.

Figure 4.13 shows a comparison of whipping components of VBM at SS5.5. Since the subject scenario in this study assumed a severe condition for ship structure, i.e. wave height 10m with service speed under heading wave, peak amplitudes of the whipping components have appeared remarkably large. Discrepancies in terms of the vibration frequencies are observed among the respective numerical results. One possible cause of these discrepancies is the difference of the natural frequency of the structural models used in each numerical method. The other is the added mass effect from the elastic deformation of the ship. Frequency of the whipping vibration from the experimental result is found about 6.4Hz in model scale, which is close to the natural frequency of 2-node vibration in wet condition. As the one-way CFD-FEA coupling method does not consider the added mass effect in the flexible deformation, the frequency of the whipping vibrations is found around 8.5Hz in model scale, which is close to the natural frequency of 2-node vibration in dry condition of FE model. Nevertheless, the CFD-FEA coupling method predicts the amplitudes of whipping components which are comparable to those from the experiment as well as other numerical methods.

The effect of the CFD calculation time step on the VBM is further investigated. Figures 4.14 and 4.15 show comparisons of normal wave-induced and whipping components of VBMs at SS5.5. By comparing the hydroelastic responses from different time step in CFD (Case 2 and Case 3 as defined in Table 4.1), small differences are found in the VBM results. It indicates that time step size 0.002 seconds in the CFD phase is sufficient to evaluate not only the wave propagation but VBM evaluations.

4.5.2 Validation of two-way coupled methods

The VBMs derived from the two-way coupled methods are validated. Derived VBMs are decomposed into the wave-induced and the whipping components as well. Time step size during the CFD computations is kept 0.002 seconds (Case 2 model). A comparison of the wave-induced VBMs at the midship section (SS5.5) is shown in Figure 4.16. VBMs are expressed in the model scale. Subject wave condition is; Hw is 10m, Fn is 0.179 and λ/L_{pp} is 1.0, and results are compared in the model scale (scale ratio 94.6). As seen from Figure 4.16, the wave-induced components derived from the weakly and strongly coupled

method agree well with the experimental one, as well as the one-way coupling results.

A comparison of the whipping components at SS5.5 is shown in Figure 4.17. When the weakly coupled results are focused on, the underestimation of the amplitudes of whipping VBM can be found. One of the conceivable reason of this underestimate is that the under-relaxation factor is too small to calculate the pressure temporal values appropriately at each coupling time step. However, the instability of the weakly coupled solution in the case of α=0.3 is also confirmed as described above. To overcome these issues, decreasing the coupling time step Δt is reportedly considered to be one of the efficient approaches [4.11]. Nonetheless, it may require quite a few computational efforts to find the proper coupling time step by using the weakly coupled method and consequently the benefits of the weakly coupled method would be detracted.

As already mentioned in 4.4.1, the whipping components in the one-way coupling results oscillate about 8.5Hz, which is close to the natural frequency of 2-node vibration of the FE model in dry condition (8.7Hz). Meanwhile, the frequency of the vibration of whipping components from the strongly coupled results is observed around 6.0Hz. This decrease of the vibration frequency is originated from the FSI effect, in fact the frequency of whipping vibrations measured from the experiment, about 6.2Hz from the figure, has decreased in the same range compared with the natural frequency in dry condition. From these results, one may conclude that the strongly coupled method gives a quantitative estimation for the FSI effect on the whipping VBM.

When Figure 4.17 is revisited, the whipping component derived from the strongly coupled method agree well in terms of the peak amplitudes of the moments with the one-way coupling method or the experimental results. Amplitudes of the whipping moment irregularly deviate from the experimental result or the one-way coupling result, as found around 0.5 seconds to 0.9 seconds or around 1.9 seconds. One of the conceivable causes of these irregularities is the inaccuracy of pressure estimations at these time, as in Figure 4.11. As already discussed, this can be improved by implementing convergence check on the displacement field. The other cause of these irregularities may be that the displacement fields at these time have not yet converged properly. To prevent such inconsistencies, it is recommended to increase the number of sub-iterations, which in turn leads to the increase of computational efforts though. From these prospects, if we consider the practical application of the two-way coupled CFD-FEA, an alternate prediction method which can predict the strong two-way coupled results in a sufficient and inexpensive manner may be ideal. Several researchers have grappled with the similar problems by constructing the Reduced Order Method (ROM) for FSI [4.12]. If an appropriate ROM for representing the strong two-way coupled CFD-FEA results is

developed, further case studies or even the evaluation of FSI effect under irregular wave would be attained.

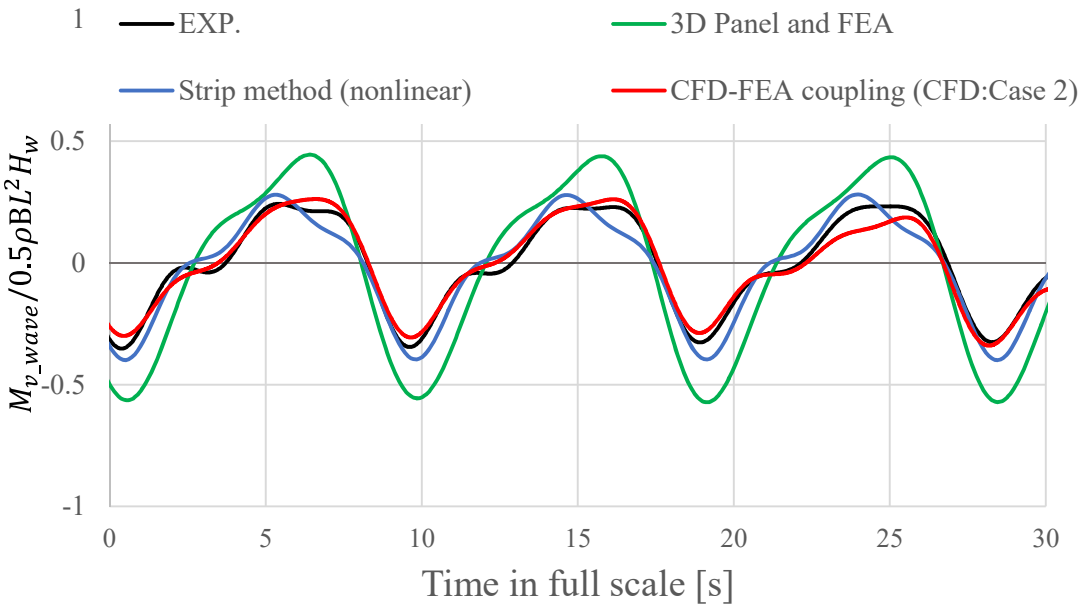

Figure 4.12 Comparison of wave-induced components of VBMs at SS5.5 (Hw=10m, Fn=0.179, λ/L_{pp}=1.0 in full scale)

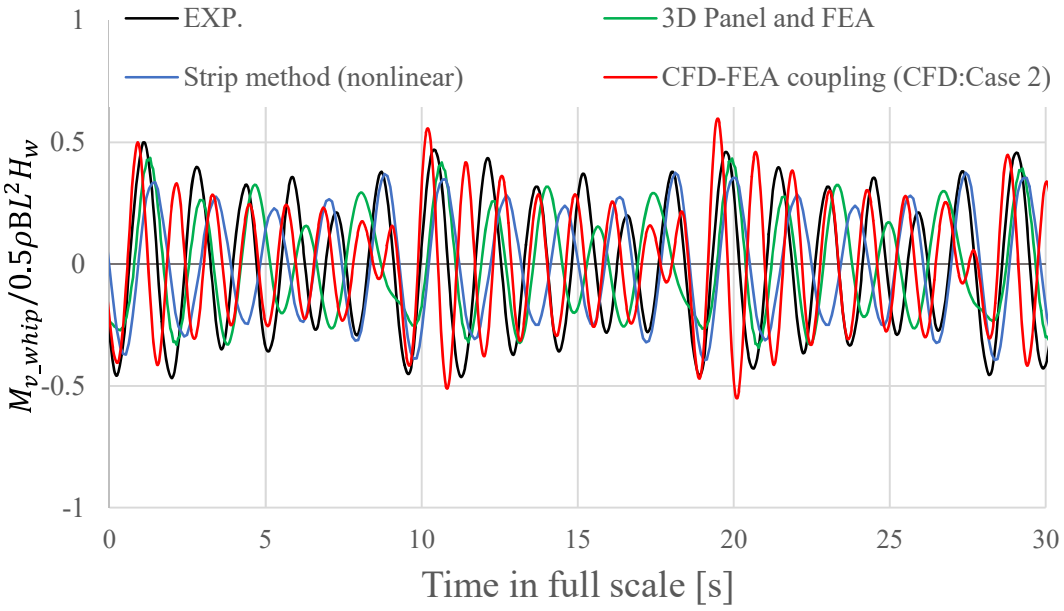

Figure 4.13 Comparison of whipping components of VBMs at SS5.5 (Hw=10m, Fn=0.179, λ/L_{pp}=1.0 in full scale)

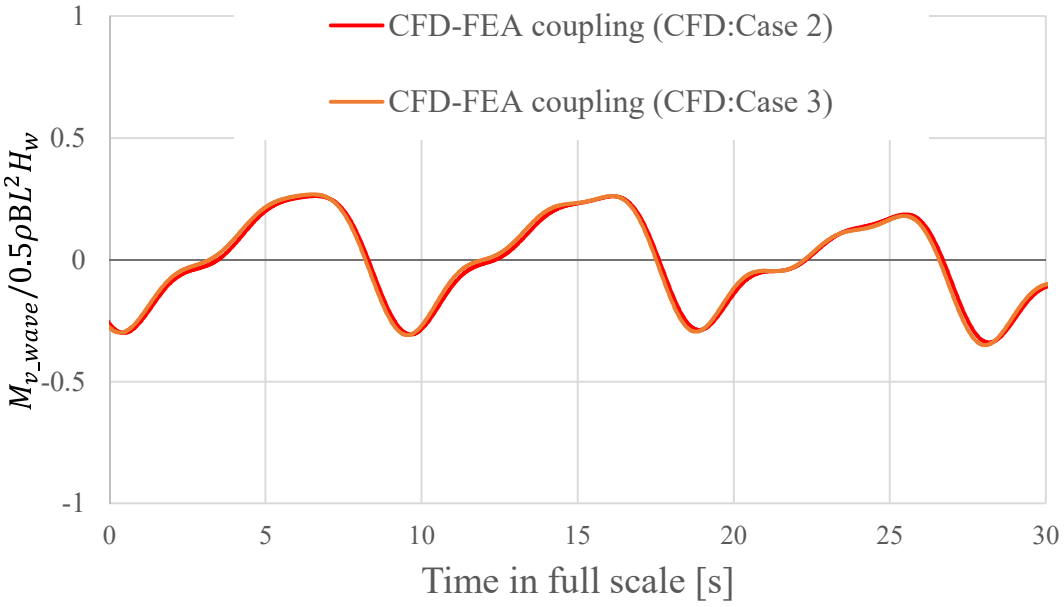

Figure 4.14 Comparison of wave-induced components of vertical bending moments at SS5.5 by changing the CFD calculation time step

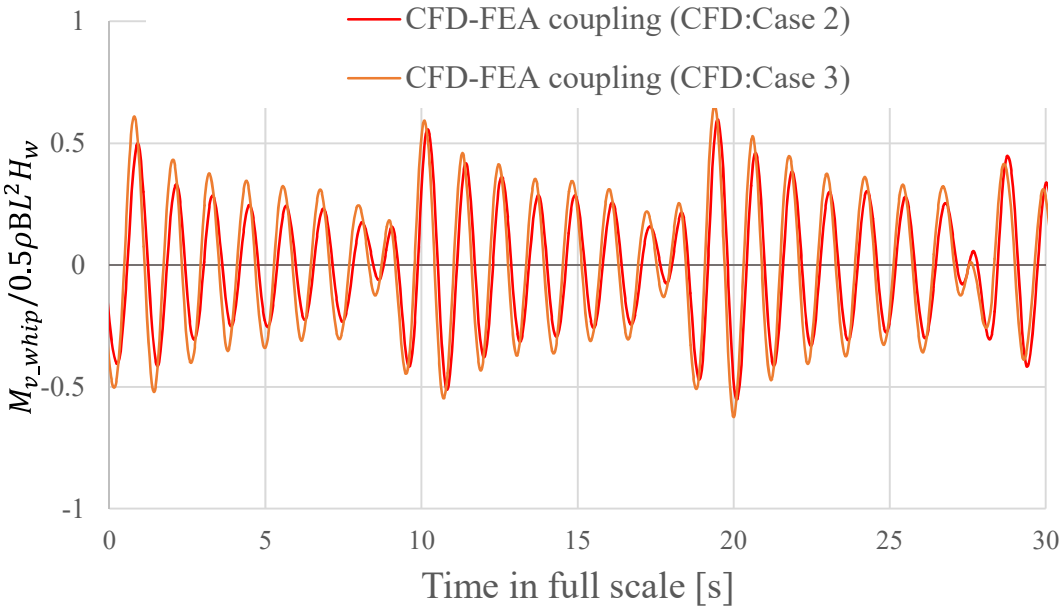

Figure 4.15 Comparison of whipping components of vertical bending moments at SS5.5 by changing the CFD calculation time step

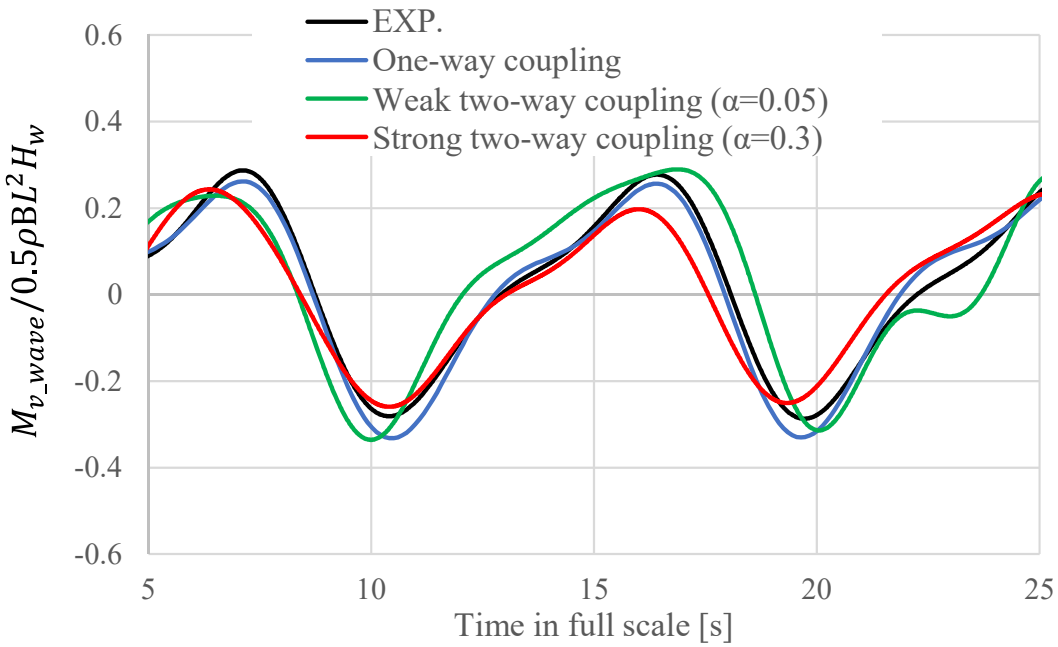

Figure 4.16 Comparisons of wave-induced bending moment between the experiment and numerical methods (Hw=10m, Fn=0.179, λ/L_{pp}=1.0 in full scale)

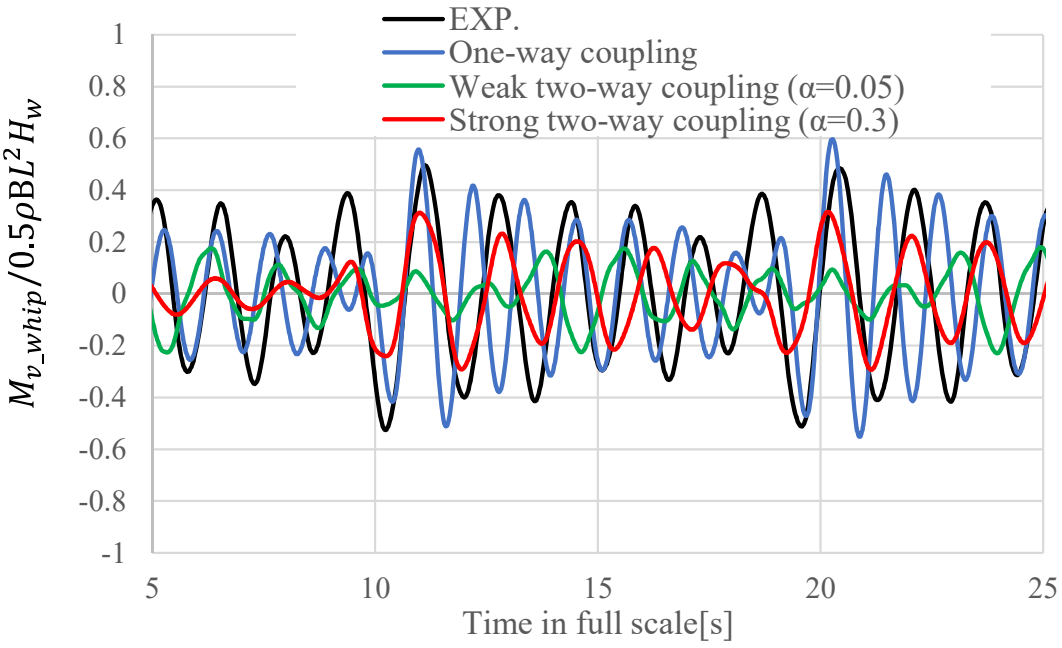

Figure 4.17 Comparisons of whipping bending moment between the experiment and numerical methods (Hw=10m, Fn=0.179, λ/L_{pp}=1.0 in full scale)

4.6 Application to DBM evaluation

4.6.1 General

The hull girder ultimate strength of container ships, whose deck structure is small in width, is governed by the structural strength of the bottom structure. In estimating the hull girder ultimate strength, the stress distribution along the double bottom structure is checked. The longitudinal stress distribution on the outer bottom plate is given by a sum of global stress due to VBM M_{glob} and local stress including double bottom stress due to DBM M_{db} [4.13], expressed as follows:

$$\sigma_x(z) = \sigma_{x,glob}(z) + \sigma_{x,db}(z)$$
$$\sigma_{x,glob}(z) = \frac{M_{glob}(z - g_{glob})}{I_{glob}} \tag{4.1}$$

where σ_x is the longitudinal stress component, g_{glob} is the height of neutral axis about the whole section, I_{glob} is the second moment of the cross sectional area. Note that M_{glob} will be estimated from the numerical method, in this study CFD-FEA coupling methods, and $\sigma_{x,glob}$ can be obtained in an analytical manner assuming the Bernoulli Euler beam. Meanwhile, σ_x may be evaluated directly from the stress on the FE element at the evaluation point. Thus, the local stress component including the DBM, $\sigma_{x,db}$ in Eq. (4.1), is estimated by subtracting the global stress $\sigma_{x,glob}$ from the stress value on the FE element σ_x. In this section, the one-way coupled CFD-FEA, in which the prototype full scale FE model (see subsection 2.3.3) is used, is adopted to evaluate the wave-induced response of a full scale 3D container ship model. Then, through the decomposition process as per Eq. (4.1), the effect of DBM on the longitudinal stress on the outer bottom plate is investigated.

4.6.2 Results and discussion

Global vertical bending moment at mid-ship section (SS5.25, see Figure 2.7) is compared with the experiment result on the backbone model. The environmental condition is: Hw is 10m, Fn is 0.179 and λ/L_{pp} is 1.0. Static bending moments and wave-induced bending moments are eliminated from both the results then whipping components M_{v_whip} are compared in Figure 4.18. Rayleigh damping method with the damping ratio 1.66%, obtained by an investigation on container ships by Storhaug et al. [4.14], is adopted for the first bending mode. Since the structural model and the impact forces in full scale simulation are not necessarily the same as those in the experimental

model, the amplitude of M_{v_whip} by the full scale simulation differs from that by the experiment. In terms of the period and peak values of M_{v_whip}, however, a good estimation is confirmed. The power spectrum density of M_{v_whip} from full scale simulation is shown in Figure 5.19. Local peaks are found at the vicinity of 0.66Hz and 1.30Hz, which respectively correspond to 2-node and 3-node global vibration modes (see Figure 4.20). Moreover, it is noteworthy that the 2-node vibrational component is still dominant in global vertical bending moment in the full scale simulation.

The effect of the DBM on the stress at the bottom is investigated according to the first line of Eq. (4.1). Prior to this, the eigen frequencies in the double bottom bending mode are also confirmed. An overview of the FE partial model for calculating double bottom bending modes is shown in Figure 4.21. 6 holds (2 watertight bulkheads) span between SS3.5 and SS6.5 is taken out from the whole ship model including the container cargo elements. Then, a modal analysis is carried out on the partial model. For the eigenvalue analysis, translations of nodes on SS3.5 and SS6.5 are constrained. The detected vertical bending mode of the double bottom structure is shown in Figure 4.22. The contour indicates distribution of vertical displacements. The local one half-wave deformation mode between 2 holds span, superposed to the overall one half-wave deformation between SS3.5 and SS6.5 is found at 1.33Hz. Figure 5.22 indicates the comparisons of longitudinal stress histories on the outer bottom at SS5.25 among the full scale CFD-FEA coupling simulation result ($\sigma_{x,from\ CFD\text{-}FEA}$), $\sigma_{x,glob}$ which is derived from the second term of Eq. (4.1), and $\sigma_{x,db}$ in Eq. (4.1). Here, in order to evaluate the global bending moment M_{glob} and induced stress component $\sigma_{x,glob}$ accurately, axial stress components are estimated by summing up the longitudinal stresses over the elements in the cross section then divided by the whole section area, and subtracted from $\sigma_{x,from\ CFD\text{-}FEA}$. The negative values of the longitudinal stress imply that the cross section is subjected to the hogging bending moment which induces compression in the outer bottom. By comparing $\sigma_{x,from\ CFD\text{-}FEA}$ and $\sigma_{x,glob}$ at the time of sagging or hogging peaks, it is found out that the magnitude of the longitudinal stresses from the CFD- FEA result is slightly higher than the hull girder global stress $\sigma_{x,glob}$. It is thus necessary to estimate the structural response on the outer bottom structure taking $\sigma_{x,db}$ into account. Strength evaluating only by the hull girder stress may lead to non-conservative side from the viewpoint of design.

The frequency spectrum of $\sigma_{x,db}$ is given in Figure 4.24. Peaks are observed at the vicinity of 0.1Hz, 0.65Hz and 1.3Hz. The lowest component, around 0.1Hz, may be regarded as the wave-induced component; the pressure applied at the double bottom gives rise to this component. The peak around 0.65 Hz is regarded as that from 2-node vibration. As for the highest component, around 1.3Hz, it is inferred that the DBM

induced vibration and global 3-node vibration give rise to the high frequency response, as the eigen frequency of double bottom vertical bending mode and global 3-node vibration mode is found respectively at 1.33Hz and 1.28Hz.

In order to compare the magnitudes of different modes in $\sigma_{x,db}$ more clearly, BPF is applied to $\sigma_{x,db}$ with the cut-off frequency varied. The comparison of time histories of each vibration mode is shown in Figure 4.25. In the figure, the time histories with the cutoff frequencies set to 0.0Hz-0.2Hz, 0.2Hz-1.0Hz and 1.0Hz-2.0Hz, respectively, are presented. The curves correspond to the wave induced component, 2-node global bending component, and the DBM component, respectively. One can find that the contribution from the DBM induced vibration is significant. The same tendency at the mid-ship hold was reported in Kawasaki et al. [4.15] for a 12,000TEU size container ship. These results indicate that the consideration of the local double bottom bending stress with the dynamic amplification effect is necessary to be included for a more accurate stress evaluation.

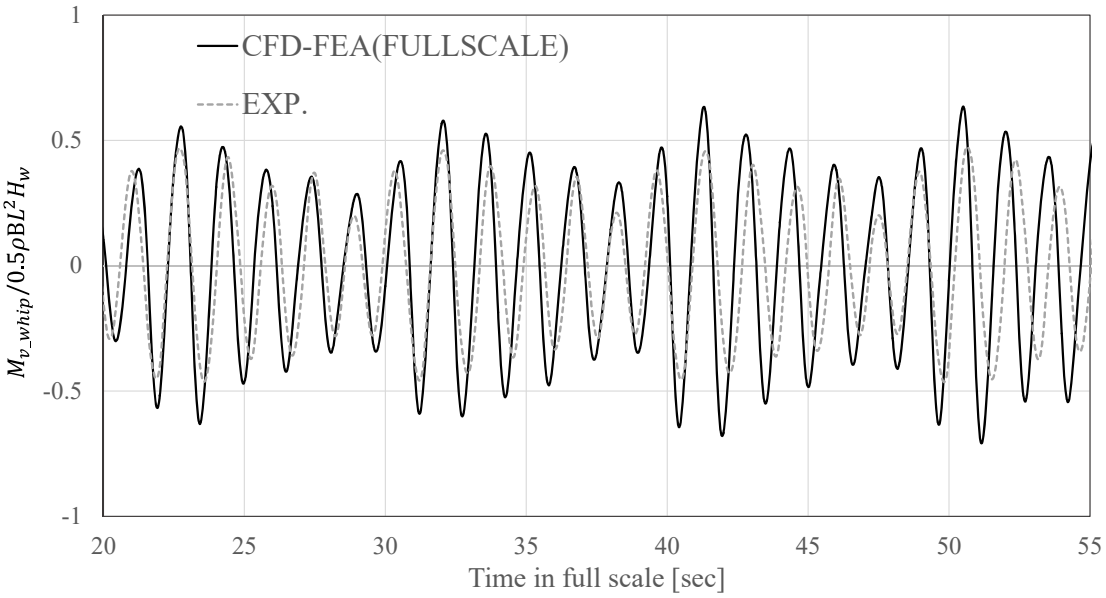

Figure 4.18 Comparison of whipping components of global VBMs between full scale simulation and the experiment (Hw=10m, Fn=0.179, λ/L_{pp}=1.0 in full scale)

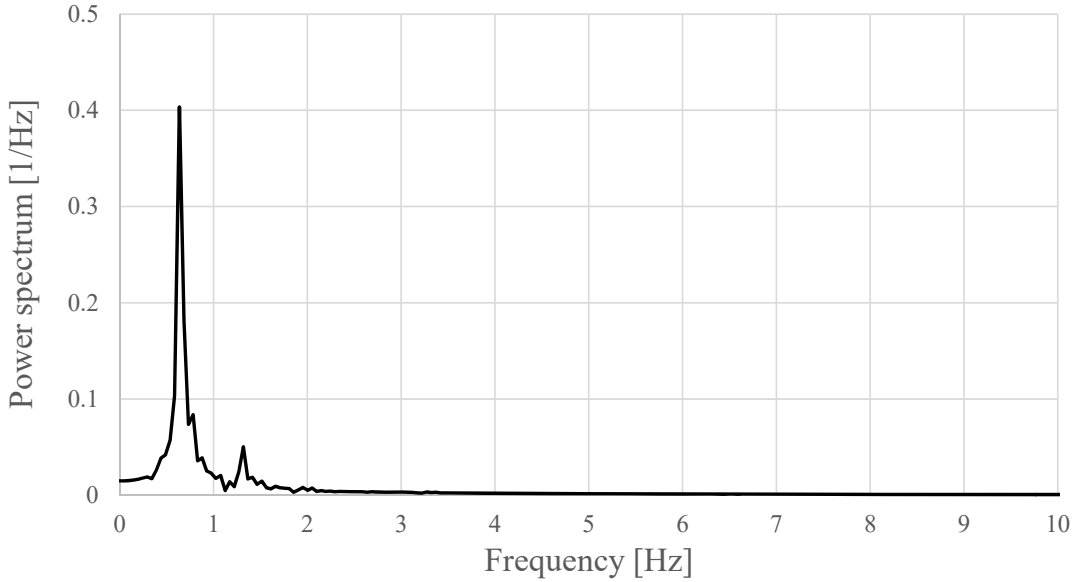

Figure 4.19 Power spectrum density of M_{v_whip} from full scale simulation

Figure 4.20 3-node vibration mode shape of prototype full scale ship FEA model (1.28Hz)

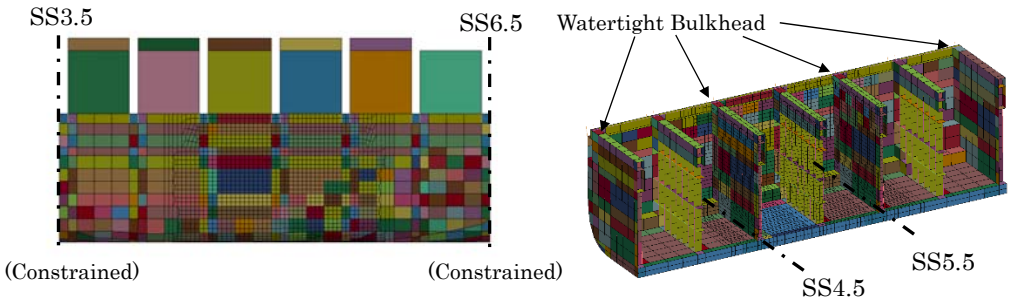

Figure 4.21 Overview of the FEA meshing for calculating double bottom bending eigen modes

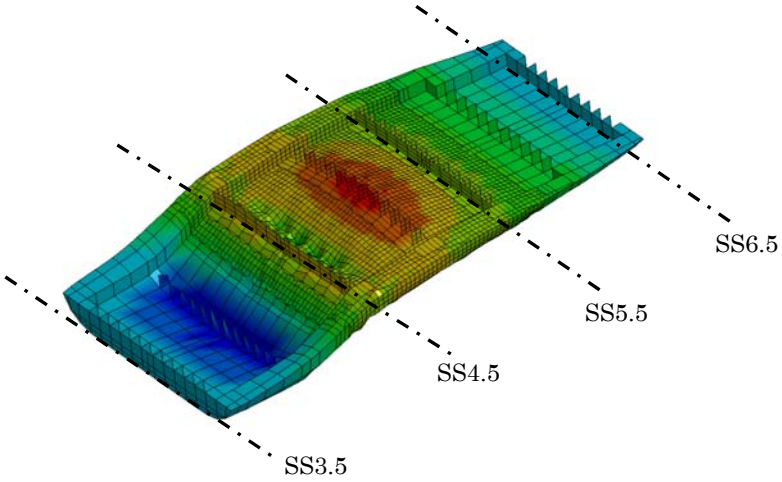

Figure 4.22 Double bottom bending mode shape (1.33Hz)

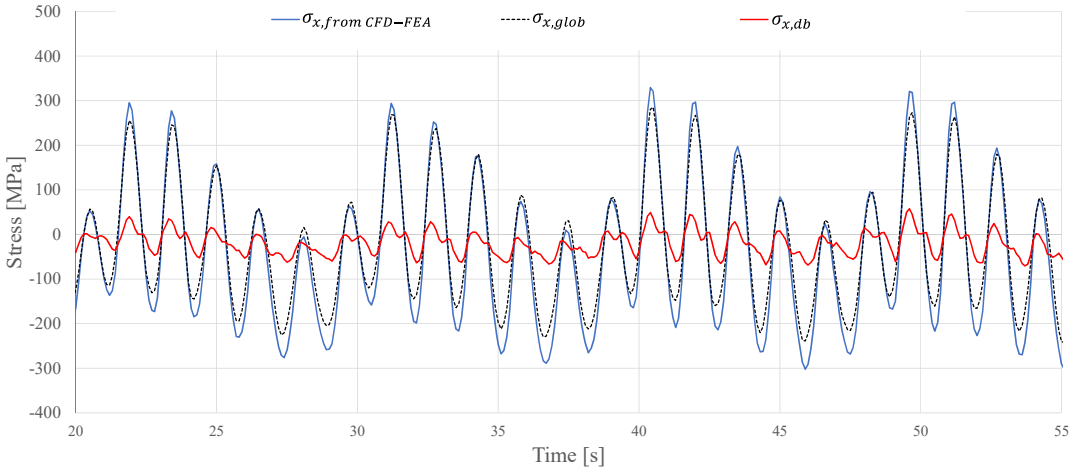

Figure 4.23 Comparison of longitudinal stress components on outer bottom panel at SS5.25

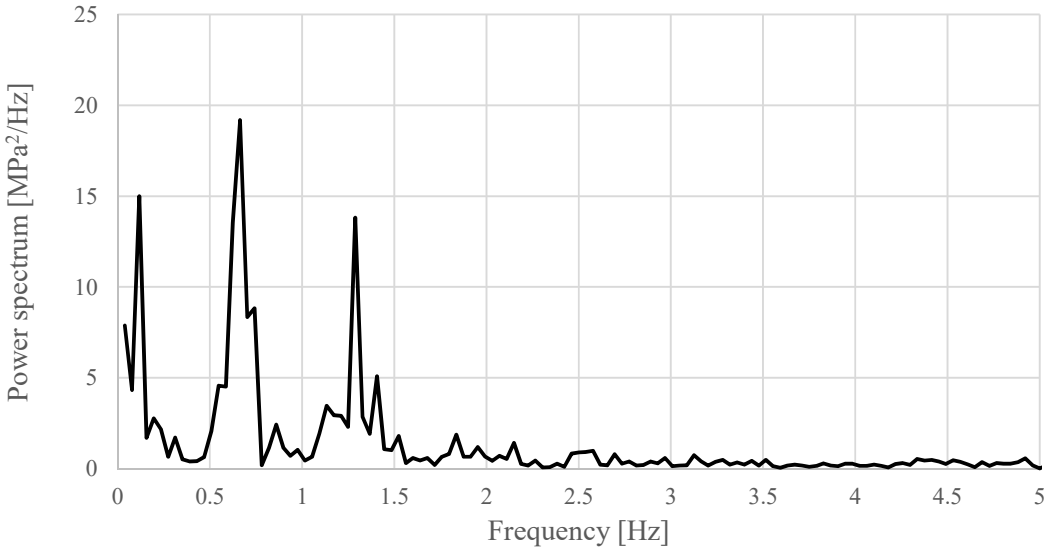

Figure 4.24 Power spectrum density of $\sigma_{x,db}$

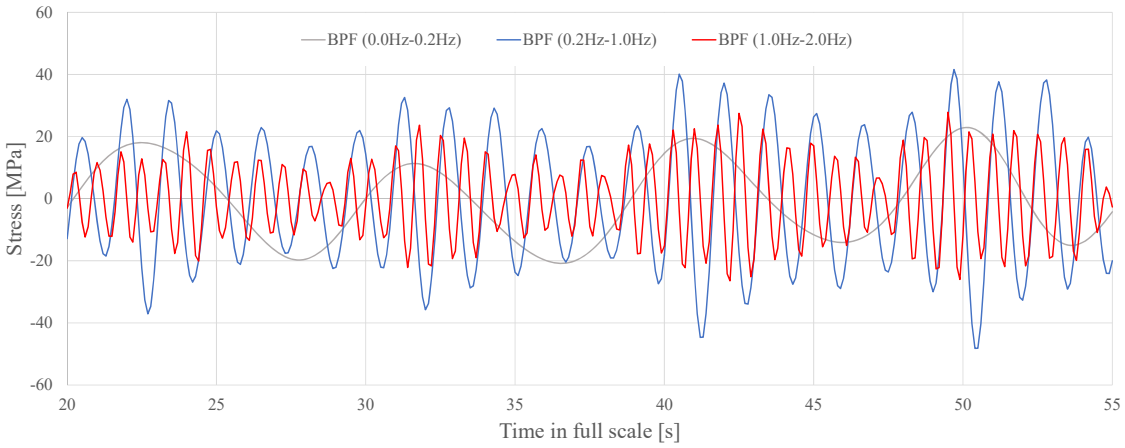

Figure 4.25 Comparison of time histories of several vibration modes included in $\sigma_{x,db}$

4.7 Summary of Chapter 4

In Chapter 4, a validation of the one-way and two-way coupled CFD and FEA for predicting the response of a ship in severe regular waves is conducted. A series of validation works of the developed method against linear/non-linear strip method, 3D panel method and tank test using the backbone model is firstly presented. The validation ranges over rigid body motions, slamming impact pressure and whipping moment in a severe wave condition. In order to demonstrate the effectiveness of the method developed in this study, investigations into the effect of global and local bending moment in a realistic large container ship are made. The followings are concluded.

<u>One-way coupled CFD-FEA:</u>

1. The present CFD based model predicts the rigid body motions of ships with good accuracy when compared with the experimental results. The prediction accuracy is almost comparable to the linear/nonlinear strip methods and 3D panel method. However, the accuracy tends to become less for the longer wave range with the wave length ratio λ/L_{pp} over 1.0.
2. The present CFD based model can consistently predict the slamming impact pressure with high accuracy. This is one of the advantages of the developed method since other methods based on the momentum theory cannot capture the impact pressure distribution in a consistent manner.
3. The results from one-way coupled CFD and FEA agree well with the experimental results in terms of the VBM including the whipping component. The results are almost comparable to those by the weakly nonlinear method based on 3D potential theory or nonlinear strip method. Meanwhile, the difference of natural frequency between the numerical prediction from CFD-FEA coupling and experimental results is observed.
4. Through the full scale CFD and dynamic FEA coupling analysis over a realistic large container ship, the combined VBM and DBM effect on the double bottom structure is observed. Besides, it turned out that the magnitude of the local stress due to the DBM is of non-negligible level from a view point of the strength assessment of the double bottom structure.

Two-way coupled CFD-FEA:

1. When the weakly coupled method is applied, good accuracies are confirmed for the local pressure time series and wave-induced VBMs. Discrepancies in the whipping vibrations arise from the poor representation of the added mass associated with the elastic deformation.
2. When the strongly coupled method is applied, Good accuracies are confirmed for the local pressure time series and wave-induced vertical bending moments. Further, the whipping vibrations are predicted with good accuracy, due to the appropriate evaluation of the added mass effect associated with the elastic deformation.

To achieve further investigations into the influence of the fluid-structure interaction effect on the local structural response of full scale ships, an alternate method to predict the strong two-way coupled CFD-FEA method in a sufficient and inexpensive manner may be needed in the future. To the knowledge of the author, the ROM is presumed to be that. Moreover, for a consistent assessment of the post-ultimate strength behavior of ships, further extension of the present CFD and FEA coupling to hydro-elastoplastic problems is expected in the future [4.16].

References in Chapter 4

[4.1] M. Takagi and M. Ganno, “On the accuracy of the strip theory, used for a calculation of ship motions in waves,” *J. Zosen Kiokai*, vol. 121, pp. 48–61, 1967.

[4.2] C. Murakami *et al.*, “Advanced Assessment from Wave Loads to Structural Strength by Means of Whole Ship Model,” in *Proceedings of The 16th Research Presentation Meeting in National Maritime Research Institute*, 2016, pp. 92–100.

[4.3] N. Salvesen, E. O. Tuck, and O. Faltinsen, “Ship Motions and Sea Loads,” *SNAME Trans.*, vol. 78, pp. 250–287, 1970.

[4.4] Th. Von Karman, “THE IMPACT ON SEAPLANE FLOATS DURING LANDING,” *Tech. Notes Natl. Advis. Comm. Aeronaut.*, vol. 321, 1929.

[4.5] Y. Yamamoto, M. Fujino, and T. Fukasawa, “Motion and Longitudinal Strength of a Ship in Head Sea and the Effects of Non-Linearities,” *J. Soc. Nav. Archit. Japan*, vol. 143, pp. 179–187, 1978.

[4.6] K. Iijima, T. Yao, and T. Moan, “Structural response of a ship in severe seas considering global hydroelastic vibrations,” *Mar. Struct.*, vol. 21, pp. 420–445, 2008.

[4.7] A. Papanikolaou *et al.*, “A three-dimensional panel method for motions and loads of ships with forward speed,” *Sh. Technol. Res.*, vol. 39, no. 4, pp. 147–156, 1992.

[4.8] S. Seng, “Slamming And Whipping Analysis Of Ships,” Technical University of Denmark, 2012.

[4.9] H. Wagner, “Über Stoß und Gleitvorgänge an der Oberfläche von Flüssigkeiten, Zeitschrift für Angewandte Mathematik und Mechanik,” *Zeitschrift für Angew. Math. und Mech.*, vol. 12, no. 4, pp. 193–215, 1932.

[4.10] P. Causin, J. F. Gerbeau, and F. Nobile, “Added-mass effect in the design of partitioned algorithms for fluid-structure problems,” *Comput. Methods Appl. Mech. Eng.*, vol. 194, no. 42–44, pp. 4506–4527, 2005.

[4.11] S. Seng, J. J. Jensen, and Š. Malenica, “Global hydroelastic model for springing and whipping based on a free-surface CFD code (OpenFOAM),” *Int. J. Nav. Archit. Ocean Eng.*, vol. 6, no. 4, pp. 1024–1040, 2014.

[4.12] M. F. Barone, I. Kalashnikova, M. R. Brake, and D. J. Segalman, “Reduced order modeling of fluid/structure interaction,” 2009.

[4.13] H. K. K. Amlashi and T. Moan, “Ultimate strength analysis of a bulk carrier hull girder under alternate hold loading condition, Part 2: Stress distribution in the double bottom and simplified approaches,” *Mar. Struct.*, vol. 22, no. 3, pp. 522–544, 2009.

[4.14] G. Storhaug, K. Laanemets, I. Edin, and J. W. Ringsberg, “Estimation of damping from wave induced vibrations in ships,” in *Progress in the Analysis and Design of Marine Structures*, 2017, pp. 121–130.

[4.15] Y. Kawasaki *et al.*, “Strength Evaluation of Containerships Based on Dynamic Elastic Response

Calculation of Hull Girder. 2nd Report - Influence of Hull Girder Rigidity and Correlation between Double Bottom Bending and Hull Girder Bending," *J. Japan Soc. Nav. Archit. Ocean Eng.*, vol. 25, pp. 191–203, 2017.

[4.16] K. Iijima, K. Kimura, W. Xu, and M. Fujikubo, "Hydroelasto-plasticity approach to predicting the post-ultimate strength behavior of a ship's hull girder in waves," *J. Mar. Sci. Technol.*, vol. 16, no. 4, pp. 379–389, 2011.

Chapter 5
FORM BASED EXTREME VALUE PREDICTION

The final goal in this study is to achieve extreme value predictions making use of the developed coupled CFD-FEA method. Considering the accurate evaluation of extremes, it is obviously ideal that direct MCS is applied using the coupled CFD-FEA, but it poses a problem concerning the expensive computational efforts, as already mentioned in Chapter 1. In this study, FORM based approach is adopted to extreme value predictions instead of direct MCS. In addition, alternative methods to the coupled CFD-FEA, by which fast approximations of the coupled CFD-FEA results are achieved, are employed to be incorporated with FORM. In this chapter, theoretical background of FORM based approach is firstly given. Then, alternative methods to the coupled CFD-FEA used in this study, the *predictor-corrector* approach and the ROM, are elaborated.

5.1 Theoretical Background

5.1.1 General

A fundamental theory for predicting the extreme value and the MPWEs in Jensen [5.1] and Iijima et al. [5.2], is adopted in this study. When one considers linear, long-crested irregular waves, the free surface elevation can be represented as a superposition of N discrete harmonic wave components:

$$\eta(t) = \sum_{i=1}^{N} u_i \sqrt{S(\omega_i) d\omega_i} \cos(\omega_i t) + \sum_{i=1}^{N} \overline{u}_i \sqrt{S(\omega_i) d\omega_i} \sin(\omega_i t) \tag{5.1}$$

where $S(\omega_i)$ denotes the wave spectrum, ω_i is discrete frequencies, and $d\omega_i$ is the increment between discrete frequencies. u_i and $\overline{u}_i$ are the independent and Gaussian distributed stochastic variables. Let any structural response at a target time t_0 under the irregular wave train given by Eq. (5.1) be $r_t\left(t_0 \mid u_1, u_2, \cdots u_N, \overline{u}_1, \overline{u}_2, \cdots \overline{u}_N\right)$. Response r_t can be estimated by using any time domain analyses, e.g. nonlinear strip theory, the coupled CFD and FEA, etc. According to the FORM, the design point, $(u_i^*, \overline{u}_i^*)$, is defined

as a point on the limit surface, with the shortest distance from the origin, see Figure 5.1. When the limit state function g is defined as a function of a given limit state R as follows,

$$\begin{aligned} g(\cdot) &= g\left(t_0 \mid u_1, u_2, \cdots u_N, \overline{u}_1, \overline{u}_2, \cdots \overline{u}_N\right) \\ &= 1 - R\left(r_t\left(t_0 \mid u_1, u_2, \cdots u_N, \overline{u}_1, \overline{u}_2, \cdots \overline{u}_N\right)\right) \end{aligned} \tag{5.2}$$

the reliability index β is resolved as a constrained optimization problem:

$$\begin{aligned} &\text{Minimize} \quad \beta = \sqrt{\sum_{i=1}^{N} u_i^{\,2} + \sum_{i=1}^{N} \overline{u}_i^{\,2}} \\ &\text{subject to} \quad g(\cdot) = 0 \end{aligned} \tag{5.3}$$

The MPWE exceeding a given response level, R in Eq. (5.2), is eventually predicted by assigning the derived design point $(u_i^*, \overline{u}_i^*)$ to Eq. (5.1).

Once the reliability index is given as per Eq. (5.3), the mean up-crossing rate over R may be given analytically [5.3].

$$\nu(R) = \nu_0 \exp\left(-\frac{\beta^2}{2}\right) \tag{5.4}$$

where ν_0 is the mean zero-up-crossing rate. Assuming that up-crossings of high levels are statistically independent events (or Poisson process), the probability of exceedance (PoE) of the maximum value R in period T may then by obtained by the following.

$$F_{\max}(R) = \exp\left(-\nu(R)T\right) \tag{5.5}$$

It is known that Eq. (5.5) may be well fitted with Gumbel type distribution [5.4].

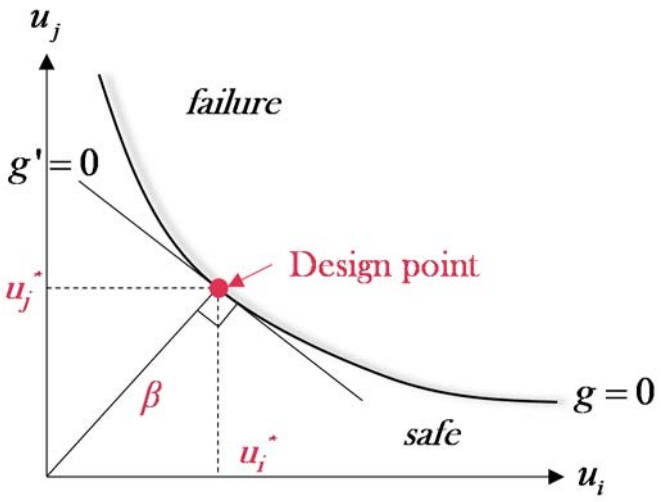

Figure 5.1 Schematic of design point determination based on FORM

5.1.2 Design point detection

An iterative scheme is required to detect the design point based on FORM, if some nonlinearities, e.g. whipping effect, are incorporated in the target structural response. The general procedure of the iterative scheme is described in Figure 5.2. Combinations of random variables u_i and $\overline{u}_i$ are generated according to the Box-Muller algorithm. The limit state function *g* is then approximated as a function of u_i and $\overline{u}_i$, by applying the polynomial based Response Surface Method (RSM).

$$g\left(t_0 \mid u_1, u_2, \cdots u_N, \overline{u}_1, \overline{u}_2, \cdots \overline{u}_N\right) \approx$$
$$c_0 + \sum_{i=1}^{N}\left\{c_i\left(u_i - u_i^*\right) + \overline{c}_i\left(\overline{u}_i - \overline{u}_i^*\right)\right\} \tag{5.6}$$

Note that in order to estimate the response surface relevant to *g*, substantial estimations of *g* under various combination of u_i and $\overline{u}_i$ is needed. As can be seen from Eq. (5.6), the limit state function is approximated around the tentative design point $(u_i^*, \overline{u}_i^*)$. In order to search the design point, a Lagrangian function *f* is defined as below in conjunction with approximated *g*.

$$f\left(u_1, u_2, \cdots u_N, \overline{u}_1, \overline{u}_2, \cdots \overline{u}_N, \lambda\right) =$$
$$\sum_{i=1}^{N}\left(u_i^2 + \overline{u}_i^2\right) - \lambda g\left(t_0 \mid u_1, u_2, \cdots u_N, \overline{u}_1, \overline{u}_2, \cdots \overline{u}_N\right) \tag{5.7}$$

By applying Lagrange's multipliers method to Eq. (5.7), a new design point is estimated by solving simultaneous linear equations, which assumes that the partial differentials of f in terms of each variable, $u_1, u_2, \cdots u_N, \overline{u}_1, \overline{u}_2, \cdots \overline{u}_N, \lambda$, are zero. As shown in Fig. 5.2, such updating processes of the design point are repeated until the convergence of design point will be found (inner iteration).

Even if the design point is found from the inner iteration schemes, it should be noted that the VBM under the estimated design point does not necessarily indicate the extreme value at the target time t_0. To prevent this, further iterative scheme (outer iteration) is implemented during the detection processes, see Fig. 5.2. In the outer iteration, the target time t_0 will be updated depending on occurrence time of extreme response value, $R_e\left(r_t\left(t_0^{'} \mid u_1^*, u_2^*, \cdots u_N^*, \overline{u}_1^*, \overline{u}_2^*, \cdots \overline{u}_N^*\right)\right)$. The outer iteration process is repeated until the coincidence of the occurrence time of R_e (i.e. t_0' becomes equal to t_0) and the convergence of R_e are found. The convergence criterion, ε in Figure 5.2, is set to be 0.001 throughout this thesis.

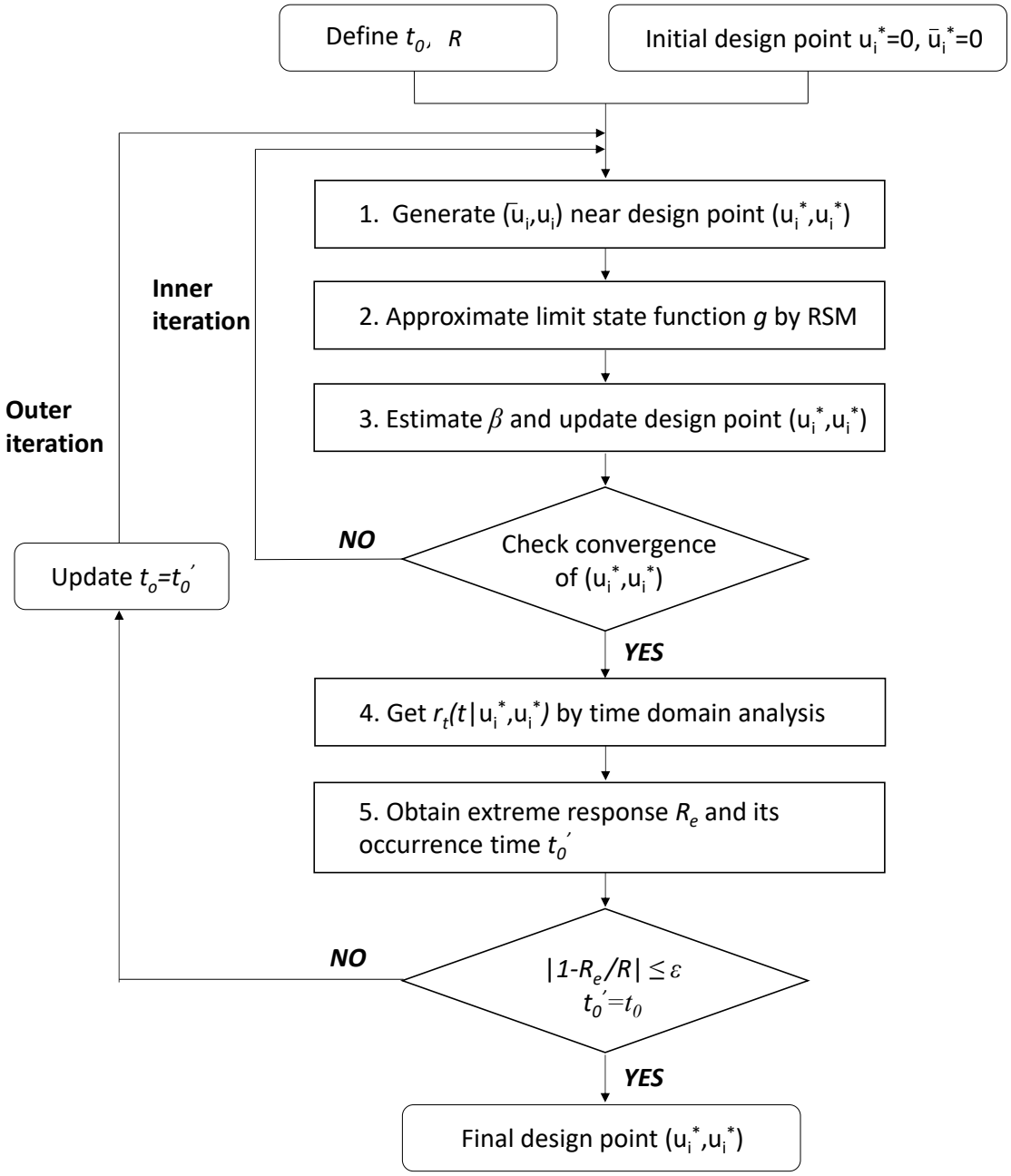

Figure 5.2 Workflow of design point detection based on FORM

5.2 Predictor-Corrector Approach

In this section, an approach for estimating extreme values based on the coupled CFD-FEA (*corrector*), by using other numerical method (*predictor*) is introduced. This approach is called the *predictor-corrector* approach, previously presented by Seng et al. [5.5]. Obviously, it is ideal that the well-validated and well-formatted sea-keeping code is used as the *predictor*. In this study, the in-house code NMRIW-II [5.6] whose theoretical background is conformed to the nonlinear strip theory is adopted as a

predictor. The design point is first derived from a combination of FORM and the *predictor*. Subsequently, the Model-correction factor (MCF) is determined such that the *predictor* can reproduce the extreme response derived from the coupled CFD-FEA on the predicted design point. Suppose that the responses at the design point $(u_i^*, \overline{u}_i^*)$ calculated by the *predictor* and the *corrector* are expressed as $r_{t,pre}$ and $r_{t,cor}$, respectively, let the correction factor c be as follows:

$$c = \frac{r_{t,cor}\left(u_1^*, u_2^*, \cdots u_N^*, \overline{u}_1^*, \overline{u}_2^*, \cdots \overline{u}_N^* \mid t_0 - \tau\right)}{r_{t,pre}\left(u_1^*, u_2^*, \cdots u_N^*, \overline{u}_1^*, \overline{u}_2^*, \cdots \overline{u}_N^* \mid t_0\right)} - 1 \tag{5.8}$$

where τ is the correction factor for target time. The limit state function g is modified by using c as below, then the *predictor* stage is carried out again.

$$g(\cdot) = 1 - R\left(\left(1 + \alpha c\right) r_{t,pre}\left(u_1, u_2, \cdots u_N, \overline{u}_1, \overline{u}_2, \cdots \overline{u}_N \mid t_0 - \tau\right)\right) \tag{5.9}$$

where α means a relaxation factor, which can be defined arbitrarily in the range of 0 to 1. Hereinafter, let us call factors c, τ, and α as MCF [5.7], collectively. In these ways, the number of the simulations by using the *corrector* method is fairly reduced, consequently the design point prediction associated with the *corrector* method can be performed in realistic time. The *predictor-corrector* approach is used for extreme value predictions concerning the combined VBM and DBM by using appropriate limit state functions described later.

5.3 Reduced Order Method

The second alternative is the reduced order method (ROM), which is newly developed in this study. Nowadays, in order to represent high-fidelity numerical methods, e.g. three dimensional CFD, ROMs have been constructed in several research fields during the last few decades [5.8], [5.9]. Research efforts using ROMs were spent to apply it for problems on fluid dynamics [5.10], structural responses [5.11], or fluid-structure interactions [5.12], for instance. Although ROM based approach covers a wide variety of research topics, the fundamental notion of the ROMs is common; substitute the high-fidelity models with a low-dimensional physic-based model such that the dominant behaviors of interest can be reproduced via near real-time computations. ROM may be a potential alternative to the existing approaches for extreme value predictions, if the wave-induced

VBM, whipping VBM, and the DBM are realized by using simple mathematical formulations. In this section, the newly developed ROMs for the wave-induced/whipping VBM and the DBM are explained in detail.

5.3.1 ROM for wave-induced VBM

Prediction of the wave-induced component of VBM is made based on the transfer function (TF) of VBM and simple correction of peak values to account for a nonlinearity of wave-induced VBM. Let the wave-induced VBM M_{wave} under the irregular wave expressed by Eq. (5.1) be as follows:

$$M_{wave}(t) = (1 + c_{rel}) \sum_{i=1}^{N} R(\omega_i) \begin{Bmatrix} u_i \sqrt{S(\omega_i) d\omega_i} \cos(\omega_i t + T(\omega_i)) \\ + \bar{u}_i \sqrt{S(\omega_i) d\omega_i} \sin(\omega_i t + T(\omega_i)) \end{Bmatrix} \tag{5.10}$$

where $R(\omega_i)$ and $T(\omega_i)$ are the amplitude and phase of the TF, respectively, c_{rel} means the correction factor for the nonlinearity. Suggest that the nonlinearity of wave-induced VBM is relevant to the amplitude of wave elevation, let c_{rel} be approximated by a nth-degree equation in terms of peak wave amplitude η_p:

$$c_{rel} = \sum_{i=0}^{n} c_i \eta_p{}^i \tag{5.11}$$

It should be noted that the solution time to measure the TF must be long enough to estimate each component of $R(\omega_i)$ and $T(\omega_i)$ appropriately. However, it needs quite a few computational efforts to obtain time domain results from the coupled CFD-FEA. Hence, in this study, the nonlinear strip theory implemented in in-house code NMRIW-II is used for obtaining TF and c_{rel} in lieu of direct computation by the coupled CFD-FEA. General procedure to determine the TF and c_{rel} can be summarized as follows:

1. Generate random variables u_i and $\bar{u}_i$ then compute NMRIW-II to obtain wave-induced VBM.
2. Apply the Fast Fourier Transform (FFT) to the calculated wave-induced VBM to estimate the TF.
3. Assume c_{rel}=0, then predict several design points associated with various target levels of extreme VBM by combining with FORM.
4. Define η_p as the maximum wave amplitude under the design points, then compute

NMRIW-II under the design points.

5. By comparing the correct results and M_{wave} (with c_{ref}=0), c_i in Eq. (5.11) is determined by using the least-square approach.

An instance of TF of VBM, $R(\omega_i)$ and $T(\omega_i)$, estimated from the NMRIW-II results is plotted in Figure 5.3. Here, note that significant high local peaks of $R(\omega_i)$ are found when ω is larger than 1.0. These are attributed to the fact that the contribution of higher wave frequency components to the wave-induced VBM amplitudes is subtle, but the round-off error in FFT results in such violent $R(\omega_i)$. To mitigate this effect, a linear interpolation is applied to obtained $R(\omega_i)$ then higher frequency components of $R(\omega_i)$, where ω is larger than 1.0, are cut out. The modified $R(\omega_i)$ is also plotted in the figure by a black solid line. $R(\omega_i)$, $T(\omega_i)$, and c_{rel} are once determined based on the NMRIW-II results, then further correction is subsequently made by using an additional correction factor c_{CFD}. Therefore,

$$M_{wave,CFD}(t) = c_{CFD}(\beta) M_{wave,strip}(t) \tag{5.12}$$

where c_{CFD} is defined as a function of reliability index β, and $M_{wave,strip}$ is wave-induced VBM derived from the nonlinear strip method. The whole procedure to estimate ROM for wave-induced VBM based on the coupled CFD-FEA is summarized in Figure 5.4.

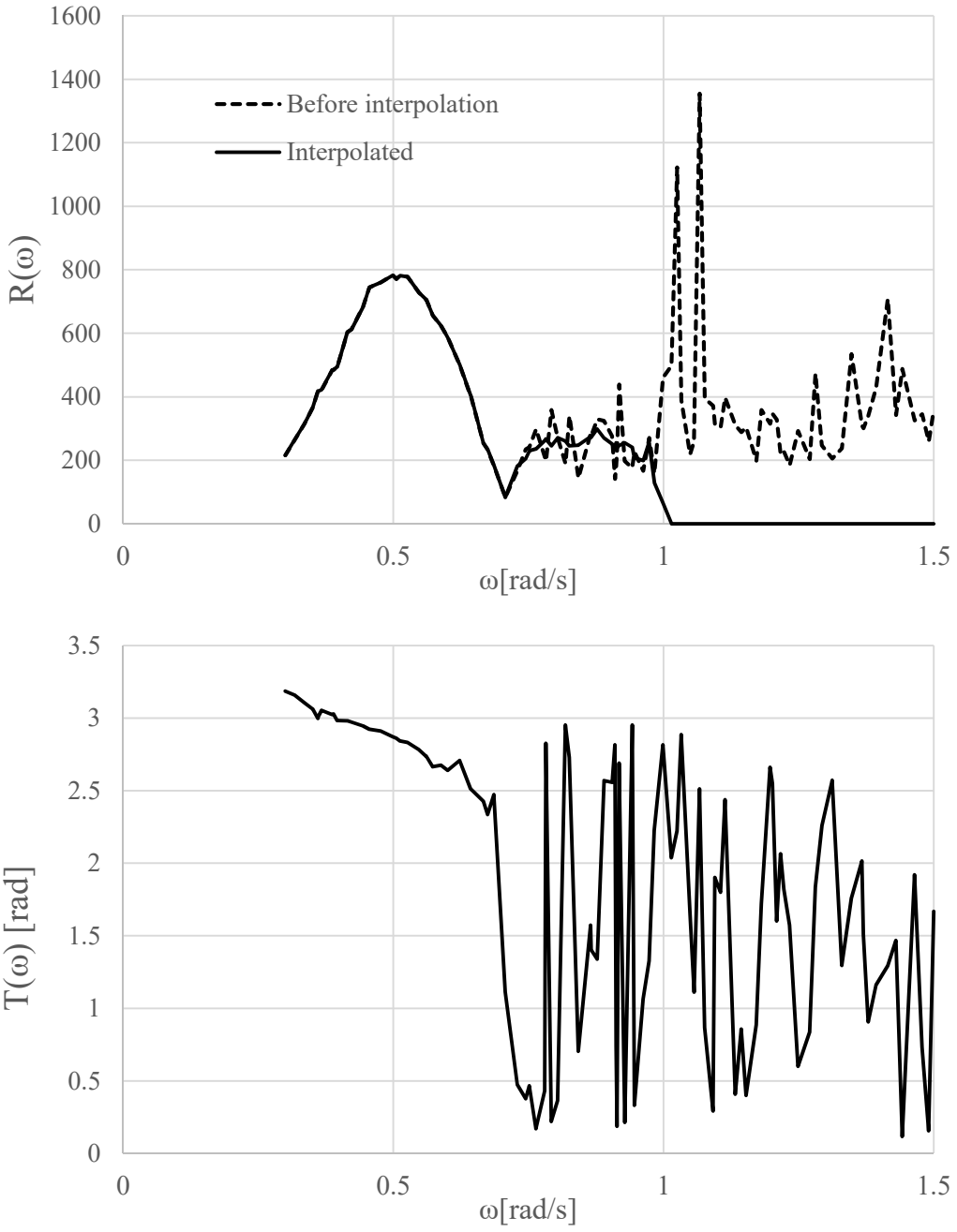

Figure 5.3 Example of TF for wave-induced VBM

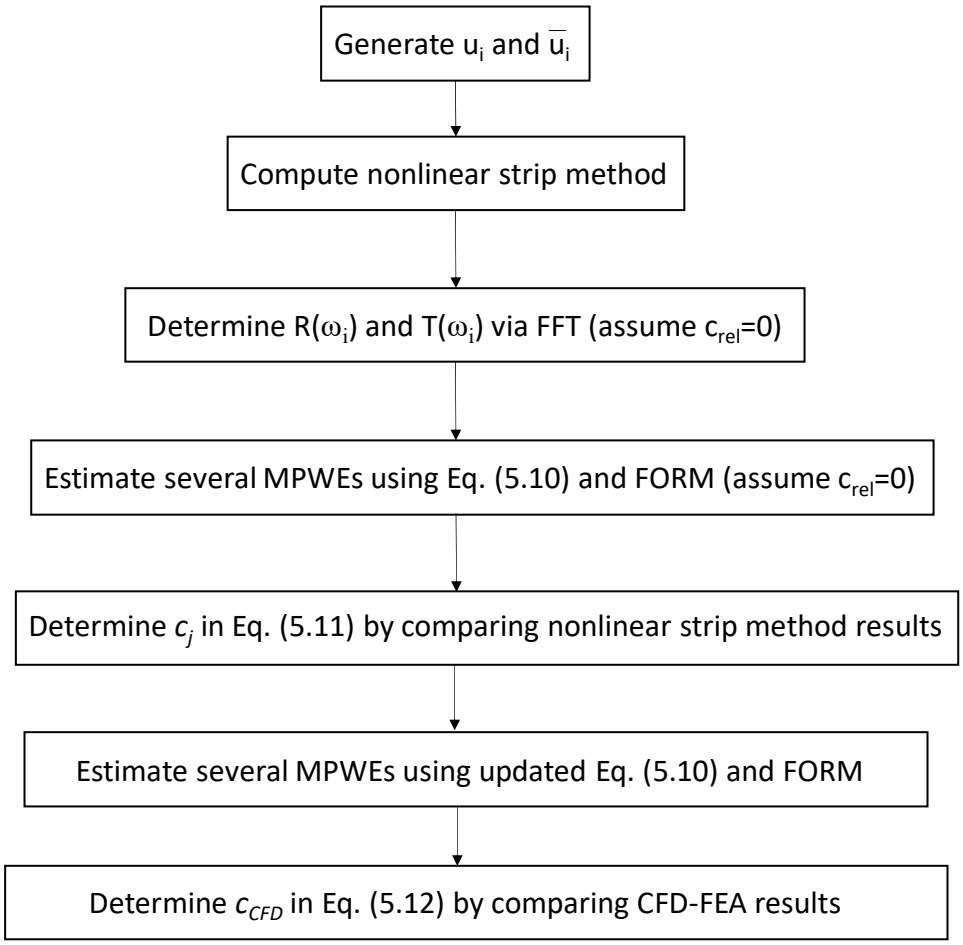

Figure 5.4 Workflow to estimate ROM for wave-induced VBM

5.3.2 ROM for DBM

Prediction of the DBM is also made based on the transfer function (TF) of water pressure acting on the outer bottom plate. According to Tatsumi et al. [5.13], simplified DBM bears a proportionate relationship to the water pressure. Thus, let the DBM M_{db} under the irregular wave expressed by Eq. (5.1) be as follows:

$$M_{db}(t) = c_p \sum_{i=1}^{N} R_p(\omega_i) \begin{Bmatrix} u_i \sqrt{S(\omega_i) d\omega_i} \cos(\omega_i t + T_p(\omega_i)) \\ +\bar{u}_i \sqrt{S(\omega_i) d\omega_i} \sin(\omega_i t + T_p(\omega_i)) \end{Bmatrix} \tag{5.13}$$

where $R_p(\omega_i)$ and $T_p(\omega_i)$ are the amplitude and phase of the TF of water pressure, respectively, and c_p is a transfer factor from water pressure to DBM. As in the case of the wave-induced VBM, the solution time to measure the TF must be longer enough to estimate each component appropriately. Hence, $R_p(\omega_i)$ and $T_p(\omega_i)$ are once determined

based on NMRIW-II, then a correction is subsequently made by using additional correction factors. Therefore,

$$M_{db,CFD}(t) = c_{db,CFD}(\beta) M_{db,strip}(t - \tau_{db}) \tag{5.14}$$

where $c_{db,CFD}$ is defined as a function of reliability index β, and τ_{db} is a correction factor for peak time. $M_{db,strip}$ is DBM derived from NMRIW-II. Determination processes of TFs and $c_{db,CFD}$ is in a similar way to those of wave-induced VBM, cf. Figure 5.4.

5.3.3 ROM for whipping VBM

In addition to above-mentioned ROMs, a ROM for whipping VBM is formulated. The first step for this end is to estimate the TF of ship motion, viz. heave and pitch motions. These TFs can be evaluated in the same way with estimating $R(\omega_i)$ and $T(\omega_i)$ in Eq. (5.10), without considering the nonlinearity. Thus,

$$h(t) = \sum_{i=1}^{N} R_h(\omega_i) \begin{Bmatrix} u_i \sqrt{S(\omega_i) d\omega_i} \cos(\omega_i t + T_h(\omega_i)) \\ + \bar{u}_i \sqrt{S(\omega_i) d\omega_i} \sin(\omega_i t + T_h(\omega_i)) \end{Bmatrix} \tag{5.15}$$

$$\theta(t) = \sum_{i=1}^{N} R_\theta(\omega_i) \begin{Bmatrix} u_i \sqrt{S(\omega_i) d\omega_i} \cos(\omega_i t + T_\theta(\omega_i)) \\ + \bar{u}_i \sqrt{S(\omega_i) d\omega_i} \sin(\omega_i t + T_\theta(\omega_i)) \end{Bmatrix} \tag{5.16}$$

where h and θ are heave and pitch motion, respectively, (R_h, T_h) and (R_θ, T_θ) are TFs of heave and pitch motion, respectively. Heave motion h takes positive values along the Z-axis upward and positive values of pitch motion θ follow the rotation about Y-axis based on the right-hand rule, see Figure 5.5. Assuming that the heave and pitch motion histories are predicted from the numerical simulations, the time history of relative distance between the bow and the wave surface, η_{rel}, is expressed as follows:

$$\eta_{rel}(t) = \eta_{bow}(t) - \{h(t) - l_{bow} \tan(\theta(t))\} \tag{5.17}$$

where l_{bow} denotes the distance between the center of gravity (CoG) of the ship and target bow section. η_{bow} denotes the wave elevation from the calm water surface at target bow section (see Figure 5.5) which can be calculated according to Eq. (5.18).

$$\eta_{bow}(t) = \sum_{i=1}^{N} u_i \sqrt{S(\omega_i) d\omega_i} \cos(\omega_i t + k_i x_{bow}) + \sum_{i=1}^{N} \bar{u}_i \sqrt{S(\omega_i) d\omega_i} \sin(\omega_i t + k_i x_{bow}) \tag{5.18}$$

where k_i is the wavenumber, x_{bow} is location of target bow section from amidships.

The slamming impact force acting on the bow is approximated by the two-dimensional water impact theory. According to the Karman's momentum theory [5.14], let the slamming impact force F_{imp} on a two dimensional wedge profile be as below:

$$F_{imp}(t) = \dot{M}_a(t)\dot{\eta}_{rel}(t) \tag{5.19}$$

where overdot in each variable means differentiation with respect to time t. M_a denotes the virtual added mass, which can be derived from the following equation without considering the water pile-up effect based on the Wagner theory [5.15],

$$M_a(t) = \frac{1}{2}\pi\rho C^2 = \frac{\pi\rho\left(\eta_{rel} - d\right)^2 \cot^2\delta}{2} \tag{5.20}$$

where ρ is the fluid density, d is the height of the wedge beneath the water surface, δ is the deadrise angle of the wedge against calm water surface, see Figure 5.6. One can adjust the time of onset of slamming impact and its magnitude by arbitrarily changing d and δ.

Suggest that the whipping vibration can be realized by the oscillatory system with one degree of freedom. In that sense, the whipping VBM M_{whip} is expressed as follows:

$$M_{whip}(t) = \int_0^{\infty} I(t-\tau) c_{imp} F_{imp}(\tau - \tau_{imp}) d\tau \tag{5.21}$$

where I is the impulse response function. c_{imp} and τ_{imp} are the correction factor for the magnitude and phase of slamming impact force, respectively. As the main contribution to the whipping VBM is 2-node vibration of the ship beam, which may be realized by the damped free vibration (see Figure 5.7), I can be approximated by using the general solution of it.

$$I(t) \approx \exp\left(-\zeta\omega_0 t\right)\left(I(0)\cos(\omega_d t) + \frac{\zeta\omega_0 I(0) + \dot{I}(0)}{\omega_d}\sin(\omega_d t) \right) \tag{5.22}$$

$$where \quad \omega_d = \omega_0\sqrt{1-\zeta^2}$$

where ζ and ω_0 are the damping ratio and the natural angular frequency of 2-node vibration, respectively. In this study, $I(0)$=0 and $\dot{I}(0)$=-1 are adopted to express the impulse response function. Figure 5.8 represents an example of $I(t)$.

Once a coupled CFD-FEA computation under a certain wave packet is carried out, whipping VBM may be obtained by cutting out the wave-induced component using the BPF. The unknown variables d, δ, c_{imp}, and τ_{imp} in Eq. (5.20) and Eq. (5.21) should be determined so that M_{whip} will be able to capture the magnitude and phase of the whipping VBM well at the target time t_0. The whole procedure to estimate the ROM for whipping VBM can be summarized as follows (see Figure 5.9);

1. Estimate an arbitrary MPWE using ROM for wave-induced VBM and FORM.
2. Compute CFD under identified MPWE.
3. Determine TFs of the heave and pitch motions.
4. Compute combined CFD-FEA under identified MPWE then extract whipping BPF.
5. Find optimal values of d, δ, c_{imp}, and τ_{imp}.

Once the ROM for wave-induced VBM is determined according to the procedures mentioned in sub-section 5.3.1, a MPWE for arbitrary extreme wave-induced VBM can be estimated by combining with FORM. TFs for heave and pitch motions are then determined from the CFD result under a MPWE. Following the coupled CFD-FEA computation, the whipping VBM is extracted. Through a screening process of optimal values of d, δ, c_{imp}, and τ_{imp}, the ROM for whipping VBM is eventually constructed. In this paper, these unknown variables are determined via a trial-and-error adjustment. A more exact optimization may be set aside as a future work, which will be somehow achieved e.g. by applying multi-objective optimization methods, or utilizing machine learning techniques.

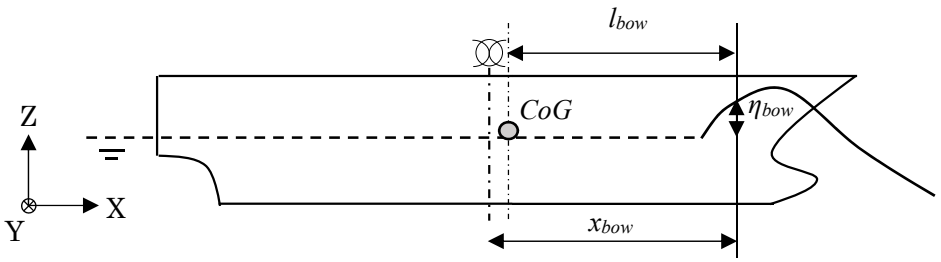

Figure 5.5 Schematic of definition of relative distance between the bow and the wave surface

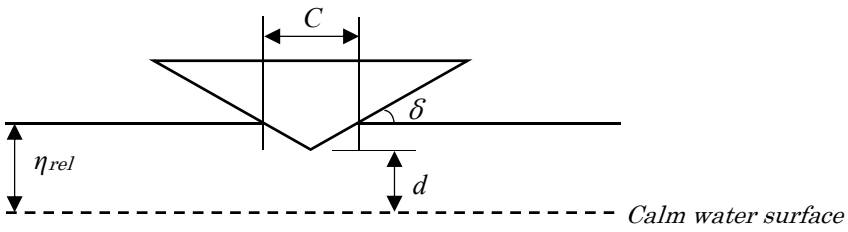

Figure 5.6 Definition of parameters for slamming impact force approximation

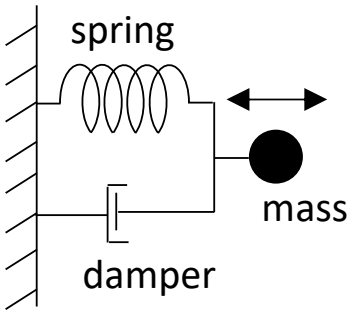

Figure 5.7 Schematic of damped free vibration system with one degree of freedom

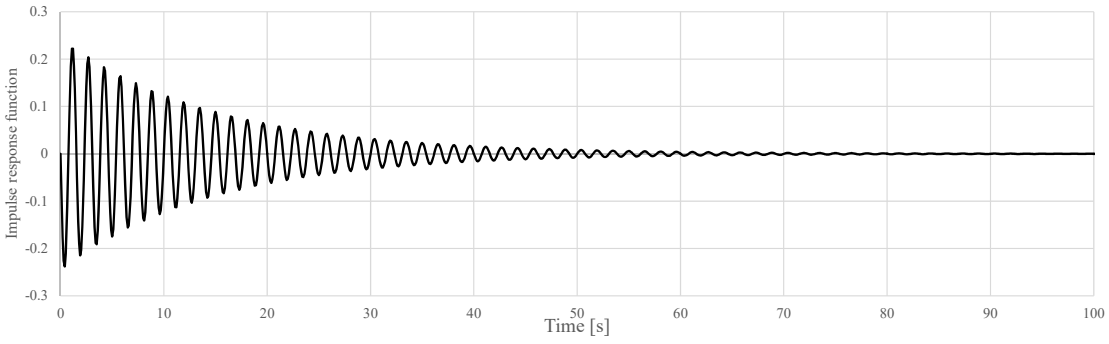

Figure 5.8 Example of impulse response function based on Eq. (5.22) (damping ratio: 1.66%)

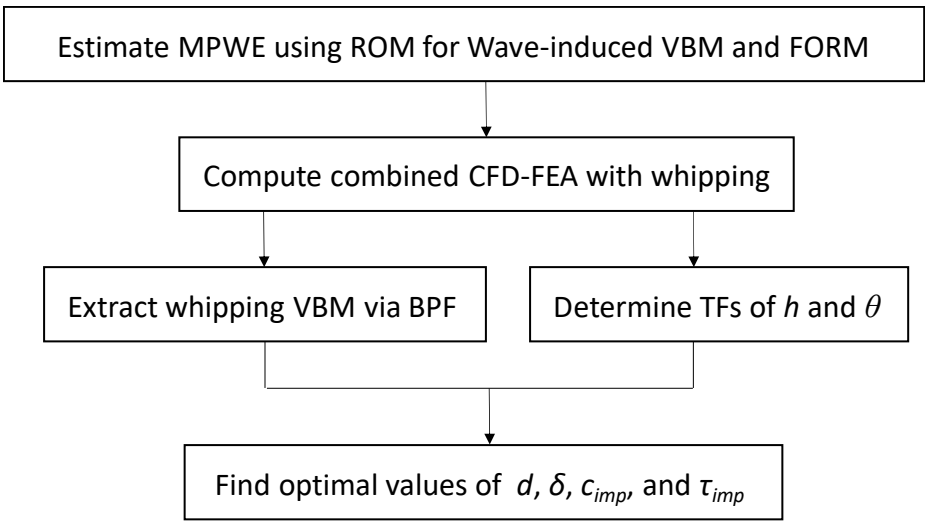

Figure 5.9 Workflow to estimate ROM for whipping VBM

5.4 Limit State Functions for VBM and DBM

In this section, the limit state functions (LSFs) for VBM and combined VBM and DBM used in this study are explained. The limit state assumed in this study is; the longitudinal stress on the outer bottom panel at amidships reaches target compressive stress levels under hogging conditions.

5.4.1 LSF for VBM

In considering only the effect from VBM on the stress level, the LSF, g in Eq. (5.2), is given as follows.

$$g = 1 - \left(\frac{r_{t,glob}}{M_{uh,glob}} \right) \qquad (5.23)$$
$$where \quad r_{t,glob} = M_{h,glob}\left(u_1, u_2, \cdots u_N, \overline{u}_1, \overline{u}_2, \cdots \overline{u}_N \mid t_0\right)$$

where $M_{h,glob}$ denotes the VBM on amidships at the target time t_0, and $M_{uh,glob}$ denotes the VBM value when the longitudinal stress on the outer bottom panel reaches the target stress level σ_t. Assuming that the longitudinal stress distribution on amidships obeys the Bernoulli-Euler beam theory, $M_{uh,glob}$ can be expressed as follows with the aid of the section modulus on amidships Z:

$$M_{uh,glob} = (\sigma_t - \sigma_s)Z \qquad (5.24)$$

where σ_s is the longitudinal stress on the outer bottom panel under the still water bending moment. The LSF given by Eq. (5.23) is adopted to extreme value predictions concerning the wave-induced VBM and combined wave-induced and whipping VBM.

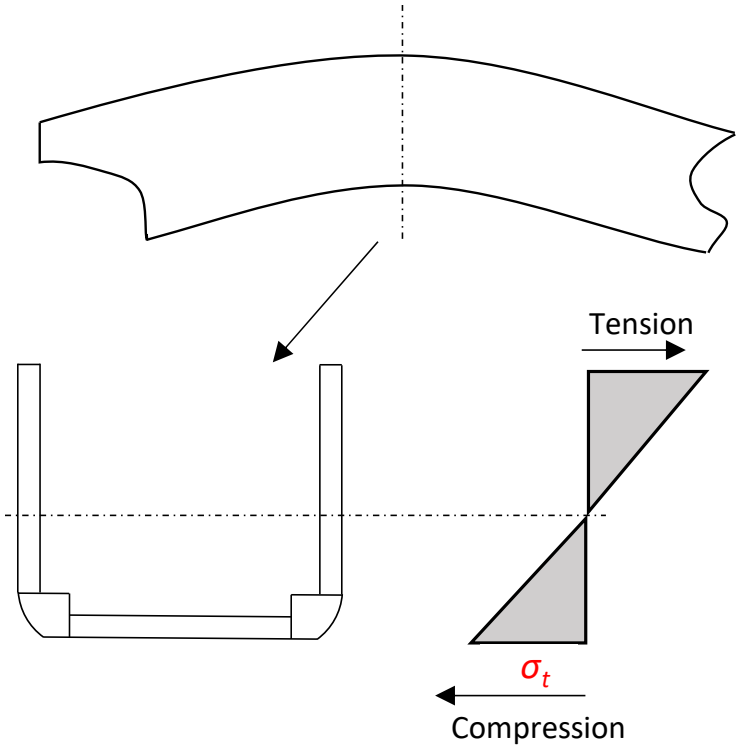

Figure 5.10 Limit state of outer bottom panel subjected to VBM

5.4.2 LSF for combined VBM and DBM

To consider the effect from both of the VBM and DBM on the stress level on the outer bottom panel, let the LSF g be as follows, cf. Amlashi et al. [5.16] and Tatsumi et al. [5.13],

$$g = 1 - \frac{(\sigma_b - \sigma_{b,st})}{(\sigma_t - \sigma_{b,st})} = 1 - \left(\frac{r_{t,glob}}{M_{uh,glob}} + \frac{r_{t,db}}{M_{uh,db}} \right) \tag{5.25}$$

$$where \quad r_{t,db} = M_{h,db}\left(u_1, u_2, \cdots u_N, \overline{u}_1, \overline{u}_2, \cdots \overline{u}_N \mid t_0\right)$$

where $M_{h,db}$ is the DBM, σ_b is the mean longitudinal stress on the outer bottom panel which can be explicitly estimated e.g. from the coupled CFD-FEA computations using the prototype full scale ship. $\sigma_{b,st}$ denotes the mean longitudinal stress on the outer

bottom panel under a calm water surface. Assumed limit state of the outer bottom panel is schematically found from Figure 5.11. The derivations of $r_{t,db}$ and $M_{uh,db}$ are explained in the following chapters, see Chapter 6 and Chapter 7.

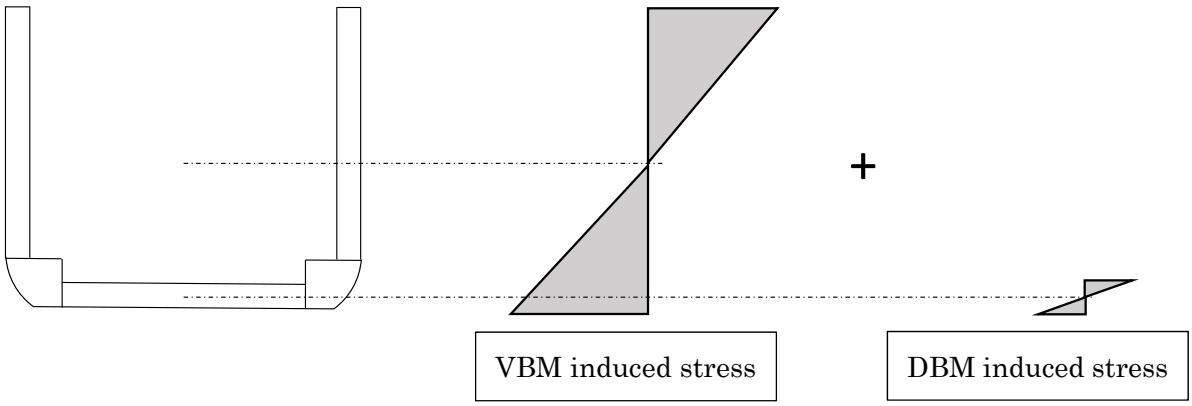

Figure 5.11 Limit state of outer bottom panel subjected to combined VBM and DBM

References in Chapter 5

[5.1] J. J. Jensen, “Stochastic procedures for extreme wave load predictions - Wave bending moment in ships,” *Mar. Struct.*, vol. 22, no. 2, pp. 194–208, 2009.

[5.2] K. Iijima, H. Hotta, M. Fujikubo, and K. Nakamura, “Design irregular wave train for nonlinear response by FORM,” *J. Japan Soc. Nav. Archit. Ocean Eng.*, vol. 19, pp. 101–110, 2014.

[5.3] K. Iijima, R. Nabeshima, K. Kinugawa, T. Takami, and M. Fujikubo, “Extreme Value Distribution of Combined Hull Girder and Double Bottom Bending Moments in a Container Ship by FORM,” in *Proceedings of 32nd Asian-Pacific Technical Exchange and Advisory Meeting on Marine Structures*, 2018.

[5.4] H. Kawabe, Y. Maeno, H. Ohtani, Y. Fujii, and T. Yao, “Assessment of Ultimate Hull Girder Strength in Longitudinal Bending,” *J. Kansai Soc. Nav. Archit. Japan*, vol. 2005, no. 243, pp. 97–107, 2005.

[5.5] S. Seng and J. J. Jensen, “An Application of a Free Surface CFD Method in the Short-Term Extreme Response Analysis of Ships,” in *Proceedings of PRADS2013*, 2013, pp. 747–754.

[5.6] C. Murakami *et al.*, “Advanced Assessment from Wave Loads to Structural Strength by Means of Whole Ship Model,” in *Proceedings of The 16th Research Presentation Meeting in National Maritime Research Institute*, 2016, pp. 92–100.

[5.7] D. Ove and A.-N. Torben, “Model-correction-factor method in structural reliability,” *J. Eng. Mech.*, vol. 120, no. 1, pp. 1–10, 1994.

[5.8] D. Amsallem and C. Farhat, “Interpolation Method for Adapting Reduced-Order Models and Application to Aeroelasticity,” *AIAA J.*, vol. 46, no. 7, pp. 1803–1813, 2008.

[5.9] G. Rozza *et al.*, “Advances in Reduced Order Methods for Parametric Industrial Problems in Computational Fluid Dynamics,” in *7th European Conference on Computational Fluid Dynamics (ECFD 7)*, 2018.

[5.10] T. Lassila, A. Manzoni, A. Quarteroni, and G. Rozza, “Model Order Reduction in Fluid Dynamics: Challenges and Perspectives,” in *Reduced Order Methods for Modeling and Computational Reduction*, 2014, pp. 235–273.

[5.11] A. Przekop, “Dynamic Snap-Through of Thermally Buckled Structures by a Reduced Order Method,” *AIAA J.*, vol. 45, no. 10, pp. 2510–2519, 2007.

[5.12] D. Xiao, P. Yang, F. Fang, J. Xiang, C. C. Pain, and I. M. Navon, “Non-intrusive reduced order modelling of fluid-structure interactions,” *Comput. Methods Appl. Mech. Eng.*, vol. 303, pp. 35–54, 2016.

[5.13] A. Tatsumi and M. Fujikubo, “Ultimate Longitudinal Strength Analysis of Container Ships Considering Bottom Local Loads- Part 3: Development of Simplified Estimation Method of Ultimate Longitudinal Bending Strength -,” *J. Japan Soc. Nav. Archit. Ocean Eng.*, vol. 25, pp. 133–142, 2017.

[5.14] Th. Von Karman, “THE IMPACT ON SEAPLANE FLOATS DURING LANDING,” *Tech. Notes Natl. Advis. Comm. Aeronaut.*, vol. 321, 1929.

[5.15] H. Wagner, “Über Stoß und Gleitvorgänge an der Oberfläche von Flüssigkeiten, Zeitschrift für Angewandte Mathematik und Mechanik,” *Zeitschrift für Angew. Math. und Mech.*, vol. 12, no. 4, pp. 193–215, 1932.

[5.16] H. K. K. Amlashi and T. Moan, “Ultimate strength analysis of a bulk carrier hull girder under alternate hold loading condition, Part 2: Stress distribution in the double bottom and simplified approaches,” *Mar. Struct.*, vol. 22, no. 3, pp. 522–544, 2009.

Chapter 6
EXTREME VALUE PREDICTION BY PREDICTOR-CORRECTOR AND FORM

6.1 Premises

In this chapter, the extreme value predictions of VBM and DBM under a short-term sea state, where the significant wave height Hs=11.5m, the mean wave period Tz=12.0s, the ship speed 10knots (Fn=0.0975) is conducted. The target extreme response in common throughout this chapter is; the longitudinal stress levels on the outer bottom plate reach 170 MPa under in-plane compression. This extreme response premise is based on the permissible bending stress on the structural part prescribed by IACS [6.1]. The target time for the extreme VBM prediction is set 112.8s. The ISSC wave spectra, Eq. (6.1), within ω_i range of 0.3-1.5 [rad/s] is adopted in formulating the irregular wave, cf. Eq. (5.1).

$$\frac{[f(\omega)]^2}{Hs^2} = 0.11\omega_1^{-1}\left(\frac{\omega}{\omega_p}\right)^{-5}\exp\left\{-0.44\left(\frac{\omega}{\omega_p}\right)^{-4}\right\} \tag{6.1}$$

$$\eta(t) = \sum_{i=1}^{N} u_i\sqrt{S(\omega_i)d\omega_i}\cos(\omega_i t) + \sum_{i=1}^{N}\overline{u}_i\sqrt{S(\omega_i)d\omega_i}\sin(\omega_i t) \tag{5.1}$$

where ω_p means the peak circular frequency. The number of discrete harmonic wave components N is equal to 100 using equidistant discrete frequencies.

The nonlinear strip method is used for the *predictor*, and the one-way coupled CFD-FEA is used for the *corrector*. The numerical modeling for the nonlinear strip method is in accord with that described in sub-section 4.2.2. The prototype full scale ship model (see subsection 2.2.3) is adopted in processing the one-way coupled CFD-FEA.

6.2 MPWE Generation by CFD

The CFD model based on section 2.1 is used for MPWE generations. CFD computations are conducted in the model scale with the scale ratio 94.6. The mesh resolution of the present CFD over the free surface region is; Δx = 7.09m (horizontal direction) and Δz= 1.77m (vertical direction), in full scale. A tentative MPWE in which the maximum wave

elevation 12m appears at the target time is generated by the present CFD. A comparison of wave trains between Eq. (5.1) and the present CFD is shown in Figure 6.1. As seen from the figure, the present CFD reproduces the wave train generally in a good manner, but a deviation in terms of peak amplitudes and the peak time from the target wave train is found in the vicinity of 100 seconds. The mesh resolution of the present CFD in the vertical direction is making up to 13 cells from crest to trough at the steepest location, and it may be considered to be sufficient for free surface reproduction, as deduced from the section 4.1 results. In the horizontal direction, on the other hand, the mesh resolution is making up to 97 cells for the longest wave component and 4 cells for the shortest wave component. It can be deduced that the mesh resolution in the horizontal direction is too low to reproduce shorter wave component appropriately. Having said that, however, the present CFD demands quite a few computational efforts, as the calculation time costed in computing 150 physical seconds is about 40 hours by using 8 cores parallel computation. For these reasons, the present CFD is adopted for MPWE generations and more refinement of the CFD model is set aside for future works.

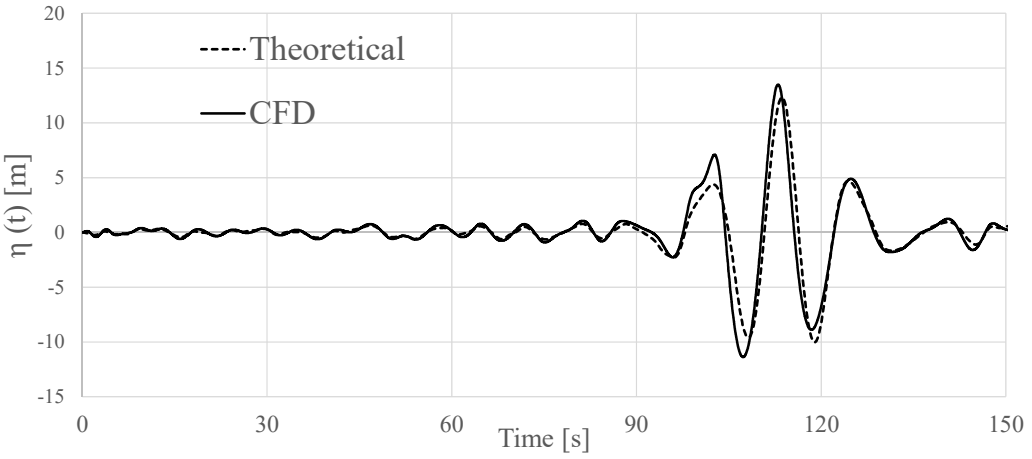

Figure 6.1 Comparison of irregular wave trains among theoretical value (Eq. 5.1) and CFD reproductions

6.3 Wave-induced VBM

In this section, the MPWE estimations associated only with the wave-induced VBM are provided. For the subject ship, the still water bending moment is found at 4115MNm. Thus according to Eq. (5.24), $M_{uh,glob}$ becomes 4505MNm without the static component.

$$M_{uh,glob} = (\sigma_t - \sigma_s)Z \tag{5.24}$$

where σ_t=170 [MPa]. The convergence history of limit state function, g, during the FORM process is shown in Figure 6.2. After 12 iterations, successful convergence of FORM is found. First specified MPWE via the *predictor* in conjunction with the limit state function expressed by Eq. (5.23) is shown in Figure 6.3, plotted by a thin solid line. Predicted reliability index β is 3.20. A comparison of wave-induced VBMs ($M_{h,glob,wave}$) derived from the *predictor* and the *corrector* under the specified MPWE is shown in Figure 6.4. Here, the wave-induced VBM from the *corrector* is calculated by setting the damping ratio of the FE model to its critical damping ratio (the same is true for following sections in chapter 6). As seen from Figure 6.4, the nonlinear strip method over predicts the peak value of $M_{h,glob,wave}$ comparing with the CFD-FEA coupling. Peak time of $M_{h,glob,wave}$ also differs among two methods. These discrepancies are attributed to the difference in assumed transfer functions of wave-induced VBM.

Next the deviation of peak amplitude and time is corrected as per Eq. (5.8), then the second prediction is conducted using updated limit state function (see Eq. 5.9). Here, adopted relaxation factor is α=0.5. Specified MPWE via the second *predictor* stage is shown in Figure 6.3, plotted by a black solid line. Predicted reliability index β is 3.83. A comparison of wave-induced VBMs ($M_{h,glob,wave}$) derived from the *predictor* and the *corrector* under the second specified MPWE is shown in Figure 6.5. One can recognize that peak time of $M_{h,glob,wave}$ is successfully modified by the correction. Besides, the modified *predictor* can predict a scenario close to the target response level. One may conclude that the present *predictor-corrector* functions well for the MPWE and extreme wave-induced VBM predictions. For more rigorous scenario, it would be attained by applying the iterative scheme of *predictor-corrector* and MCF determinations.

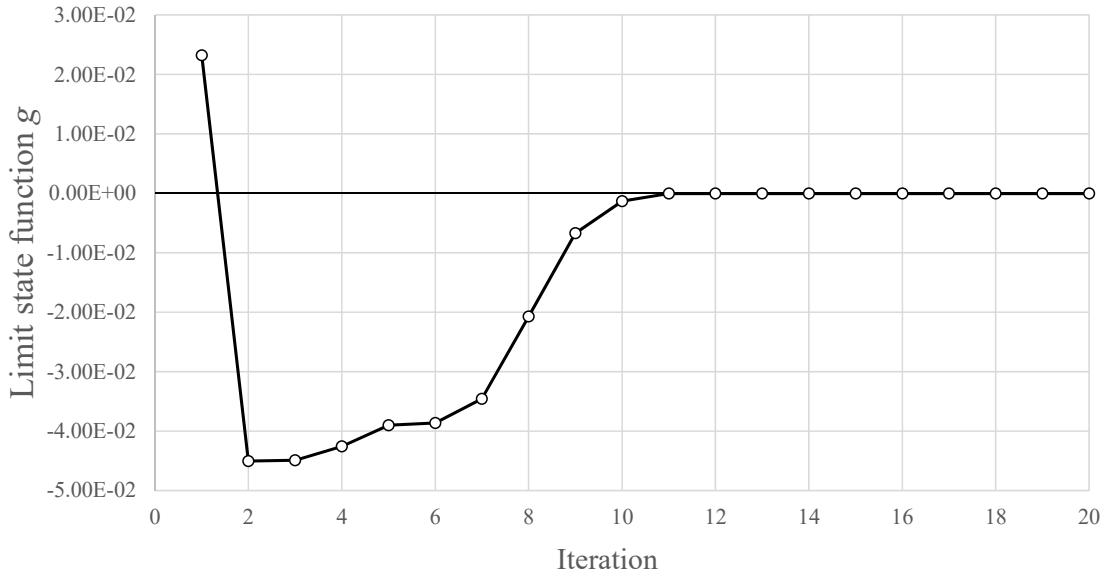

Figure 6.2 Convergence of limit state function

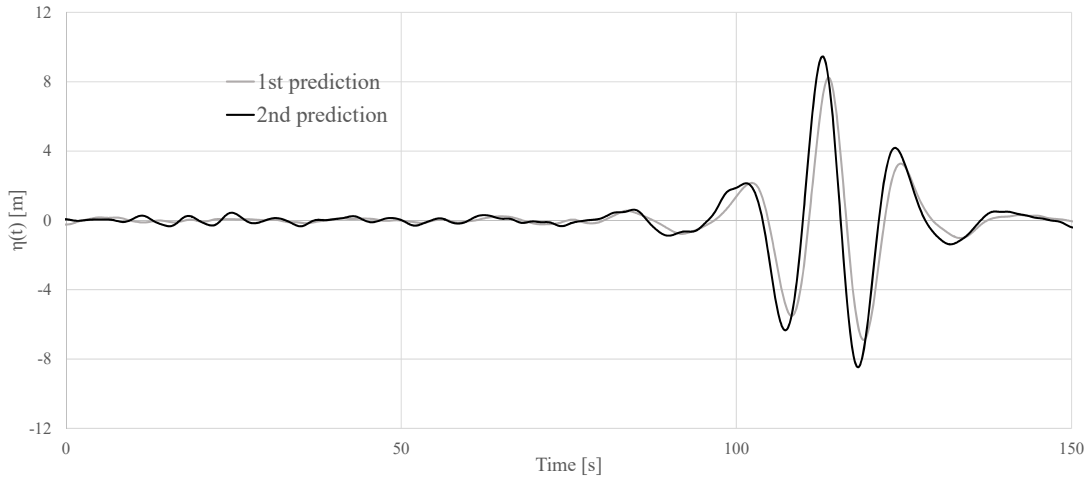

Figure 6.3 Specified MPWEs for wave-induced VBM

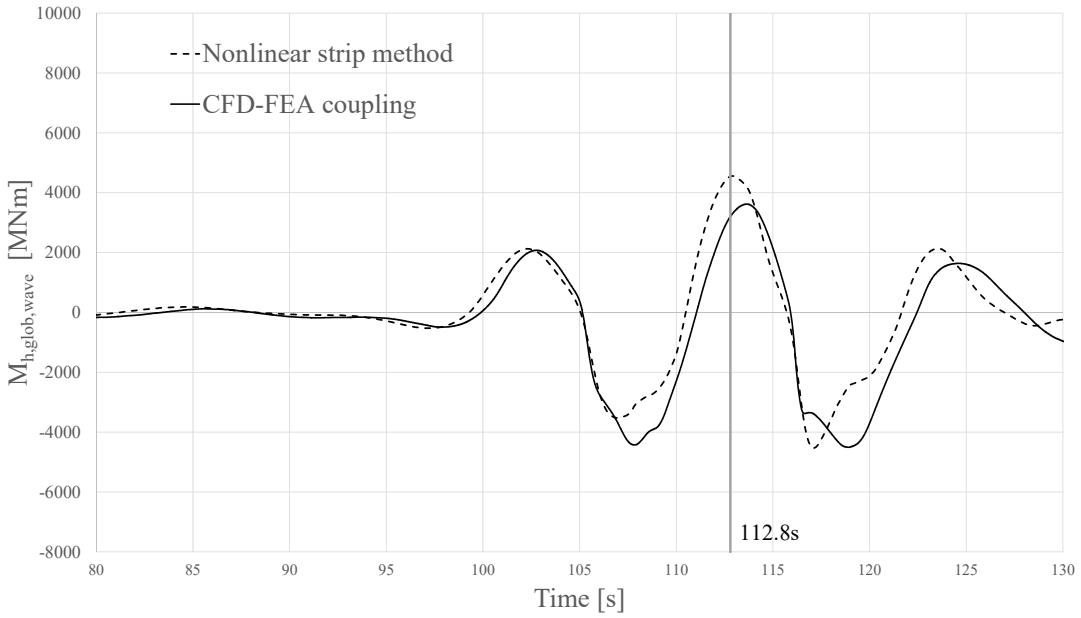

Figure 6.4 Comparison of wave-induced component of $M_{h,glob}$ under MPWE from first prediction (without MCF)

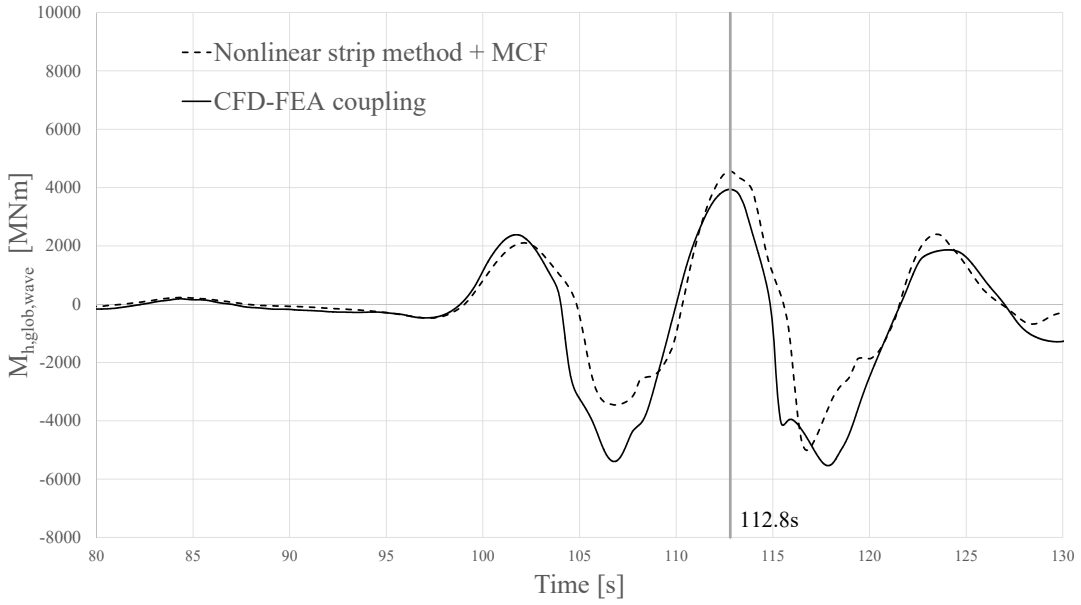

Figure 6.5 Comparison of wave-induced component of $M_{h,glob}$ under MPWE from second prediction (with MCF)

6.4 Combined Wave-induced VBM and DBM

In this section, the MPWE estimations associated with combined wave-induced VBM

and DBM are provided. A one-way coupled CFD-FEA analysis under a calm water is preliminarily conducted then the static component of the longitudinal stress on the outer bottom plate is obtained. By taking the average of longitudinal stress over the outer bottom panel elements, the static component which corresponds to $\sigma_{b,st}$ in Eq. (5.25) is found at $67MPa$.

$$g = 1 - \frac{(\sigma_b - \sigma_{b,st})}{(\sigma_t - \sigma_{b,st})} = 1 - \left(\frac{r_{t,glob}}{M_{uh,glob}} + \frac{r_{t,db}}{M_{uh,db}} \right) \tag{5.25}$$
$$where \quad r_{t,db} = M_{h,db}\left(u_1, u_2, \cdots u_N, \overline{u}_1, \overline{u}_2, \cdots \overline{u}_N \mid t_0\right)$$

Consider the prediction of $r_{t,db}$ during the *predictor* stages. $\sigma_{b,st}$ in Eq. (5.25) can be preliminarily estimated via the coupled CFD-FEA computations afloat on a calm water. To estimate g in Eq. (5.25), a simplified estimation of $M_{h,db}$ is needed. In this study, presuming that the double bottom bending deformation due to the water pressure is regarded as the deformation of a beam which has the fixed ends at the bulkhead (BHD) locations (Figure 6.6),

$$M_{h,db} = \frac{1}{24} P_{out} l_{db} \tag{6.2}$$

here, P_{out} is the water pressure per unit length without still water component.

$M_{uh,db}$ in Eq. (5.25) denotes the limit state induced only by the DBM. In this study, $M_{uh,db}$ is considered to be the bending moment when the longitudinal stress on outer bottom panel reaches σ_t-$\sigma_{b.st}$,

$$M_{uh,db} = \frac{I_{db}}{h_{db}} (\sigma_t - \sigma_{b,st}) \tag{6.3}$$

I_{db} and h_{db} in Eq. (6.3) are the second moment of area and the distance between the neutral axis and the outer surface, respectively. In this study, I_{db} and h_{db} are calculated in a straightforward manner from the cross section of the double bottom surrounded by a dotted line as shown in Figure 6.7.

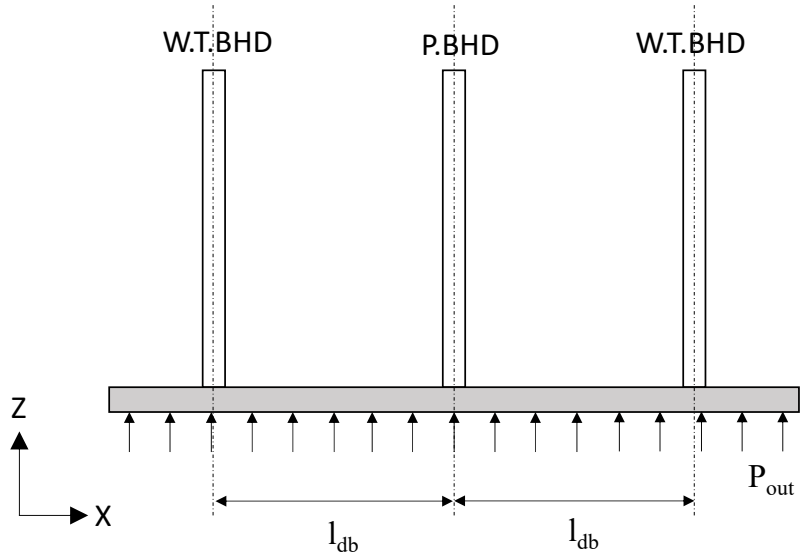

Figure 6.6 Distribution of local loads applied to double bottom

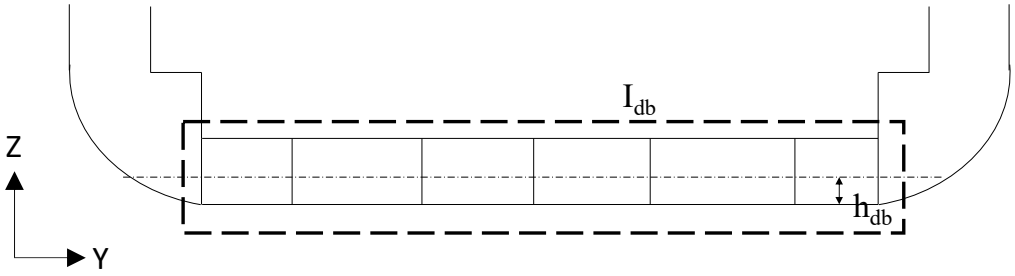

Figure 6.7 Cross section of double bottom

The convergence history of limit state function, *g*, during the FORM process is shown in Figure 6.8. After 9 iterations, successful convergence of FORM is found. First specified MPWE via the *predictor* in conjunction with the limit state function expressed by Eq. (5.25) is shown in Figure 6.9, plotted by a thin solid line. Predicted reliability index β is 3.10. A comparison of dimensionless values of average longitudinal stress on the outer bottom panel, the second term of the right hand of Eq. (5.25), derived from the *predictor* and the *corrector* under the specified MPWE is shown in Figure 6.10. The non-dimensional stress from the *corrector* is defined by substituting the longitudinal stress evaluated from CFD-FEA ($\sigma_{b,CFD}$) into σ_b. As seen from Figure 6.10, the nonlinear strip method over predicts the peak value of longitudinal stress, and peak time also differs among two methods.

To make a correction of the limit state function g, let the following correction factor c_b be defined by using the longitudinal stress evaluated from CFD-FEA ($\sigma_{b,CFD}$) and the target stress σ_t,

$$c_b = \frac{\sigma_{b,CFD}\left(u_1^*, u_2^*, \cdots u_N^*, \overline{u}_1^*, \overline{u}_2^*, \cdots \overline{u}_N^* \mid t_0 - \tau\right) - \sigma_{b,st}}{\sigma_t - \sigma_{b,st}} - 1 \tag{6.4}$$

where τ is the correction factor for peak time. By employing MCF, the subsequent *predictor* stage is conducted by using following updated limit state function g.

$$\begin{aligned} & g = 1 - \left(1 + \alpha c_b\right)\left(\frac{r_{t,glob}}{M_{uh,glob}} + \frac{r_{t,db}}{M_{uh,db}}\right) \\ & where \quad r_{t,glob} = M_{h,glob}\left(u_1, u_2, \cdots u_N, \overline{u}_1, \overline{u}_2, \cdots \overline{u}_N \mid t_0 - \tau\right) \\ & where \quad r_{t,db} = M_{h,db}\left(u_1, u_2, \cdots u_N, \overline{u}_1, \overline{u}_2, \cdots \overline{u}_N \mid t_0 - \tau\right) \end{aligned} \tag{6.5}$$

By reflecting the first prediction result, MCF is determined. Specified MPWE via the second *predictor* stage is shown in Figure 6.9, plotted by a black solid line. Here, adopted relaxation factor is α=0.5. Predicted reliability index β is 3.60. A comparison of dimensionless values of average longitudinal stress on the outer bottom panel derived from the *predictor* and the *corrector* under the second specified MPWE is shown in Figure 6.11. Peak time of the non-dimensional stress is successfully modified by the correction. Besides, the modified *predictor* can predict a scenario close to the target response level, as in the case of wave-induced VBM. One may conclude that the present *predictor-corrector* functions well too for the MPWE and extreme longitudinal stress subjected to combined wave-induced VBM and DBM.

Based on the second *corrector* result, the effect of DBM on the extreme longitudinal stress is further investigated. By utilizing $\sigma_{b,CFD}$ and $M_{h,glob,CFD}$ calculated from the coupled CFD-FEA, the longitudinal stress on the outer bottom panel is decomposed into the VBM induced component (σ_{glob}) and the DBM induced component (σ_{db}) [6.2].

$$\begin{aligned} & \sigma_{b,CFD} = \sigma_{glob} + \sigma_{db} + \sigma_{b,st} + \sigma_{axial} \\ & \sigma_{glob} = \frac{M_{h,glob,CFD}}{Z} \end{aligned} \tag{6.6}$$

where σ_{axial} denotes the axial stress component, which can be calculated by dividing the section force at SS5.25 by its sectional area. A comparison of σ_{glob} and σ_{db} is shown in Figure 6.12. In Figure 6.12, negative values denote that the subject panel is subjected to in-plane compression. At the vicinity of target time, 112.8 seconds, σ_{glob} and σ_{db} are 78MPa and 18MPa under compression, respectively. As the static component of the longitudinal stress is 67MPa, as mentioned earlier, σ_{db} accounts for 11.1% of total stress. This fact proves that the effect of DBM is of non-negligible amount for evaluating realistic double bottom structure response.

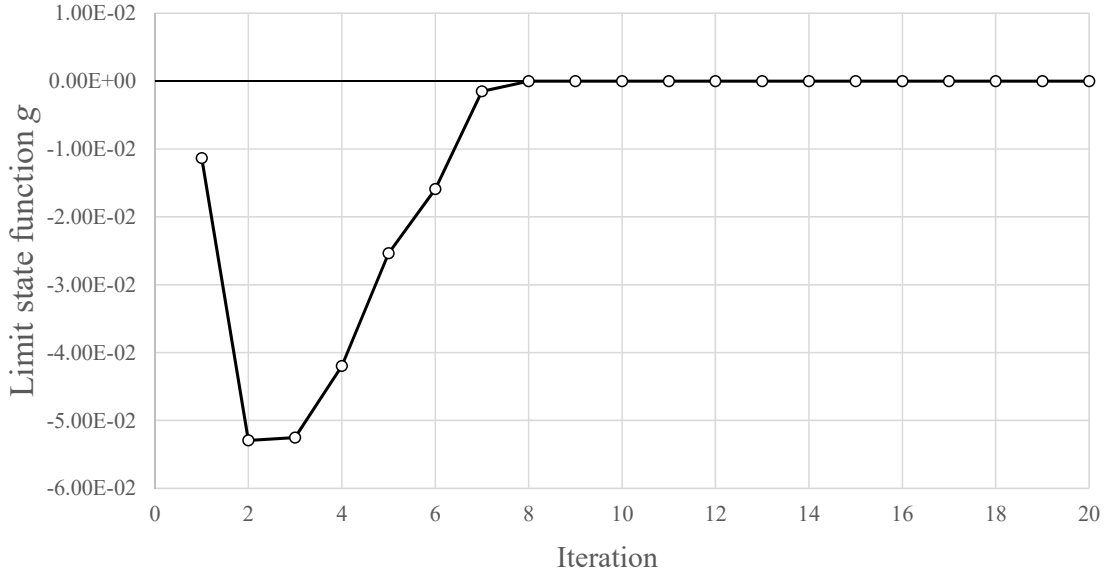

Figure 6.8 Convergence of limit state function

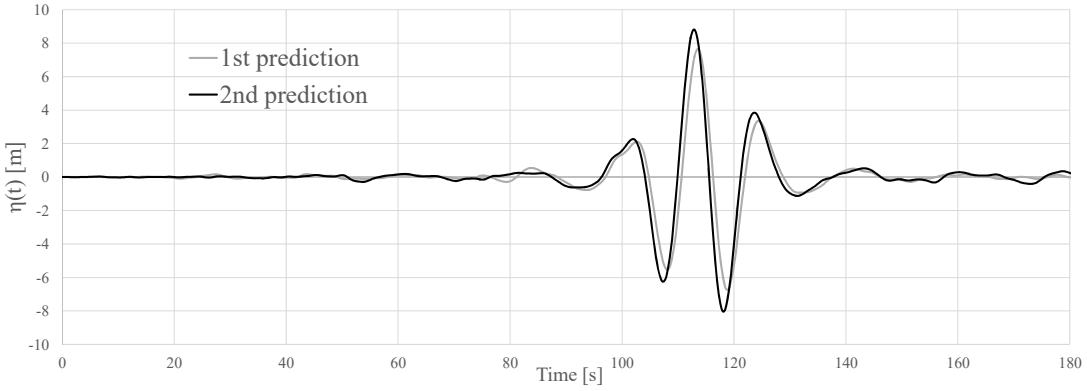

Figure 6.9 Specified MPWEs for combined wave-induced VBM and DBM

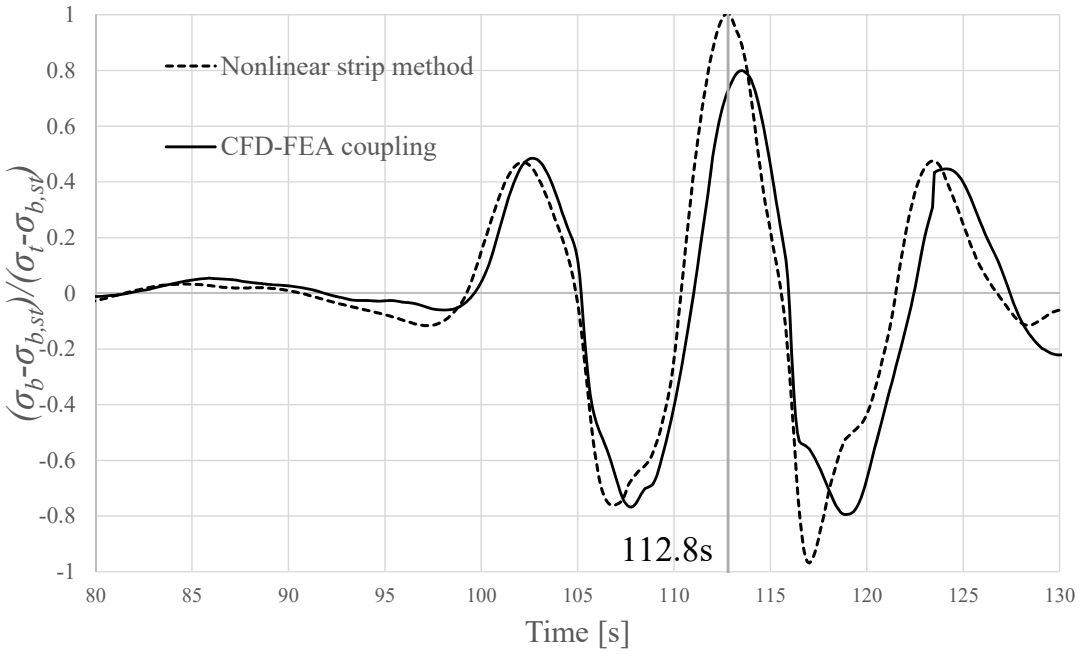

Figure 6.10 Comparison of non-dimensional average stress at outer bottom under specified MPWE from first prediction (without MCF)

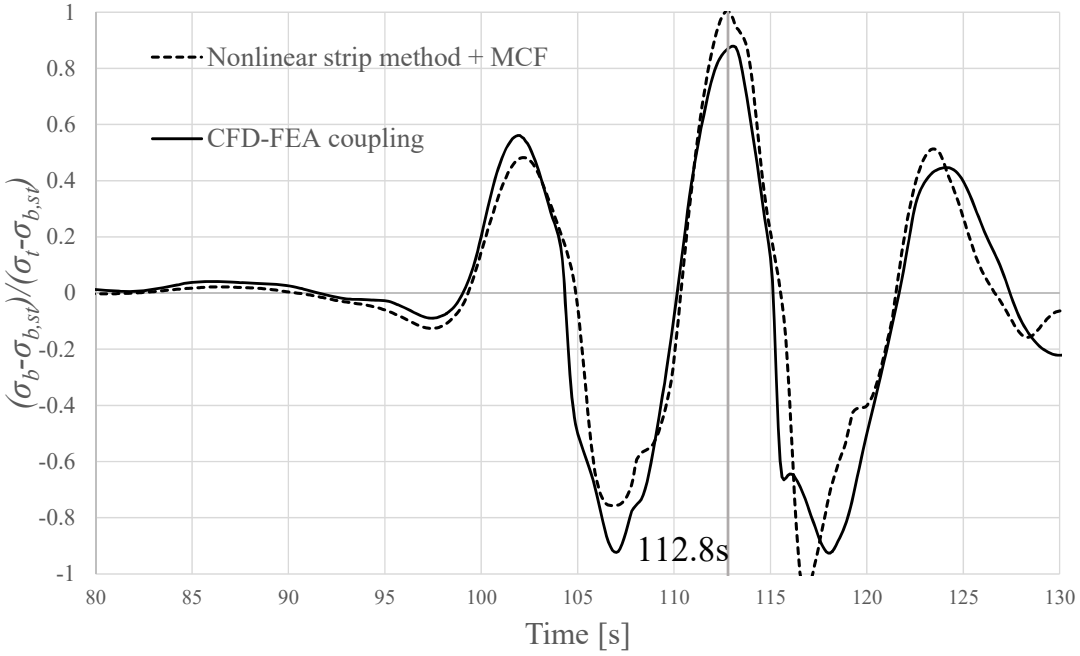

Figure 6.11 Comparison of non-dimensional average stress at outer bottom under specified MPWE from second prediction (with MCF)

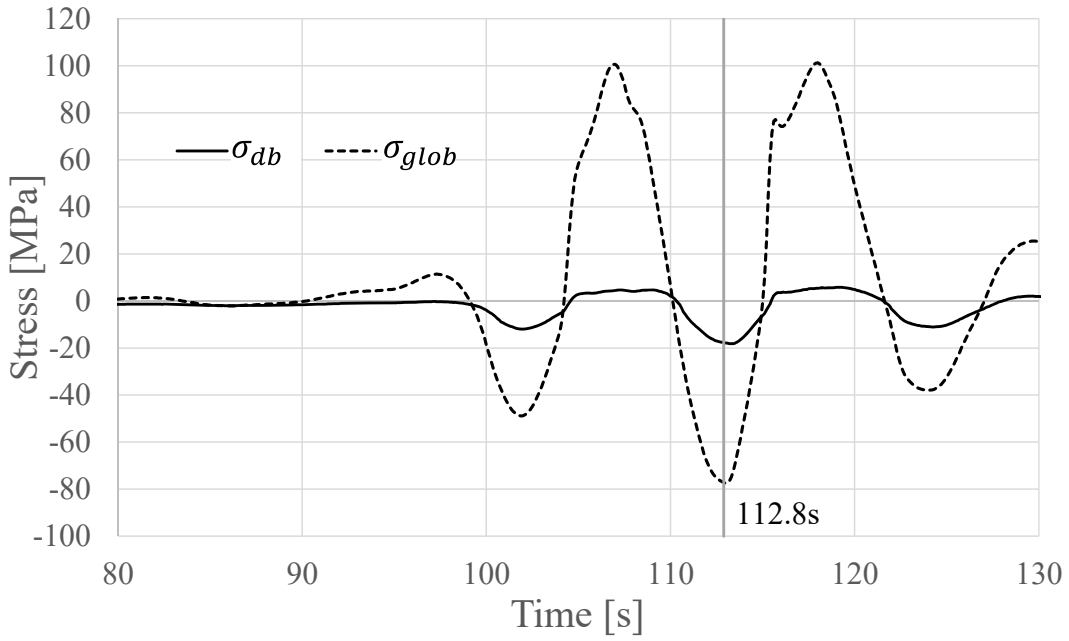

Figure 6.12 Time series of stress components at outer bottom derived from the coupled CFD-FEA under specified irregular wave train based on second prediction (with MCF)

6.5 Combined Wave-induced and Whipping VBM

Finally, results of extreme value predictions for combined wave-induced and whipping VBM. The convergence history of limit state function, *g*, during the FORM process is shown in Figure 6.13. After 13 iterations, successful convergence of FORM is found. First specified MPWE via the predictor in conjunction with the limit state function expressed by Eq. (5.23) is shown in Figure 6.14, plotted by a thin solid line. Predicted reliability index β is 3.17. A comparison of VBMs ($M_{h,glob}$) derived from the *predictor* and the *corrector* under the specified MPWE is shown in Figure 6.15. To derive the whipping VBM from the *corrector*, first the computation by setting the damping ratio of the FE model to 1.66% [6.3] is conducted, and then the high frequency component is extracted by applying the BPF with the cutoff frequency of 0.4Hz to the obtained result. From Figure 6.15, the peak values of $M_{h,glob}$ themselves from the *predictor* and the *corrector* are close, but the phase of whipping VBM from the *predictor* apparently differs from that from the *corrector*.

Next the MCF determination and second prediction are conducted in the same manner as is the case of wave-induced VBM. Specified MPWE via the second *predictor* stage is shown in Figure 6.14, plotted by a black solid line. Here, adopted relaxation factor is α=0.5. Predicted reliability index β is 3.80. A comparison of VBMs ($M_{h,glob}$) derived from the *predictor* and the *corrector* under the second specified MPWE is shown in Figure

6.16. One can find that the intended correction has not functioned, as both of the peak amplitude and peak time have not being corrected.

Figure 6.17 shows a comparison of the whipping component of VBM, named $M_{h,glob,whip}$, derived from the *predictor* and the *corrector* under second specified MPWE. As found from the figure, the phase and amplitude of whipping VBM significantly deviate from each other. This deviation may be attributed to the difference of impact force estimation methods used in these methods. Since the MCF adopted in this study functions merely to correct the instantaneous value of $M_{h,glob}$, cf. Eqs. (5.8) and (5.9), deviations in terms of the characteristic of whipping vibration cannot be corrected. Hence, an unintentional MPWE has been identified through the present *predictor-corrector* approach. Such misleading of MCF approach was also reported by Seng et al. [6.4]. It can be inferred that the present *predictor-corrector* approach is unadaptable when the target response includes the whipping unless the effective MCF or *predictor* are found.

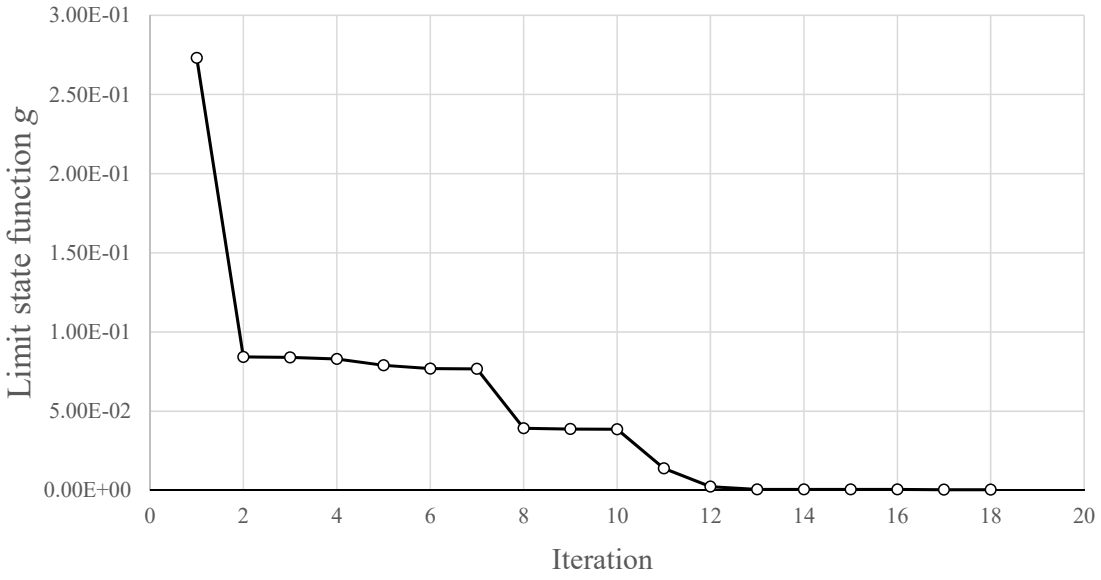

Figure 6.13 Convergence of limit state function

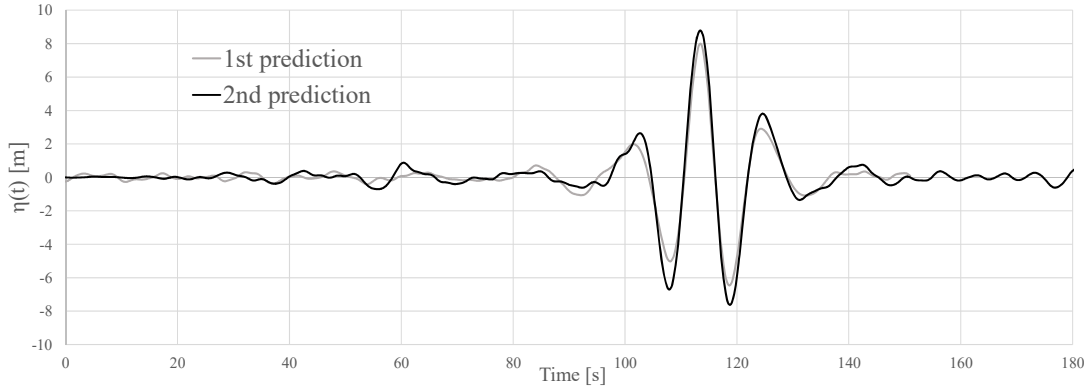

Figure 6.14 Specified MPWEs for combined wave-induced and whipping VBM

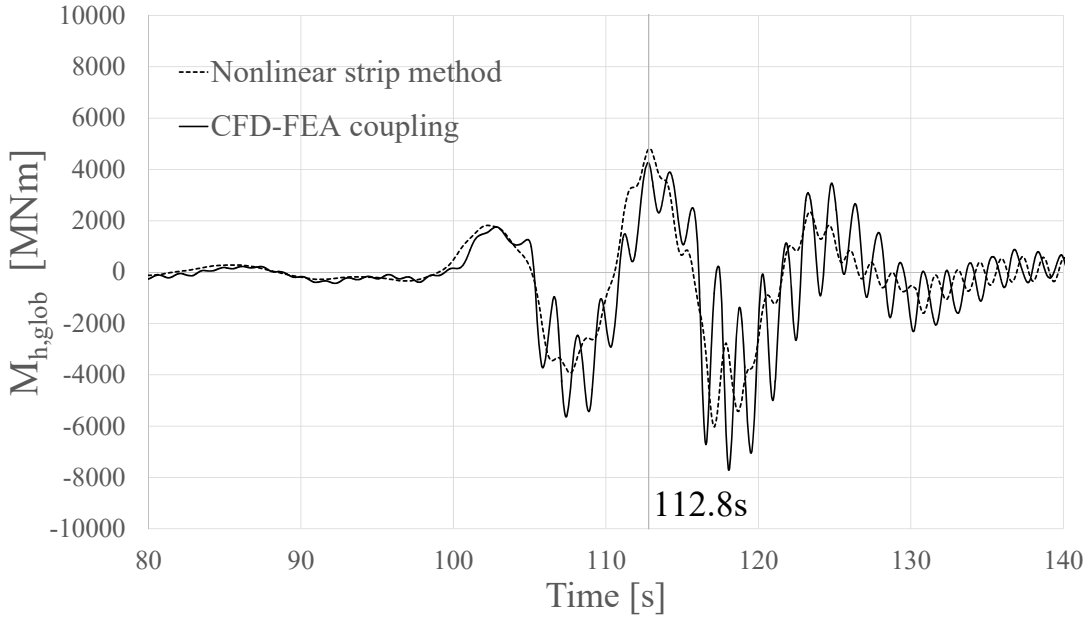

Figure 6.15 Comparison of $M_{h,glob}$ under the specified MPWE from first prediction (without MCF)

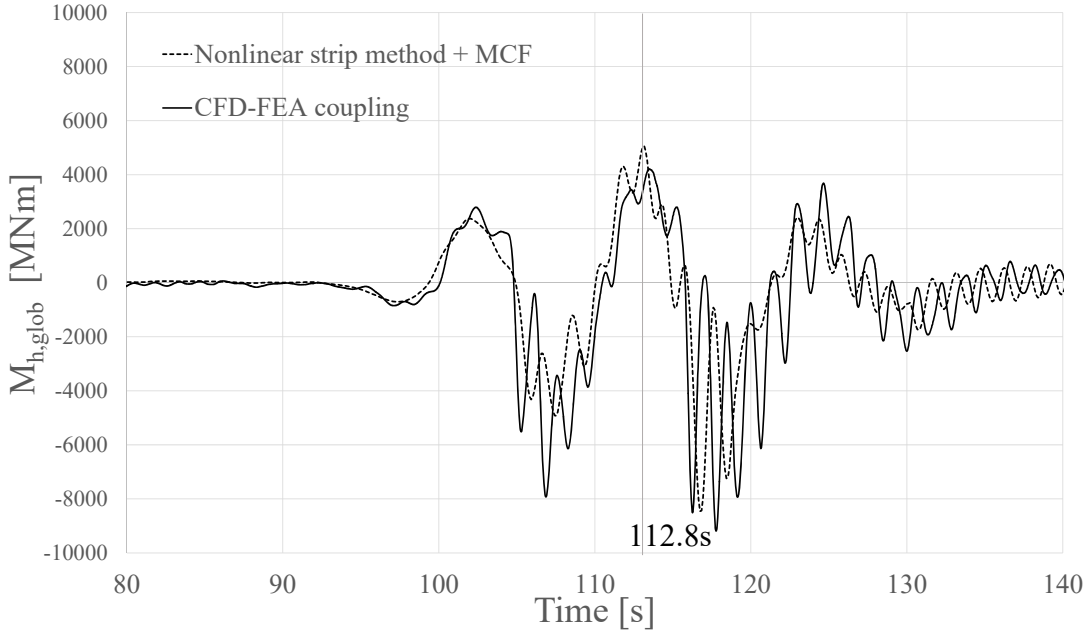

Figure 6.16 Comparison of $M_{h,glob}$ under the specified MPWE from second prediction (with MCF)

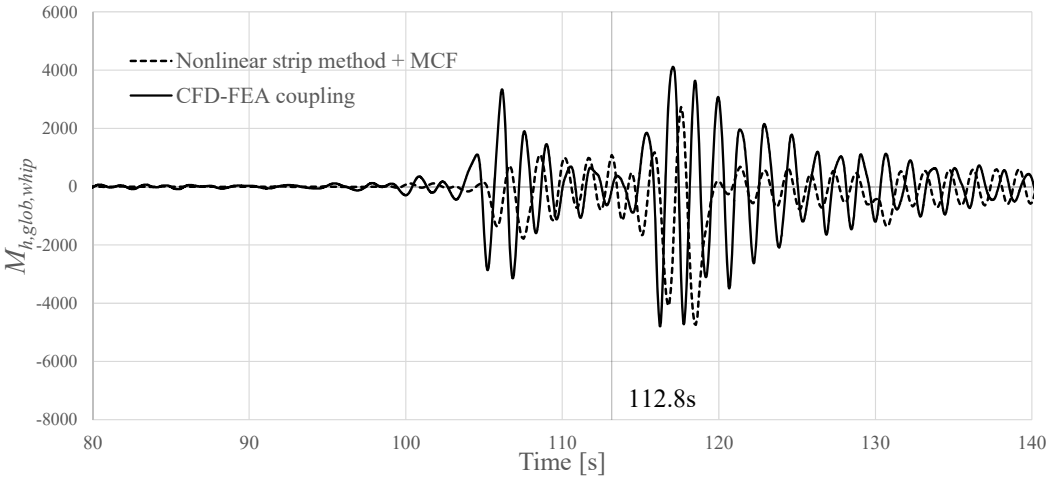

Figure 6.17 Comparison of whipping component of $M_{h,glob}$ under the specified MPWE from second prediction (with MCF)

6.6 Summary of Chapter 6

In this chapter, the FORM and the *predictor-corrector* approach (see Chapter 3) is employed to estimate extreme structural response under combined load based on developed one-way coupled CFD-FEA. The nonlinear strip method is adopted to the *predictor*. The following may be concluded.

1. By applying the *predictor-corrector* approach, the MPWE associated with the extreme wave-induced VBM is successfully identified.
2. When the present *predictor-corrector* approach is applied to the extreme value prediction under combined wave-induced VBM and DBM, the prediction is successfully attained as well.
3. However, the present *predictor-corrector* approach fails to predict the extreme value of combined wave-induced and whipping VBM, due to the significant deviation of whipping response estimation between the nonlinear strip method and the CFD-FEA coupling.

When the previous work by Seng et al. [6.4] is reviewed, the difference of stern slamming induced component was found between their *predictor* (nonlinear strip method) and *corrector* (OpenFOAM+Timoshenko beam), and they concluded that the prediction failing arose from this difference. In the case of this study, however, the stern slamming has not large contribution throughout the calculations under MPWEs from the *predictor* and *corrector*. From this result, it can be inferred that the present *predictor-corrector* approach using the nonlinear strip theory is unadaptable when the target response includes the whipping component to a large degree, unless more efficient MCF or the *predictor* itself are found.

References in Chapter 6

[6.1] IACS, *Longitudinal Strength Standard*. 2010, pp. 1–12.

[6.2] Y. Kawasaki *et al.*, "Strength Evaluation of Containerships Based on Dynamic Elastic Response Calculation of Hull Girder. 2nd Report - Influence of Hull Girder Rigidity and Correlation between Double Bottom Bending and Hull Girder Bending," *J. Japan Soc. Nav. Archit. Ocean Eng.*, vol. 25, pp. 191–203, 2017.

[6.3] G. Storhaug, K. Laanemets, I. Edin, and J. W. Ringsberg, "Estimation of damping from wave induced vibrations in ships," in *Progress in the Analysis and Design of Marine Structures*, 2017, pp. 121–130.

[6.4] S. Seng and J. J. Jensen, "An Application of a Free Surface CFD Method in the Short-Term Extreme Response Analysis of Ships," in *Proceedings of PRADS2013*, 2013, pp. 747–754.

Chapter 7
EXTREME VALUE PREDICTION BY ROM AND FORM

7.1 Introduction

In this chapter, the extreme value predictions of VBM and DBM under two short-term sea states, State 1 and State 2, see Table 7.1, are targeted. These sea states are the same condition with the towing tank experiment using the OU model. For State 1, the whipping vibration effect is not accounted for, over the experiment and numerical results. For State 2, the whipping vibration effect is accounted for, over the both results. The ISSC wave spectra (cf. Eq. (6.2)) within ω_i range of 0.3-1.5 [rad/s] is adopted in formulating the irregular wave, Eq. (7.1), and the number of discrete harmonic wave components N is equal to 100 using non-equidistant discrete frequencies ($d\omega_i$).

$$\eta(t) = \sum_{i=1}^{N} u_i \sqrt{S(\omega_i) d\omega_i} \cos(\omega_i t) + \sum_{i=1}^{N} \bar{u}_i \sqrt{S(\omega_i) d\omega_i} \sin(\omega_i t) \tag{7.1}$$

First, constructions and validations of ROM for the wave-induced VBM, the DBM, and the whipping VBM are introduced. The one-way coupled CFD-FEA where the 1D beam model is adopted in the FEA phases is used for ROM construction. The weight distribution and the gyration radius with regards to pitch motion (k_{yy}) of the present 1D beam model comply with those of prototype full scale ship. Young's modulus of the 1D beam model is adjusted so that the target 2-node natural frequency can be reproduced. A half size model cutting off and setting a symmetry boundary condition at Y=0 section is adopted in CFD. The mesh resolution of the CFD over the free surface region is; Δx = 4.26m (horizontal direction) and Δz= 0.99m (vertical direction), in full scale. A series of validations in terms of the PoEs and MPWEs predicted by combined ROM and FORM is then carried out by comparing with the experiment using the OU model.

Table 7.1 Short-term sea states for towing tank test of OU model under irregular waves

	Significant wave height (H_s)	Mean wave period (T_z)	Froude number (Fn)	Whipping
State 1	6.5 m	15.0 seconds	0.000	Not considered
State 2	11.5 m	15.0 seconds	0.078	Considered

7.2 Verification of ROM

7.2.1 Wave-induced VBM

The reduced order model (RO model) for wave-induced VBM is constructed first. The methodology for constructing ROM for wave-induced VBM is explained in subsection 5.3.1. Random variables u_i and $\bar{u}_i$ are generated first then make the wave elevation as per Eq. (7.1) in order to obtain the TFs under State 1 and State 2 via the nonlinear strip method (NMRIW-II). The wave elevation histories of 7500 seconds and 6500 seconds (Figures 7.1 and 7.2) in full scale are used to obtain a sufficient amount of data for FFT. Derived TFs under State 1 and State 2 are shown in Figures 7.3 and 7.4. Next correction factor for the nonlinearity against the peak wave height, c_{rel} in Eq. (5.10), is examined. Figures 7.5 and 7.6 provide identified c_{rel} under State 1 and State 2. 6 degrees of polynomial approximation is applied to represent c_{rel}. Estimated c_{rel} is;

State 1:

$$\begin{aligned} &c_{rel} = 0 \quad (\eta_{\max} \le 3.0) \\ &c_{rel} = -7.00E^{-9}\eta_{\max}^6 + 6.83E^{-7}\eta_{\max}^5 - 2.83E^{-5}\eta_{\max}^4 \\ &+6.23E^{-4}\eta_{\max}^3 - 7.37E^{-3}\eta_{\max}^2 + 4.16E^{-2}\eta_{\max} - 8.45E^{-2} \quad (3.0 < \eta_{\max} \le 15.0) \\ &c_{rel} = -0.01 \quad (15.0 \le \eta_{\max}) \end{aligned} \tag{7.2}$$

State 2:

$$\begin{aligned} &c_{rel} = 0 \quad (\eta_{\max} \le 3.0) \\ &c_{rel} = -5.36E^{-8}\eta_{\max}^6 + 4.01E^{-6}\eta_{\max}^5 - 1.23E^{-4}\eta_{\max}^4 \\ &+2.00E^{-3}\eta_{\max}^3 - 1.79E^{-2}\eta_{\max}^2 + 7.96E^{-2}\eta_{\max} - 1.29E^{-1} \quad (3.0 < \eta_{\max} \le 15.0) \\ &c_{rel} = -0.018 \quad (15.0 \le \eta_{\max}) \end{aligned} \tag{7.3}$$

Assuming that the difference of phase on wave-induced VBM between the nonlinear strip method and the CFD is insignificant, the correction factors for expressing the CFD-FEA results (c_{CFD}, in Eq. (5.12)) are examined. Estimated c_{CFD} are plotted in Figures 7.7

and 7.8. One can find that the magnitudes of c_{CFD} are approximately 0.8 and 0.77 under State 1 and State 2, respectively.

By using constructed RO model, a prediction of MPWE leading to an extreme values of the wave-induced VBM is conducted by combining with FORM under State 1 and State 2. The target time is 150 seconds (in full scale), and the target magnitude of VBM is 4000MNm (hogging) in full scale. c_{CFD} is assumed to be constant value 0.80 for State 1 and 0.77 for State 2. Figures 7.9 and 7.10 show the predicted MPWEs. The reliability indices β are 7.43 under State 1 and 4.04 under State 2. To validate the accuracy of the present ROM, the CFD-FEA coupled simulation is conducted under the predicted MPWEs. To compute wave-induced VBM from the simulation, the damping ratio of the FE model is set to its critical damping ratio. Comparisons between predicted VBM from the ROM and that from the CFD-FEA coupled simulation are shown in Figures 7.11 and 7.12. As found from the figures, the present ROM could predict well the extreme VBM from the CFD-FEA coupled method in terms of its magnitude and phase. Since the TF is estimated based on the nonlinear strip method in this study, it should be kept in mind that if more suitable TF for predicting CFD-FEA results is found, the deviation of VBM from the CFD-FEA results would be further improved. Nonetheless, the present RO model can predict the extreme value of hogging wave-induced VBM in a sufficient manner. In the following sections, the present RO model for wave-induced VBM is employed for both State 1 and State 2.

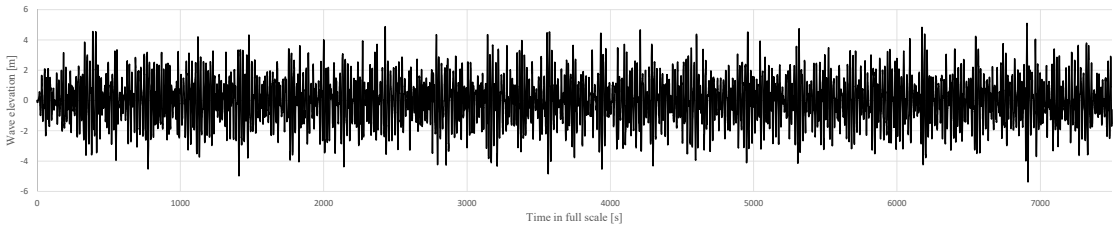

Figure 7.1 Generated irregular wave to estimate TF under State 1

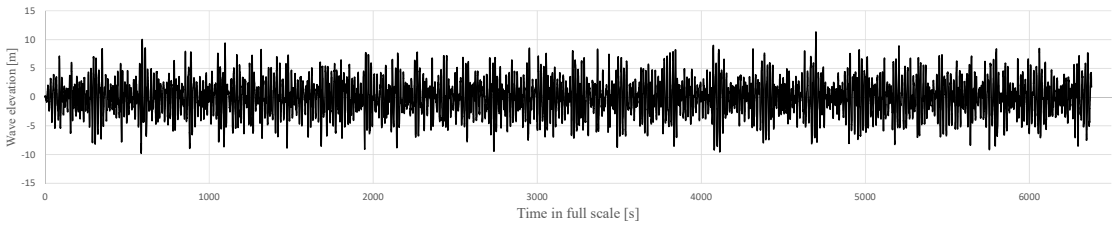

Figure 7.2 Generated irregular wave to estimate TF under State 2

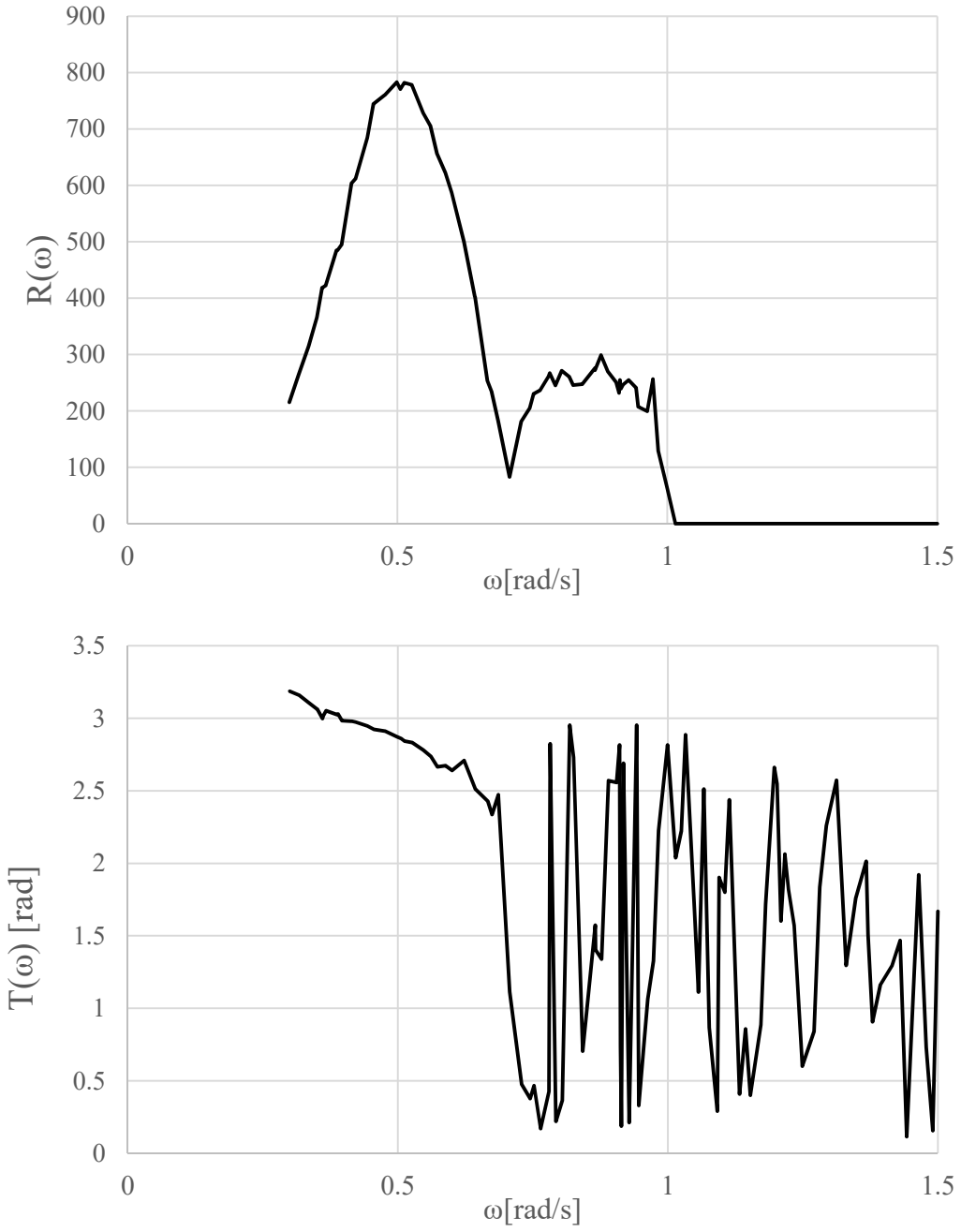

Figure 7.3 TF of wave-induced VBM ($R(\omega_i)$, $T(\omega_i)$) under State 1

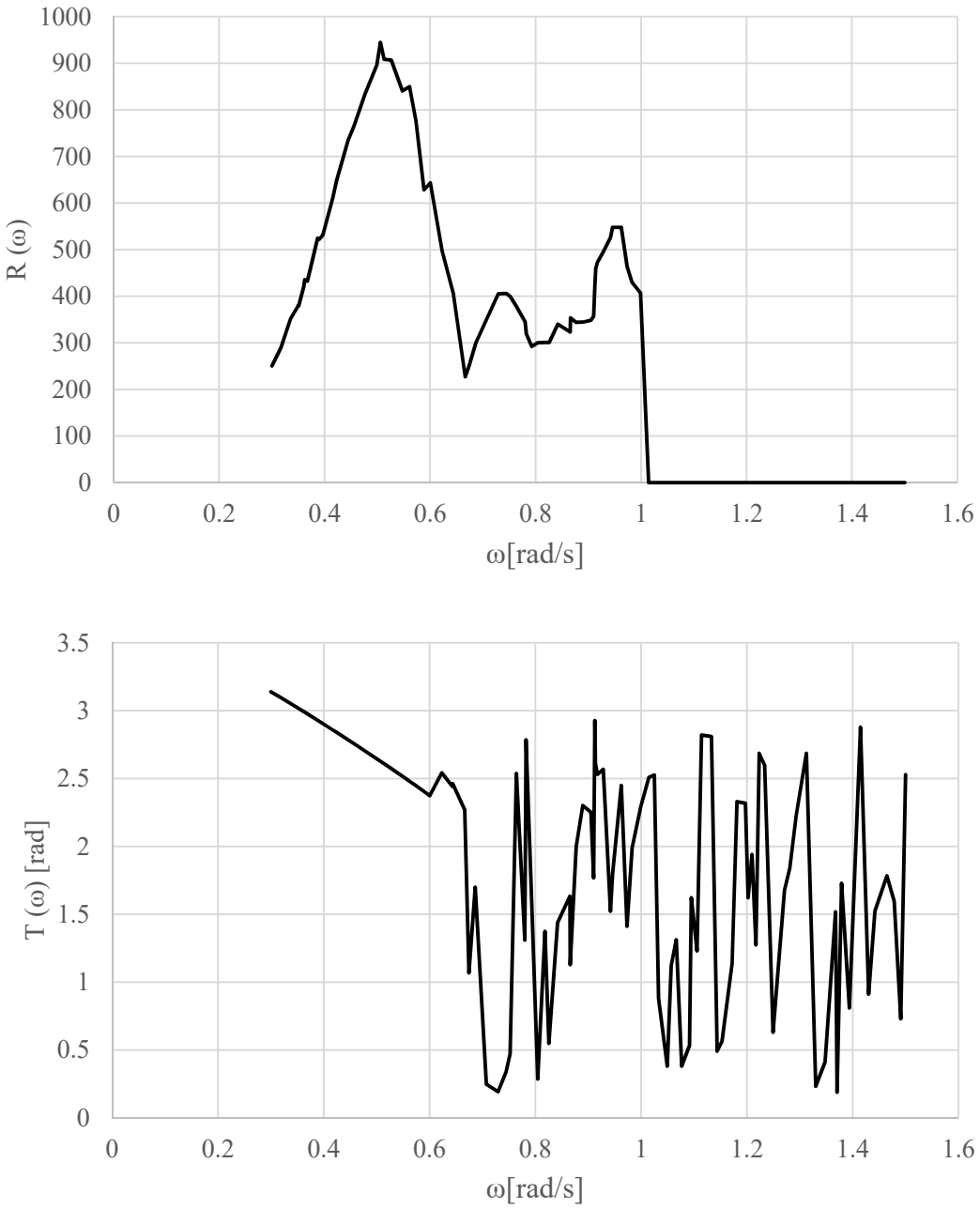

Figure 7.4 TF of wave-induced VBM ($R(\omega_i)$, $T(\omega_i)$) under State 2

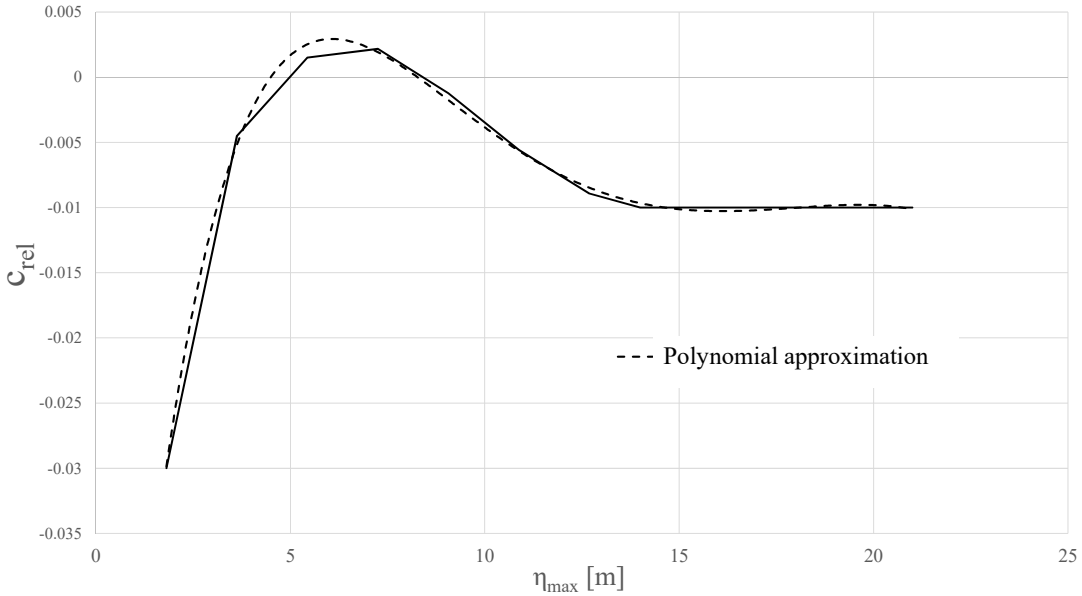

Figure 7.5 Correction factor for nonlinearity on wave-induced VBM (State1)

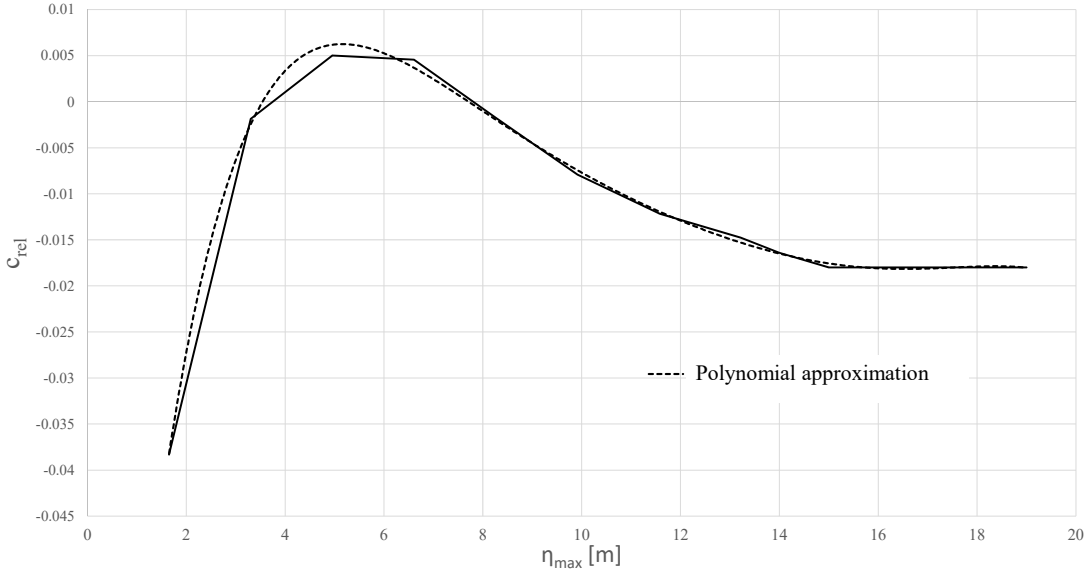

Figure 7.6 Correction factor for nonlinearity on wave-induced VBM (State2)

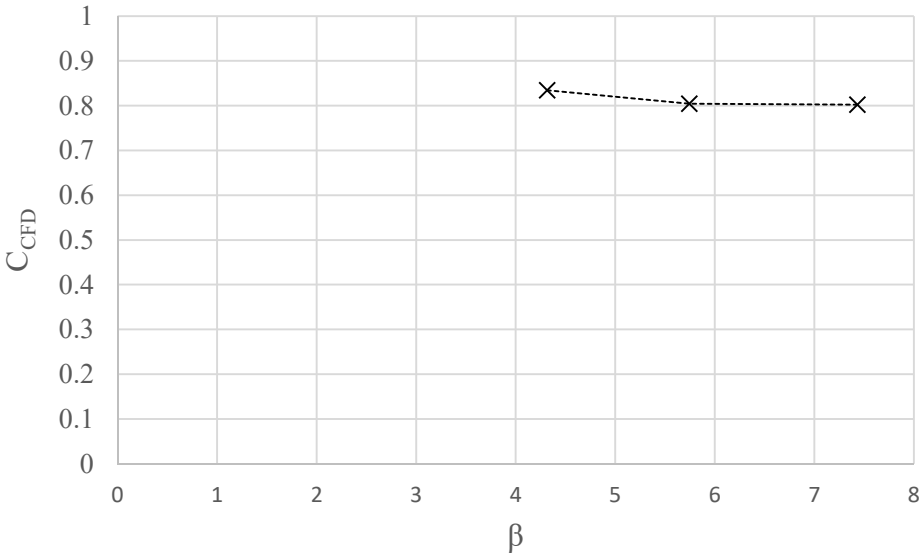

Figure 7.7 Correction factor to express CFD-FEA result on wave-induced VBM (State1)

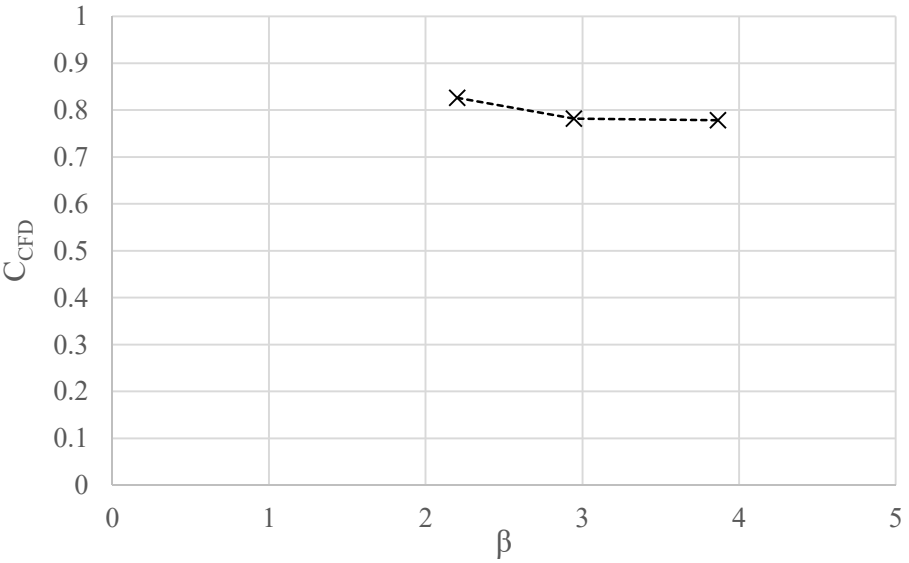

Figure 7.8 Correction factor to express CFD-FEA result on wave-induced VBM (State2)

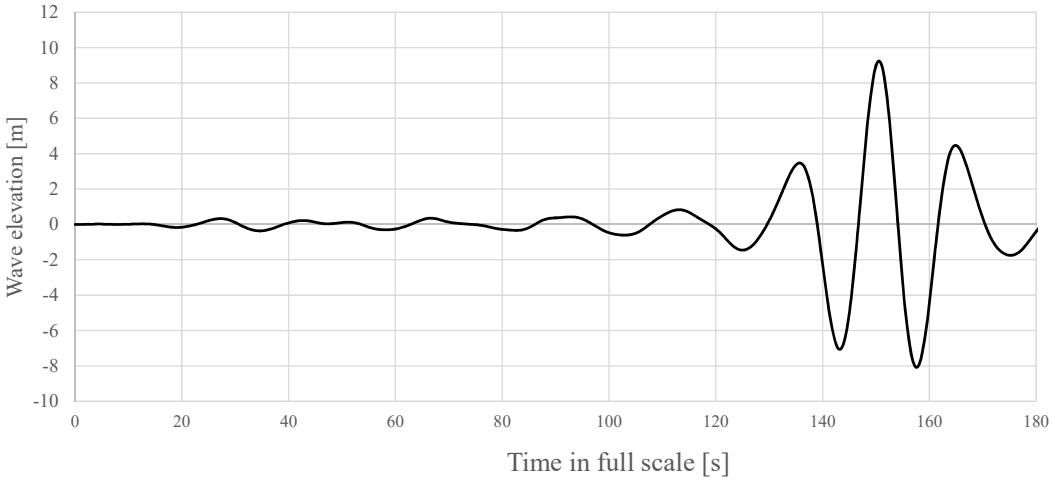

Figure 7.9 Predicted MPWE by using constructed ROM and FORM for wave-induced VBM (State 1)

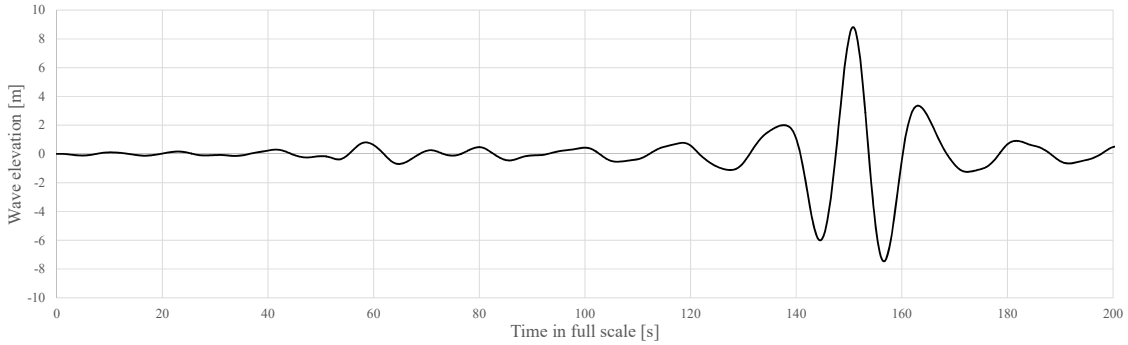

Figure 7.10 Predicted MPWE by using constructed ROM and FORM for wave-induced VBM (State 2)

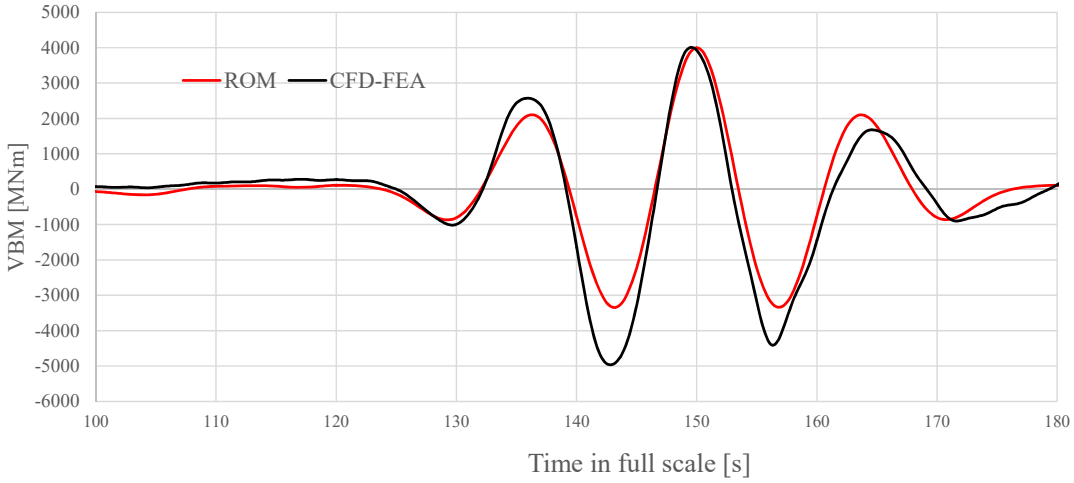

Figure 7.11 Comparison of wave-induced VBM between ROM and CFD-FEA coupled method under predicted MPWE (Figure 7.9)

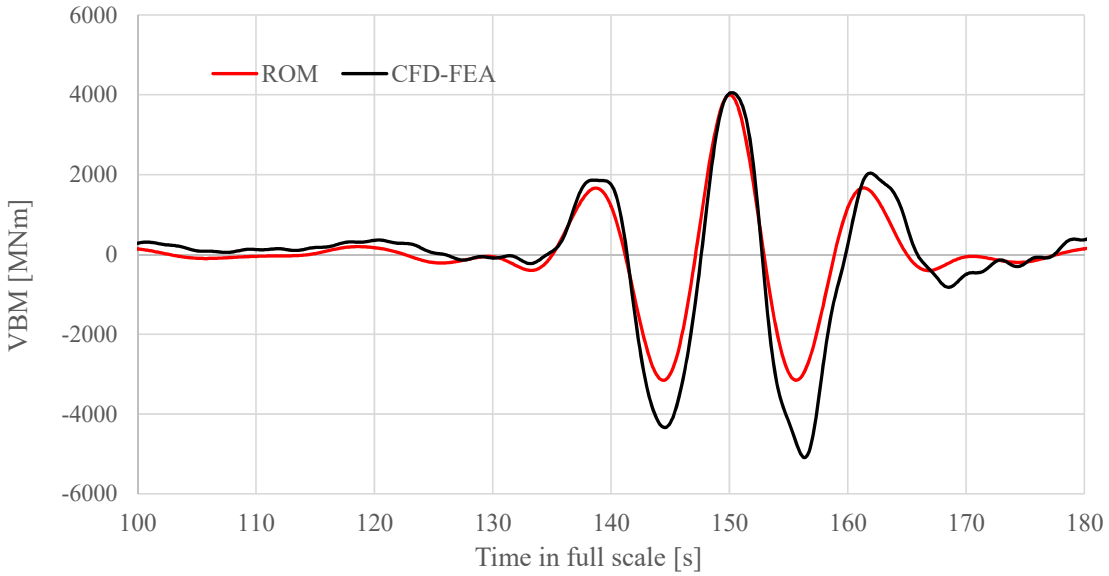

Figure 7.12 Comparison of wave-induced VBM between ROM and CFD-FEA coupled method under predicted MPWE (Figure 7.10)

7.2.2 DBM

The reduced order model (RO model) for DBM is constructed in the same manner as the wave-induced VBM. The methodology for constructing ROM for DBM is explained in subsection 5.3.2. The target section of DBM evaluation is SS4.5 of the ship. First estimation of TF in terms of water pressure acting on SS4.5 is conducted based on the nonlinear strip method. Derived TFs under State 1 is shown in Figures 7.13. According

to Tatsumi et al. [7.1], the transfer factor from water pressure to DBM c_p is found be 43.619 in the case of subject ship. Supposing that the nonlinearity of the water pressure is subtle, the MPWE leading to extreme DBM at 7.2MNm (with still water component) is estimated by combining with FORM. Identified MPWE is shown in Figure 7.14. The reliability index β is 2.91. A comparison between predicted DBM from the ROM and that from the CFD simulation is shown in Figure 7.15. Water pressure acting on SS4.5 is obtained from the CFD, then the DBM is calculated according to Eq. (5.13). As found from the figure, the amplitude and phase of DBM deviate from the CFD result. This difference is attributed to the three-dimensionality of the model or discrepancy of assumed still water components of DBM, as the TF for DBM is estimated based on the nonlinear strip method. This small difference may be complemented with the simple correction according to Eq. (5.14). After the revision of ROM, the DBM under the same MPWE is compared with each other again in Figure 7.16. Good correlation is found between the revised ROM and the CFD. In the following sections, this revised RO model for DBM is employed to demonstrate extreme value predictions under combined VBM and DBM.

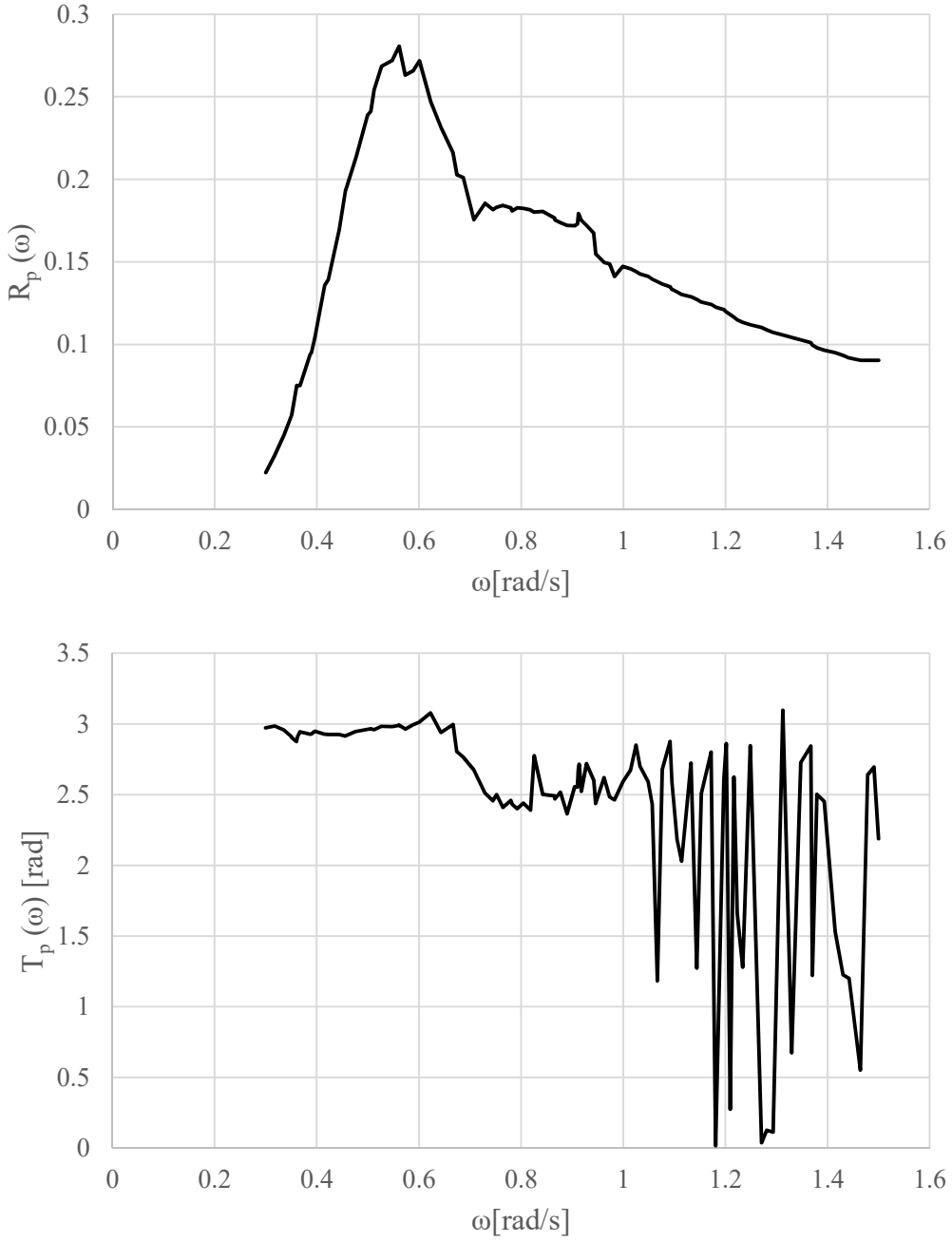

Figure 7.13 TF of water pressure ($R_p(\omega_i)$, $T_p(\omega_i)$) under State 1

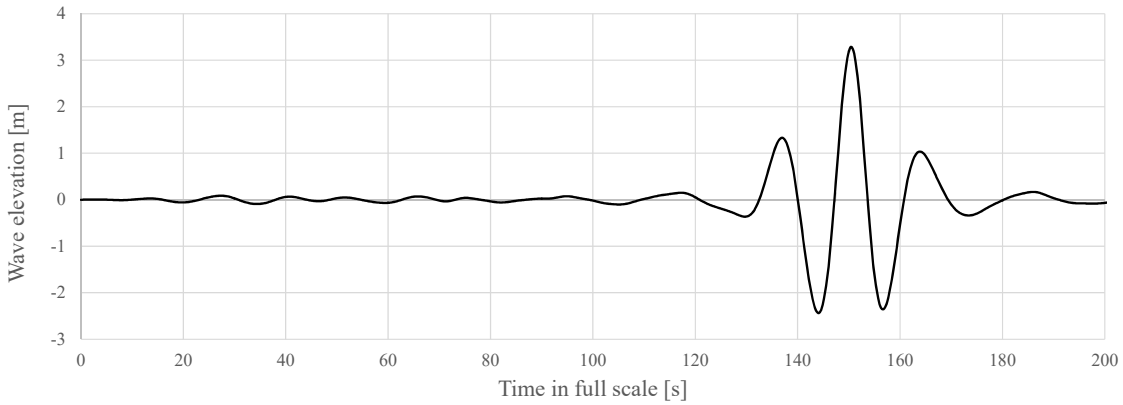

Figure 7.14 Predicted MPWE by using constructed ROM and FORM for DBM (State 1)

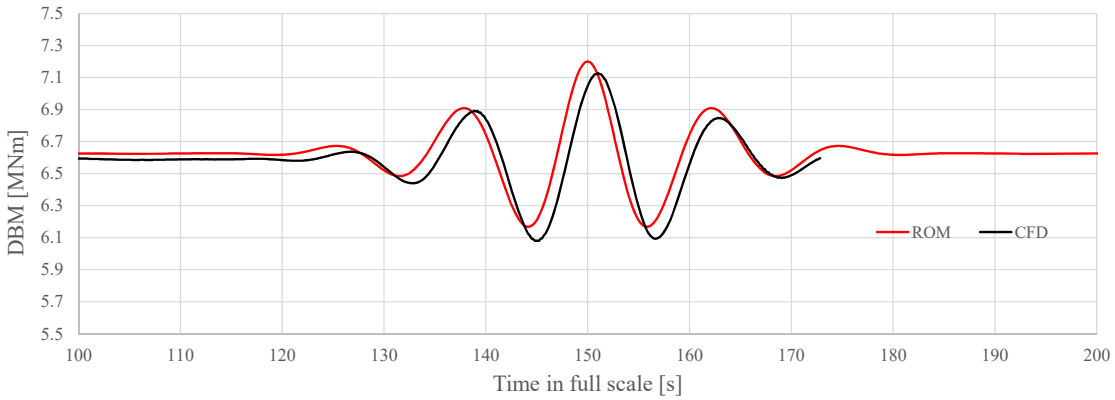

Figure 7.15 Comparison of DBM between ROM and CFD under predicted MPWE (Figure 7.14)

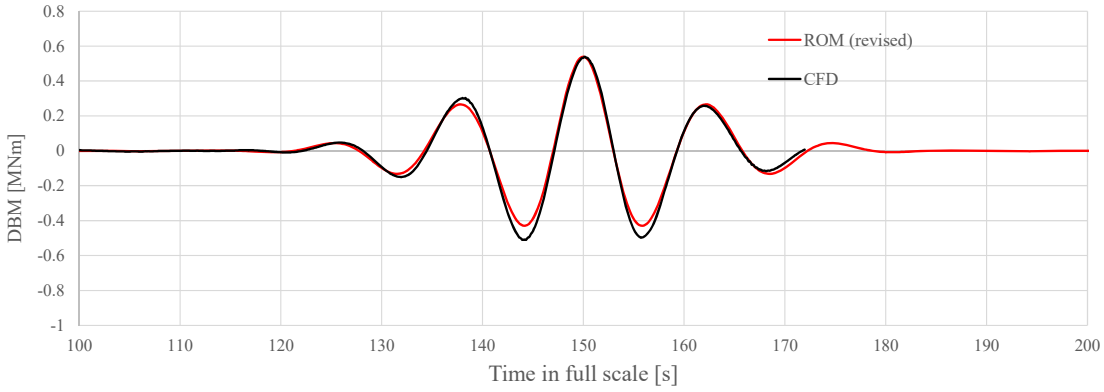

Figure 7.16 Comparison of DBM between revised ROM and CFD under predicted MPWE (Figure 7.14)

7.2.3 Whipping VBM

Finally, the construction of RO model for whipping VBM is made. State 2 is the subject sea state. The methodology for constructing ROM for whipping VBM is explained in subsection 5.3.3. An arbitrary MPWE (Figure 7.17) is obtained first by using the above-mentioned ROM for wave-induced VBM. The CFD computation under the MPWE is conducted then the TFs of heave and pitch motions are estimated as are the case with the wave-induced VBM or DBM. Estimated TFs are shown in Figures 7.18 and 7.19.

Young's modulus of the 1D beam model is set to 118,000 N/mm^2 so that the natural frequency of 2-node vibration mode (f_{2n}) becomes 0.67Hz in full scale. To derive the whipping VBM from the CFD-FEA result, the damping ratio of the FE model is set to 1.66%, and then the high frequency component is extracted by applying the BPF with the cutoff frequency of 0.4Hz to the obtained result. By exploiting the TFs of heave and pitch motions, optimal values of unknown variables, d, δ, c_{imp}, and τ_{imp} in Eq. (5.20) and Eq. (5.21), are inspected. In this study, slamming impact forces are calculated at 6 cross sections (SS9.75, SS9.5, SS9.25, SS9.0, SS8.75, SS8.5) then these sum is used for the whipping evaluation. Figure 7.20 shows a comparison of VBM (with whipping) between results from constructed ROM and CFD-FEA. Adopted unknown variables are; d=22.0 [m], δ=45.0 [deg], c_{imp}=10.0, and τ_{imp}=0.8 [s] in full scale. As seen from Figure 7.20, the present ROM can capture the peak amplitudes and phases of the coupled CFD-FEA result in the vicinity of target time, 150 seconds, by using these values.

By using the present ROM and FORM, the extreme value predictions are conducted. In the case of whipping component is incorporated into the ROM, several design points are detected. A plurality of ROM+FORM computations are carried out to identify MPWEs leading to target extreme VBM of 4000MNm, then three of them are shown in Figure 7.21. As found from the figure, the reliability index β varies among each MPWE. Such variation stems from a fact that several local solutions have emerged when the whipping component is incorporated into the ROM. The validation of ROM presented below is made under one episode out of several MPWEs derived from ROM+FORM.

Figures 7.22 and 7.23 show identified MPWEs from the ROM+FORM processes leading to extreme VBM of 4000MNm and 5000MNm, respectively. The reliability indices β are 3.71 and 4.58, respectively. To validate the accuracy of the present ROM, the CFD-FEA coupled simulation is conducted under the predicted MPWEs. Comparisons between predicted VBM with whipping component from the ROM and that from the CFD-FEA coupled simulation are shown in Figures 7.24 and 7.25. As found from the figures, the present ROM could predict well the extreme VBM from the CFD-FEA coupled method in terms of its magnitude and phase. Small deviation of the

amplitude can be found from Figure 7.25, where the peak VBM from the coupled CFD-FEA represents 5430MNm. This deviation will be corrected by reviewing the values of d, δ, c_{imp}, and τ_{imp}. Nonetheless, the present ROM could capture the peak VBM within 9% error. For more accuracy, further optimization of d, δ, c_{imp}, and τ_{imp} is ideal, which may be somehow achieved, e.g. by applying multi-objective optimization methods to this, or utilizing machine learning techniques.

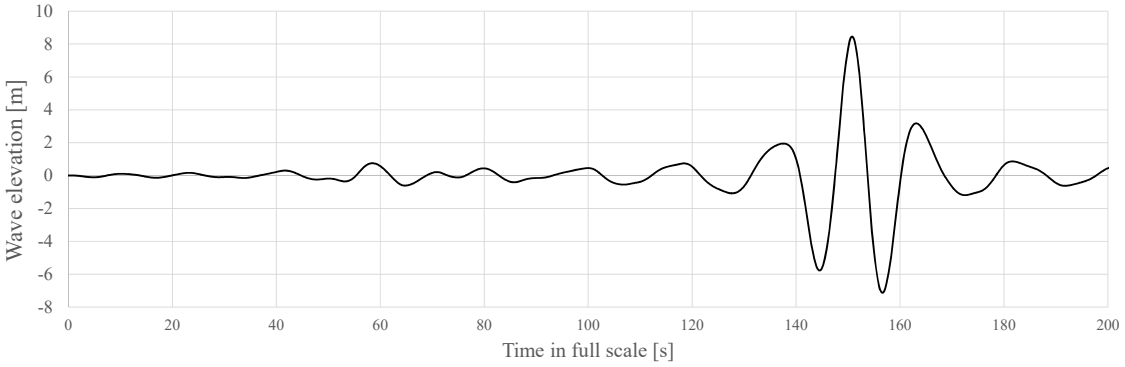

Figure 7.17 Tentative MPWE for constructing ROM for whipping VBM

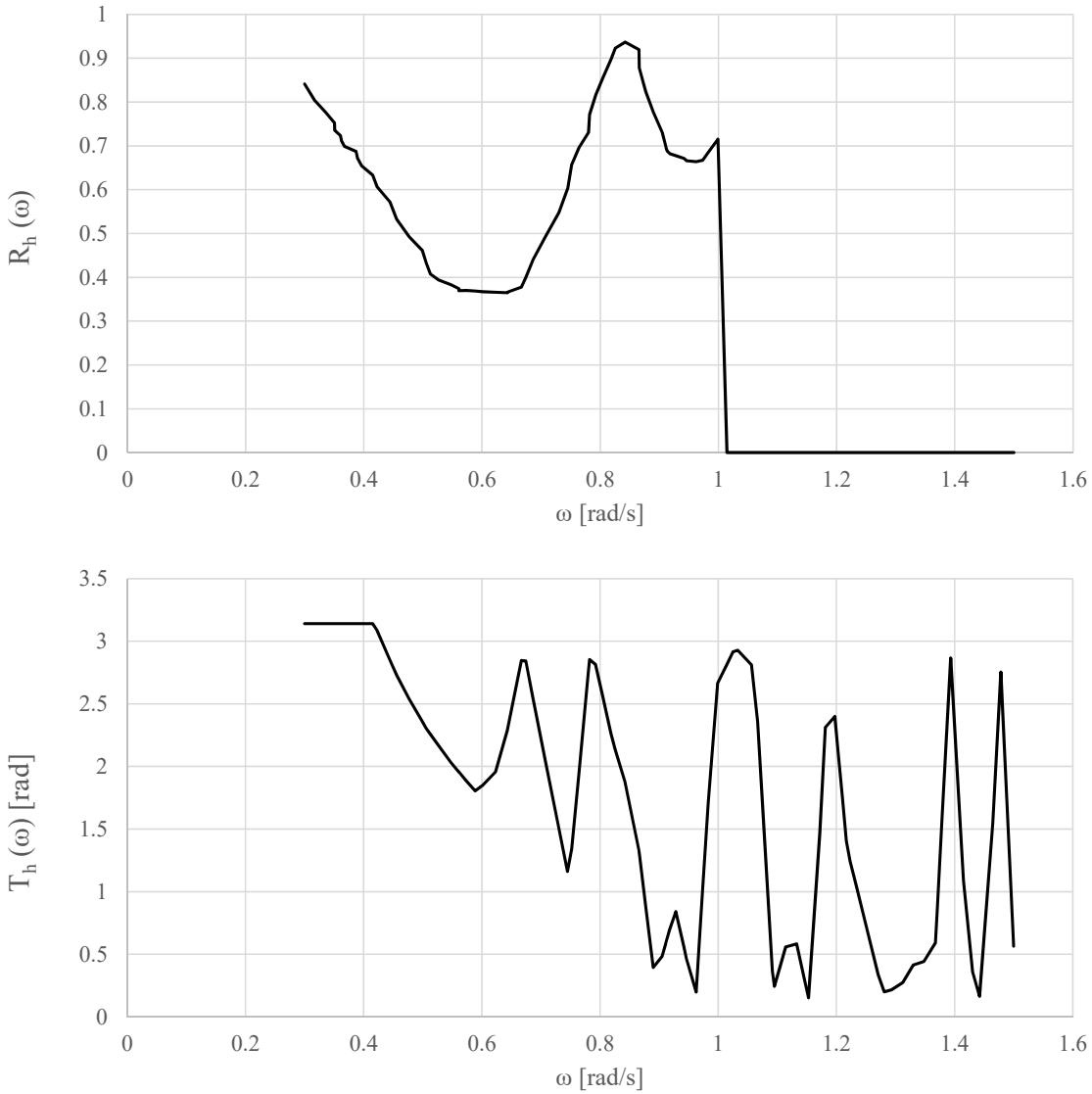

Figure 7.18 TF of heave motion ($R_h(\omega_i)$, $T_h(\omega_i)$) under State 2

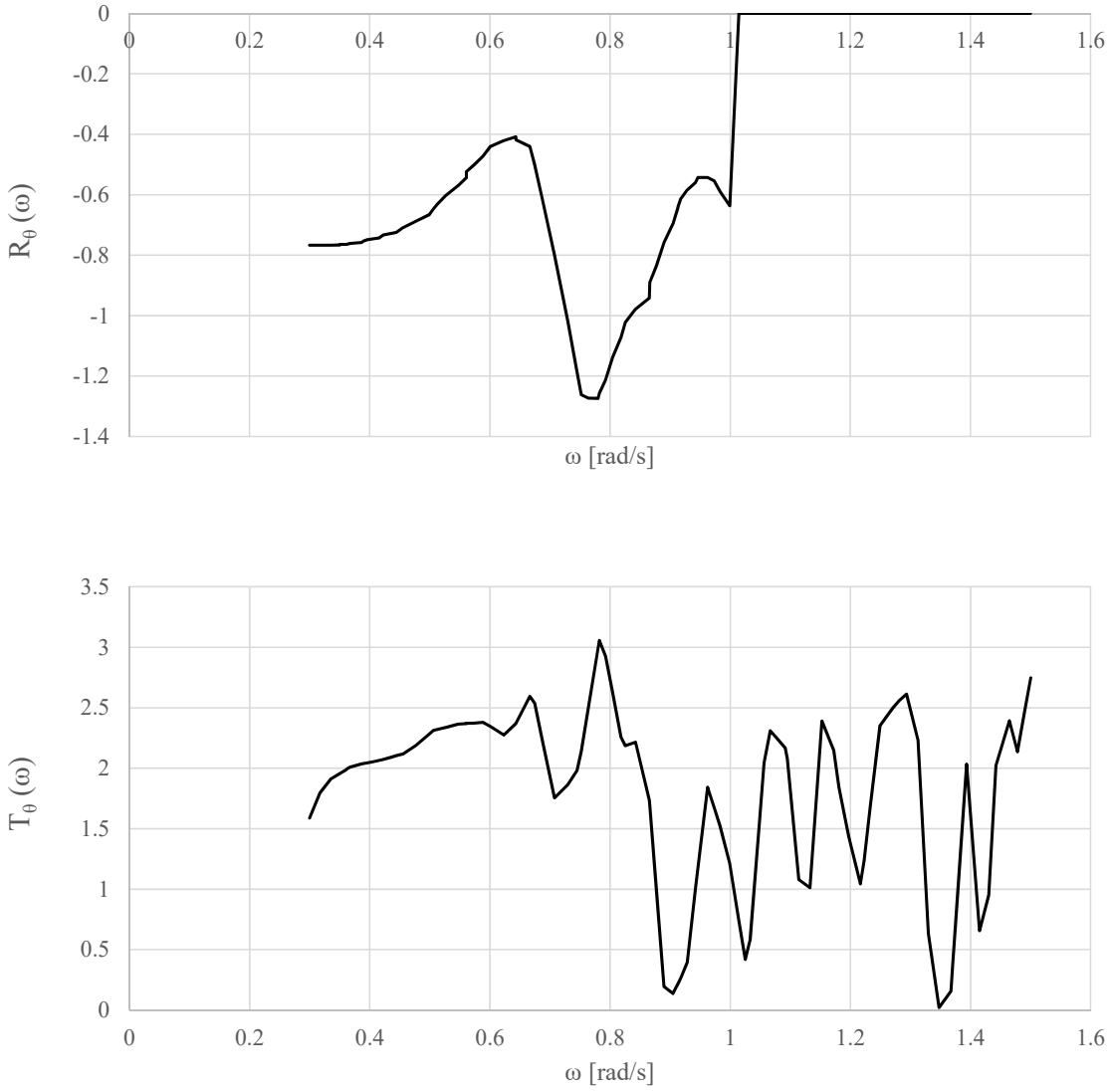

Figure 7.19 TF of pitch motion ($R_\theta(\omega_i)$, $T_\theta(\omega_i)$) under State 2

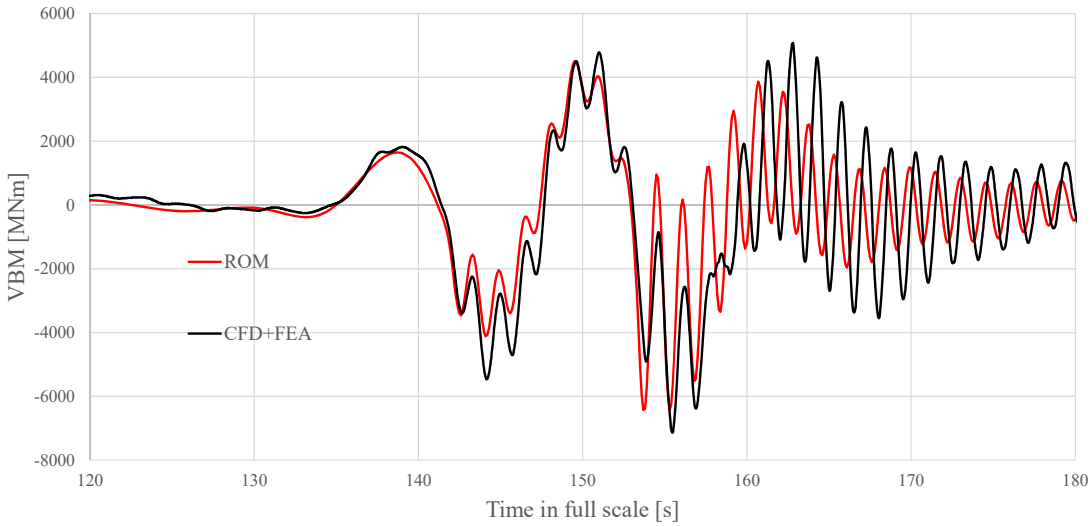

Figure 7.20 Comparison of VBM with whipping component between results from ROM and coupled CFD-FEA method under tentative MPWE (f_{2n}=0.67Hz, Figure 7.17)

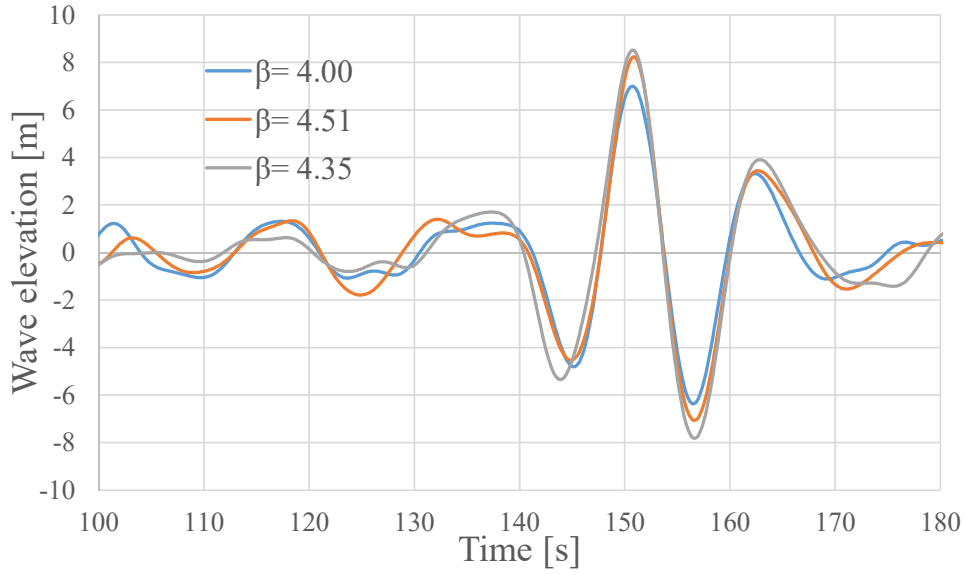

Figure 7.21 Identified MPWEs by a combination of ROM and FORM with whipping component (State 2, target; 4000MNm)

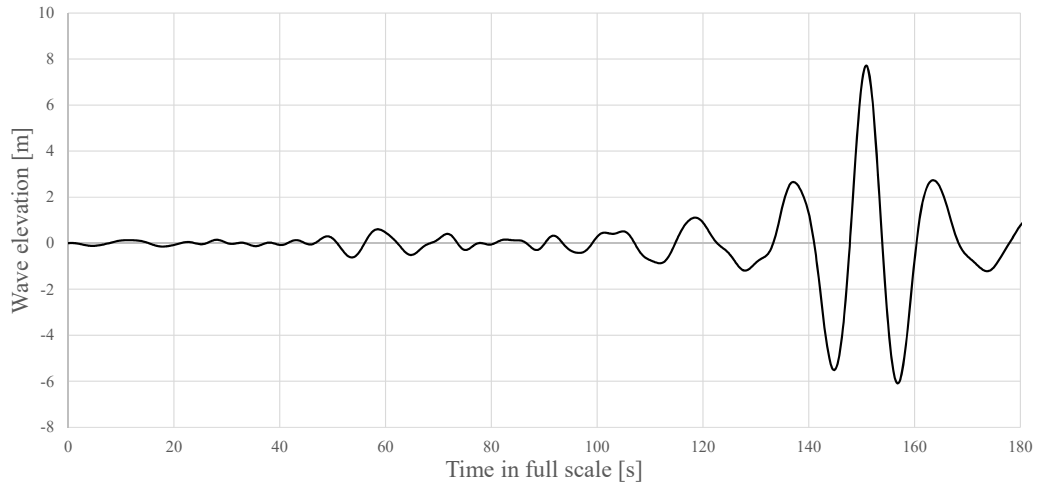

Figure 7.22 Predicted MPWE by using constructed ROM and FORM for combined wave-induced and whipping VBM (State 2, target; 4000MNm)

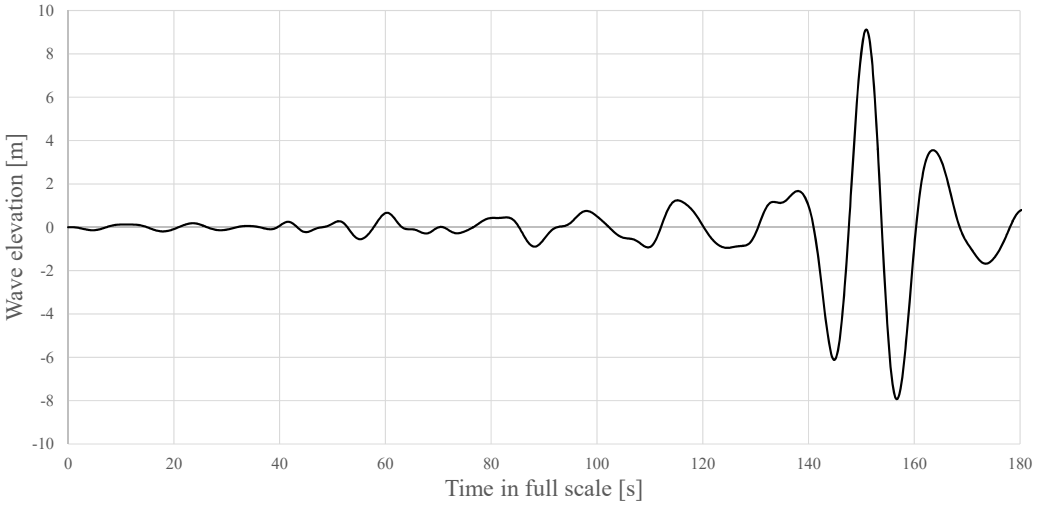

Figure 7.23 Predicted MPWE by using constructed ROM and FORM for combined wave-induced and whipping VBM (State 2, target; 5000MNm)

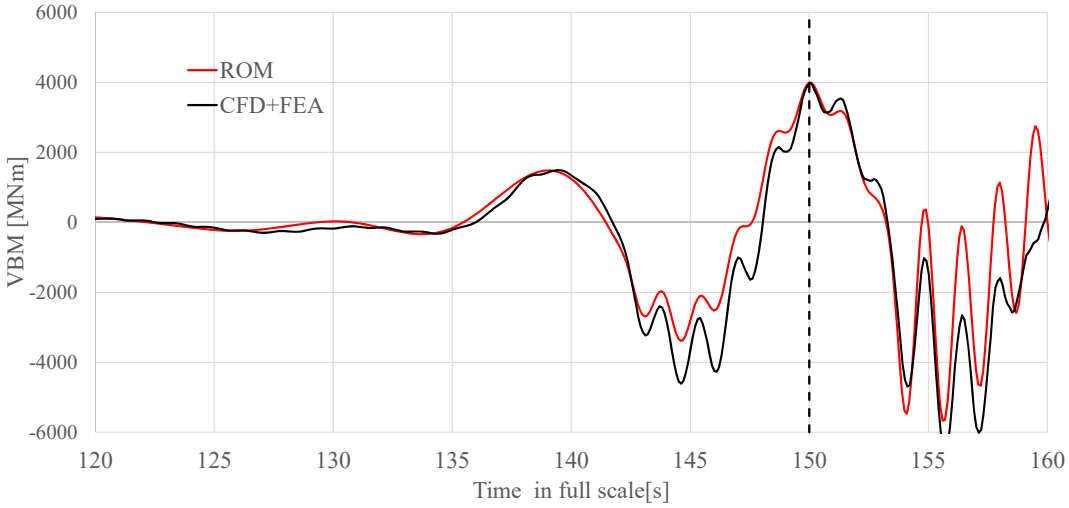

Figure 7.24 Comparison of VBM with whipping component between results from ROM and coupled CFD-FEA method under predicted MPWE for target response; 4000MNm (f_{2n}=0.67Hz, Figure 7.22)

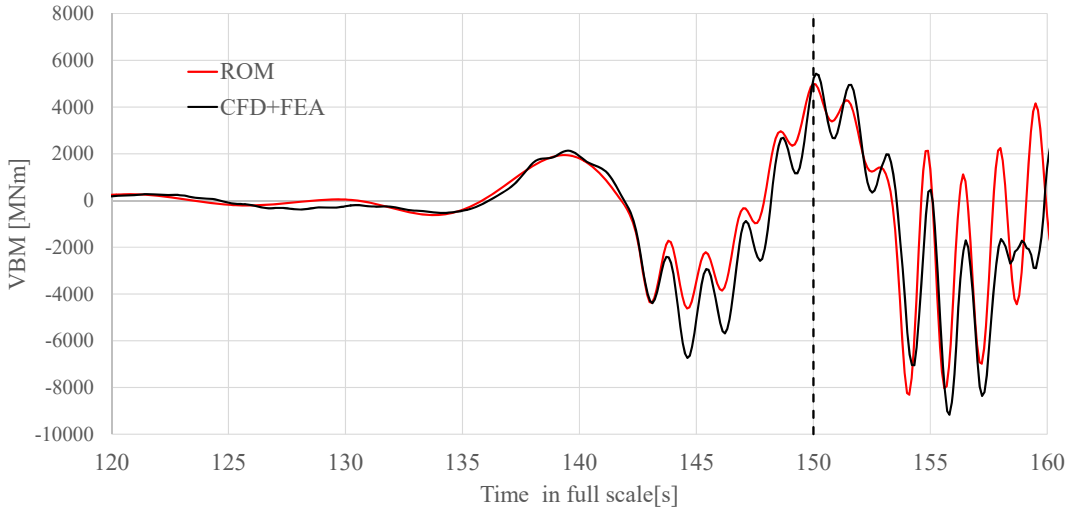

Figure 7.25 Comparison of VBM with whipping component between results from ROM and coupled CFD-FEA method under predicted MPWE for target response; 5000MNm (f_{2n}=0.67Hz, Figure 7.23)

7.3 Validation of ROM+FORM approach

In this section, the present ROM+FORM approach is validated by comparing with the towing tank test with the OU model. As the 2-node natural frequency of the OU model is 5.47Hz (0.55Hz in full scale), the present RO model for whipping VBM is reconstructed to be suitable for the OU model. Through the inspection process of optimal unknown variables, d, δ, c_{imp}, and τ_{imp} in Eq. (5.20) and Eq. (5.21), a comparison of VBM between

the reconstructed ROM and the CFD-FEA under tentative MPWE, Figure 7.17, is given in Figure 7.26. Adopted unknown variables are; d=22.0 [m], δ=70.0 [deg], c_{imp}=55.0, and τ_{imp}=0.8 [s] in full scale. In this section, this reconstructed ROM is used for validation studies. The target response is the VBM with and without whipping component.

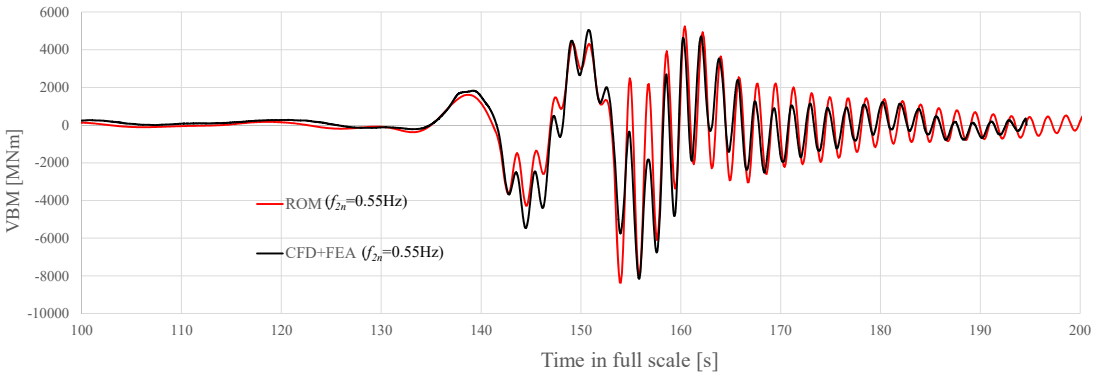

Figure 7.26 Comparison of VBM with whipping component between results from ROM and coupled CFD-FEA method under tentative MPWE (f_{2n}=0.55Hz, Figure 7.17)

7.3.1 Validation under deterministic MPWEs

By using the ROM+FORM, two MPWEs under State 2 are identified. The target extreme responses are the combined wave-induced (WF) and whipping (HF) VBM. Identified MPWEs (named MPWE 1 and MPWE 2) where the extreme VBMs are set to 4000MNm (MPWE 1) and 5000MNm (MPWE 2) are shown in Figures 7.27 and 7.28. The target time is 150 seconds in full scale. The reliability indices β are 4.09 and 4.26, respectively. These two MPWEs are generated in the towing tank and the VBM of the OU model are measured. To confirm the repeatability of the experiment, 5 trials are carried out on each case. Measured VBM from these trials under MPWE 1 and MPWE 2 are shown in Figures 7.29 and 7.30. A slight deviation in terms of the phase of VBM is found from Figure 7.29 in particular, which is mainly due to the difference in the initiation time of the experiments. Having said that, however, the uncertainty underlying the measurement from the experiment is quite small. Snapshots of the OU model at time T1 and T2 in Figure 7.30 is presented in Figures 7.31. From the figure, it can be seen that the bow flare slamming has surely occurred in the experiment at T1 and T2.

Comparisons of VBM between results from the present (reconstructed) ROM and the experiment under MPWE 1 and MPWE 2 are shown in Figures 7.321 and 7.33. The fifth trial results are plotted for experimental results. It should be emphasized that the

present ROM based on the coupled CFD-FEA could well predict not only the peak amplitudes of VBM but the phase of whipping VBM comparing with the experiment. When the extreme VBM values from each result are compared, the time to record the extreme value of VBM differs from the ROM and the experiment. One possible cause is the difference in phase of wave-induced VBM. The wave-induced (WF) components from the ROM and the experiment are also plotted in Figures 7.34 and 7.35. Although the extreme amplitude of the wave-induced VBM from the ROM is comparable to the experiment, approximately 0.4 seconds deviation is found concerning the time to record the extremes. This discrepancy would be able to be modified by using authentic TF of the wave-induced VBM of the experimental model itself. Figures 7.36 and 7.37 provide that of the whipping (HF) component. As to the whipping components, deviations in the phase of whipping VBM can be seen. Since the present ROM is constructed based on the 1D beam FE model and the oscillatory system with one degree of freedom, it can be inferred that more suitable RO modeling to reproduce the whipping characteristics would give us more plausible whipping VBM. This is able to be attained by finding plausible vibration characteristics of the OU model itself. After the target time 150s, the ROM overestimates the whipping VBM after the second slamming has occurred. Since the present ROM is constructed based on the one-way coupled CFD-FEA, the added-mass associated with the elastic deformation is not considered in the ROM. For more accurate prediction on whipping, the ROM should be reconstructed based on the (strong) two-way coupled CFD-FEA.

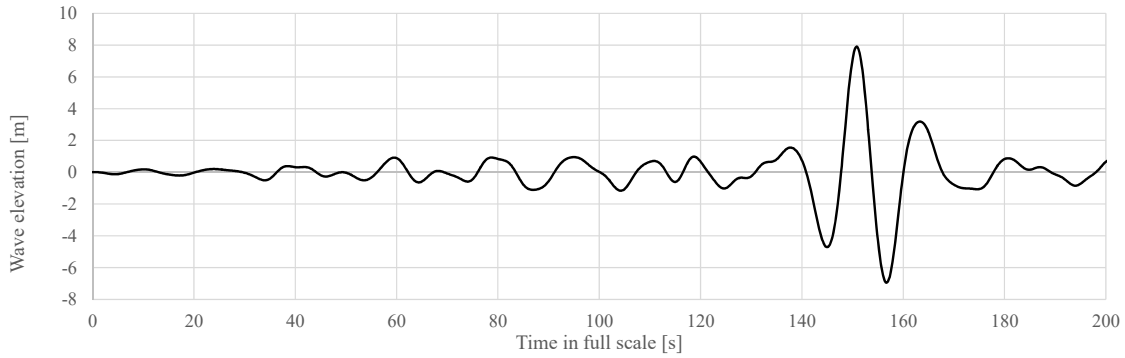

Figure 7.27 Predicted MPWE by using ROM and FORM for combined wave-induced and whipping VBM (State 2, OU model, MPWE 1)

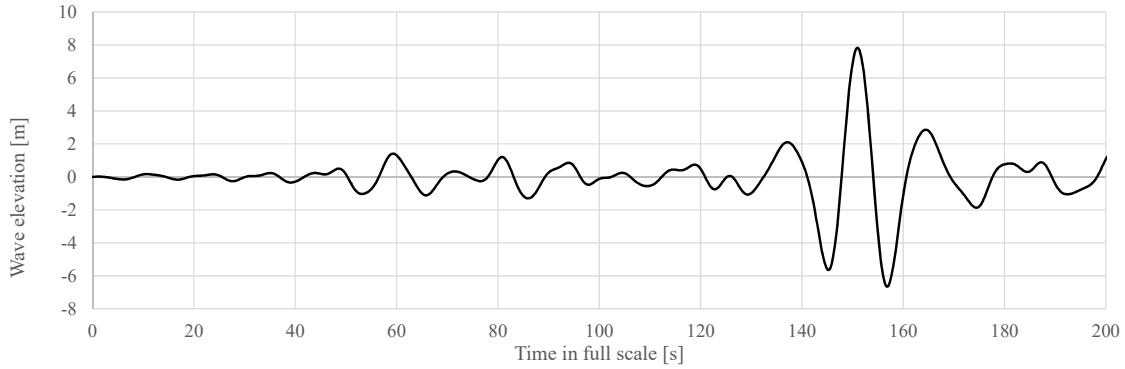

Figure 7.28 Predicted MPWE by using ROM and FORM for combined wave-induced and whipping VBM (State 2, OU model, MPWE 2)

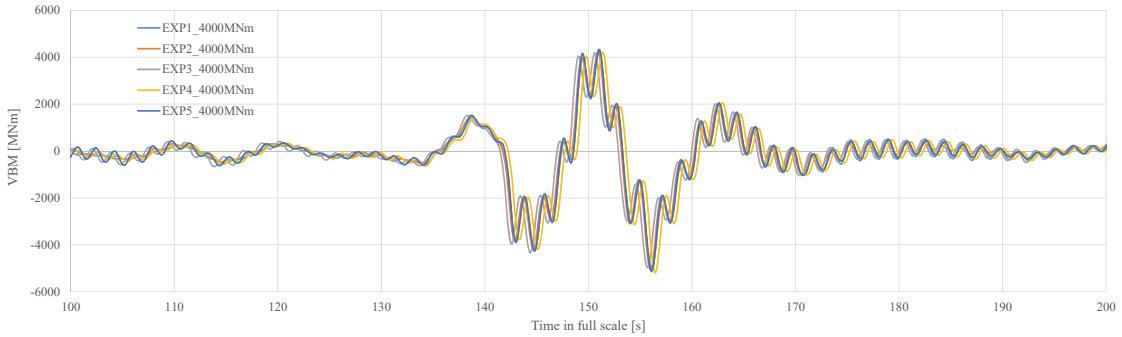

Figure 7.29 Measured VBMs by experiment with OU model under MPWE 1

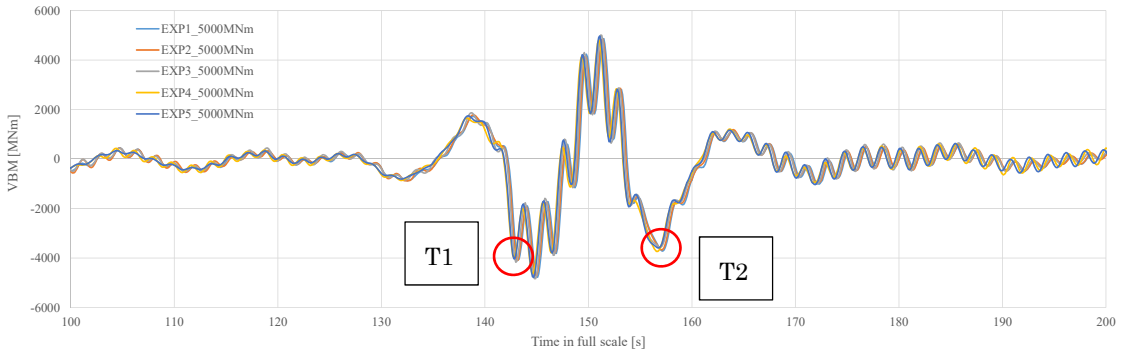

Figure 7.30 Measured VBMs by experiment with OU model under MPWE 2

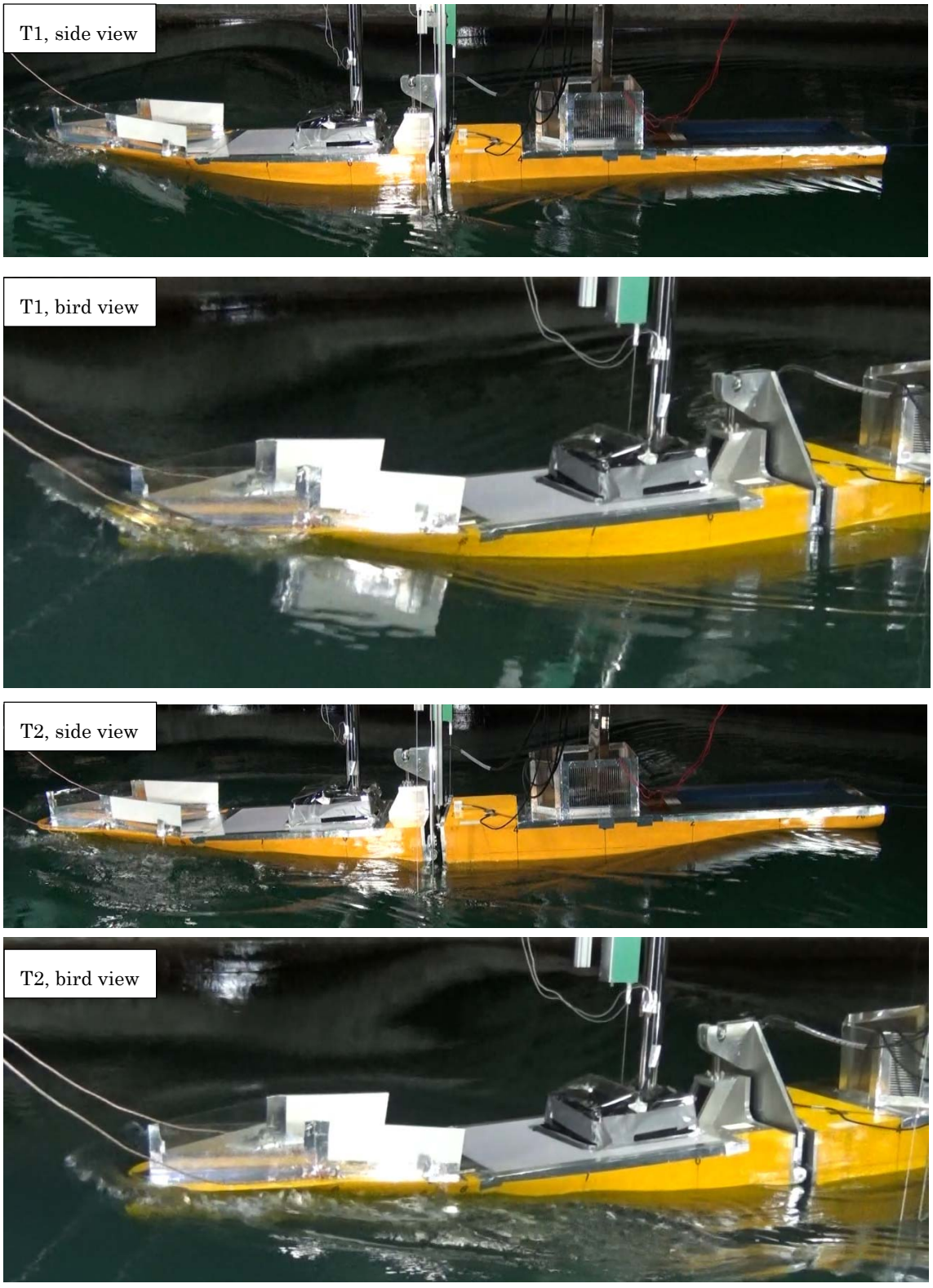

Figure 7.31 Snapshots of the OU model at time T1 and T2

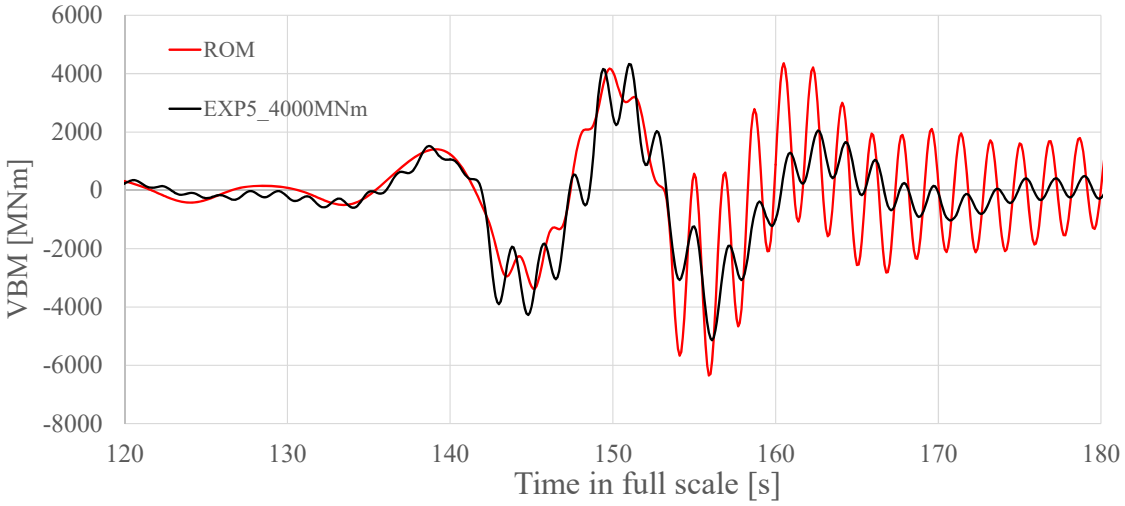

Figure 7.32 Comparison of VBM with whipping component between results from ROM and the experiment with OU model under MPWE 1

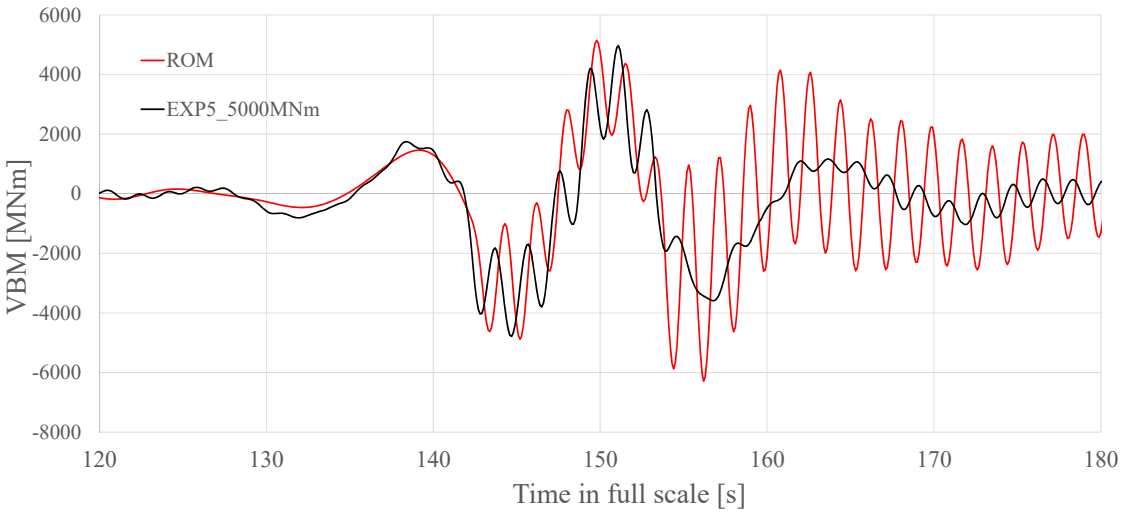

Figure 7.33 Comparison of VBM with whipping component between results from ROM and the experiment with OU model under MPWE 2

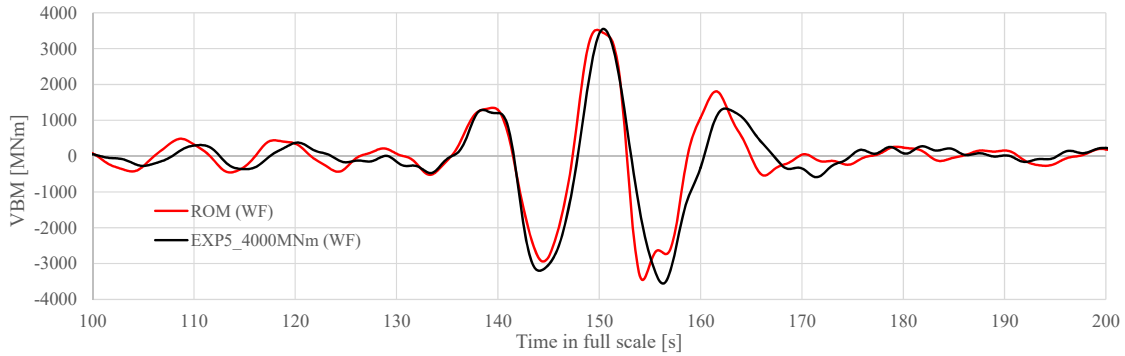

Figure 7.34 Comparison of wave-induced VBM between results from ROM and the experiment with OU model under MPWE 1

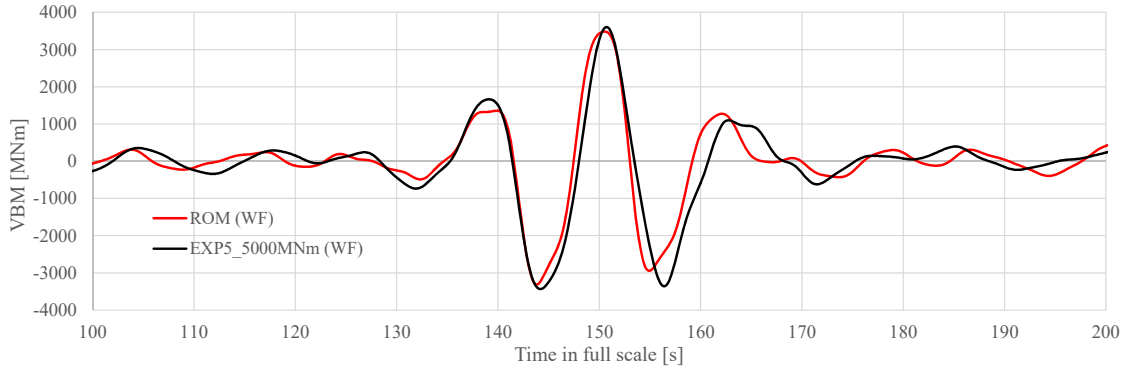

Figure 7.35 Comparison of wave-induced VBM between results from ROM and the experiment with OU model under MPWE 2

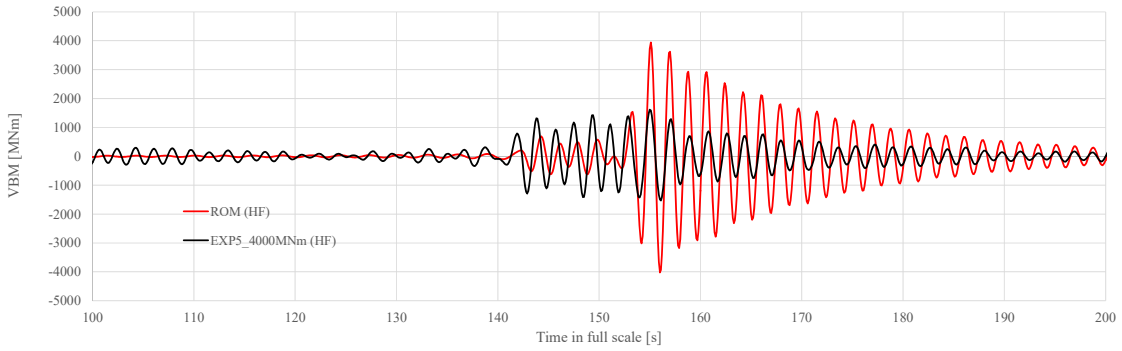

Figure 7.36 Comparison of whipping VBM between results from ROM and the experiment with OU model under MPWE 1

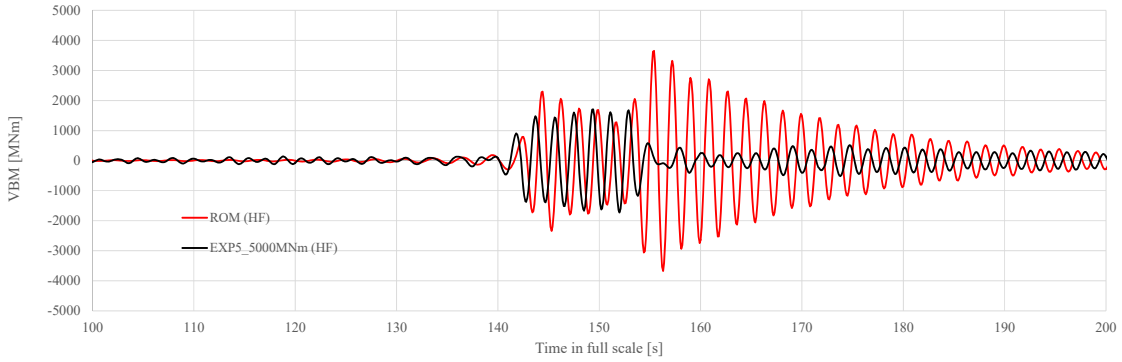

Figure 7.37 Comparison of whipping VBM between results from ROM and the experiment with OU model under MPWE 2

7.3.2 Validation of PoE

Next the PoEs of VBM (with and without whipping) under State 1 and State 2 are compared between the experiment and combined ROM and FORM. Here, c_{CFD} is assumed to be constant value 0.80 in the ROM. Figure 7.38 provides a comparison of PoE of wave-induced (WF) hogging VBM under State 1. In this figure, a result from combined nonlinear strip method and FORM (strip+FORM) is plotted as a reference. One may find that a difference in PoE between strip+FORM and the experiment is prominent. One possible cause of this discrepancy is that as the nonlinear strip method adopted in this study does not account for so-called memory effect [7.2], its accuracy of calculation might be poor.

When we look at the result from the present ROM+FORM, evaluated PoE shows closer level to the experiment than strip+FORM. Though the present ROM premises the constant value of c_{CFD} (=0.80), it is ideal that c_{CFD} is defined as a function of β somehow. Moreover, in order to improve ROM accuracy more, mesh refinement of the present CFD model may be further needed especially in the case of high PoEs such that the CFD model captures low wave heights. For instance, MPWE corresponds to Case 1 in Figure 7.38, where β=1.46, is shown in Figure 7.39. The maximum wave height is 3.3m from crest to trough, in that case. Since the mesh resolution of the present CFD over the free surface region is Δz= 0.99m in vertical direction, this makes up to 4 cells from crest to trough. This may be insufficient to correctly capture the wave elevation by the CFD [7.3]. Further refinement of the CFD and reconstruction of the ROM to represent higher PoE region are set aside as a future work. Nonetheless, the natural interpretation is that the present ROM+FORM predicts the PoE of wave-induced VBM in an acceptable manner.

Next the PoEs under State 2 are validated. As already described in sub-section 7.2.3, multiple design points with different β are derived from the ROM+FORM computations

in the case of the whipping component is included. For the sake of consistent evaluation of the PoE of target response, identified MPWE should be linked with the minimum value of β. In this study, 20 computations of ROM+FORM are conducted then among those taking minimum β are adopted to evaluate PoEs. Figure 7.40 provides a comparison of PoE of hogging VBM with and without whipping (HF) component under State 2. In this figure, a result from combined nonlinear strip method and FORM (strip+FORM) is plotted as well, in terms of wave-induced component. When the PoEs of wave-induced VBM are compared, a difference in PoE between strip+FORM and the experiment is also prominent under State 2. Meanwhile, the PoE of wave-induced VBM predicted by the present ROM+FORM method shows good agreement with the experiment in both the high and low PoE regions. It can be concluded that the present ROM+FORM approach can predict not only the wave-induced VBM under deterministic wave episode but also the probability of its occurrence.

When the PoEs of combined wave-induced and whipping (WF+HF) VBM are focused on, the PoEs derived from the present ROM+FORM show lower probability levels than the experiment. Since the POE being plotted is the minimum value of β within 20 ROM+FORM results, more probable design points may be found by increasing ROM+FORM calculation times. Note, however, that there may be other possible causes of this discrepancy;

A) Discrepancy in slamming impact force assumed in the ROM and the OU model.
B) The stern slamming might affect the PoE level from the experiment. (the present ROM accounts for only the bow flare slamming)
C) Springing effect.

As to A), since the whipping VBM in the ROM is formulated based on the two-dimensional slamming impact forces, it can be deduced that the three-dimensional distribution of the slamming force might affect the PoE levels. Thus, it is necessary to investigate how the three-dimensional distribution of the impact force influence the PoE levels, then the reformulation of the ROM to cope with this is ideal. It can be achieved by utilizing the direct combination of FORM and the coupled CFD-FEA in the future. B) stern slamming effect will be considered in the ROM with the same approach as the bow flare slamming. C) springing is the well-known phenomenon which appears as the steady-state vibrations due to the resonance of wave and the ship. As a reference, Figure 7.40 shows an example of measured VBM time series from the experiment. From Figure 7.40, high vibration components can be seen around 1300-1350 seconds (see (WF+HF)

result) despite the small wave height, which may be due to the springing effect. The springing might influence to the PoE levels over the lower VBM region, and obviously, we should consider its superposition with whipping to capture reliable PoE. Although the present ROM could predict the extreme VBM with and without the whipping effect under the deterministic MPWEs with good accuracy, as discussed in sub-section 7.3.1, re-construction of the ROM addressing the above causes is necessary in the future.

The long term effect of the whipping on VBM is finally investigated. Kawabe et al. [7.4] defined a quantitative parameter γ_{wh} to evaluate the long-term effect of the whipping.

$$\gamma_{wh} = \frac{M_{wh-1/1000}}{M_{w-1/1000}} \tag{7.4}$$

where $M_{w\text{-}1/1000}$ denotes the wave-induced VBM at the probability of exceedance of 10^{-3}, and $M_{wh\text{-}1/1000}$ the combined wave-induced and whipping VBM at the probability of exceedance of 10^{-3}. Table 7.2 compares γ_{wh} among the experiment in this study, numerical results from Kawabe et al. [7.4] and Lee et al. [7.5], and the experimental result given by Zhu and Moan [7.6]. All parameters are written in full scale. As found from the comparisons, the whipping effect factor γ_{wh} varies within the range of $\gamma_{wh}<1.5$. In the future, further investigation into the stochastic characteristic of γ_{wh} is necessary to ensure the ship's safety, hopefully, it is expected to be achieved by making use of a consistent numerical simulation method.

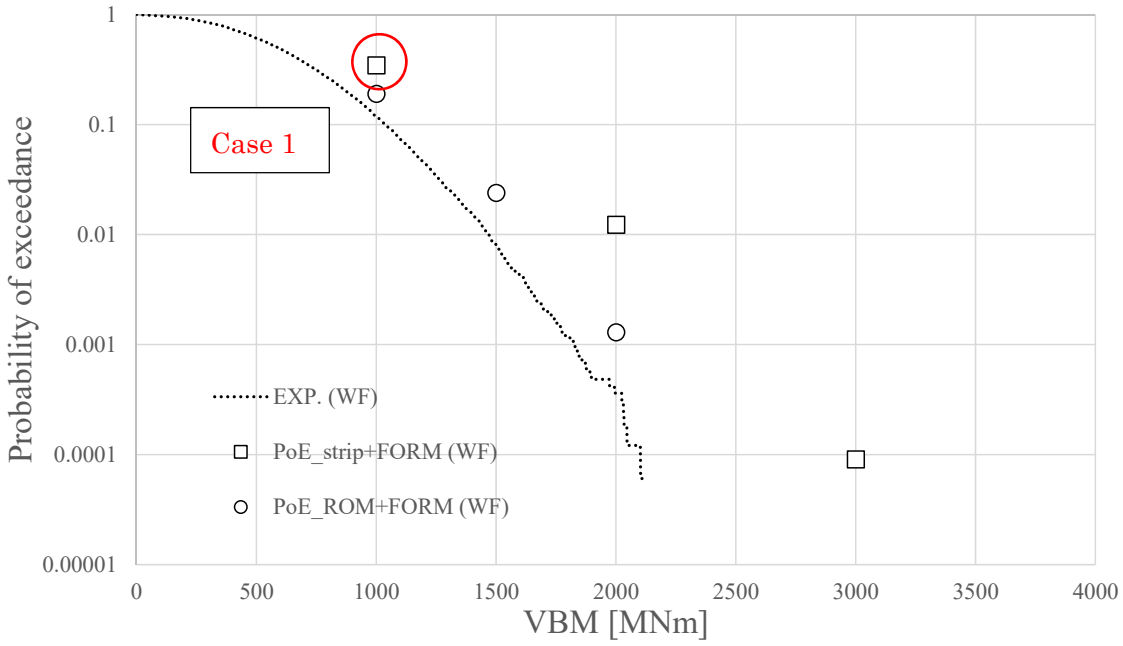

Figure 7.38 Comparison of PoE of wave-induced VBM among results from nonlinear strip method+FORM, ROM+FORM, and the experiment with OU model under State 1

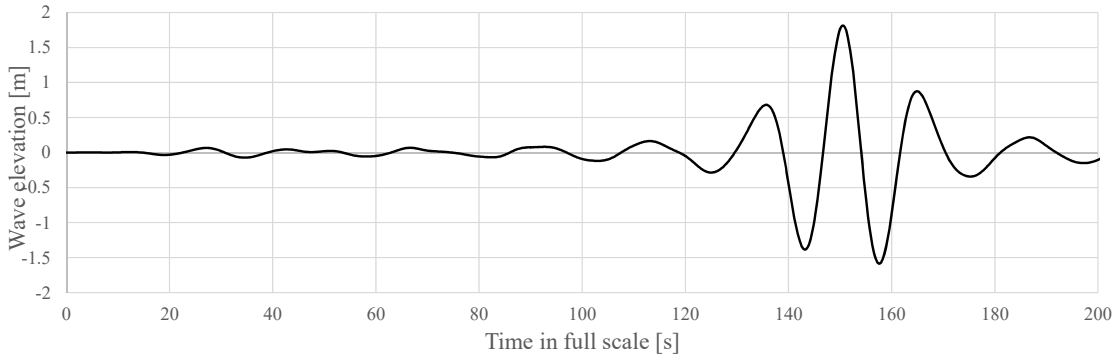

Figure 7.39 MPWE corresponds to Case 1 in Figure 7.37

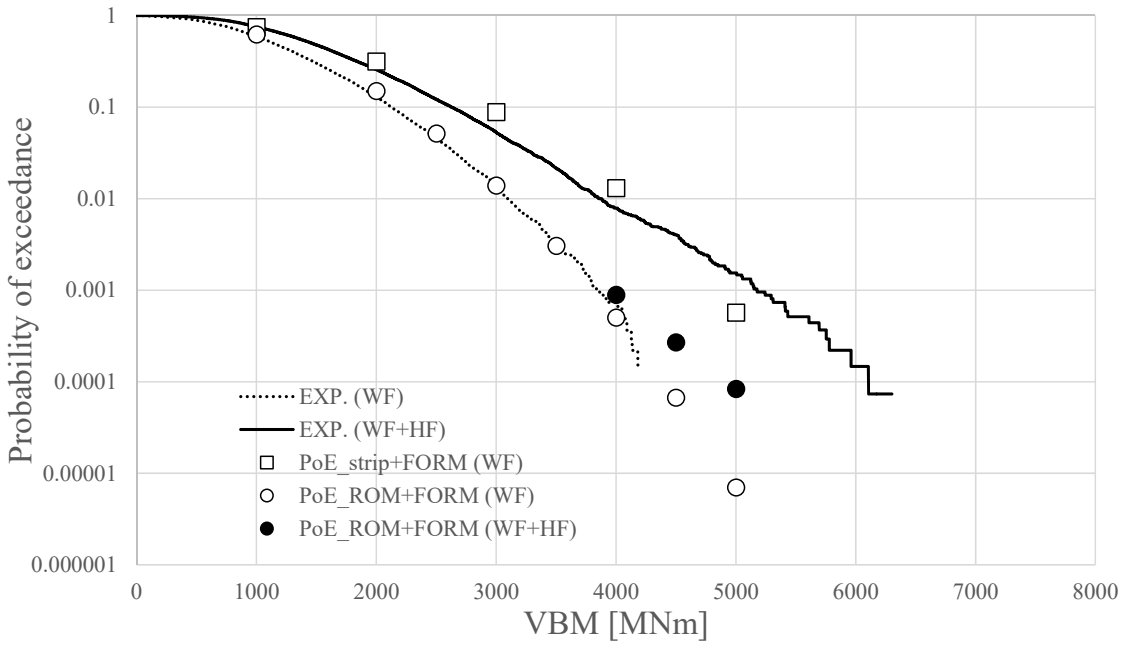

Figure 7.40 Comparison of PoE of wave-induced VBM among results from nonlinear strip method+FORM, ROM+FORM and the experiment with OU model under State 2

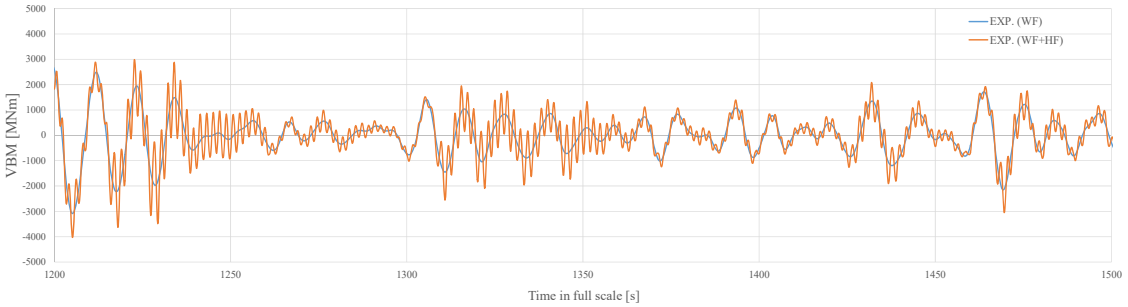

Figure 7.41 An example of measured VBM (with and without high frequency component) from the experiment with OU model under State 2

Table 7.2 Comparison of long-term whipping factors among previous studies and the experiment with OU model

	L_{pp}	H_s	T_z	Forward speed	γ_{wh}
OU model (This paper)	283.8m	11.5m	15.0s	8kt	1.32
Kawabe et al. (2016)	280-350m	15.0m	11-12s	5kt	1.47 (mean value)
Lee et al. (2012)	350m	14.5m	11.5s	5kt	1.42
Zhu and Moan (2014)	350m	11.5m	11.5s	10kt	1.43

7.4 Investigation into Effect of DBM

It is a generally recognized that the DBM could impair the structural capacity on the outer bottom panel. In this section, the effect of DBM on the probability of failure is investigated by utilizing the present ROM and FORM. Combined wave-induced VBM and DBM under State 1 is targeted to be evaluated. The formulation of the limit state function is basically compliant with Eq. (5.25);

$$
\begin{aligned}
g &= 1 - L \\
&= 1 - \left(\frac{r_{t,glob}}{M_{uh,glob}} + \frac{r_{t,db}}{M_{uh,db}} \right) = 1 - \left(\frac{M_{wave} + M_s}{M_{uh,glob}} + \frac{M_{db} + M_{s,db}}{M_{uh,db}} \right) \\
&where \quad r_{t,db} = M_{h,db}\left(u_1, u_2, \cdots u_N, \overline{u}_1, \overline{u}_2, \cdots \overline{u}_N \mid t_0\right)
\end{aligned}
\tag{7.5}
$$

where M_{wave} denotes the wave-induced VBM, M_s denotes the still wave VBM, M_{db} denotes the wave-induced component of DBM, and $M_{s,db}$ denotes the DBM under still water. Both the VBM and DBM are calculated via the present ROMs. In the case of the subject ship, M_s and $M_{s,db}$ are found at 4431MNm and 6.63MNm. Adopted $M_{uh,glob}$ and $M_{uh,db}$ are 13,200MNm and 34.4MNm, respectively. To examine the DBM effect on the PoEs of combined load L in Eq. (7.5), extreme value predictions under the following two cases are carried out.

Case 1

M_{wave}: Estimated by ROM

M_s: 4431MNm

M_{db}: 0MNm

$M_{s,db}$: 6.63MNm

Case 2

M_{wave}: Estimated by ROM

M_s: 4431MNm

M_{db}: Estimated by ROM

$M_{s,db}$: 6.63MNm

Figure 7.42 provides a comparison of PoEs of combined load L estimated by ROM and FORM under Case 1 and Case 2. Dotted lines denote the Weibull fitted results. One may find that a significant difference of PoEs appears between Case 1 and Case 2. Figure 7.43 shows a comparison of MPWEs evaluated from two where the extreme combined load L=0.7. Predicted β are 4.09 in Case 1 and 3.72 in Case 2. The respective maximum wave elevations of each MPWE are 5.07m and 4.62m. From Figure 7.42, the difference of phase between two MPWEs is subtle, and this implies that the VBM peak and DBM peak appear at around the same time. From the aspect of difference of response level at the same PoE, e.g. PoE level at 0.001, associated combined load L is 0.682 in Case 1 and 0.70 in Case 2. This indicates that the DBM influences 2.1% of ultimate strength of the hull girder. From this insight, it can be concluded that one should account for the DBM effect in assessing hull girder capacity, on top of the whipping VBM effect, to ensure the structural safety.

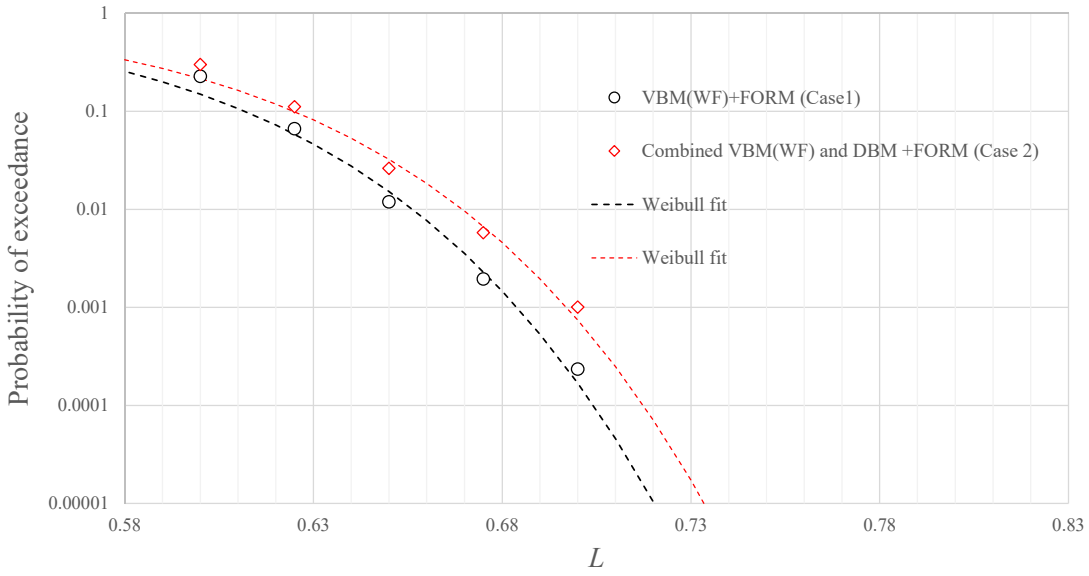

Figure 7.42 Comparison of PoEs of combined load L between Case 1 (not consider DBM) and Case 2 (consider DBM) under State 1

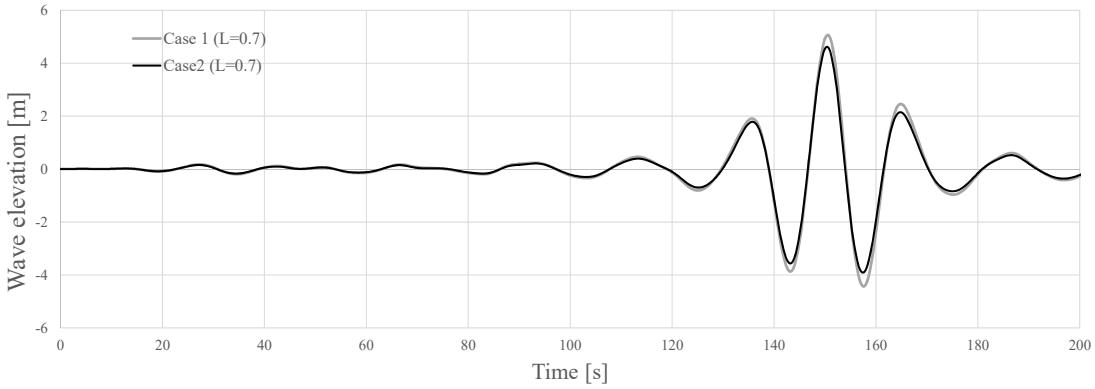

Figure 7.43 Comparison of MPWEs leading to *L=0.7* under Case 1 (not consider DBM) and Case 2 (consider DBM)

7.5 Summary of Chapter 7

In this chapter, the construction process of ROM for predicting the MPWEs leading to extreme values of VBM and DBM of a container ship under a given short-term is introduced. The validity of the present ROM is first demonstrated by comparing with the coupled CFD-FEA results in terms of prediction accuracy of wave-induced VBM and whipping VBM. Then, the accuracy of the present ROM is validated by comparing with towing tank test results using the OU model. The followings are concluded.

1. The present ROM can consistently predict the extreme wave-induced hogging VBM with and without the ship's forward speed obtained by the coupled CFD-FEA.
2. The present ROM can sufficiently predict the extreme hogging VBM superimposing the whipping component obtained by the coupled CFD-FEA, in terms of the amplitude and phase of the whipping VBM.
3. Through the comparisons between the ROM and the towing tank experiment, it turned out that the present ROM can quantitatively predict the extreme VBMs with whipping under deterministic MPWEs.
4. The present ROM can consistently predict the probability of exceedance (PoE) of wave-induced VBM by combining the FORM, which is comparable to the experimental results. A consideration of the stern slamming and springing effects may be necessary to capture PoE more accurately.
5. Through the investigation into the effect of the DBM on the PoEs, it is demonstrated that the DBM influences 2.1% of ultimate strength of the hull girder.

7.6 Suggestions for Future Study

Enhancement of the ROM

As the ROM constructed in this study is based on the one-way coupled CFD-FEA, the development of the ROM for two-way coupled method is an urgent work. The present ROM formulation shown in Chapter 5 may still be useful for it, if the numerical models for two-way coupled CFD-FEA under irregular waves are successfully organized and well validated.

The considerations of the stern slamming and springing effect on VBM may be also needed to predict PoEs of VBM in flexible ship body accurately. The stern slamming effect may be accounted for in the ROM as is in the case of bow flare slamming. As for the springing, RANS based CFD has been recently applied to higher order resonant springing estimations by Hänninen et al. [7.7]. They demonstrated that the careful prediction of three-dimensional and impact-type behavior of the flow is relevant for the modelling of excitation of second-order resonant springing. Finding appropriate CFD model would be the first step to this end.

ROM for other purposes

Within the maritime field, there may be several problems that the ROM is likely to be adoptable. The torsional moment of the ship, which is regarded as problematic for recent large container ships, is one of them. Recently, Houtani et al. [7.8] proposed a new designing strategy to estimate a combination of VBM and torsional moment and

performed a series of towing tank experiments. They have successfully measured the torsional moment while keeping the similarity against the full scale ship, thus their reports may be helpful for the validation of the ROM. Since the torsional moment in the container ship is mainly attributed to the bow flare slamming impact, the ROM in this study is presumably adaptable if the proper LSF for torsional moment is given. Note, however, that the CFD computations in this study have been performed only in head waves. As the torsional vibration is generally excited under oblique sea conditions, establishment of CFD computation techniques in oblique waves would be necessary.

The response forecasting is also a conceivable theme where the ROM is adoptable. Nielsen et al. [7.9] recently proposed a prediction method for the ship motion based on the measured autocorrelation function. Their approach is interesting in the sense that it made us possible to achieve near real time and deterministic prediction of future ship motion. As the present ROM can instantaneously provide the combined VBM and DBM predictions under the given irregular wave episode, if the TF of the ship motion has been clarified, it will be also possible to achieve near real time prediction of combined load by using the autocorrelation function of ship motion.

As a matter of course, adoptable structure may not be limited to the ship. From the viewpoint of structural safety, the determination of Equivalent Design Wave (EDW) is of importance for any floating offshore structures (e.g. Ref. [7.10]). It would be necessary to take into account the wave impact load and subsequent hydroelastic vibration effects appropriately.

Addressing other extreme value problems

Looking at the maritime field, there may be several problems which are concerned with extreme values. Extreme ship roll motion is one of them. Recently, Choi et al. [7.11] conducted an application of FORM to extreme roll angle estimations up to capsize, based on a physic-based 1D roll motion model. Although their work was conducted using a fictitious vessel, extreme roll angle prediction would be one of the problems to be addressed in the future. Nonetheless, more efforts would be necessary as the roll motion has a strong nonlinearity.

Extreme sloshing load prediction would also be one of them. Graczyk et al. [7.12] carried out a probabilistic analysis of sloshing loads based on the peak-over-threshold (POT) method. Up until now, however, there may be no research activities which applied FORM to extreme sloshing load predictions. Sloshing load has a strong nonlinearity in general, notably in sloshing impact load, regardless of the tank shapes. Thus one should carefully conduct the extreme value predictions in this context. Further, as found from

the recent trend of relevant research activities (e.g. [7.13]), the mutual interactions between the ship motion and liquid sloshing in tanks are ought to be taken into account.

Although the subject ship in this study is 6000TEU class container ship, much larger container ships that reach up to 20000TEU size are in service nowadays. From a practical viewpoint, stochastic characteristics of whipping VBM in more recent container ships should be thoroughly investigated in the near future.

References in Chapter 7

[7.1] A. Tatsumi and M. Fujikubo, “Ultimate Longitudinal Strength Analysis of Container Ships Considering Bottom Local Loads- Part 3: Development of Simplified Estimation Method of Ultimate Longitudinal Bending Strength -,” *J. Japan Soc. Nav. Archit. Ocean Eng.*, vol. 25, pp. 133–142, 2017.

[7.2] K. Saito and H. Higashi, “Time Domain Analysis of Ship Responses in Waves Part 2 : Memory Effect on Ship Maneuvering in Waves,” *J. Soc. Nav. Archit. Japan*, vol. 1993, no. 174, pp. 319–325, 1993.

[7.3] CD-ADAPCO, “User Guide STARCC+ 10.06.009.” 2015.

[7.4] H. Kawabe, T. Shigemi, T. Matsumoto, K. Ishibashi, and K. Toyoda, “Quantitative Estimation Method for Vertical Wave-induced Bending Moments of Very Large Container Ships in Consideration of the Effects of Whipping,” in *Proceedings of 3rd International Conference on Violent Flows*, 2016.

[7.5] Y. Lee, N. Whitea, Z. Wang, and J.-B. Park, “Whipping Responses and Whipping Effects on Design Bending Moments of a Large Container Ship,” in *Hydroelasticity in Marine Technology 2012 Tokyo, JAPAN*, 2012.

[7.6] S. Zhu and T. Moan, “Nonlinear effects from wave-induced maximum vertical bending moment on a flexible ultra-large containership model in severe head and oblique seas,” *Mar. Struct.*, vol. 35, pp. 1–24, 2014.

[7.7] S. K. Hänninen, T. Mikkola, and J. Matusiak, “Development of vertical second harmonic wave loads of a large cruise ship in short and steep head waves,” *Ocean Eng.*, vol. 118, pp. 17–27, 2016.

[7.8] H. Houtani *et al.*, “Designing a hydro-structural model ship to experimentally measure its vertical-bending and torsional vibrations,” in *8th International Conference on HYDROELASTICITY IN MARINE TECHNOLOGY*, 2018.

[7.9] U. D. Nielsen, A. H. Brodtkorb, and J. J. Jensen, “Response predictions using the observed autocorrelation function,” *Mar. Struct.*, vol. 58, no. November 2017, pp. 31–52, 2018.

[7.10] J. M. Sohn, H. J. Cheon, K. Hong, and S. H. Shin, “Equivalent design wave approach for structural analysis of floating pendulum wave energy converter,” *Ships Offshore Struct.*, vol. 11, no. 6, pp. 645–654, 2016.

[7.11] J. Choi, J. J. Jensen, H. O. Kristensen, U. D. Nielsen, and H. Erichsen, “Intact Stability Analysis of Dead Ship Conditions using FORM,” *J. Sh. Res.*, vol. 61, no. 3, pp. 167–176, 2017.

[7.12] M. Graczyk, T. Moan, and O. Rognebakke, “Probabilistic Analysis of Characteristic Pressure for LNG Tanks,” *J. Offshore Mech. Arct. Eng.*, vol. 128, no. 2, p. 133, 2006.

[7.13] X. Wang, G. Karuka, and M. Arai, “Nonlinear Effects of Wave Heights on Coupled Sloshing and Seakeeping Responses,” in *Proceedings of the ASME 2018 37th International Conference on*

Ocean, Offshore and Arctic Engineering, 2018.

Chapter 8
CONCLUSIONS

In this thesis, a coupled CFD and FEA method for evaluating the combined load of ships consistently, is developed. The method is validated through a comparative study against other seakeeping codes and the towing tank tests, in terms of the wave-induced VBM, the whipping VBM and DBM in a POST PANAMAX size container ship. The method is then applied to the extreme value prediction of the combined loads by FORM. The *predictor-corrector* approach is adopted to estimate extreme wave-induced VBM and DBM in lieu of direct combination of the FORM and coupled CFD-FEA. Then, a ROM is newly constructed to estimate the extremes on the wave-induced VBM, DBM, and whipping VBM. The validation studies of the ROM are carried out by comparing with the towing tank experiments.

First the development and validation of the coupled CFD-FEA is carried out. The straightforward one-way coupling is firstly developed then the weak/strong two-way coupling is subsequently developed to take account of the added-mass effect from the elastic deformation of the ship. The coupled CFD-FEA is further applied to the DBM estimation. The following conclusions are drawn.

- The present CFD model predicts the rigid body motions of the ship with good accuracy when compared with the experimental results under regular head sea conditions. The prediction accuracy is almost comparable to the linear/nonlinear strip methods and 3D panel method. The accuracy of the present CFD tends to become less for the longer wave range with the wave length ratio λ/L_{pp} over 1.0.
- The bow-flare slamming impact pressure can be estimated by the present CFD with high accuracy, which is comparable to the experimental results.
- The results from one-way coupled CFD and FEA agree well with the experimental results in terms of the VBM including the whipping component. The results are almost comparable to those by the weakly nonlinear methods based on 3D potential theory or nonlinear strip method. However, the difference of natural frequency between the one-way coupled CFD-FEA and experimental results is observed.
- With the coupled CFD and FEA over a realistic large container ship, the combined VBM and DBM is observed on the double bottom structure. Besides, it turned out that the magnitude of the local stress due to the DBM is of non-negligible level from

a view point of the strength assessment of the double bottom structure.

- When the weakly two-way coupled method is applied to predicting the ship loads, good accuracies are shown in terms of the local pressure time series and wave-induced VBMs. Discrepancies in the whipping vibrations arise from the poor representation of the added mass associated with the elastic deformation.
- When the strongly two-way coupled method is applied to predicting the ship loads, good accuracies are shown even for the whipping vibrations due to the appropriate evaluation of the added mass effect. Meanwhile, the computational effort has significantly increased as the strongly two-way coupled method needs the sub-iteration process to secure the convergence.

Next, in an attempt to employ the (one-way) coupled CFD-FEA towards the extreme value predictions, the FORM is used for the predictions. To overcome the issue regarding the increase of computational efforts in detecting design points during FORM, the *predictor-corrector* approach where the nonlinear strip method is used as the *predictor* is applied. The following conclusions are drawn.

- By applying the *predictor-corrector* approach, the MPWE leading to the extreme wave-induced VBM is successfully identified.
- The prediction accuracy of the *predictor* with the MCF is found good in terms of combined wave-induced VBM and DBM when compared with the coupled CFD-FEA using a realistic large container ship.
- However, the present *predictor-corrector* approach fails to predict the extreme values of combined wave-induced and whipping VBM, due to the significant deviation of whipping response estimation between the nonlinear strip method and the CFD-FEA coupling.

Further, the ROM is newly constructed to accomplish the fast and robust prediction of the coupled CFD-FEA results including the whipping VBM. A series of numerical demonstrations to verify the ROM against the coupled CFD-FEA is conducted, then the prediction accuracy is validated by comparing with the experimental results. The following conclusions are drawn.

- The present ROM can consistently predict the extreme wave-induced VBM with and without the ship's forward speed obtained by the coupled CFD-FEA.
- The present ROM can sufficiently predict the extreme VBM superimposing the

whipping component obtained by the coupled CFD-FEA, in terms of the amplitude and phase of the whipping VBM.

- Through the comparisons between the ROM and the towing tank experiment, it turned out that the present ROM can quantitatively predict the extreme VBMs with whipping under deterministic MPWEs.
- The present ROM can consistently predict the PoE of wave-induced VBM by combining the FORM, which is comparable to the experimental results. A consideration of the stern slamming and springing effects may be necessary to capture PoE more accurately.
- The ROM can be also useful for the DBM. Through a comparative demonstration of PoEs, non-negligible DBM effect is found at the probability level 10^{-3}, i.e. 2.1% increase against ultimate strength of the hull girder.

ACKNOWLEDGEMENTS

First and foremost, I would like to express the deepest appreciation to my supervisor, Professor Kazuhiro Iijima, for his invaluable support, encouragement, inspiration, supervision, and fruitful discussions throughout this research. Without his kind and intelligent guidance or support, this dissertation would not have been completed. His enthusiasm for research work always motivated me. I am sincerely proud to be one of his students.

Special thanks to Professor Masahiko Fujikubo, for his constructive suggestions, encouragement and personal attention for my PhD. I am also grateful to Associate Professor Atsuo Maki, for his helpful comments and suggestions from his deep knowledge about probability statistics.

I would also like to thank Dr. Toichi Fukasawa, for his precious comment and suggestion about extreme value prediction from his vast knowledge. Without his knowledge, I could not have conducted fulfilling experiment. Highly appreciate his guidance towards the right direction.

I want to thank all colleagues in Structural Analysis Research Group, National Maritime Research Institute. Dr. Masayoshi Oka gave me a chance to get PhD degree, and of course, he always showed understanding in my work. I owe a debt of gratitude to Dr. Chong Ma, for meaningful discussions about CFD computation and FSI methodologies. I thank Mr. Takahiro Ando and Mr. Yusuke Komoriyama for their cooperation to conduct experiment. I will never forget the hot days we spent. I also thank Mr. Sadaoki Matsui for offering NMRIW-II code and helping me to make a model.

I would like to dedicate this thesis to the late Dr. Yusuke Tahara, NMRI. His gentle and heartfelt encouragement always motivated me, and often I could be advised by him through a lot of discussions about CFD and FSI. Even now he is a role model for me to work as a researcher. I wanted to work with him more and learn from him more, I never forget the days with him.

My heartfelt appreciation goes to Mr. Shohei Ozeki, Siemens PLM Software Computational Dynamics K.K., for his kind support to construct CFD models.

The part of this research is funded by JSPS Grant-in-Aid for Scientific Research (B) (17H03488) from the Japan Society for the Promotion of Science. I would like to acknowledge this support.

I want to thank my parents, for their continued backup. I really appreciate your kind and considerate supports throughout my life. Finally, I would like to thank my wife,

Ayaka. Throughout the three years, you have always expressed a deep understanding of my research, continued physical and mental support, provided encouragement, and trusted me.